Tuneable Liquid Crystal Elastomer Devices with Electric-field Induced Alignment

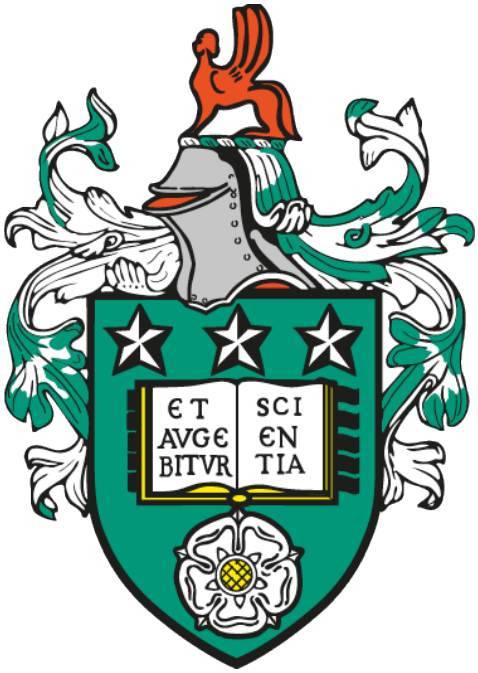

Zhenming Wang

University of Leeds

Department of Physics and Astronomy

Submitted in accordance with the requirements for the degree of

Doctor of Philosophy

April 2025

Declaration

The candidate confirms that the work submitted is his own and that appropriate credit has been given where reference has been made to the work of others. The contribution of the candidate and the other authors to this work has been explicitly indicated below. The candidate confirms that appropriate credit has been given within the thesis where reference has been made to the work of others.

Chapter 2 contain work that has been published in the following review paper: Zhenming Wang, Ming Cheng, Zixuan Wu, Yuyuan Qiu, Yan Jun Liu, “Advances of complex molecular alignments and multiplex deformations in liquid crystal elastomers”. Chinese journal of liquid crystals and displays, **2024**, *40*, 1-20. The writing of the alignment methods review in this paper was performed by Zhenming Wang, Ming Cheng, Zixuan Wu and Yuyuan Qiu reviewed the LCEs deformation part, Prof. Yan Jun Liu provided feedback, edits, and advice on the paper and its contents throughout. All authors provided feedback during writing.

Chapter 3 and Chapter 5 contain work that has been published in the following paper: Zhenming Wang, Thomas Raistrick, Aidan Street, Matthew Reynolds, Yan Jun Liu, Helen F, Gleeson, “Direct Observation of Biaxial Nematic Order in Auxetic Liquid Crystal Elastomers”. *Materials* **2022**, *16*, 393. Writing of this paper was performed by Zhenming Wang, Aidan Street, Thomas Raistrick and Helen F. Gleeson (supervisors of Zhenming Wang). Yan Jun Liu and Helen F. Gleeson (supervisors of Zhenming Wang) provided feedback, edits, and advice on the paper and its contents throughout. Fabrication of the samples and the mechanical measurements were performed by Zhenming Wang. The order parameter measurement was performed by Aidan Street. The conoscopy was performed by Thomas Raistrick. All authors provided feedback during writing.

Below, the specific contributions from the authors towards this paper will be provided, as well as any additional contributions towards this thesis that are separate from the paper.

Thomas Raistrick performed the measurement of the dielectric constants of IALCE precursor in Chapter 4. Thomas Raistrick performed the conoscopy in Chapter 5. Thomas Raistrick also provided the mathematical model for investigating the tuneable threshold strains in Chapter 6.

Aidan Street performed the order parameter measurement in Chapter 5.

Matthew Reynolds provides the anisotropic deswelling measurement in Chapter 6.

List of publications:

- **Wang, Z.**, Cheng, M., Wu, Z., Qiu, Y., Liu, Y. Advances of complex molecular alignments and multiplex deformations in liquid crystal elastomers. *Chinese journal of liquid crystals and displays*, 2024, 1-20..
- **Wang, Z.**, Raistrick, T., Street, A., Reynolds, M., Liu. Y. J., Gleeson, H. F. Direct Observation of Biaxial Nematic Order in Auxetic Liquid Crystal Elastomers. *Materials* 2022, *16*, 393.
- **Wang, Z.**, Liu, J., Wang, J., Ma, Z., Kong, D., Jiang, S., Luo. D., Liu. Y. J. *Nanomaterials* 2022, *12*, 1202.
- **Wang, Z.**, Liu, J., Fang, X., Wang, J., Yin, Z., He. H., Jiang. S., Zhao, M., Yin. Z., Luo. D., Liu. Y. J. Plasmonically enhanced photoluminescence of monolayer MoS_2 via nanosphere lithography templated gold metasurface. *Nanophotonics* 2021, *10*, 1733-1740.

Conferences

- **Poster** Presentation at the International Liquid Crystal Society Conference, 2022, Lisbon, Portugal.

Prizes and Bursaries

- **Bursary** from the British Liquid Crystal Society to attend the International Liquid Crystal Society Conference, 2022, Lisbon, Portugal.
- **Bursary** from the Soft Matter Physics Group at the University of Leeds to attend the International Liquid Crystal Elastomer Conference, 2025, Tampere, Finland.

This thesis is dedicated to my family, my friends and myself

Acknowledgements

I never expected that writing the acknowledgements would be the most difficult part of this thesis. Reaching this point feels almost like a dream. Completing a PhD is undeniably a milestone in my life, yet the decision to embark on this journey was, in many ways, made in haste. For a long time, I couldn't quite understand the version of myself who made that choice. But as I look back over the past four years, I begin to see things differently. I see the incredible progress I've made, the surprising ways in which I've grown, and I have come to appreciate that impulsive decision — even feel grateful for it. I'm beginning to understand the true meaning of this journey. There are countless complex problems in this world, and perhaps what I have truly learned is how to begin understanding them — how to explore the world, to seek the objective laws that govern its development, and to accept both the logic behind everything that exists and the possibility of all that may happen. Most importantly, I have learned how to grow into a whole person — someone capable of understanding himself, managing himself, and facing challenges with clarity and confidence. Perhaps reaching a far-off destination was never the true purpose. Maybe it lies instead in learning to believe in yourself even after accepting your own ordinariness — to take that brave first step, and then keep going, with steady determination. That, I believe, is the true meaning of this journey.

First and foremost, I would like to express my deepest gratitude to my supervisor, Prof. Helen F. Gleeson — a highly respected and truly inspiring female scientist. Your encouragement and affirmation have been the greatest driving force on my journey. Thank you for teaching me how to approach problems methodically and for instilling in me the importance of rigorous, critical scientific thinking. You have always led by example — not only in research, but in life as well — generously sharing your wealth of experience. Your influence has shaped me in lasting ways that will benefit me throughout my life. Thank you for your unwavering kindness and support, which have made my PhD life both meaningful and fulfilling. As an international student, I often felt the need to prove myself, afraid to show uncertainty or ask for help. But you reminded me that I am here to learn, it is okay to seek guidance, and that we are all still learning, no matter where we are in our journey. These words stayed with me, helping me come to terms with my own limitations and embrace the space for growth. They also gave me the courage to believe in myself. None of this work would have been possible without you. I cannot thank you enough! I would also like to

sincerely acknowledge my supervisor at the Southern University of Science and Technology (SUSTech), Prof. Yanjun Liu, for your continuous support throughout my PhD. Over the years, I have learned from you the value of perseverance, the strength in resilience, and many meaningful lessons about life. During my most difficult and uncertain times, thank you for choosing to believe in me and for giving me opportunities, which means a lot to me.

I would like to express my thanks to every member of the Soft Matter Group at the University of Leeds and of Lab 338 at SUSTech. Thank you all for providing a supportive and stimulating research environment, as well as a warm and collaborative learning atmosphere. The experiments we carried out together and the discussions we had all contributed meaningfully to the completion of my PhD. I would like to extend special thanks to Dr. Jianxun Liu at SUSTech and Dr. Thomas Raistrick at the University of Leeds. Whenever I encountered difficulties, you were always there — generous with your time, patient in your explanations, and encouraging in your support. As seniors in the lab, your guidance not only helped me overcome challenges, but also offered me valuable insights that have stayed with me. In addition, I am grateful to everyone in the Light Robots group at Tampere University. Thank you for the warm welcome during my research visit to Finland, and for the many useful discussions that enriched my experience.

I would like to give my deepest thanks to my friends who have become like family to me. A heartfelt shoutout to everyone in Chaos Band, FAB 4, H2O A Cappella Band, and CONC. A Cappella Band — your presence has been like a beam of light on my path forward. That light, with its full spectrum, has gently eased my loneliness and melancholy, recorded both my happiness and sorrow, shared my vulnerability and touched moments, and helped me balance emotion and rationality. You have protected the softest, most tender part of my heart. Though we are different in many ways, we have always resonated on the same spiritual frequency — our souls harmonizing like music. There are countless precious memories we've shared, and every single one of them is vivid and beautiful. Together, they have become a part of who I am. Because of you, I carry more weight in my heart as I step into the next chapter — not as a burden, but as warmth, strength, and love. The future is uncertain, but I truly believe that wherever life takes you, you will shine and thrive. When you miss me, just light up your phone screen or look up at the starlit sky — I'll be somewhere out there, quietly thinking of you, sending you my love from afar. Thank you for appearing in my life. I am deeply grateful for the beautiful memories we've created together.

Wherever you go, know that your light now lives within me. Thank you, from the bottom of my heart.

Last but by no means least, I would like to express my deepest gratitude to my parents and my sister. Thank you for your selfless love and unwavering support, without you, I would never have been able to complete this PhD. This achievement belongs not only to me, but also to you. Thank you for giving me the freedom to grow in my own way. No matter what choices I made, you always believed in me unconditionally and supported me wholeheartedly. Because of you, I was able to follow my own path without fear, and with full confidence. Thank you for teaching me the meaning of home, a place that is more than just a physical space. Home is like a fixed point in the universe, a bright lighthouse that guides me no matter where I roam. Even when I drift far across the world, I can always find peace in knowing you are there. Thank you for everything you've given me, without asking for anything in return. I love you with all my heart.

As a PhD student, I have spent the past four years learning, growing, and solving problems. Most of the challenges I encountered had solutions — patterns to follow, methods to apply. But there is one question I still haven't figured out to this day: how did I become so incredibly lucky? I've gained so much more from this PhD journey than I ever imagined possible. Now, standing at the top of this mountain, I look forward with excitement and curiosity to the path that lies ahead. Whatever awaits me, I'm ready to embrace it.

Abstract

As a class of stimuli-responsive materials, liquid crystal elastomers (LCEs) have attracted increasing attention due to their ability to translate microscale orientational changes into macroscale deformation. Considerable efforts have been devoted to controlling the molecular alignment of LCEs to enable their functionality across various applications. Among them, intrinsic auxetic liquid crystal elastomers (IALCEs) represent an emerging system, where the regulation of auxetic responses through alignment control remains unexplored. Moreover, there is significant potential for designing practical applications based on their tuneable auxetic responses. This thesis aims to achieve orientation control of IALCEs via electric fields, by introducing the Fréedericksz transition alignment, thereby enabling tuneable auxetic responses in IALCEs polymerized under electric fields. Furthermore, by patterning distinct auxetic responses, this work demonstrates a pathway toward tuneable and functional implementations of IALCEs, with particular emphasis on applications such as information encryption.

Due to the elastic and dielectric properties of liquid crystals, the director can deform under an external electric field. In this thesis, we conduct electro-optical experiments to characterize the threshold voltage of the IALCE precursor, which was determined to be 0.9 ± 0.1 V_{rms}. Together with the measured elastic constants (K_{11} = 4.6 pN and K_{33} = 4.3 pN), we construct a detailed schematic illustrating the relationship between applied voltages and the director profile under Fréedericksz transition alignment in the IALCE precursor. Through applying electric fields during polymerizations, we represent the first successful attempt to obtain high-quality homeotropic alignment in 100μm thick films of IALCEs. We also fabricate planar-aligned samples for comparison. Both types of LCE sample show an auxetic response with threshold strains in excellent agreement; 0.56 ± 0.05 for the homeotropic alignment sample and 0.58 ± 0.05 for the planar alignment sample. Furthermore, we demonstrate that the system became biaxial even at very low strains with the high-quality homeotropic sample. To explore the tunability of auxetic responses, we introduce Fréedericksz transition alignments by polymerizing the IALCE precursor under varying electric field strengths. By adjusting the applied voltages, we fabricate IALCEs with distinct director profiles, exhibiting the maximum angle induced in the Fréederisksz transition alignment from 40° to 88°, and realize a wide tuneable range of threshold strain of auxetic responses from 0.58 ± 0.05 to 0.91 ± 0.05. Thermal deformation and

birefringence measurements confirm the successful introduction of the Fréedericksz transition alignment, showing that IALCEs with the Fréedericksz transition alignment exhibit minimized actuations due to modified order parameters. DSC and stress-strain curve measurements confirm consistent glass transition temperatures (15.0 ± 1.0 °C) and hyper elastic properties across all samples, indicating that the tunability of the auxetic response originates solely from variations in the director alignment.

To explore the potential of tunable devices based on IALCEs, we fabricate two demonstrations of multilevel, multidimensional information storage and encryption by integrating electric field-assisted polymerization with photomask patterning. These devices respectively showcase 2D optical and 3D tactile information encoding. For the 2D optical information, binary codes (000 100 110), (011 001 000), and (100 010 001) are encrypted into a single IALCE film via masked polymerization under electric fields. The encoded patterns are sequentially decrypted by stretching the film to specific strain levels of approximately 0.60, 0.70, and 0.80, respectively. In the case of 3D tactile information, we encode the haptic letters "K", "O", and "R" using a set of four IALCE films. Upon sequential stretching to strains of approximately 0.75, 0.85, and 1.00, the corresponding haptic letters appear in order. Owing to the intrinsic auxetic response of the material, a fourth haptic letter, "W", emerges on the reverse side of the IALCE set, completing the word "WORK" during the final stage of decryption. The decryption processes for the 2D optical and 3D tactile information remain mutually independent and highly secure, as successful decryption relies not only on the strain magnitude but also on the strain direction.

In summary, this work demonstrates that polymerization under electric fields enables precise control over the director profile in IALCE precursors, thereby tuning the auxetic responses of polymerized IALCEs. The successful fabrication of high-quality homeotropic alignment confirms that the emergence of biaxiality is an intrinsic feature of the auxetic response in nematic LCEs. What’s more, by patterning distinct auxetic responses, we realize multilevel, multidimensional information storage and encryption, highlighting the potential of IALCEs in tuneable information devices. This study offers a new strategy for designing and implementing tuneable devices based on programmable auxetic responses in IALCEs.

Contents

Symbols and Abbreviations

Symbols

$\hat{n}$	The director
S	The order parameter
θ	The angle between the long axis of the LC molecules and the director
λ_n	The strain in elasticity figure
ν	The Poisson's ratio
ε	The strain
ε_x	Strains in *x*-direction
ε_y	Strains in *y*-direction
ε_z	Strains in *z*-direction
$d\varepsilon_{trans}$	The incremental strain in the transverse direction of expansion
$d\varepsilon_{expan}$	The incremental strain in the expansion direction
T_{ni}	Phase transition temperature
T_g	Glass transition temperature
ε_{th}	Threshold strain
$\vec{k}$	Wave vector
n_e	Extraordinary refractive index
n_o	Ordinary refractive index
n_{eff}	Effective refractive index

α	Angle between the wave vector and the optical axis
Δn	Birefringence
$\frac{dQ}{dt}$	The heat flow
ε_0	Free space permittivity
$\varepsilon_{\parallel}$	Dielectric constant component parallel to the director
$\varepsilon_{\perp}$	Dielectric constant component perpendicular to the director
$\Delta\varepsilon$	Dielectric anisotropy
K_{11}	Splay elastic constant
K_{22}	Twist elastic constant
K_{33}	Bend elastic constant
$F_{elastic}$	Frank free energy
F_{field}	Free energy induced by external fields
∇	The divergence operator
V	The applied voltage
V_{th}.	The threshold voltage
d	Cell thickness
$\vec{E}$	The electric field
$\hat{\mathrm{n}}_{field}$	The distorted director field
θ_{field}	The z-dependent director angle
$\theta(z/d)$	The z-dependent director angle function
z/d	Position in the cell

ϕ	The integration variable
ψ	The integration variable
θ_{max}	Maximum angle induced in Fréedericksz transition alignment
Γ	Phase retardance
I	Light intensity through the cell
I_o	Initial light intensity
β	The angle between the director and the polariser
ε_{eng}	Engineering strain
ε_{true}	True strain
d_B	The thickness of the compensator
α_{avg}	The average pretilt angle of the optical axis of TiO_2
n_{oB}	The ordinary refractive indices of the compensator.
n_{eB}	The extraordinary refractive indices of the compensator.
$\alpha_{\parallel}$	Contraction coefficient along the director
$\alpha_{\perp}$	Expansion coefficient perpendicular to the director
$L_{\parallel}$	Length along the director of LCEs
$L_{\perp}$	Length perpendicular to the director of LCEs
L_0	Original lengths of LCEs
L_{iso}	Final lengths of LCEs
dT	Temperature change
ν_s	The Poisson's ratio in the mathematical model

ε_V	Threshold strain for the sample polymerized under applied voltage V
h	Designed protrusion height
ΔH	Measured protrusion height
ΔH_i	Expected protrusion height
$\Delta \varepsilon_z$	Strain difference in z-axis
T_R	The skeleton reset temperature

Abbreviations

LC	Liquid Crystal
LCE	Liquid Crystal Elastomer
IALCE	Intrinsic Auxetic Liquid Crystal Elastomer
LCN	Liquid Crystal Network
CLCE	Cholesteric Liquid Crystal Elastomer
SSE	Semi-soft Elasticity
MFT	Mechanical Fréedericksz Transition
UV	Ultraviolet
PI	Polyimide
PVA	Polyvinyl Alcohol
POM	Polarized Optical Microscopy
DSC	Differential Scanning Calorimetry
6OCB	4’-Hexyloxybiphenyl
A6OCB	6-(4-cyano-biphenyl-40-yloxy)hexyl acrylate
RM82	1,4-bis-[4-(6-acryloyloxyhex-yloxy)benzoyloxy]-2-methylbenzene
EHA	2-Ethylhexyl acrylate

MBF	Methyl Benzoylformate.
DI	Deionized Water
DCM	Dichloromethane
NOA61	Norland Optical Adhesive
MESSE	Microscope Elastomer Stress Strain Enclosure
N_2	Nitrogen gas
P-LCE	LCE with Planar Alignment
H-LCE	LCE with Homeotropic Alignment
40°–IALCE	IALCE with Fréedericksz Transition alignment (maximum angle at 40°)
60°–IALCE	IALCE with Fréedericksz Transition alignment (maximum angle at 60°)
70°–IALCE	IALCE with Fréedericksz Transition alignment (maximum angle at 70°)
80°–IALCE	IALCE with Fréedericksz Transition alignment (maximum angle at 80°)
88°–IALCE	IALCE with Fréedericksz Transition alignment (maximum angle at 88°)
CTAB	Cetyltrimethylammonium Bromide
ITO	Indium Tin Oxide
PET	Polyethylene Terephthalate
PRS	Polarized Raman spectroscopy
TiO_2	Titanium Dioxide
M^2ISE	Multidimensional Multilevel Information Storage and Encryption
HB-IALCEs	IALCEs with hydrogen bonds introduced
FTIR	Fourier Transform Infrared Spectroscopy
WAXS	Wide-Angle X-ray Scattering

List of Figures

List of Tables

Chapter 1 Motivation and Thesis roadmap

The hypothesis of this thesis was simple at the outset:

"Can tuneable auxetic liquid crystal elastomer devices be realised by employing electric-field induced alignment ? "

In recent years, liquid crystal elastomers (LCEs) have become significantly promising stimulus-response materials in various fields such as robotics, optics, electronics and medicine. The successful fabrication of intrinsic auxetic LCEs (IALCEs) has further enlarged the intrinsic deformation mode of the LCE family, though the extent to which the auxetic response can be tuned and mechanisms to do so still require more investigation. What is more, as a unique category of LCEs first synthesised in 2018, there is still a big space for designing and realizing actual devices based on the auxetic response. The microscale alignment of mesogens decides the macroscale deformation of LCEs so that it is possible to alter the alignment of mesogens in auxetic LCEs to control the auxetic response and further explore the possibilities of the tuneable auxetic responses in applicable devices.

This PhD began with the investigation into the alignment control of mesogens in IALCE precursor under electric field. The mesogen in the precursor will reorient according to the electric field, so that the auxetic response of the IALCEs polymerized under electric fields will be tuned, corresponding to the manipulated orientations. The tuneable auxetic response lays a solid foundation for the development of tuneable LCE devices. The distinct optical and morphological features exhibited under different auxetic responses highlight the potential of auxetic LCEs in information encryption applications. Patterning auxetic responses for the storage and encryption of optical or morphological information is a challenging yet highly appealing and pioneering strategy.

This thesis is structured as follows.

This thesis begins in chapter 2 with an introduction to the fundamental background required to place the experimental work in context, covering liquid crystals (LCs), LCEs, how the mesogen alignment in LCEs affects their deformations and a brief review on strategies to manipulate the mesogen alignment in LCEs. Chapter 3 describes the

materials, equipment and experimental methods utilized to fabricate and characterize the auxetic LCEs in the experimental chapters. Chapter 4 details the electric field induced alignment of mesogens, specifically the Fréedericksz transition alignment, that is achieved with the nematic IALCE precursor in a planar cell through the application of an electric field.

The thesis dives into the experimental results and discussion from chapter 5. Chapter 5 presents the fabrication of the IALCEs in high-quality planar and homeotropic alignments and characterizes their mechanical deformations. The high-quality homeotropic IALCE sample is fabricated with assistance of an external electric field; this is the first example of electric-field alignment of an auxetic LCE. The Raman spectroscopy and conoscopy results directly show that the emergence of biaxial nematic order is directly associated with the auxetic response in nematic intrinsic auxetic LCEs. Chapter 6 moves on to the fabrication and characterization of IALCEs with Fréedericksz transition alignment. We induce the Fréedericksz transition alignment that can be produced within a film of the IALCEs through applying an external electric field during polymerization. We then characterize the extent to which the auxetic response is manipulated by this process, demonstrating the influence of the Fréedericksz transition alignments on the tuneable auxetic properties and laying a foundation for the design and realization of information encryption applications in the following chapter. Building upon the tuneable auxetic responses demonstrated in Chapter 6, Chapter 7 explores the application of IALCEs in information storage and encryption by leveraging the distinct optical and morphological features associated with different auxetic responses. Through the patterning of auxetic responses, chapter 7 showcases the realization of multilevel binary and tactile signal storage and encryption.

In chapter 8, the key findings in the thesis are summarized and potential directions for future work are proposed, in which we plan to induce the dynamic bonds inside IALCEs to endow the auxetic response programmability.

Chapter 2 Introduction

In this thesis, we will focus on the basic properties of intrinsic auxetic liquid crystal elastomers (IALCEs) and their deformations when fabricated with various alignments. The work includes an application relating to information encryption, based on the tuneable auxetic response of electric field aligned IALCEs. To better understand the IALCEs we are using and the design logic for applications we utilize, some fundamentals of liquid crystals (LCs) and (liquid crystal elastomers) LCEs need to be introduced before the specific projects are described. In this introductory section, we will start with a brief outline of the fundamentals of LCs and LCEs. Subsequently, we will move on to the unique category of IALCEs. The definition of an auxetic response will be presented and the investigation into the mechanism of the auxetic response in IALCEs will be summarised. Finally, the alignment methods that can be applied to mesogens will be introduced to better comprehend methods that facilitate the manipulation of the anisotropic response of LCEs. The review on the alignment methods has been published in “Advances of complex molecular alignments and multiplex deformations in liquid crystal elastomers. *Chinese journal of liquid crystals and displays*, 2024, *40*, 1-20.” and this chapter follows much of that paper.

2.1 Introduction to Liquid Crystals

Generally, the term ‘liquid crystal’ (LC) is used to refer to a liquid crystal phase or materials in a liquid crystalline phase. LC phases are thermodynamically stable physical phases that exist between the crystalline solid phase and the isotropic liquid phase. An LC phase was first observed in 1888 by the Austrian botanist, Friedrich Reinitzer who observed that cholesteryl benzoate had two “melting” points [1]. Following that seminal observation, the German physicist, Otto Lehmann carried out more detailed research into the optical properties of the material and observed its birefringence [2]. Then this state of matter was formally named “Liquid Crystal” by Lehmann. As LC phases sit between the crystal phase and liquid phase, they exhibit a certain degree of long-range orientational order, similar to that in crystals, but are disordered position, with mobility of molecules typical of that seen in a liquid. There are many combinations of order that make up the zoo of liquid crystal phases that are reviewed in excellent text book [3]. In this work, we consider the simplest

kind of liquid crystal, the nematic phase, which can be described as follows. Consider the example of a material with rod-like molecules; the schematic of possible molecular organization is shown in Figure 2.1. Phase transitions occur as the temperature changes, when the temperature is lower than the melting point, the LC is an ordinary crystal while when the temperature is higher than the clearing point, the LC becomes an isotropic liquid.

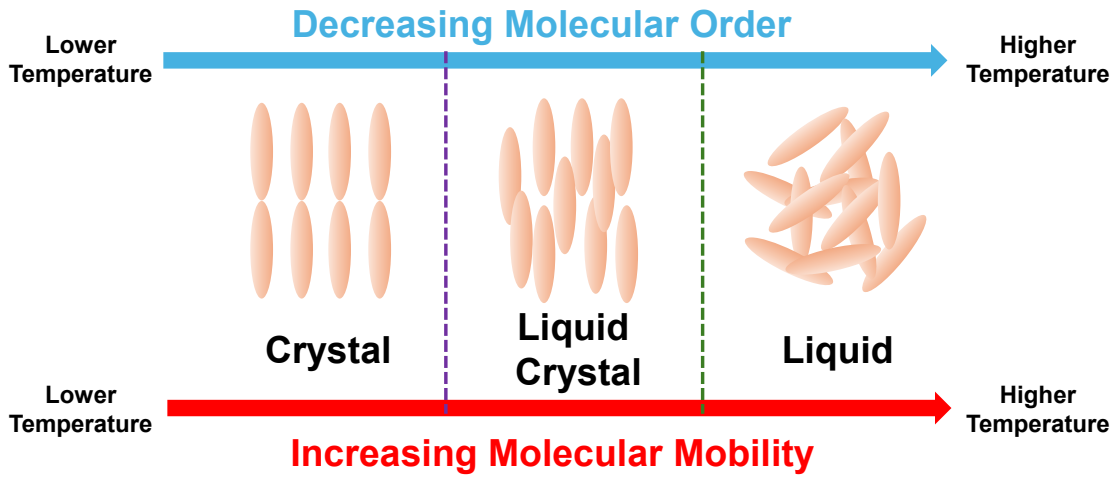

Figure 2.1 The general schematic of molecular organization in crystal, LC and liquid phase. The direction of the arrow indicates the trend of temeperature increase. The purple dashed line reprensents the melting point, the temperature at which it changes from a solid phase to a liquid crystal phase while the green dashed line reprensents the clearing point, the temperature at which it changes from a liquid crystal phase to a liquid phase.

LC can generally be divided into two categories according to the chemical composition and modes of formation: lyotropic and thermotropic. Lyotropic LCs are formed by dissolving organic matter in a solvent and ordered micellar-like structures are formed through changes in solution concentration and temperature. On the other hand, thermotropic LCs normally consist of rod-like, disk-like or bent-core compounds, exhibiting LC phase in a certain temperature range. In this thesis, we focus on the rod-like LC compounds. For a classic rod-like LC molecule, it is generally formed by a rigid “core” and a flexible “tail”. The rigid “core” consists of two or more aromatic rings while the flexible “tail” is often alkyl or alkoxy chains. The rigid “core” guarantees the molecular ordered alignment, and the soft “tail” increases entropy, supressing crystallisation. This molecular structure endows LCs with outstanding anisotropic properties in several aspects, such as birefringence, dielectric constant, conductivity and so on. Moreover, because of the inherent fluidity of nematic LCs, they will respond readily and align according to the external stimuli, such as rubbed

surfaces, electric fields, magnetic fields, mechanical force and so on.

Due to differences in molecular structures and the intermolecular interactions of thermotropic LCs, phases with different degrees of order could be further categorized into smectic phases, nematic phases and chiral nematic phase. The structure of these three phase types is shown in Figure 2.2. The smectic LC phases have the most similar structure to the crystal phase. The molecules are orientated in a layer formation, which combines orientational order with positional order. Among the various smectic phases, the Smectic A phase, as shown in Figure 2.2(a), has the structure where molecules tend to align perpendicularly to the layer planes, making it structurally analogous to the nematic phase. As for the nematic LC phase, it is the least ordered phase among these three phases and has the best fluidity and the lowest viscosity. It has only long-range orientational order where the long axes of the molecules point in the same direction on average. Chiral nematic LC is the LC first discovered. There are no layered structures, and the local ordering is identical to that of the nematic phase. A chiral nematic phase can be induced in a nematic phase through the addition of a small concentration of chiral dopant molecules. Low molar mass LC and polymers are both able to exhibit one or multiple LC phases. This thesis will focus on the nematic phase.

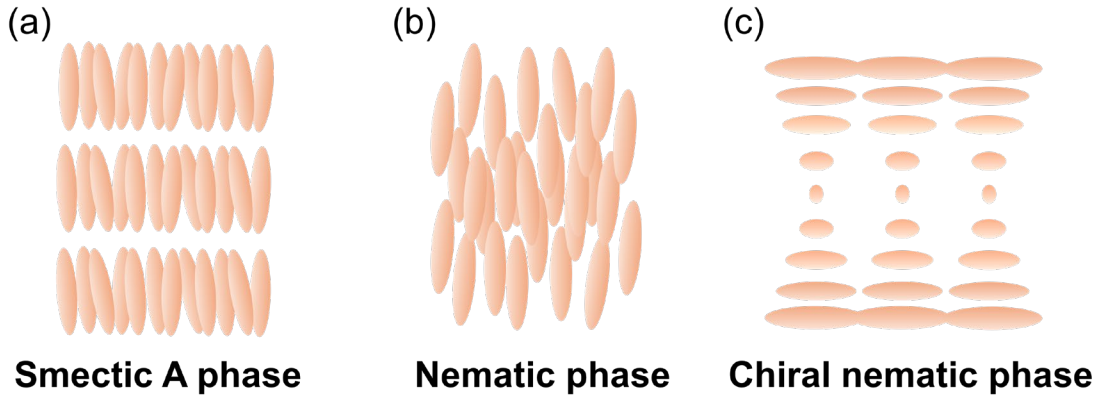

Figure 2.2 The three phase states of thermotropic LC. (a) smectic phase; (b) nematic phase; (c) chiral nematic phase.

To the long-range orderering in nematic LCs, is such that the long axis of the molecules tend to align parallel to a common direction, usually represented by a unit vector, $\hat{n}$, known as the director. For nematic LC, $\hat{n}$ and $-\hat{n}$ are generally considered equivalent [3]. To update this understanding, recent studies have revealed the existence of polar nematic phases, where the symmetry between $\hat{n}$ and $-\hat{n}$ is broken due to the emergence of

spontaneous polarity along the director axis [4]. The LC molecules orient along $\hat{n}$, and exhibit a certain statistical distribution. For different LC materials and at different temperatures, the molecular long axes deviate from the director to the extent of various degrees. Therefore, an average physical quantity is used to describe the degree of order in the alignment of LC molecules, known as the order parameter, *S*. The equation for the order parameter is given by [3]:

$$S = \frac{1}{2}\left\langle 3\cos^2\theta - 1 \right\rangle \tag{2.1}$$

where θ is the angle between the long axis of the LC molecules and the director $\hat{n}$. S is a scalar quantity and it represents the average alignment of LC molecule relative to the director on a macroscopic scale. For the ideal alignment condition mentioned above, $S = 1$ while for totally isotropic LC nematic phase, $S = 0$. For a typical nematic LC at temperature relatively far from the clearing point, S is between 0.5 and 0.7 [5]. Due to the mobility of LC molecules, LC could be aligned in a customized and unified direction through the external stimuli, a feature which will be discussed further in Section 2.3.

2.2 Introduction to Liquid Crystal Elastomers

2.2.1 Fundamentals of Liquid Crystal Elastomers

LCEs are moderately cross-linked LC polymer networks, composed of liquid crystalline molecules (mesogens) connected through a flexible polymer backbone. LCEs represent a class of polymer materials that is capable of reversible deformations in response to external stimuli, such as heat [6,7], light [8,9], electric fields [10,11], magnetic fields [12,13], humidity [14,15], and mechanical stress [16,17]. As an active soft material, LCEs have shown significant potential in various applications such as soft robotics [18-20], soft actuators[21-23], sensors [24,25], artificial muscles [26,27], biomedicine [28,29], flexible electronics [30,31], and optical devices [32-34], and their functional versatilities have attracted extensive attention from researchers in various fields.

The unique structures enable LCEs to maintain the anisotropic properties of LCs along with the elasticity of the polymer network. In comparison with liquid crystal networks (LCNs), LCEs have lower crosslinking density and, in result, exhibit lower glass transition temperature, greater order-driven variations in magnitude upon stimulation and greater elasticity to the mechanical load [7]. In conventional LCEs based on low-molar-mass LC

systems, the mesogens are usually rod-like molecules, which are usually composed of interconnected aromatic or cyclohexyl rings. Before polymerization, the liquid crystalline properties of the LCE precursor depend on intermolecular interactions among the mesogens (π-stacking, dipole-dipole interactions). During polymerization, reactive groups in the mesogens and cross-linkers (such as alkenes, acrylates, thiols, and epoxides) interact and cross-link to form the soft polymer chains [35-37]. Figure 2.3 [38] demonstrates the common synthetic processes for cross-linked LCEs, including the acrylate homopolymerization, hydrosilylation, aza-Michael chain extension, thiol-Michael chain extension, and radical chain transfer reactions.

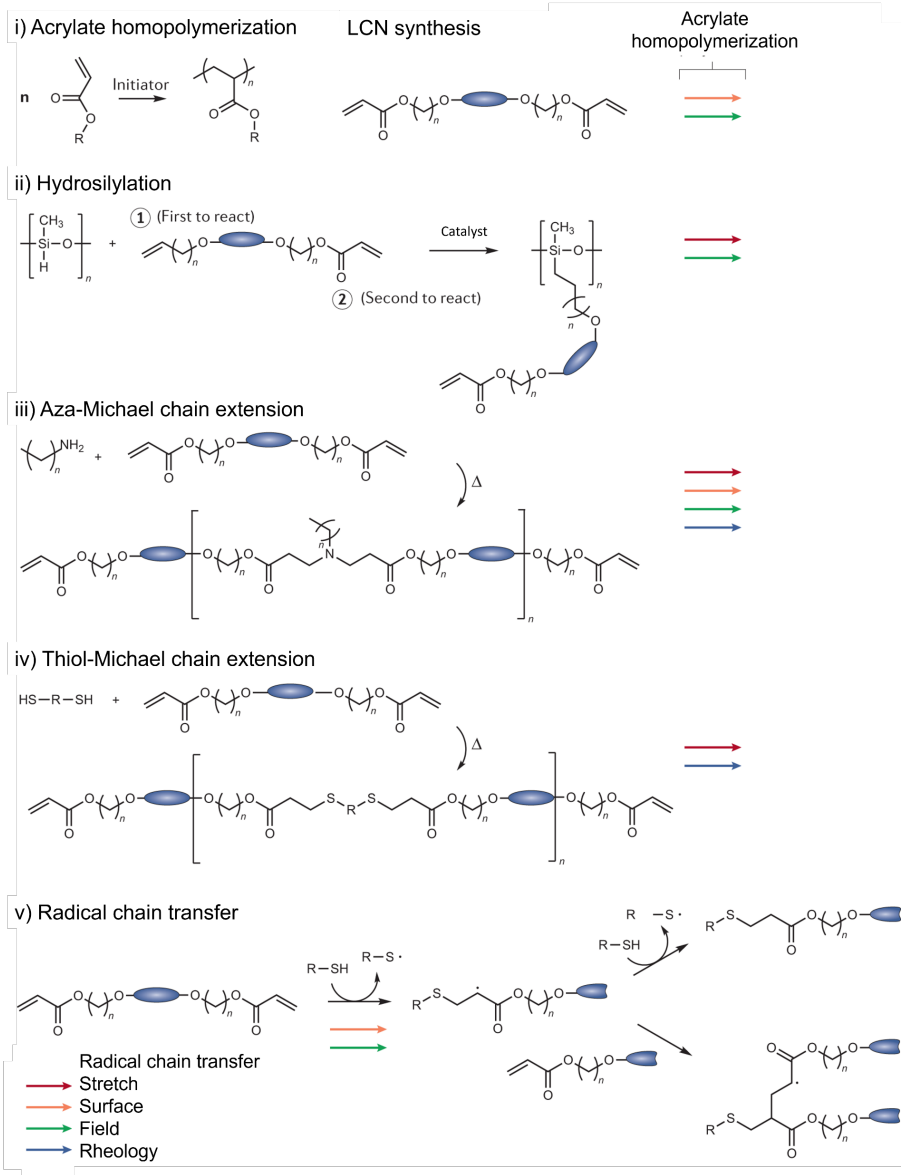

Figure 2.3 Synthetic methods for preparation of crosslinked LCEs, reproduced from [38], including i) acrylate homopolymerization, ii) hydrosilylation, iii) aza-Michael chain

extension, iv) thiol-Michael chain extension, and v) radical chain transfer reactions. The arrows in different colours stand for the different alignment methods, which will be introduced in the section on alignment (Section 2.3)

Depending on the linkage between mesogens and polymer chains, LCEs can be categorized into two main types: main-chain and side-chain LCEs. Side-chain LCEs can be further classified into side-on and end-on side-chain LCEs, as shown in Figure 2.4 [37]. It is worth mentioning that the widely utilized side-chain LCEs are the initial LCEs proposed and developed by Finklemann. They are primarily synthesized through a hydrosilylation reaction involving a flexible polysiloxane backbone, reactive mesogens and cross-linkers [39,40]. The chain extension reactions, such as aza-Michael chain extension and thiol-Michael chain extension, have become the main synthesizing methods of main-chain LCEs. In comparison to main-chain LCEs, the interactions between mesogenic units and backbones are weaker in side-chain LCEs, resulting in weaker mechanical strength, and, crucially, weaker recoverability of backbones in reversable deformations [38,41].

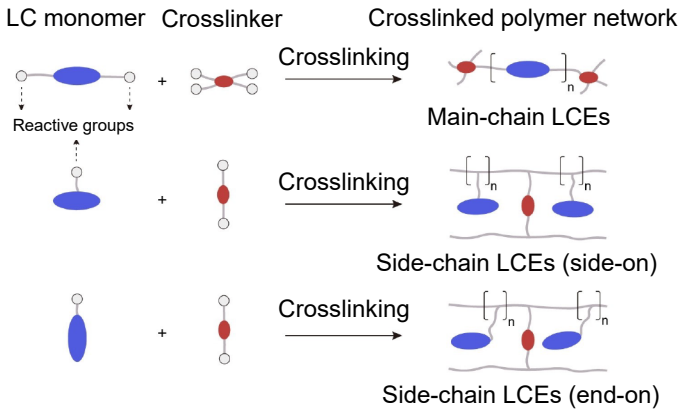

Figure 2.4 Configuration and classification of LCEs, reproduced from [37], including depictions of main-chain LCEs and side-chain LCEs.

2.2.2 Deformations and Actuations of Liquid Crystal Elastomers

The tremendous attraction of LCEs is based on their fascinating stimulus-response properties. The facile reorientation of the mesogens and macroscopical deformations endow LCEs with potential in several aspects.

The mechanical response of an LCE depends on both the direction of the loading stress to the alignment directions of LCEs and on the LC phase (smectic, nematic, chiral nematic or isotropic) exhibited by the LCEs. For monodomain nematic LCEs, the most famous

feature of the stress-strain response is the “semi-soft elasticity (SSE)”. [42-44]. The SSE response model was first constructed with a uniformly aligned monodomain main chain nematic LCEs. As illustrated in Figure 2.5(a) [45], in the SSE response, after the initial linear behaviour, the mechanical response experiences a plateau-like region in the stress-strain curve. This softened stress-strain region is due to the continuous rotation of the director to align along the stress direction and the rotation process minimizes the shear affects. In the ideal scenario, the rotation process occurs without any space distortion and energy cost, and the LCEs absorb strain energy at constant stress [46]. When the rotation of the director, $\hat{\mathbf{n}}$, is finished, the stress increases again with the strain. For special cases, when the stress is loaded along the director direction or the LCEs are in an isotropic phase, the mechanical response of LCEs exhibits the classical elastic response associated with rubbers [47]. Many nematic LCEs are polydomain, rather than monodomain (the director is not uniformly aligned) and these exhibit a “soft elasticity” response where the materials display near-zero stress when the director realigns along the strain direction. [48-49]. For monodomain nematic LCEs, an alternative mechanical response is reported with a sudden director rotation at a threshold strain reported for a few acrylate-based LCEs [43,45,49,50], so called mechanical Fréedericksz transition (MFT) response as shown in Figure 2.5(b) [43]. Recent works, including that in this thesis, has shown that MFT is not discontinuous but that the nematic LCE becomes biaxial on distortion [17,45,47]. Compared to the SSE response, the MFT response share the quite similar stress-strain curve while the biaxial order emerges at a threshold strain.

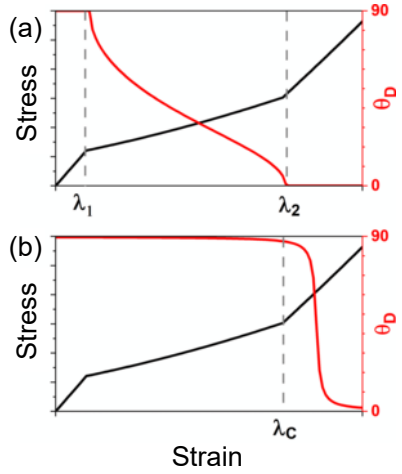

Figure 2.5 The illustrative stress-strain curve (black) and director rotation (red) in the mechanical deformation of LCEs with (a) SSE response and (b) a so-called MFT response, reproduced from [45]. In SSE response, λ_1 is the strain where the continuous

rotation of the director begins and λ_2 is the strain where the director is totally reoriented, and the material gets stiffed again. In MFT response, λ_c is the critical strain where the biaxial order emerges with the re-stiffening process.

The stimulus-response of LCEs (i.e. to heat, light etc.) studied to date is mainly based on ordered-disorder phase transition of mesogens caused by external physical or chemical stimuli. Similar to low molar mass LCs, upon heating from anisotropic phase to isotropic phase, the loosely crosslinked mesogens in LCEs exhibit a decrease in order and LCEs process obvious shrinkage strain along the director $\hat{\mathbf{n}}$. As predicted by de Gennes in 1969 [51] microscopical polymer-backbone changes will result in macroscopical deformations of LCEs during the nematic-isotropic phase transition. Figure 2.6 shows the microscopical change of the polymer backbone inside the polymer on transforming from a liquid crystal to isotropic state [35], together with an example of four general alignments of mesogens inside monodomain films of LCEs and the corresponding macroscopical deformations [52] that occur for them on changing order.

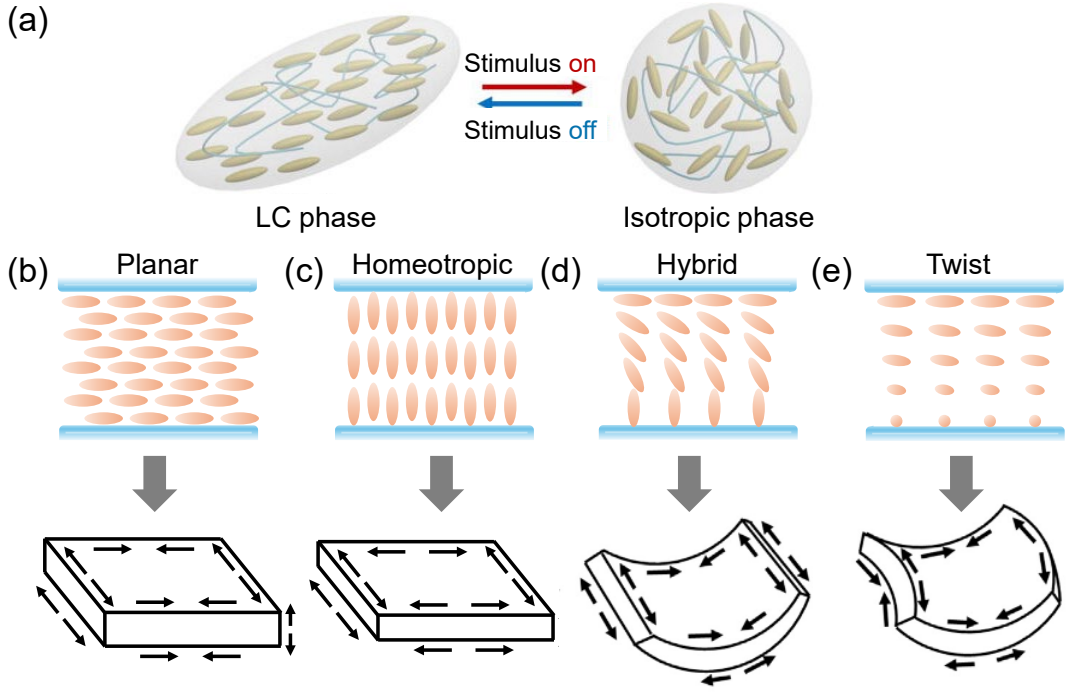

Figure 2.6 (a) The change of the polymer backbone in LCEs during the order-disorder phase transition under the external stimulus. Reproduced from [35]. Schematic illustration of four basic alignment configurations of LCEs including (a) planar, (b) homeotropic, (c) hybrid, and (d) twisted, and their corresponding bulk deformations. Reproduced from [52].

As the temperature decreases to initial state, the mesogen alignment microscopically

recovers and the LCEs macroscopically return to their original shape [35-38]. In the process of LCEs being stimulated by an external field and causing the arrangement of mesogen molecules to change from anisotropy to isotropy, the sample will shrink along the orientation direction and stretch perpendicular to the orientation direction, thereby producing anisotropic deformation. Considering the polymer molecule itself, when the mesogens are uniformly aligned in a nematic phase, the polymer backbones will usually orientate along the alignment direction, while in isotropic phase, the entropy drives the backbones into a random-coil formation [7]. Optothermal (the thermal energy from light resources, for example, through the mixed dye) mechanical and electrothermal (the thermal energy from electric, for example, through the built-in circuit) mechanical response of LCEs also follow the mechanism of thermal mechanical response. For phototropic LCEs (azobenzene-functionalized), irradiation with ultraviolet (UV) light triggers photoisomerization, converting azobenzene segments from a rod-like trans-isomer to a bent cis-isomer and inducing a phase transition from anisotropic to isotropic [74].

2.2.3 The unique category in LCEs---Intrinsic Auxetic Liquid Crystal Elastomers

Auxetics are a remarkable class of materials which display anomalous expansion in at least one dimension along the direction perpendicular to an applied extension, i.e. they have a negative Poisson's ratio [53]. There is a zoo of associated properties that are enhanced compared to conventional materials including indentation resistance, shock absorbance and delamination resistance, making auxetic materials exciting contenders in applications areas as diverse as biomedical, aerospace, architecture and sporting equipment [54-58]. In nature, auxetic materials are known in crystalline materials [59-62] e.g. α-cristobalite which is a silicon-dioxide polymorph; additionally, biological materials such as cat skin [63] or the Achilles tendon [64] have been found to display an auxetic response. The mechanisms responsible for the auxetic response in re-entrant materials are well-known and are based on their geometry; they are designed with porous, honeycomb structures [57, 65, 66] that 'unfold' under strain. Many ideas have been put forward for realizing molecular auxeticity [67, 68] and liquid crystalline polymers have long been recognized as promising materials [69-73]. For example, He et al. [71,72] studied a main-chain liquid crystalline polymer by X-ray diffraction and suggested a potential auxetic response from the rotation of mesogenic units into the direction transverse to the initial nematic director under the strain [72]. However, only a positive Poisson's ratio was recorded for this material.

A special category of LCEs was found in 2018 by Mistry et al. [16], in an acrylate side chain LCE which exhibited the same general thermomechanical response as other LCEs but unique mechanical deformations — an auxetic response beyond a critical threshold strain. Auxetic materials are materials with a negative Poisson's ratio. The Poisson's ratio is defined as the negative ratio of transverse (lateral) to longitudinal (axial) strain; briefly, it describes how a material deforms in one direction when it's actively deformed in a perpendicular direction. The Poisson's ratio, ν, can be written as:

$$\nu = -\frac{d\varepsilon_{\text{trans}}}{d\varepsilon_{\text{expan}}} \tag{2.2}$$

where the $d\varepsilon_{\text{trans}}$ is the incremental strain in the transverse direction of expansion while $d\varepsilon_{\text{expan}}$ is the incremental strain in the expansion direction.

As for using the incremental strains instead of total strains, the rationale lies in how the mechanical deformation measurement of auxetic LCEs in *x*-*z* plane is characterized. As shown in Figure 2.7(a), during the deformation process, the Poisson's ratio calculated from total strains remains positive even at an *x*-strain of 1.0. In contrast, when incremental strains are considered, the Poisson's ratio transitions from a positive value to nearly zero at an *x*-strain of 1.0, signaling the onset of the auxetic response. In other words, the auxetic response of auxetic LCEs is a partial auxetic response in the mechanical deformation which happens beyond a critical strain. By analyzing the Poisson's ratio based on incremental strains, we can more clearly analyse the Poisson's ratio change of auxetic LCEs during the mechanical deformation and better capture the auxetic responses of auxetic LCEs.

The non-linear strain-strain relation is due to the hyper eslaticity, by which the film is softening during the mechanical deformation. The hyper elasticity will be discussed more in Section 6.3.5.

Figure 2.7(b) is provided for an intuitive understanding of the auxetic responses of auxetic LCEs. As shown in the geometry schematic in Figure 2.7(b) [16], for stress (in the *x*-axis) perpendicular to the director direction (in the *y*-axis), a monodomain film of auxetic LCE expands after a critical strain rather than contracts orthogonally to these two directions (in the *z*-axis). The alignment of the mesogens endows this mechanical auxetic response anisotropy, where the negative Poisson's ratio is only in the z-axis and the strain in y-axis has a positive Poisson's ratio. The specific Poisson's values of auxetic LCEs will be discussed more in Section 5.3.

In the mechanical deformation of this side-chain, monodomain, nematic LCE material,

there is no evidence showing the emergence of porosity as occurs for many auxetic structures. The volume is constant and the auxetic response happens at a molecular level, consequently, this LCE is an intrinsic auxetic LCE. The underlying of the auxetic response is due to the emergence of the biaxial order. The initial director is along the *y*-direction, as the strain in *x*-axis increases, a biaxial axis keeps emerging. When the biaxial optical indicatrix changes from y-direction to x-direction, the auxetic responses starts in z-direction. The strain, at which the biaxial optical indicatrix changes, is the critical strain of auxetic response, we also call it threshold strain, $V_{th.}$ The underlying mechanism will be discussed more in Section 5.3.

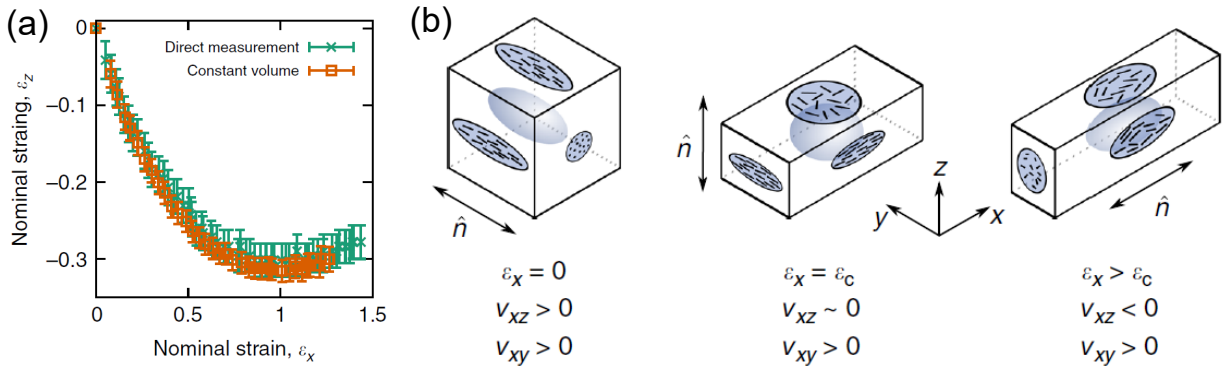

Figure 2.7 (a) The mechanical deformation measurement of auxetic LCE in x-z plane. (b) Relationships between the molecular orientation and the strain-dependent Poisson's ratios of the auxetic LCE. For the auxetic response, the strains (ε_x) are applied along the *x*-axis and the auxetic response is observed along the *z*-axis. ε_c stands for the critical strain beyond which the auxetic response starts. Reproduced from [16].

Investigation into the mechanism of the auxetic response started initially with the elastic response and then the order parameter. When the material was initially synthesized, the mechanical response of this unique LCE was proved to exhibit an MFT response rather than the more common SSE response [16, 47]. During the deformation process, it is observed that the nematic order changes, resulting in an apparent SSE stress-strain curve. However, the biaxial order emergence actually drives the MFT response. As an uncommon response, rather few LCEs exhibit MFT response in the mechanical deformations and so far, they all are acrylate-based materials [16,47,50,75-77]. The measurements and analysis done by Raistrick *et al.* on these LCEs has shown that they all exhibit a partial auxetic response, which emphasizes the importance of MFT related to the auxetic responses. It is worth mentioning that, the clue to understand the mechanism of auxetic response of these LCEs is not directly described in the MFT theory, it is related to Bladon et al.'s work which

illustrated that the LCE with MFT response will exhibit a decrease in uniaxial order and an increase in biaxial order. [78,79]. Like the prediction by Bladon, uniaxial order parameter changes were indeed observed in auxetic response [16,47], however, the physics behind the auxetic response was still not understood at that time. Subsequently, Dr. Raistrick investigated the uniaxial and biaxial order parameter changes in the auxetic responses via Raman scattering and explained the physical mechanism of the auxetic response by the emergence of the biaxial order under strain. [45]. In this thesis, the first project is to directly observe the emergency of the biaxial optical axis with a homeotropic aligned IALCE, which will be discussed more in Chapter 5.

2.3 The alignment methods of LCEs

The orientation of LCEs significantly influences the maximum deformation achievable under external stimuli, and the micro-orientation of LCEs determines their macroscopic deformation characteristics. The programmability of mesogenic alignment lays the foundation for complex, multifunctional deformations in LCEs, while unique control of mesogen molecular orientation introduces diverse and intriguing properties into LCE-based complex systems. Selecting appropriate orientation methods for different LCE sample forms is crucial to achieving pre-designed complex deformations in LCEs.

There are three primary methods to align the mesogens inside LCEs, including mechanical alignment, surface anchoring alignment and field effect alignment. Among these methods, mechanical alignment is particular for LCEs while the others also apply to low molar mass LCs.

2.3.1 Mechanical alignment

The principal characteristics of mechanical alignment of LCEs are observed when the long axes of mesogens align either parallel or perpendicular to the direction of an applied mechanical stress. The primary types of mechanical stress inducing such alignments include tensile stress, compressive stress, and shear force.

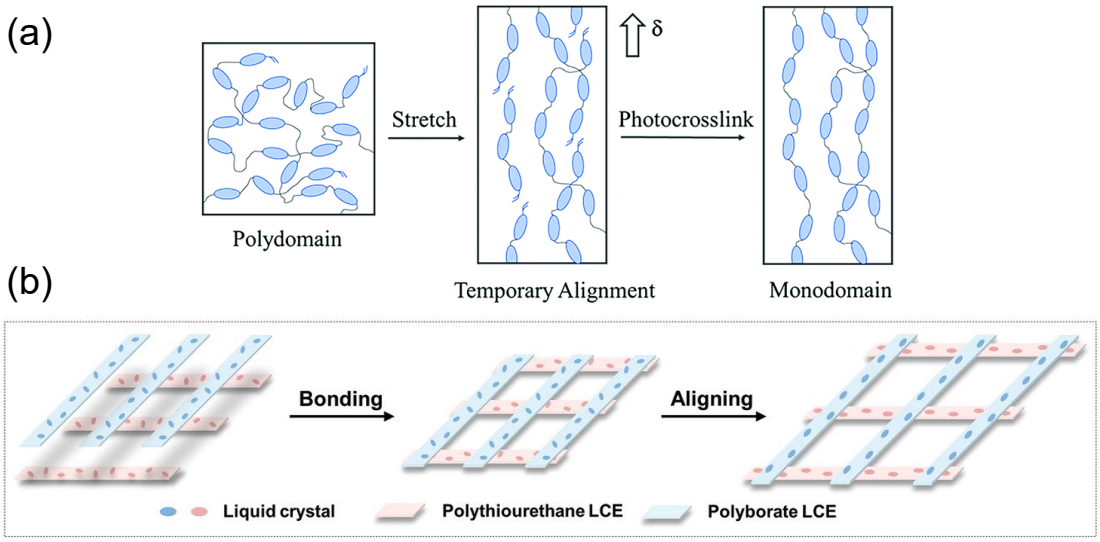

Figure 2.8 Mechanical alignment of LCEs by tensile stress. (a) Stretching the pre-crosslinked polydomain LCEs during polymerization to align it into monodomain LCEs. Reproduced from [81]; (b) A LCE mesh with multiple shape-morphing modes fabricated with two different LCEs and aligned by bidirectional tensile stresses. Reproduced from [82].

The process of tensile stress-induced alignment was first proposed by Finkelmann in 1991 [39,40] and later refined by Bowman in 2015 [80]. The tensile stress-induced alignment is often utilized in the fabrication of monodomain LCEs and typically follows a two-step crosslinking approach, illustrated in Figure 2.8(a) [81]. This technique involves partial polymerization of a mesogenic monomer mixture to create a pre-crosslinked LCE oligomer containing reactive groups. Uniaxial mechanical stretching is then applied to align the mesogens in the oligomer, followed by a secondary crosslinking reaction between reactive groups to fix the structure and produce monodomain LCEs capable of reversible contraction. Due to the mobility of the mesogens, the angle between the mesogenic alignment direction and the stretching direction rapidly decreases during stretching, enhancing the alignment of LCEs to a higher order degree (general monodomain) which will be eventually fixed by polymerization. For more complex alignment and actuation patterns, the stretching direction and extent can be further controlled during the orientation of pre-crosslinked LCE oligomers [82-86], as shown in Figure 2.8(b) [82]. However, the tensile stress method is limited in producing complex, high-resolution, three-dimensional multiaxial alignments.

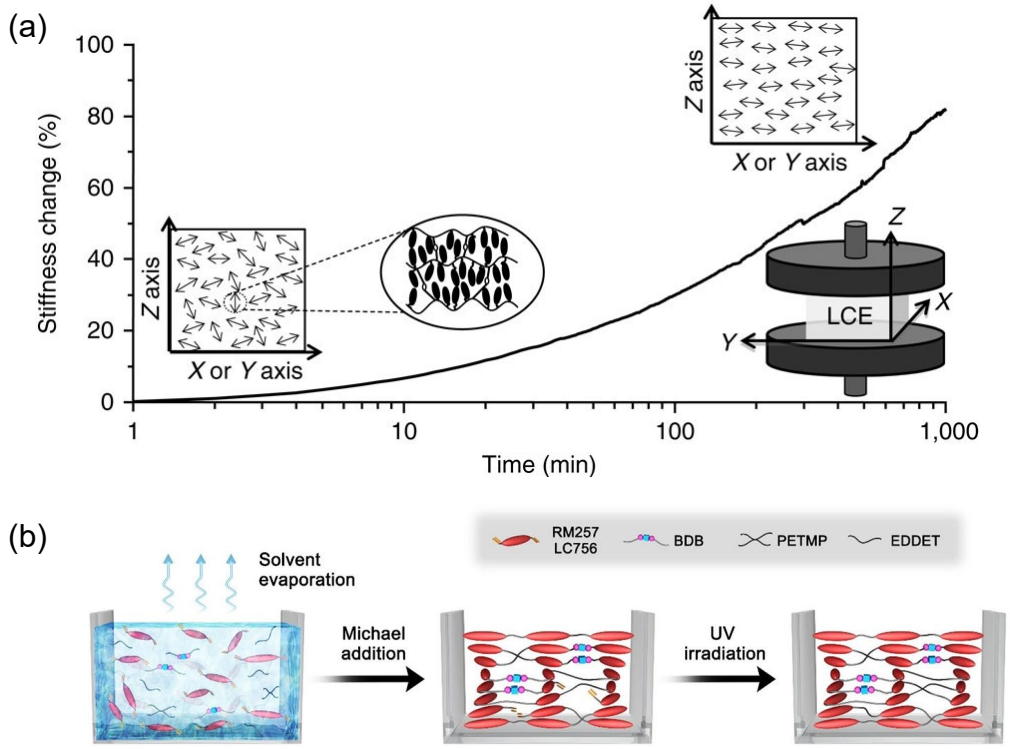

Figure 2.9 Mechanical alignment of LCEs by compressive stress. (a) Alignment of mesogens under the compressive stress. Reproduced from [87]; (b) In the cholesteric LCE system, the compressive stress generated by anisotropic deswelling induces the layered and helical orientations of mesogens perpendicular and parallel to the evaporation direction, respectively. Reproduced from [91].

Unlike tensile stress, compressive stress consistently induces mesogenic units to align perpendicularly to the applied pressure direction, as shown in Figure 2.9(a) [87]. Through uniaxial compression, mesogenic molecules align and stack perpendicularly to the pressure [64-91]. This alignment can also be achieved through the deswelling of LCE prepolymers with chiral dopants [89-91]. The anisotropic deswelling method is often used in fabricating cholesteric LCEs (CLCEs) and was first introduced by Finkelmann in 2001 [89]. After undergoing chain-extension addition reactions, LCE prepolymers form pre-crosslinked gels adhered to a substrate. During solvent evaporation, these gels do not shrink laterally, restricting evaporation to the direction perpendicular to the substrate, thereby inducing mesogenic layers aligned perpendicular to the evaporation and a helical orientation parallel to it, as illustrated in Figure 2.9(b) [91]. This method substitutes the use of internal alignment layers or external fields with the anisotropic volatility of solvents. However, it is limited to CLCE systems with volatile organic solvents and without chemical

bonding facilitating interface assembly during evaporation, the resulting film may exhibit poor mechanical strength and reproducibility.

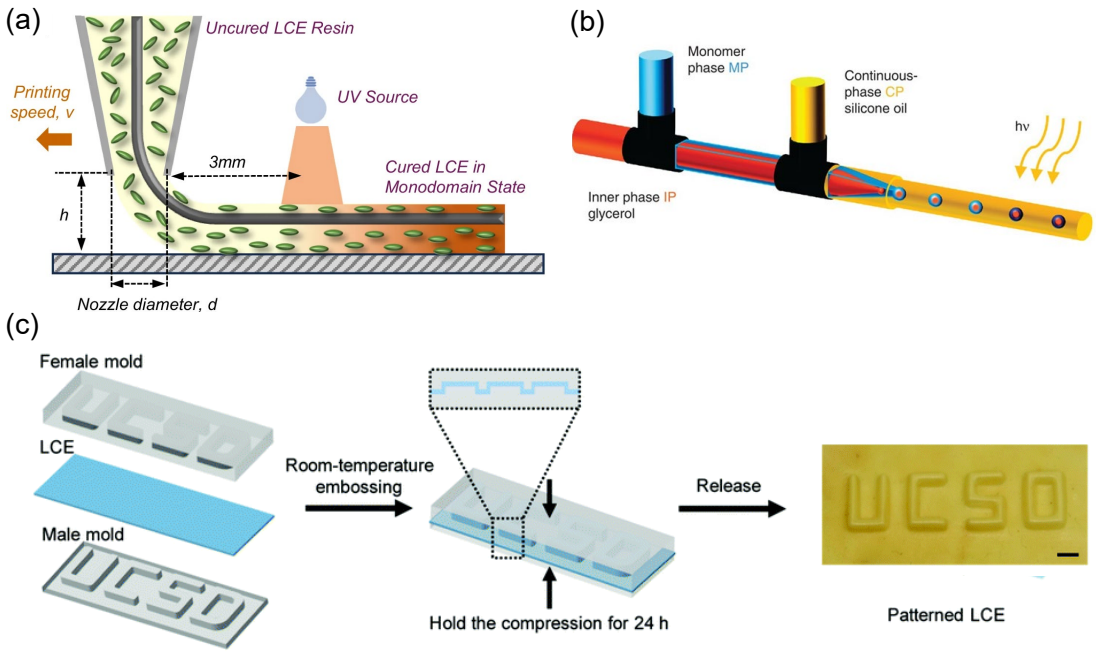

Figure 2.10 Mechanical alignment of LCEs by shear force. (a) The mechanism illustration of mesogen alignment during 4D printing that mesogens in LCEs are aligned by combining stretch stress and shear stress during the 4D printing process; h represents the distance between the needle tip and the substrate and d represents the nozzle diameter. Reproduced from [92]. (b) The fabrication process of aligned LCE-droplets by the shear force. Reproduced from [104]. (c) The schematic illustrating that tensile stress, compressive stress and shear force work together to directly fabricate LCEs with preset patterned structures. Reproduced from [108].

Shear force-induced alignment is applicable in the 4D printing of LCEs using direct ink writing (DIW). In this process, shown in Figure 2.10(a) [92], pre-crosslinked, solvent-free LCE oligomer ink is extruded, where shear and tensile forces align the mesogenic molecules along the printing path. The structure is subsequently stabilized using UV-induced polymerization [92-97]. This extrusion process involves three distinct regions: a core gel layer maintaining consistent flow, the partially formed laminar shell layer, and a thin flow layer near the nozzle. The molecular weight and viscosity of the LCE ink are influenced by its chemical composition and pre-crosslinking conditions, while the nozzle size, internal pressure, temperature, and writing speed impact the final dimensions and orientation of the printed LCEs. Although LCEs 4D printing offers a simple and effective

method for patterning orientation and complex three-dimensional shape transformations of LCEs, it faces limitations in printing speed and spatial resolution (≥ 50μm). In addition to DIW, shear force is also used in microfluidic techniques for aligning mesogenic molecules during LCE preparation, for example, the application in the electrospinning of LCE shells [98-100], fibres [98-100], and biomimetic muscle structures [98-103]. Figure 2.10 (b) [104] demonstrates the production of LCE droplets using shear alignment [104,105]. Mechanical stress alignment can also incorporate various stress types, such as imprinting or embossing, to achieve complex, pre-designed alignment patterns in LCEs [106-108], as shown in Figure 2.10 (c) [85].

2.3.2 Surface anchoring alignment

Surface anchoring alignment is determined by the interactions between the alignment layer and mesogens, while the patterning resolution of the alignment layer determines the precision of the mesogenic unit's orientation. The surface anchoring effect is governed by the molecular interactions between mesogenic molecules and the alignment layer material, as well as the anisotropic anchoring effects imposed by microchannel structures if there are microchannel structures on the surfaces. This effect is predominantly realized through methodologies such as rubbing, microstructure alignment and photoalignment.

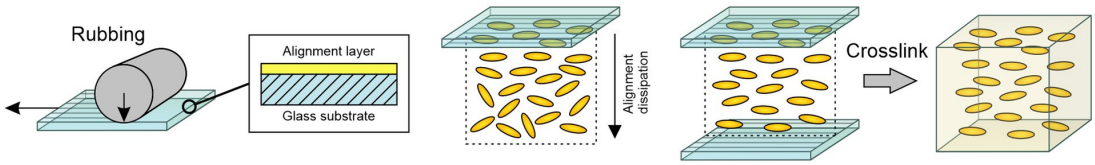

Figure 2.11 Surface anchoring alignment of LCEs by rubbing. Two substrates spin-coated with alignment layer are rubbed and assembled to alignthe filled LCE precursor. Reproduced from [109].

The rubbing technique, extensively utilized in liquid crystal display panel fabrication, is also frequently employed to achieve large-scale, uniform alignment of LCEs. This process involves spin-coating alignment materials, typically polyimide (PI) or polyvinyl alcohol (PVA), onto a substrate, followed by anisotropic molecule alignment through mechanical rubbing, as illustrated in Figure 2.11 [86]. However, due to the inherent limitations of the mechanical rubbing process, precise control over rubbing direction is challenging, making it unsuitable for producing high-resolution or complex spatial alignment patterns. As a result, this method is generally more effective for large-area uniform alignment rather than for creating

specific patterns.

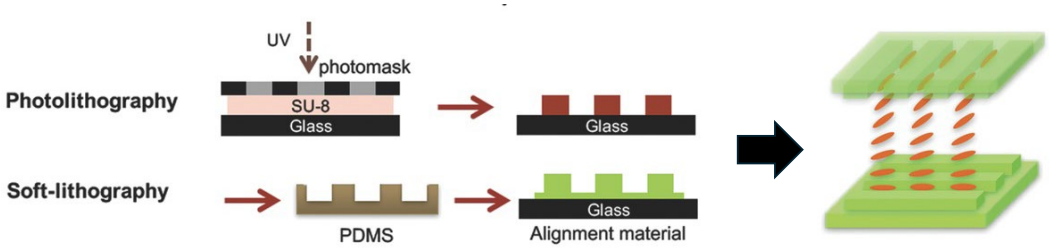

Figure 2.12 Surface anchoring alignment of LCEs by microstructures. Reproduced from [114].

In comparison, the microstructure alignment method, rooted in microgroove alignment theory [110,111], offers the capability to generate high-resolution, large-area, and continuously varying complex spatial orientations [112-114]. Figure 2.12 [114] demonstrates how continuous microchannel structures enable the consistent alignment of mesogenic molecules within thin-film LCEs. Microchannels are fabricated by micro/nano-processing techniques. First, a template with microchannel structures is fabricated using the photolithography technique. Second, the templated structures are transferred to the PDMS and then the epoxy resin (SU-8) subsequently through the soft lithography by replica moulding. Finally, two pieces of glass substrates with the epoxy resin microchannel structures are assembled to form a cell. The epoxy resin microchannel structures are used as the alignment layer for LCEs.The precision and scale of alignment achieved by this method are dependent on micro- and nanofabrication techniques. The microstructure anisotropy aligns the long axis of mesogens, and the alignment precision is determined by the resolution of the microstructures. However, the fabrication process of micro- and nanofabrication are generally complicated and costly.

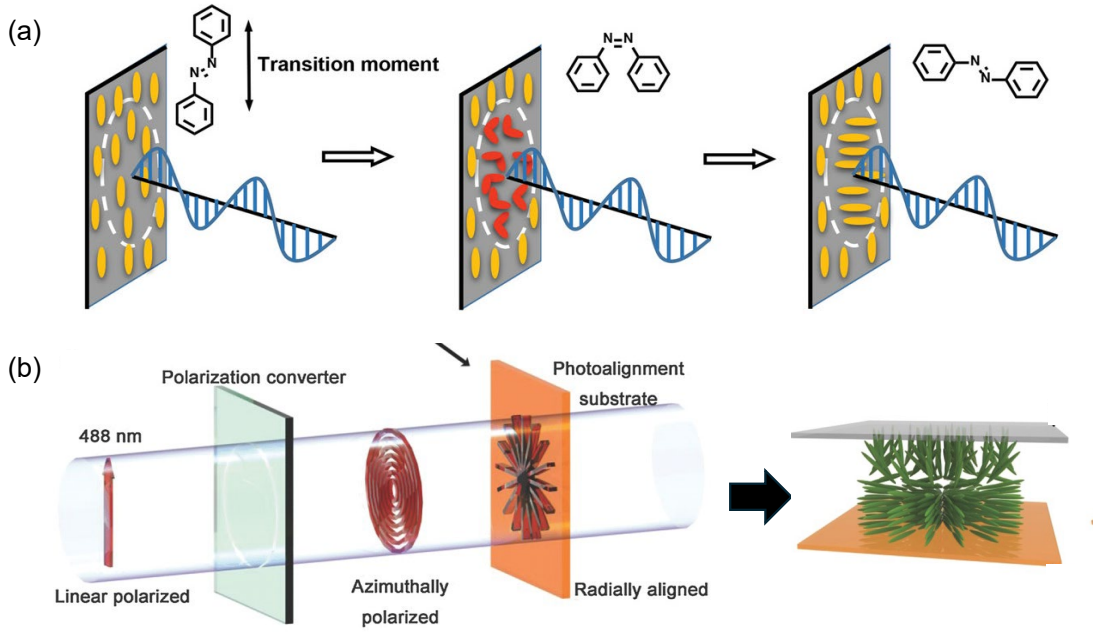

Figure 2.13 Surface anchoring alignment of LCEs by photoalignment. (a) Photoalignment of azobenzene mesogens induced by linearly polarized blue light (Weigert effect). Reproduced from [115]. (b) Complex photoalignment in LCEs realized by compiling the polarization of the incident light, such as radial alignment of mesogens. Reproduced from [101];

To further enable patterned alignment without complicated fabrication process, the photoalignment process [115-121], shown in Figure 2.13(a) [115], offers a more versatile approach. This technique employs photo-responsive materials such as azobenzene dyes or thiol-azobenzene dyes, coated on a glass substrate as the alignment layer. Under exposure to linearly polarized UV light, the dye molecules reorient in accordance with the incident light polarization due to the Weigert effect [122]. When the linearly polarized blue light is incident onto a monodomain azobenzene with the mesogen alignment parallel to the polarization direction, the azobenzene mesogen molecules within the illumination region absorb the photon energy to the excited state and undergo a cis-trans isomerization transition. As a result, the alignment of the molecules changes from an ordered alignment to a disordered alignment. Since the trans-molecules do not absorb energy when their optical axes are perpendicular to the polarization direction of the incident light, after multiple trans-cis-trans isomerization processes, all azobenzene mesogen molecules within the illumination area are finally reorientated perpendicular to the polarization direction of the incident light. This method enables the embedding of intricate spatial alignment

distributions within the photo-responsive alignment layer, which are subsequently transferred to the mesogens through intermolecular interactions. Devices such as digital micromirror devices [116,117] and spatial light modulators [118] facilitate the writing of intricate spatial orientations onto the alignment layer. As shown in Figure 2.13(b) [123], advancements in LCE alignment technologies have enabled photoalignment to achieve high-precision complex spatial orientations through the integration of polarized light modulation and template exposure [123-126]. Nonetheless, while photoalignment is capable of producing high-resolution pixelated alignments, it remains constrained by the maximum attainable alignment area.

Surface anchoring techniques are extensively utilized in LCE research; however, due to limitations associated with anchoring energy, these approaches are predominantly applied to the fabrication of thin films with thicknesses below 100 μm.

2.3.3 Field effect alignment

Field effect alignment primarily includes both magnetic and electric field alignment, wherein mesogens are oriented under the influence of an external field. The effectiveness of this alignment method depends on the anisotropy of the diamagnetic susceptibility or dielectric constant of the mesogens.

For alignment induced by magnetic fields, most mesogens exhibit positive diamagnetic anisotropy due to their aromatic ring structures, aligning along the magnetic field lines. Consequently, under a magnetic field, the long axes of mesogens tend to orient parallel to the external magnetic field of a permanent magnet or along the field lines of an electromagnetic field [127-130]. For alignment induced by electric fields, mesogens with polar functional groups, such as esters, nitriles, or halogens, display positive dielectric anisotropy and align parallel to the direction of the applied electric field [131-135].

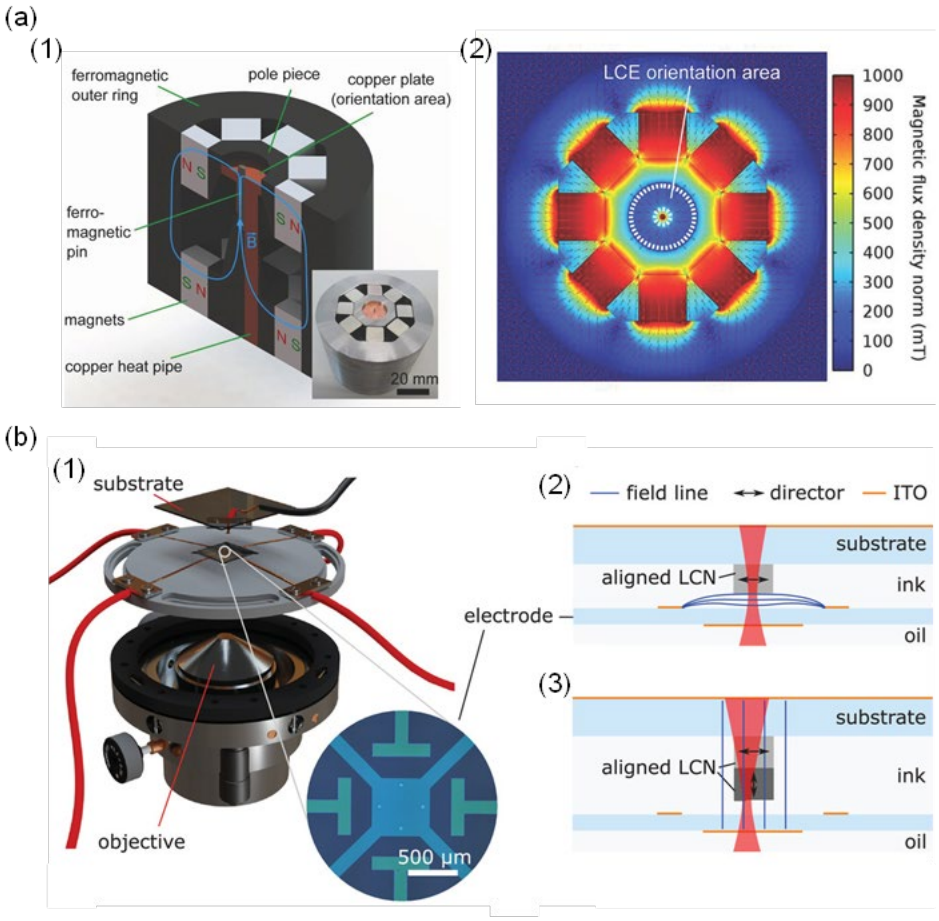

Figure 2.14 Field effect alignment of LCEs. (a) (1) The schematic diagram and the physical image of the magnetic field device to realize the mesogen radial alignment in a confined area at millimetre scale through three-dimensional magnetic field control for a bionic iris LCE; (2) Simulation of the magnetic field with a continuous radial field for alignment. Reproduced from [128]. (b). (1) Schematic of the LCE 4D printing device with electrical alignment control, with an enlarged view of the electrode arrangement for electric field generation. The printing prosses involves the (2) two-photon absorption polymerization, fixing the director direction and (3) electric field direction changes. Reproduced from [139].

The direction and degree of deflection of the mesogens under external fields can be controlled and encoded by adjusting the field's orientation and strength. Field effect alignment offers uniform orientation at the microscale in three-dimensional space. When combined with additive or subtractive manufacturing techniques, this approach facilitates the fabrication of LCEs with not only various enhanced micro-scale orientation but also complex macro-scale structures [136-139]. For example, Figure 2.14(a) [128] shows the device to realize the fabrication of a biomimetic iris LCE, where uniform radial alignment of

mesogenic molecules is achieved at a millimetre scale through magnetic field control. Figure 2.14(b) [139] illustrates the schematic of the device integrating electric field control with 4D printing to achieve 3D alignment of mesogens within a micrometre scale LCE actuator. Notably, field effect alignment is more efficient for radial orientation compared to other methods. However, this approach is often constrained by the complexity of electrode design and the need for extremely high electric and magnetic field strengths.

2.4 Summary

In this chapter, we introduced the relevant background of this thesis, such as the fundamentals of LCs and LCEs, the deformation and actuation of LCEs and the unique category-the IALCEs. The detailed alignment method of LCEs was summarized in Section 2.3 to better comprehend methods that facilitate the manipulation of the anisotropic response of LCEs, which establishes the context for employing an electric field to pattern the director profile in the following chapters while emphasizing the feasibility of this approach. In the next chapter, we will summarize the fundamental methods used throughout the experimental work. It introduces the chemical compounds used in synthesizing IALCEs, details the fabrication process of planar-aligned IALCEs, and outlines key experimental techniques, including POM, mechanical deformation characterization, and DSC.

References

1. Reinitzer F M. Beiträg zur Kenntnis des Cholesterins. Monatshefte für Chemie，1888，9：421-441.
2. Lehmann O. Über Fliessende Krystalle. Z. Physik. Chemie， 1889， 4：462-472.
3. de Gennes, P. G., Prost, J. The Physics of Liquid Crystals. *Clarendon Press, Oxford, 2nd ed.*, 1993.
4. Sebastian N, Cmok L, Mandle R J, et al. Ferroelectric-Ferroelastic Phase Transition in a Nematic Liquid Crystal. Physical Review Letter, 2020, 124, 037801.
5. George W G, Stephen M K. Liquid Crystals for Twisted Nematic Display Devices. Mater. Chem. 1999，9：2037–2050.
6. Ware T H, McConney M E, Wie J J, et al. Voxelated liquid crystal elastomers. Science, 2015, 347(6225): 982–984.
7. White T J, Broer D J. Programmable and adaptive mechanics with liquid crystal polymer

networks and elastomers. Nature Materials, 2015, 14(1): 1087–1098.
8. Qian N, Bisoyi H K, Wang M, et al. A visible and near-infrared light-fueled omnidirectional twist-bend crawling robot. Advanced Functional Materials, 2023, 33(16): 2214205
9. Lan R, Sun J, Shen C, et al. Near-infrared photodriven self-sustained oscillation of liquid-crystalline network film with predesignated polydopamine coating. Advanced Materials, 2020, 32(14): 1906319.
10. He Q, Wang Z, Wang Y, et al. Electrically controlled liquid crystal elastomer–based soft tubular actuator with multimodal actuation. Science Advances, 2019, 5(10): eaax5746.
11. Wang J, Zhou H, Fan Y, et al. Adaptive nanotube networks enabling omnidirectionally deformable electro-driven liquid crystal elastomers towards artificial muscles. Materials Horizons, 2024, 11(8): 1877-1888.
12. Kaiser A, Winkler M, Krause S, et al. Magnetoactive liquid crystal elastomer nanocomposites. Journal of Materials Chemistry, 2009, 19(4): 538-543.
13. Zhang J, Guo Y, Hu W, et al. Liquid crystal elastomer-based magnetic composite films for reconfigurable shape-morphing soft miniature machines. Advanced Materials, 2021, 33(8): 2006191.
14. Lan R, Shen W, Yao W, et al. Bioinspired humidity-responsive liquid crystalline materials: from adaptive soft actuators to visualized sensors and detectors. Materials Horizons, 2023, 10(8): 2824–2844.
15. Liu Y, Xu B, Sun S, et al. Humidity- and photo-induced mechanical actuation of cross-linked liquid crystal polymers. Advanced Materials, 2017, 29(9): 1604792.
16. Mistry D, Connell S D, Micklethwaite S L, et al. Coincident molecular auxeticity and negative order parameter in a liquid crystal elastomer. Nature Communications, 2018, 9(1): 5095.
17. Wang Z, Raistrick T, Street A, et al. Direct observation of biaxial nematic order in auxetic liquid crystal elastomers. Materials, 2022, 16(1): 393.
18. Cheng M, Zeng H, Li Y, et al. Light-fueled polymer film capable of directional crawling, friction-controlled climbing, and self-sustained motion on a human hair. Advanced Science, 2022, 9(1): 2103090.
19. Chen Y, Valenzuela C, Zhang X, et al. Light-driven dandelion-inspired microfliers. Nature Communications, 2023, 14(1): 3036.
20. Yang J, Zhang H, Berdin A, et al. Dandelion-inspired, wind-dispersed polymer-assembly controlled by light. Advanced Science, 2023, 10(7): 2206752
21. Deng Z, Zhang H, Priimagi A, et al. Light-fueled nonreciprocal self-oscillators for fluidic transportation and coupling. Advanced Materials, 2024, 36(12): 2209683.
22. Dradrach K, Zmyslony M, Deng Z, et al. Light-driven peristaltic pumping by an actuating

splay-bend strip. Nature Communications, 2023, 14(1): 1877.
23. Guo H, Priimagi A, Zeng H. Optically controlled latching and launching in soft actuators. Advanced Functional Materials, 2022, 32(17): 2108919.
24. Mistry D, Nikkhou M, Raistrick T, et al. Isotropic liquid crystal elastomers as exceptional photoelastic strain sensors. Macromolecules, 2020, 53(10): 3709−3718.
25. Ohm C, Brehmer M, Zentel R. Liquid crystalline elastomers as actuators and sensors. Advanced Materials, 2010, 22(31): 3366–3387.
26. Ma J, Wang Y, Sun J, et al. Liquid crystal elastomer hollow fibers as artificial muscles with large and rapid actuation enabled by thermal-pneumatic enhanced effect. Advanced Functional Materials, 2024, 2402403.
27. Li S, Bai H, Liu Z, et al. Digital light processing of liquid crystal elastomers for self-sensing artificial muscles. Science Advances, 2021, 7(30): eabg3677.
28. Li X, Yang Y, Valenzuela C, et al. Mechanochromic and conductive chiral nematic nanostructured film for bioinspired ionic skins. ACS Nano, 2023, 17(13): 12829−12841.
29. Hussain M, Jull E I L, Mandle R J, et al. Liquid crystal elastomers for biological applications. Nanomaterials, 2021, 11(3): 813.
30. Zadan M, Patel D K, Sabelhaus A P, et al. Liquid crystal elastomer with integrated soft thermoelectrics for shape memory actuation and energy harvesting. Advanced Materials, 2022, 34(23): 2200857.
31. Auguste A D, Ward J W, Hardin J O, et al. Enabling and localizing omnidirectional nonlinear deformation in liquid crystalline elastomers. Advanced Materials, 2018, 30(35): e1802438.
32. Liu J, Zeng H, Cheng M, et al. Photoelastic plasmonic metasurfaces with ultra-large near infrared spectral tuning. Materials Horizons, 2022, 9(3): 942–951.
33. Moorhouse T, Raistrick T. Sub-Micron Diffractive optical elements facilitated by intrinsic deswelling of auxetic liquid crystal elastomers. Advanced Optical Materials, 2024, 2400866.
34. Chen L, Liu J, Cheng M, et al. Light-driven phase transition of diffractive elements based on liquid crystal elastomers. Optics Express, 2024, 32(7): 12528–12536.
35. Wang Y, Liu J, Yang S. Multi-functional liquid crystal elastomer composites. Applied Physics Reviews, 2022, 9(1): 011301.
36. Zhao J, Zhang L, Hu J. Varied alignment methods and versatile actuations for liquid crystal elastomers: A review. Advanced Intelligent Systems, 2021, 4(3): 2100065.
37. Nie Z Z, Wang M, Yang H. Structure-induced intelligence of liquid crystal elastomers. Chemistry A European Journal, 2023, 29(38): e202301027.
38. Herbert K M, Fowler H E, McCracken J M, et al. Synthesis and alignment of liquid

crystalline elastomers. Nature Reviews Materials, 2021, 7(1): 23–38.
39. Küpfer J, Finkelmann H. Nematic liquid single crystal elastomers[J]. Die Makromolekulare Chemie, Rapid Communications, 1991, 12(12): 717–726.
40. Finkelmann H, Kock H -J, Rehage G. Investigations on liquid crystalline polysiloxanes Liquid crystalline elastomers - a new type of liquid crystalline material. Die Makromolekulare Chemie, Rapid Communications, 1981, 2(4): 317–322.
41. Herbert K M, Fowler H E, McCracken J M, et al. Synthesis and alignment of liquid crystalline elastomers. Nature Reviews Materials, 2021, 7(1): 23–38.
42. J. Küpfer and H. Finkelmann, Liquid crystal elastomers: Influence of the orientational distribution of the crosslinks on the phase behavior and reorientation processes, Macromol. Chem. and Phys. 195, 1353 (1994);
43. I. Kundler and H. Finkelmann, Strain-induced director reorientation in nematic liquid single crystal elastomers, Macromol. Rapid. Commun, 16, 679 (1995).
44. G. C. Verwey, M. Warner, and E. M. Terentjev, Elastic instability and stripe domains in liquid crystalline elastomers, J. Phys. II. France. 6, 1273 (1996).
45. T. Raistrick, Z. Zhang, D. Mistry, J. Mattsson, H. F. Gleeson. Understanding the physics of the auxetic response in a liquid crystal elastomer. Phys. Rev. Research, 3, 023191.
46. Mistry, D. et al. Soft elasticity optimises dissipation in 3D-printed liquid crystal elastomers. Nat. Commun. 12, 6677 (2021).
47. Mistry, D., Morgan, P. B., Clamp, J. H. & Gleeson, H. F. New insights into the nature of semi-soft elasticity and “mechanical-Freedericksz transitions” in liquid crystal elastomers. Soft Matter 14, 1301–1310 (2018).
48. Warner, M., Bladon, P. & Terentjev, E. “Soft elasticity” — deformation without resistance in liquid crystal elastomers. J. Phys. II 4, 93–102 (1994).
49. Terentjev, E. M. & Warner, M. Liquid Crystal Elastomers (Oxford Univ. Press, 2003).;
50. Mitchell, G. R., Davis, F. J. & Guo, W. Strain-induced transitions in liquid-crystal elastomers. Phys. Rev. Lett. 71, 2947–2950 (1993).
51. De Gennes P -G. Soft matter (Nobel Lecture). Angewandte Chemie International Edition, 1992, 31(7): 842–845.
52. De Haan L T, Schenning A P, Broer D J. Programmed morphing of liquid crystal networks. Polymer, 2014, 55(23): 5885–5896.
53. Greaves, G. N.; Greer, A. L.; Lakes, R. S.; Rouxel, T. Poisson’s ratio and modern materials. Nat. Mater. 2011, 10, 823–837.
54. Wieding, J.; Fritsche, A.; Heinl, P.; Körner, C.; Cornelsen, M.; Seitz, H.; Mittelmeier, W.; Bader, R. Biomechanical behavior of bone scaffolds made of additive manufactured tricalciumphosphate and titanium alloy under different loading conditions. J. Appl. Biomater.

Func. 2013, 11, 159-166.
55. Carneiro, V. H.; Meireles, J.; Puga, H. Auxetic materials—A review. Mater. Sci.-Poland 2013, 31, 561-571.
56. Papadopoulou, A.; Laucks, J.; Tibbits, S. Auxetic materials in design and architecture. Nat. Rev. Mater. 2017, 2, 1-3.
57. Saxena, K. K.; Das, R.; Calius, E. P. Three decades of auxetics research materials with negative Poisson's ratio: A review. Adv. Eng. Mater. 2016, 18, 1847–1870.
58. Zeng, H.; Wani, O. M.; Wasylczyk, P.; Kaczmarek, R.; Priimagi, A. Self-regulating iris based on light-actuated liquid crystal elastomer. Adv. Mater. 2017, 29, 1701814.
59. Yeganeh-Haeri, A.; Weidner, D. J.; Parise, J. B. Elasticity of α-cristobalite: A silicon dioxide with a negative Poisson's ratio. Science 1992, 257, 650–652.
60. Keskar, N. R.; Chelikowsky, J. R. Negative Poisson ratios in crystalline SiO2 from first-principles calculations. Nature 1992, 358, 222-224.
61. Baughman, R. H.; Shacklette, J. M.; Zakhidov, A. A.; Stafström, S. Negative Poisson's ratios as a common feature of cubic metals. Nature 1998, 392, 362–365.
62. Sanchez-Valle, C.; Lethbridge, Z. A. D.; Sinogeikin, S. V.; Williams, J. J.; Walton, R. I.; Evans, K. E.; Bass, J. D. Negative Poisson's ratios in siliceous zeolite MFI-silicalite. J. Chem. Phys. 2008, 128, 184503.
63. Kendall, K.; Fuller, K. N. G. J-shaped stress/strain curves and crack resistance of biological materials. J. Phys. D: Appl. Phys. 1987, 20, 1596-1600.
64. Gatt, R.; Wood, M. V.; Gatt, A.; Zarb, F.; Formosa, C.; Azzopardi, K. M.; Casha, A.; Agius, T. P.; Schembri-Wismayer, P.; Attard, L.; Chockalingam, N.; Grima, J. N. Negative Poisson;s ratio in tendons: An unexpected mechanical response. Acta Biomaterialia 2015, 24, 201-208.
65. Ren, X.; Das, R.; Tran, P.; Ngo, T. D.; Xie, Y. M. Auxetic metamaterials and structures: A review. Smart Mater. Struct. 2018, 27, 023001.
66. Wang, Z. Recent advances in novel metallic honeycomb structure. Composites Part B: Engineering 2019, 166, 731-741.
67. Gatt, R.; Zammit, V.; Caruana, C.; Grima, J. N. On the atomic level deformations in the auxetic zeolite natrolite. Phys. Status Solidi B 2008, 245, 502.
68. Evans, K. E.; Nkansah, M. A.; Hutchinson, I. J.; Rogers, S. C. Molecular network design. Nature 1991, 353, 124.
69. Grima, J. N.; Alderson, A.; Evans, K. Auxetic behavior from rotating rigid units. Phys. Status Solidi B 2005, 242, 561.
70. Ren, W.; McMullan, P. J.; Griffin, A. C. Poisson's ratio of monodomain liquid crystalline elastomers. Macromol. Chem. Phys. 2008, 209, 1896–1899.
71. He, C.; Liu, P.; McMullan, P. J.; Griffin, A. C. Toward molecular auxetics: Main chain liquid

crystalline polymers consisting of laterally attached paraquaterphenyls. Phys. Status Solidi B 2005, 242, 576–584.
72. Brown A. W.; Adams, J. M. Negative Poisson's ratio and semisoft elasticity of smectic-C liquid-crystal elastomers. Phys. Rev. E 2012, 85, 011703.
73. Warner, M.; Terentjev, E. M. Liquid Crystal Elastomers, 1st ed; Oxford Clarendon Press: Oxford, United Kingdom, 2003.
74. Ikeda T, Nakano M, Yu Y, et al. Anisotropic bending and unbending behavior of azobenzene liquid-crystalline gels by light exposure. Advanced Materials, 2003, 15(3): 201–205.
75. P. M. S. Roberts, G. R. Mitchell, F. J. Davis, and J. A. Pople, Mechanical switching and soft elasticity in liquid crystal elastomers, Mol. Crys. Liq. Crys. Sci. Tech. Mol. Crys. Liq. Crys. 299, 181 (1997).
76. P. M. S. Roberts, G. R. Mitchell, and F. J. Davis, A single director switching mode for monodomain liquid crystal elastomers, J. Phys. II. France. 7, 1337 (1997).
77. F. J. Davis and G. R. Mitchell, Liquid crystal elastomers: Controlled crosslinking in the liquid crystal phase, Polymer 37, 1345 (1996).
78. P. Bladon, E. M. Terentjev, and M. Warner, Transitions and instabilities in liquid crystal elastomers, Phys. Rev. E. 47, R3838(1993).
79. P. Bladon, M. Warner, and E. M. Terentjev, Orientational order in strained nematic networks, Macromol. 27, 7067 (1994).
80. Yakacki C M, Saed M, Nair D P, et al. Tailorable and programmable liquid-crystalline elastomers using a two-stage thiol–acrylate reaction. RSC Advances, 2015, 5(21): 18997–19001.
81. Guan Z, Wang L, Bae J. Advances in 4D printing of liquid crystalline elastomers: materials, techniques, and applications. Materials Horizons, 2022, 9(7): 1825–1849.
82. H. Liang, S. Zhang, Y. Liu, Y. Yang, Y. Zhang, Y. Wu, H. Xu, Y. Wei, Y. Ji, Merging the Interfaces of Different Shape-Shifting Polymers Using Hybrid Exchange Reactions. Adv. Mater. 2023, 35, 2202462.
83. Lin X, Saed M O, Terentjev E M. Continuous spinning aligned liquid crystal elastomer fibers with a 3D printer setup. Soft Matter, 2021,17(21): 5436–5443.
84. Ahn C, Liang X, Cai S. Inhomogeneous stretch induced patterning of molecular orientation in liquid crystal elastomers. Extreme Mechanics Letters, 2015, 5: 30–36.
85. Liu Z, Bisoyi H B, Huang Y, et al. Thermo- and mechanochromic camouflage and self-healing in biomimetic soft actuators based on liquid crystal elastomers. Angewandte Chemie International Edition, 2021, 61(8): e202115755.
86. Liang H, Zhang S, Liu Y, et al. Merging the interfaces of different shape-shifting polymers

using hybrid exchange reactions. Advanced Materials, 2023, 35(1): 2202462.
87. Agrawal A, Chipara, A C, Shamoo Y, et al. Dynamic self-stiffening in liquid crystal elastomers. Nature Communications, 2013, 4(1): 1739.
88. Schätzle J, Kaufhold W, Finkelmann H. Nematic elastomers: the influence of external mechanical stress on the liquid-crystalline phase behavior. Die Makromolekulare Chemie, 1989, 190(12): 3269–3284.
89. Kim S T, Finkelmann H. Cholesteric liquid single-crystal elastomers (LSCE) obtained by the anisotropic deswelling method. Macromolecular Rapid Communications, 2001, 22(6): 429–433.
90. Kizhakidathazhath R, Geng Y, Jampani V S R, et al. Facile anisotropic deswelling method for realizing large-area cholesteric liquid crystal elastomers with uniform structural color and broad-range mechanochromic response. Advanced Functional Materials, 2020, 30(7): 1909537.
91. Ma J, Yang Y, Valenzuela C, et al. Mechanochromic, shape-programmable and self-healable cholesteric liquid crystal elastomers enabled by dynamic covalent boronic ester bonds. Angewandte Chemie International Edition, 2022, 61(9): e202116219.
92. H. Jiang, C. Chung, M. L. Dunn, K. Yu, 4D printing of liquid crystal elastomer composites with continuous fiber reinforcement. Nat. Commun. 2024, 15, 8491.
93. Yang X, Valenzuela C, Zhang X, et al. Robust integration of polymerizable perovskite quantum dots with responsive polymers enables 4D-printed self-deployable information display. Matter, 2023, 6(4): 1278–1294.
94. Wang Z, Wang Z, Zheng Y, et al. Three-dimensional printing of functionally graded liquid crystal elastomer. Science Advances, 2020, 6(39): eabc0034.
95. Kotikian A, Truby R L, Boley J W, et al. 3D printing of liquid crystal elastomeric actuators with spatially programed nematic order. Advanced Materials, 2018, 30(10): 1706164.
96. Del Pozo M, Delaney C, Pilz Da Cunha M, et al. Temperature-responsive 4D liquid crystal microactuators fabricated by direct laser writing by two-photon polymerization. Small Structures, 2022, 3(2): 2100158.
97. Ambulo C P, Burroughs J J, Boothby J M, et al. Four-dimensional printing of liquid crystal elastomers. ACS Applied Materials & Interfaces, 2017, 9(42): 37332–37339.
98. J. Ma, Y. Wang, J. Sun, R. Nandi, Z. Yang, Liquid crystal elastomer hollow fibers as artificial muscles with large and rapid actuation enabled by thermal-pneumatic enhanced effect. Adv. Funct. Mater., 2024, 2402403.
99. Braun L B, Hessberger T, Zentel R. Microfluidic synthesis of micrometer-sized photoresponsive actuators based on liquid crystalline elastomers. Journal of Materials Chemistry C, 2016, 4(37): 8670–8678.

100. Li M, Gholami F, Yue L, et al. Coaxial-spun hollow liquid crystal elastomer fiber as a versatile platform for functional composites. Advanced Functional Materials, 2024, 2406847.
101. J. Wang, H. Zhou, Y. Fan, W. Hou, T. Zhao, Z. Hu, E. Shi, J. Lv, Adaptive nanotube networks enabling omnidirectionally deformable electro-driven liquid crystal elastomers towards artificial muscles. Mater. Horiz., 2024, 11, 1877-1888.
102. S. Li, H. Bai, Z. Liu, X. Zhang, C. Huang, L. W. Wiesner, M. Silberstein, R. F. Shepherd, Digital light processing of liquid crystal elastomers for self-sensing artificial muscles. Sci. Adv., 2021, 7, eabg3677.
103. He Q, Wang Z, Wang Y, et al. Electrospun liquid crystal elastomer microfiber actuator. Science Robotics, 2021, 6(57): eabi9704.
104. E. K. Fleischmann, H. L. Liang, N. Kapernaum, M. C. H. Wong, M. R. Savin, A. S. Urban, D. R. Smith, D. A. Tenne, T. J. J. Müller, D. S. M. Lee, S. J. L. Liao, P. F. B. Henry, One-piece micropumps from liquid crystalline core-shell particles. Nat. Commun. 2012, 3, 1178.
105. V. S. R. Jampani, R. H. Volpe, K. Reguengo de Sousa, J. F. Machado, C. M. Yakacki, J. P. F. Lagerwall, Liquid crystal elastomer shell actuators with negative order parameter. Sci. Adv. 2019, 5, eaaw2476.
106. Barnes M, Verduzco R. Direct shape programming of liquid crystal elastomers. Soft Matter, 2019, 15(5): 870–879.
107. J. Lee, Y. Guo, Y. Choi, S. Jung, D. Seol, S. Choi, J.-H. Kim, Y. Kim, K.-U. Jeong, S.-K. Ahn, Mechanically programmed 2D and 3D liquid crystal elastomers at macro-and microscale via two-step photocrosslinking. Soft Matter 2020, 16, 2695–2705.
108. Z. Wang, Q. He, Y. Wang, S, Programmable actuation of liquid crystal elastomers via “living” exchange reaction. Soft Matter 2019, 15, 2811–2816.
109. X. Pang, J. Lv, C. Zhu, L. Qin, Y. Yu, Photodeformable Azobenzene-Containing Liquid Crystal Polymers and Soft Actuators. Adv. Mater. 2019, 31, 1904224.
110. Berreman D W. Solid surface shape and the alignment of an adjacent nematic liquid crystal. Phys. Rev. Lett. 28, 1683–1686, 1972.
111. Berreman D W. Alignment of liquid-crystals by grooved surfaces. Mol. Cryst. Liq. Cryst. 23, 215–231, 1973.
112. J. Wang, K. Li, H. He, W. Cai, J. Liu, Z. Yin, Q. Mu, V. Hisao, D. Gérard, D. Luo, G. Li, Y. J. Liu, Metasurface enabled high resolution liquid crystal alignment for display and modulator applications. Laser Photonics Rev. 2022, 16, 2100396.
113. H. Aharoni, Y. Xia, X. Zhang, R. D. Kamien, S. Yang, Universal inverse design of surfaces with thin nematic elastomer sheets. Proc. Natl. Acad. Sci. 2018, 115, 7206–7211.
114. Y. Xia, G. Cedillo-Servin, R. D. Kamien, S. Yang, Guided folding of nematic liquid crystal

elastomer sheets into 3D via patterned 1D microchannels. Adv. Mater. 2016, 28, 9637–9643.

115. Pang X, Lv J, Zhu C, et al. Photodeformable azobenzene-containing liquid crystal polymers and soft actuators. Advanced Materials, 2019, 31(52): 1904224.
116. Kowalski B A, Tondiglia V P, Guin T, et al. Voxel resolution in the directed self-assembly of liquid crystal polymer networks and elastomers. Soft Matter, 2017, 13(24): 4335–4340.
117. Huang L, Jiang R, Wu J, et al. Ultrafast digital printing toward 4D shape changing materials. Advanced Materials, 2017, 29(7): 1605390.
118. Gao M, Cheng M, Cai W, et al. Programmable spatially-varying linearly polarized light with high degree of polarization for planar liquid crystal photonics. Optics and Lasers in Engineering, 2024, 179(1): 108254.
119. Guin T, Settle M J, Kowalski B A, et al. Layered liquid crystal elastomer actuators. Nature communications, 2018, 9(1): 2531.
120. Kowalski B A, Mostajeran C, Godman N P, et al. Curvature by design and on demand in liquid crystal elastomers. Physical Review E, 2018, 97(1): 012504.
121. Godman N P, Kowalski B A, Auguste A D, et al. Synthesis of elastomeric liquid crystalline polymer networks via chain transfer. ACS Macro Letters, 2017, 6(11): 1290–1295.
122. Weigert, F. (1919). "Über einen Effekt der Strahlung in lichtempfindlichen Schichten." Verhandlungen der Deutschen Physikalischen Gesellschaft, 21, 479.
123. Zeng H, Wani O M, Wasylczyk P, et al. Self-regulating iris based on light-actuated liquid crystal elastomer. Advanced Materials, 2017, 29(30): 1701814. De Haan L T, Sánchez-Somolinos C, Bastiaansen C M, et al. Engineering of complex order and the macroscopic deformation of liquid crystal polymer networks. Angewandte Chemie International Edition, 2012, 124(50): 12637–12640.
124. McConney M E, Martinez A, Tondiglia V P, et al. Topography from topology: photoinduced surface features generated in liquid crystal polymer networks. Advanced Materials, 2013, 25(41): 5880–5885.
125. Gibbons W M, Shannon P J, Sun S, et al. Surface-mediated alignment of nematic liquid crystals with polarized laser light. Nature, 1991, 351(6321): 49–50.
126. Xu Y, Zhang X, Song Z, et al. In situ light-writable orientation control in liquid crystal elastomer film enabled by chalcones. Angewandte Chemie Internation Edition, 2024, 63(11): e202319698.
127. Hoyle W, Watanabe T, Whitehead J B. Anisotropic network formation by photopolymerization of liquid crystal monomers in a low magnetic field. Macromolecules, 1994, 27(22): 6581–6588.
128. Schuhladen S, Preller F, Rix R, et al. Iris-like tunable aperture employing liquid-crystal

elastomers. Advanced Materials, 2014, 26(42): 7247–7251.
129. Petsch S, Khatri B, Schuhladen S, et al. Muscular MEMS—the engineering of liquid crystal elastomer actuators. Smart Materials and Structures, 2016, 25(8): 085010.
130. Legge C H, Davis F J, Mitchell G R. Memory effects in liquid crystal elastomers. Journal of Physics B Atomic and Molecular Physics, 1991, 1(10): 1253–1261.
131. Spillmann C M, Ratna B R, Naciri, J. Anisotropic actuation in electroclinic liquid crystal elastomers. Applied Physics Letters, 2007, 90(2): 021911.
132. Brömmel F, Benzie P, Osterwinter G J, et al. Orientation behaviour of the minor director of homeotropically oriented nematic elastomers in mechanical fields. Soft Matter, 2013, 9(9): 2646–2651.
133. Rogez D, Martinoty P. Mechanical properties of monodomain nematic side-chain liquid-crystalline elastomers with homeotropic and in-plane orientation of the director. European Physics Journal E, 2011, 34(69): 1–13.
134. Ge S J, Zhao T P, Wang M, et al. A homeotropic main-chain tolane-type liquid crystal elastomer film exhibiting high anisotropic thermal conductivity. Soft Matter, 2017, 13(32): 5463–5468.
135. Wang M, Wang J, Yang H, et al. Homeotropically-aligned main-chain and side-on liquid crystalline elastomer films with high anisotropic thermal conductivities. Chemical Communications, 2016, 52(23): 4313–4316.
136. Cui J, Drotlef D, Larraza I, et al. Bioinspired actuated adhesive patterns of liquid crystalline elastomers. Advanced Materials, 2012, 24(34): 4601–4604.
137. Zhao H, Wie J J, Copic D, et al. High-fidelity replica molding of glassy liquid crystalline polymer microstructures. ACS Applied materials & interfaces, 2016, 8(12): 8110–8117.
138. Yang H, Buguin A, Taulemesse J, et al. Micron-sized main-chain liquid crystalline elastomer actuators with ultralarge amplitude contractions. Journal of the American Chemical Society, 2009, 131(41): 15000–15004.
139. Munchinger A, Hahn V, Beutel D, et al. Multi-photon 4D printing of complex liquid crystalline microstructures by in situ alignment using electric fields. Advanced Materials Technologies, 2022, 7(1): 2100944.

Chapter 3 Materials and experimental methods

In the previous chapter, we provided a brief introduction to the fundamentals of LCs and LCEs, with an emphasis on the unique category of LCE–the auxetic LCE. Besides, we reviewed the relationship between the macroscopic deformations of LCEs and the microscopic alignment of mesogens inside the LCEs and illustrated the insight of manipulating the macroscopic deformations of LCEs is by controlling the microscopic alignment of mesogens inside the LCEs.

In this chapter, we will focus on the IALCEs, the main character throughout this thesis. We will start with the introduction of materials used to synthesis the IALCEs, followed by a detailed description of experimental procedure for fabrication of a general planar aligned IALCE. Then, we will outline the essential experimental methods for characterizations of IALCEs, for examples, polarized optical microscopy (POM), mechanical deformation characterizations and differential scanning calorimetry (DSC). Finally, we will give hints about some specific experimental methods which will introduced in the following chapters.

3.1 Materials in Intrinsic Auxetic Liquid Crystal Elastomers

3.1.1 Chemical compounds for synthesizing IALCE

The IALCEs were synthesised using the same monomers described by Mistry *et al.* [1] but in different proportions. The chemical compounds shown in Figure 3.1 were mixed in the proportions indicated to form the nematic LCE precursor.

The 4’-Hexyloxybiphenyl (6OCB) is a nonreactive mesogen included to broaden the nematic phase range of the precursor. The 6-(4-cyano-biphenyl-40-yloxy)hexyl acrylate (A6OCB) is a monofunctional reactive material that forms the LCE mesogenic side groups, while the bifunctional 1,4-bis-[4-(6-acryloyloxyhex-yloxy)benzoyloxy]-2-methylbenzene (RM82) is a mesogenic crosslinker. 2-Ethylhexyl acrylate (EHA) was introduced to increase the flexibility of the polymer backbone and help to reduce the glass transition temperature to below room temperature. Methyl benzoylformate (MBF) was used as the UV-photoinitiator. A6OCB, 6OCB and RM82 were obtained from Synthon Chemical GmbH (Bitter-feld-Wolfen, Germany) while EHA and MBF were bought from Sigma Aldrich (Gillingham, UK).

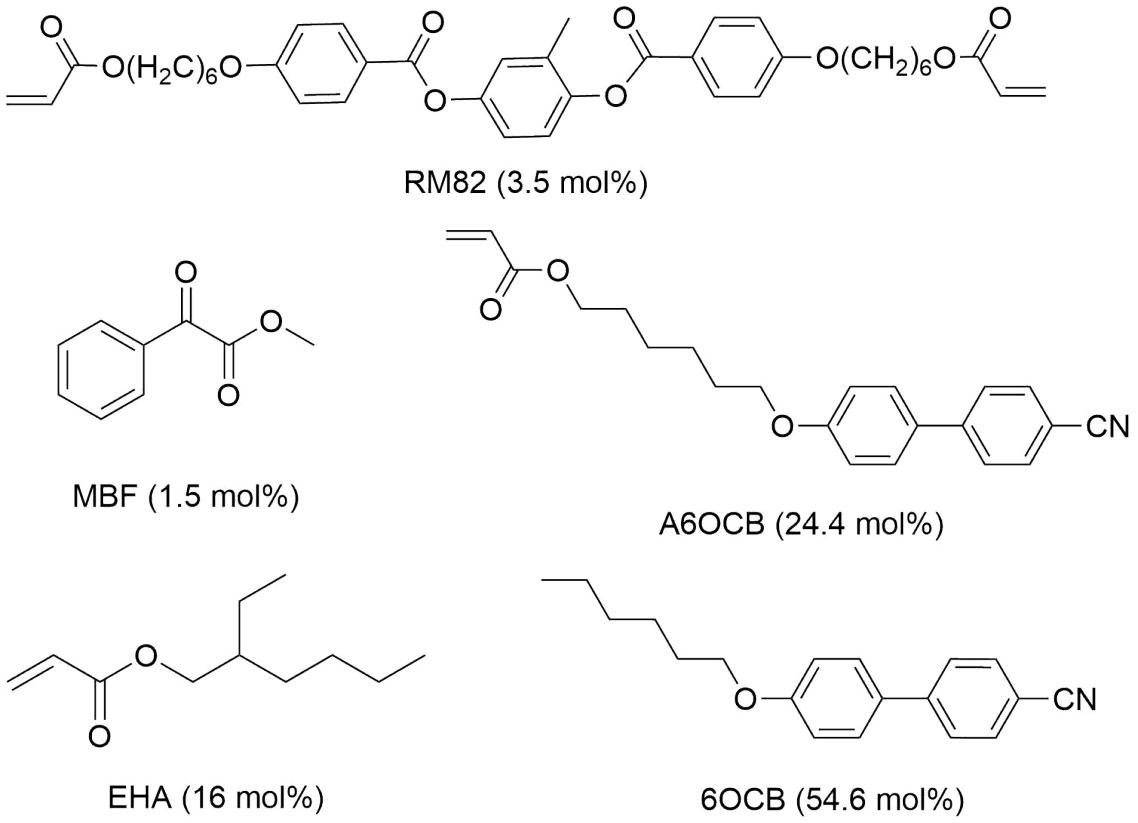

Figure 3.1 The molecular structures of the LCE monomers with proportion in the precursor mixture indicated.

3.1.2 Some additional information about how the recipe affects IALCEs

The recipe to synthesize IALCEs in this thesis is modified upon the recipe described by Mistry *et al.* [1]. The comparison of the chemical proportions in the recipe from this thesis and that provided by Mistry *et al.* is shown in Table 1. Compared to the recipe in the initial auxetic system provided by Mistry *et al.*, the proportion of the functional mesogens (A6OCB) used in this thesis is increased while the crosslinker (RM82) and the non-mesogenic unit (EHA) are reduced to keep the phase transition temperature, T_{ni} (the critical temperature at which the precursor transitions from the nematic phase to isotropic phase) of the unpolymerized mixture at ~35°C, higher than the room temperature, and the glass transition temperature (T_g) of the polymerized film at ~15°C, lower than the room temperature, while the auxetic threshold strain is tuned earlier from ~0.8 ± 0.05 to ~0.6 ± 0.05. The detailed mechanical deformation characterization of the IALCEs used in this thesis will be introduced later in Section 5.3.

Table 3.1. Comparison of chemical compositions in recipe from this thesis and Mistry [1]

Component	% by mol. of each component in the recipe	
	This thesis	By Mistry *et al.* [1]
6OCB	54.6	55.9
A6OCB	24.4	14.6
RM82	3.5	7.1
EHA	16.0	20.9
MBF	1.5	1.5

Referring to the introductory part in Section 2.2.1 Fundamentals of Liquid Crystal Elastomers, the synthesis of the IALCEs is based on acrylate homopolymerization. The polymerization of acrylate monomers into a polymer chain is realized with free radicals and the process is composed of three stages, presented in Figure 3.2. Free radicals refer to molecules or atoms with unpaired electrons, formed by the homolytic cleavage of covalent bonds in the molecules under external conditions such as light and heat [2]. During initiation stage, the free radicals generated from the photoinitiator attack the double bond in the acrylate group and connect to the carbon. Propagation occurs through the stage when the chain grows as the free radical transfers from one acrylate group to another acrylate group. As for the termination stage, two free radicals meet and the polymerization stops with a stable polymer synthesized. According to the molecular structure of the functional mesogen A6OCB in the recipe, the final IALCE samples are side-chain end-on LCEs.

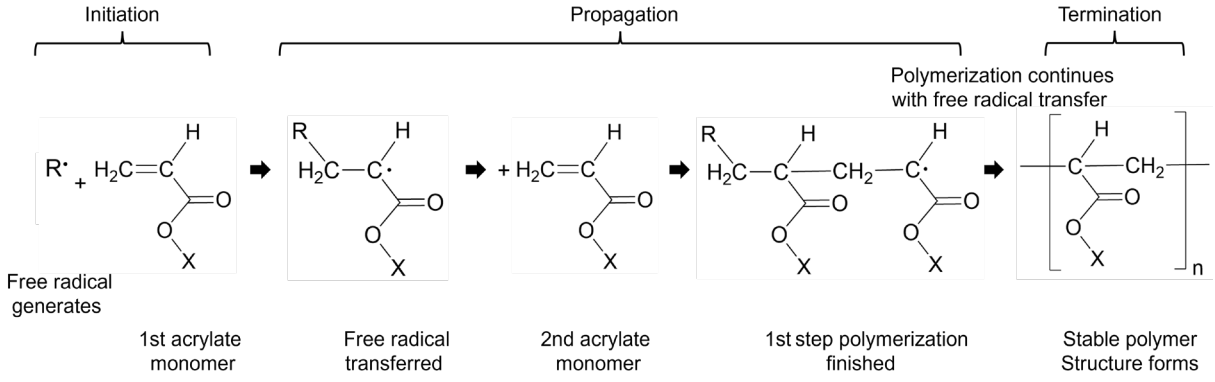

Figure 3.2 The schematic of polymerization process in which acrylate monomers are polymerized into a polymer chain with free radicals.

Several efforts have been made to investigate how the chemical compound in the recipe would affect the properties of IALCEs [3-6]. For examples, Cooper *et al.* has shown the modification on the optical properties of the auxetic LCEs with the change of mesogenic content proportions [4]. Berrow *et al.* has shown the manipulation on mechanical properties

of the auxetic LCEs with the control of the spacer lengths [5]. The most straightforward effect related to the chemical compounds is observed in the relationship between the T_g of the samples with the threshold strain, ε_{th}, the critical strain beyond which the auxetic LCE exhibit negative Poisson's ratio, in the auxetic responses. When the T_g increases, the ε_{th} will increase, as well.

3.2 Fabrication of planar aligned intrinsic auxetic Liquid Crystal Elastomers

The fabrication process of the planar aligned IALCE sample is the foundational method for all samples fabricated in this thesis. While synthesizing particular IALCE samples, the overall fabrication process remains almost consistent, with only minor modifications. Therefore, this section focuses on the detailed fabrication process of the planar aligned IALCEs.

3.2.1 Fabrication of the cells

The planar aligned IALCE samples were made by photopolymerizing the nematic precursor mixture in a cell based on a conventional LC device, shown schematically in Figure 3.3. The planar samples were constructed as described previously [1]. The empty devices were assembled using one glass microscope slide (25 × 75 mm) and one 300μm thick Melinex401 film (60 × 15 mm) substrates, with 100μm thick Melinex401 film used as spacers.

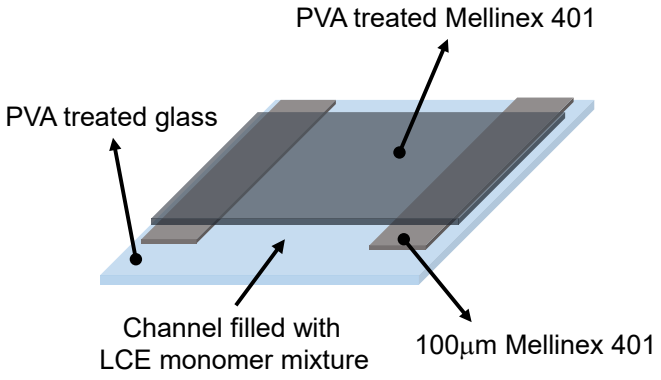

Figure 3.3 A schematic showing the assembled LCE cell used to fabricate IALCEs with planar alignment.

Glass microscope slides undergo a comprehensive cleaning protocol, which includes sonication for 20 minutes in a solution of deionized (DI) water and soap, multiple rinses in

DI water, a second sonication in ethanol for 20 minutes, and drying with an air gun, followed by sonication in acetone for 20 minutes and subsequent air drying. The Melinex401 substrates were cleaned by sonication in methanol for 20 minutes and then dried with an air gun. The polymer substrate used here allows for later ease extraction of the LCE film after polymerization. The Melinex401 films were obtained from DuPont Teijin Films.

Excellent monodomain alignment is achieved by spin-coating the inner surface of the substrates with a 0.5 wt.% polyvinyl alcohol (PVA) solution which is uniaxially rubbed when dry. To ensure complete surface coverage, the PVA solution was carefully placed on the substrates and allowed to rest for 30s to facilitate surface wetting. The substrates were first spin-coated at 400rpm for 10s. Subsequently, the spin speed was gradually increased to 1500 rpm for 30s. For the rubbing process, an in-house rubbing machine was employed. The substrates were held on a vacuum plate, and the plate moved under a rolling drum wrapped by a velvet cloth. The alignment layers were rubbed uniaxially in a desired direction and subsequently blown by the air gun to remove any residual fluff. The rolling speed was 600rpm and the substrates were rubbed four times.

The cells were assembled by placing the PVA-coated Melinex films on steel blocks with the PVA-coated side facing upward. Thin lines of UV-curable Norland Optical Adhesive (NOA61) were put along the edges of the substrate, onto which 100μm spacers were carefully placed. Additional adhesive lines were then put on the spacers, followed by the placement of the PVA-treated glass substrate (PVA side facing downward) while ensuring precise alignment of the rubbing directions in an antiparallel configuration. Magnets were evenly distributed along the cell's top surface to achieve uniform compression by magnetic attraction to the steel blocks. Finally, the cells were exposed to a low-intensity UV light source (365nm, 2.5 mW cm^{-2}) for 20 minutes to cure the adhesive, resulting in an assembled cell.

3.2.2 Synthesis of the general Intrinsic Auxetic Liquid Crystal Elastomers

The mesogenic compounds were mixed by heating to 120°C while stirring at 200rpm on a magnetic hot plate for 5 minutes. After the mixture is uniform in the isotropic phase, the temperature then decreased to 40°C and the EHA and MBF added, stirring for a further 2 minutes. A short stirring time at such a temperature was to avoid the evaporation and loss of EHA which is a volatile material.

The LCE monomer mixture was filled into the moulds via capillary action in its isotropic

phase (at 40°C) and left for around 20 min to cool to room temperature. The mesogens align with the alignment layers as the temperature decreases into the nematic phase. Once aligned, the moulds were placed under a low intensity UV florescence light source (365nm, 2.5 mW/cm^2) for 2 hours to cure. Upon exposure to the UV light, the photoinitiator MBF generates free radicals and triggers polymerizations. Such a long exposure time was to ensure complete polymerization.

After curing, the polymer substrate was carefully peeled away. Placing the exposed sample on the glass substrate into methanol caused the sample to swell slightly and delaminate at the edges. Flat-tipped tweezers were used to peel off the sample completely. Once separated, the unreacted 6OCB in IALCE was washed away by leaving the peeled film in dichloromethane (DCM) solution (30% in methanol) overnight (~8h). The mixture of DCM and methanol was to avoid tearing of the film due to the too fast swelling or deswelling process in the washing process. After washing, the IALCE film was hung in a beaker at 60°C for more than 2 hours to dry. Table 2 shows the proportions of the components for the monomer mixture and those in the final IALCE sample. MBF was completely consumed after polymerization, and 6OCB was entirely removed during the washing process after synthesis.

Table 3.2. Chemical composition of the IALCE before and after wash

Component	% by mol. of each component in the IALCE	
	Precursor mixture	Final IALCE
6OCB	54.6	0
A6OCB	24.4	55.6
RM82	3.5	8.0
EHA	16.0	36.4
MBF	1.5	0

3.3 Characterization techniques

Several experimental methods were used in this thesis, however, many of them were only utilized occasionally. In this section, we will mainly present the key characterization techniques of the basic properties of the IALCEs, including polarized optical microscopy (POM), mechanical deformation characterization and differential scanning calorimetry (DSC). Information regarding the less frequently utilized techniques will be mentioned briefly in this section while introduced in detail in later relevant chapters.

3.3.1 Polarized optical microscopy

Polarized optical microscopy (POM) is a key experimental technique in LC characterization in the identification of LC phases, LC alignment, optical properties and so on [6]. The general POM observation of a birefringent sample comprises the illumination of the birefringent sample, held between crossed polarisers (one polariser and one analyser), wherein the polarization axis of each polariser is at 90° with each other, see Figure 3.4. In this thesis, the birefringent samples are LC cells or IALCE samples.

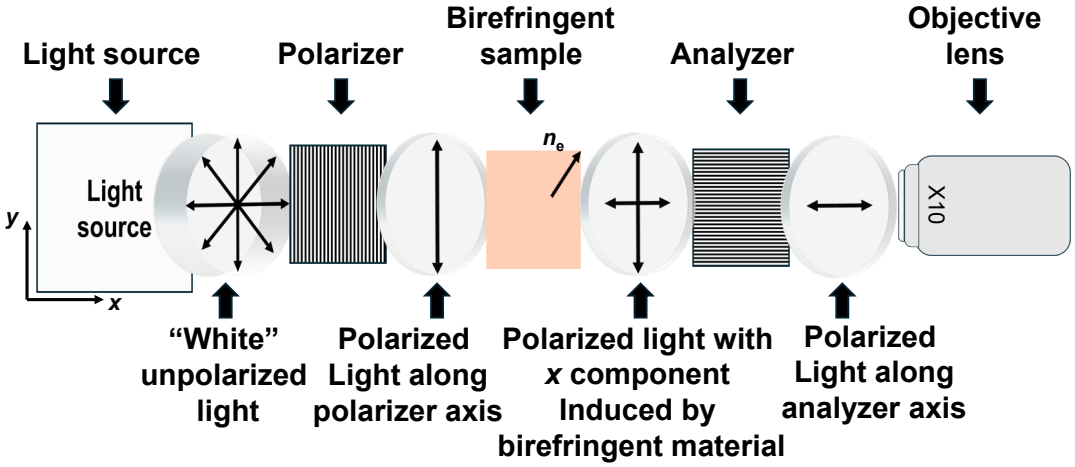

Figure 3.4 Schematic of general POM observation of a birefringent sample.

Referring to Sections 2.1 and 2.2, an LC molecule has anisotropic polarizability and when included into the LCE, the LCE in anisotropic alignments consequently exhibits anisotropic optical properties. The anisotropic optical property in LC reflects in the different refractive indexes along the principal axes of the LC, as presented in Figure 3.5.

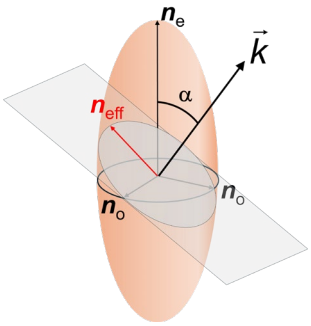

Figure 3.5 The index ellipsoid schematic of an anisotropic nematic LC material when a general light ray propagates through the material in the direction, $\vec{k}$.

The refractive index can be presented by the index ellipsoid, where the refractive index along the director denotes the extraordinary refractive index, n_e, while the refractive index

perpendicular to the director denotes the ordinary refractive index, n_o. When a light passes through a transparent anisotropic material, the light experiences different refractive indexes for the linearly polarized components of the electric field, resolved along the optical axis (the direction in the same direction as the director) of the optically anisotropic material. We define the refractive index that the electric field of the incident light experiences as the effective refractive index, n_{eff}, and this refractive index is defined by the projection of the anisotropic refractive index to the electric field polarization direction on the plane perpendicular to the wave vector, $\vec{k}$, of the incident light. The n_{eff} denoted as:

$$\frac{1}{n_{eff}} = \frac{\cos^2 \alpha}{n_e^{\,2}} + \frac{\sin^2 \alpha}{n_o^{\,2}} \tag{3.1}$$

where α is the angle between the $\vec{k}$ and the axis of n_e.

When the sample is in isotropic state, the POM figure will be dark as the polarised light experiences no effect from the isotropic medium so there is no component of resolved light along the polarization direction of analyser. The same dark POM figures can be observed when $\vec{k}$ is parallel to the extraordinary axis. In this circumstance, $n_{eff} = n_o$ and the light experiences an optical isotropic environment. Such a geometry typically describes a homeotropic alignment system. When θ is 90°, $n_{eff} = n_e$ and the birefringence is at its maximum magnitude where $\triangle n = n_e - n_o$. When a birefringent sample is observed under POM with a white light source, with the optical axis at any arbitrary angle away from the polariser axis, a bright state will usually be observed. When the optical axis is at 45° to the polariser axis, the POM figure will be observed at the brightest state. In this thesis, the POM system was Eclipse Ti200, Nikon [7,8] and will be mainly used to determine the alignment quality of IALCEs in Chapter 5 and observe the optical feature of IALCEs in mechanical deformation process in Chapter 6 and 7.

3.3.2 Mechanical deformation characterization

The mechanical properties of IALCE samples are measured by a bespoke mechanical testing equipment called Microscope Elastomer Stress Strain Enclosure (MESSE), which has been described in detail by Mistry *et al.* [1, 8-10]. MESSE is a highly integrated, software-controllable platform combining a high-resolution camera, temperature controls, actuator controls, and force sensors, making it a powerful tool for opto-mechanical measurements in LCE research. MESSE facilities simultaneous observation of samples

during mechanical deformation by capturing high-resolution images under both white light and crossed polarizers, enabling analyses such as the director reorientation and strain variations of the sample during mechanical deformations. In this thesis, MESSE will be used to investigate the change in optics and the strain of the sample during mechanical deformations for analysing auxetic responses. Additionally, the strain-stress measurements are directly obtained with the integrated sensors.

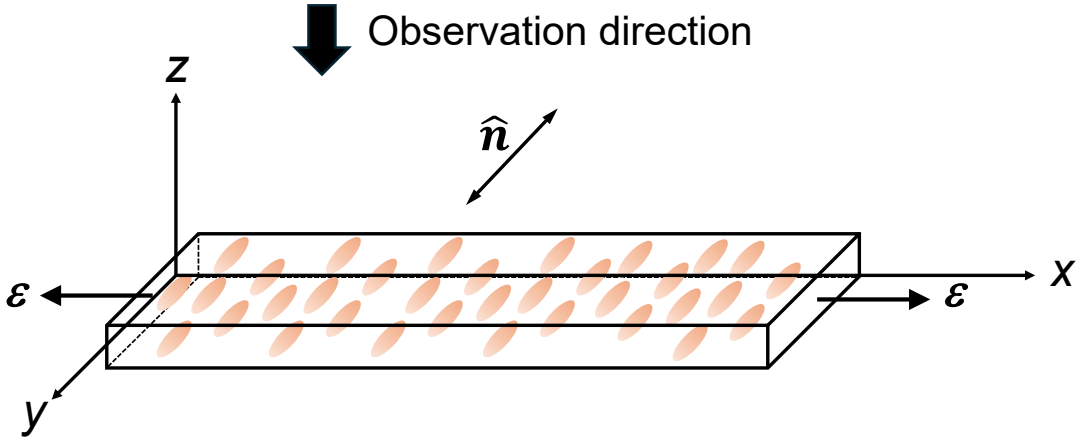

Figure 3.6 Diagram describing the undeformed sample geometry with the director parallel to the *y*-axis for the planar LCE. Strains (ε) are applied along the *x*-axis and the observation direction is along *z*-axis.

Figure 3.6 shows the schematic of an undeformed IALCE sample geometry, illustrating the observation direction and the direction of the strain applied. When the IALCE samples (thickness ~100μm) were synthesized, a 0.5 cm wide strip was cut from the whole film by a scalpel and then loaded into MESSE, held by the sample clamps in the load cell. All the mechanical deformation measurements were carried out at room temperature. The original gap between two sample clamps was 2 cm. One stage at a time, the sample was stretched with a 1 mm step strain (5% strain to the initial length) at a stretching speed of 0.02 mm s^{-1} and was held for 10 minutes to allow the sample to undergo strain relaxation. At every stage, a photograph of the sample both with and without crossed polarisers was recorded. The stress-strain data were also collected with the same device by the integrated stress sensors. The dimension of the sample was set with a constant thickness of 100 μm and width of 0.5 cm. The load cell in MESSE is capable of recording loads of up to 5 N in either tension or compression.

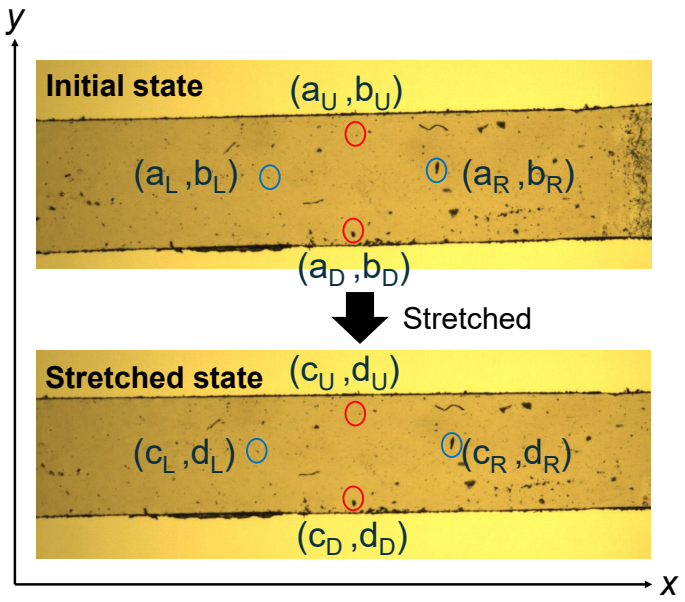

The strain of the stretched state:

In the x direction:

$$\varepsilon_x = \frac{(c_R - c_L) - (a_R - a_L)}{a_R - a_L}$$

In the y direction:

$$\varepsilon_y = \frac{(d_U - d_D) - (b_U - b_D)}{b_U - b_D}$$

Figure 3.7 The particle tracking process (left) for strain measurement (right). ε_x and ε_y is the strain along x-axis and y-axis, respectively. (an, bn) is the coordinate of the point tracked at the initial state, while (c_n, d_n) is the coordinate of the corresponding particles at the stretched state. n = L, R, U and D, representing distinct tracked particles.

The stress-strain curve of the sample was obtained directly from the stress sensors, while the deformation characterization was analysed post-experiment by tracking particles from the high-resolution optical images (taken without crossed polarisers) of every stage with ImageJ (National Institute of Health, USA) [11]. The strain in the stress direction (*x*-axis) is determined by selecting a pair of tracked particles located near the centre of the deformation and at approximately the same distance away from one edge of the film, see Figure 3.7. The strain at each stage is then calculated from the length change in the x-coordinate for further separations, with respect to the initial distance between the tracked particles, as shown in Figure 3.7. The particles are from the environment after synthesising and alocated on the film surface. The strain in the width direction (*y*-axis) is determined by the same method. While for the strain in thickness direction (z-axis), it is calculated based on the constant volume equation, referring to in Section 2.2.3, denoted as:

$$1 = (1+\varepsilon_x)(1+\varepsilon_y)(1+\varepsilon_z) \tag{3.2}$$

Here, ε_x , ε_y and ε_z represent the strains in *x*-, *y*- and *z*-axis directions for a specific deformation stage.

3.3.3 Differential scanning calorimetry

Differential Scanning Calorimetry (DSC) is a thermo-analytical technique utilized in the measurement of heat flow ($\frac{dQ}{dt}$) associated with a sample, enabling the identification of thermal behaviour of materials, for example the polymerizations, phase transitions and glass transitions [12]. DSC works in the form of measuring the difference in the heat required to raise the temperature of two pans, one empty as reference pan and the other containing a sample. The difference in heat required is attributed to the sample's heat capacity, in other words, the heat required to alter a material's temperature may vary with the thermal capacity changes. Thus, in the measurement process, the analysis on changes of the DSC curve can help to identify the thermal behaviours mentioned above. Here in this thesis, DSC measurement is used to measure the glass transition temperature, T_g of the IALCE samples. The DSC analysis is built on a baseline, which represents the material's heat capacity. When glass transition occurs, it reflects in a gradual step change of the baseline of the DSC trace [13,14]. For measuring the T_g, we determine the midpoint temperature of the step change as the T_g.

To prepare a sample for DSC measurement, a small piece was cut off from the prepared IALCE samples and then weighed. Then, the weighed part was sealed in an aluminium pan hermetically with an aluminium cover and transferred into the TA instrument Q20 DSC, operated with a heating and cooling rate at 10°C /min over the range from -60°C to 120°C. The cut sample was heavier than 5mg to ensure the result was accurate, and for each single sample, the measurement of the T_g was run for 2 rounds. During the measurement, the Nitrogen gas (N_2) was used as the protecting gas. The result was analysed by the TA instrument software. Considering the glass transition is an energy absorbing process, we mainly focused on the endothermic process. Furthermore, we took the second heating round for analysing the T_g instead of the first heating round, to avoid the inaccuracy in the measurement caused by the thermal history of the material [15]. The final determination of T_g was by finding the midpoint of the gradual step change between the onset temperature, where the steady baseline starts to deviate, and the end temperature, where the baseline stabilizes again. All these three points were determined using the fitting function of TA instrument software. A DSC measurement of the planar aligned IALCE is shown as an example in Figure 3.8. The analyse is on the second

endothermal trace, where the onset temperature is 6.7°C, the end temperature is 20.0°C and the T_g is 15.8°C. Due to the constant heating/cooling rate applied, the accuracy of the DSC transition temperatures is quoted to ± 0.1°C in the measurement. However, in the comparison of results of different samples, considering the error in the temperature calibration, thermal contact and heat rates, the accuracy should be ± 1°C with a higher associated error.

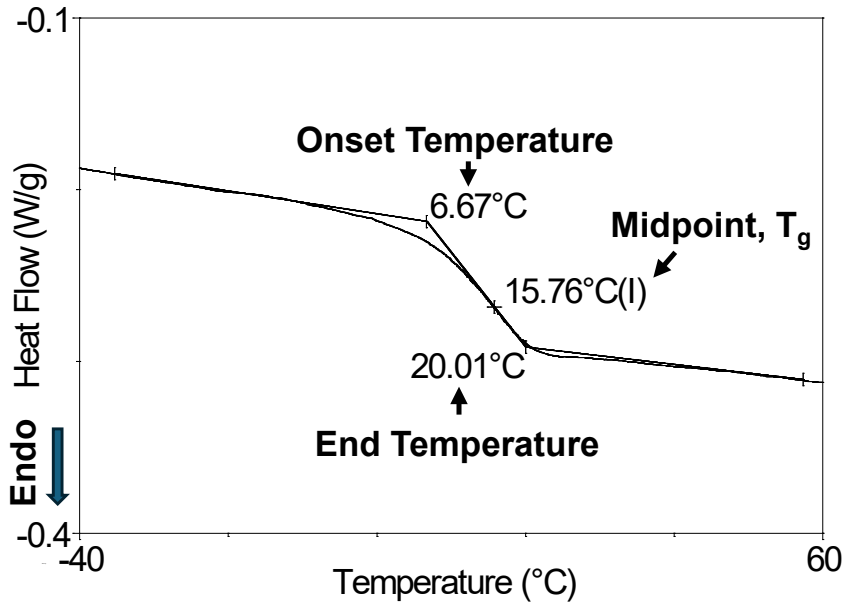

Figure 3.8 The DSC curve analysis of the planar aligned IALCE in the second endothermal trace.

3.3.4 Other experimental techniques

In this thesis, besides the techniques mentioned in the former sections, some other techniques will be briefly mentioned here and introduced in more detail later in the relevant chapters.

- A Berek Compensator was utilized in Chapter 6 for the measurements of the birefringence of the polymerized IALCE to determine the refractive index changes due to the introduction of the Fréederisksz transition alignment.
- Two translation stages (XR25/M Series, Thorlabs), a CCD (Digital microscope, RoHs) and a versatile light source (VL196, Ulanzi) were used to observe the 2D information decryption in Chapter 7.
- A laser scanning microscope (VK-X1000, Keyence) was utilized in Chapter 8 to

image and characterise the surface morphology in the decryption of 3D tactile information.

3.4 Summary

In this chapter we have introduced the chemical compounds utilized in synthesizing IALCEs and described the details of the fabrication process of the planar aligned IALCEs. We have also described all the basic experimental techniques required for this thesis, including POM, mechanical deformation characterization and DSC. Some less frequently utilized techniques were also mentioned briefly. In the next chapter, we will move on to the first project in this thesis, the modification of director orientation in IALCE precursor using external electric field control. We will introduce the electrical-optical property of the IALCEs precursor and introduce the synthesis of IALCE samples in homeotropic alignment. The mechanical deformation measurement of the IALCE samples in not only homeotropic alignment but also planar alignment will be present to experimentally observe the emergence of the biaxiality during the mechanical auxetic response.

References

1. Mistry, D.; Connell, S. D.; Mickthwaite, S. L.; Morgan, P. B.; Clamp, J. H.; Gleeson, H. F. Coincident molecular auxeticity and negative order parameter in a liquid crystal elastomer. *Nat. Commun.* 2018, *9*, 5095.
2. Penna, C.; Mancardi, D.; Rastaldo, R.; Pagliaro, P. Cardioprotection: A radical review: Free radicals in pre and postconditioning. Biochimica et Biophysica Acta (BBA) – Bioenergetics 2009,*1787*, 781-793.
3. Raistrick, T.; Reynolds, M.; Gleeson, H. F.; Mattson, J. Influence of Liquid Crystallinity and Mechanical Deformation on the Molecular Relaxations of an Auxetic Liquid Crystal Elastomer. Molecules 2021, *26*, 7313.
4. Cooper, E. J.; Reynolds, M.; Raistrick, T.; Berrow, S. R.; Jull, E. I. L.; Reshetnyak, V.; Mistry, D.; Gleeson, H. F. Controlling the Optical Properties of Transparent Auxetic Liquid Crystal Elastomers. *Macromolecules* 2024, *57*, 2030−2038.
5. Berrow, S. R.; Raistrick, T.; Mandle, R. J.; Gleeson, H. F. Structure–Property Relationships in Auxetic Liquid Crystal Elastomers—The Effect of Spacer Length. *Polymers* 2024, *16*, 1957.
6. Dierking I., *Textures of Liquid Crystals*. Wiley-VCH GmbH and Co., 2003.
7. X. Du, Doctor of Philosophy, University of Leeds, 10, 2022.
8. D. Mistry, Doctor of Philosophy, University of Leeds, 06, 2018.

9. Berrow, S. R.; Mandle, R. J.; Raistrick, T.; Reynolds, M.; Gleeson, H. F. Toward Monodomain Nematic Liquid Crystal Elastomers of Arbitrary Thickness through PET-RAFT Polymerization. *Macromolecules* 2024, *57*, 5218–5229.
10. Mistry, D., Gleeson, H. F. Toward Programmed Complex Stress-Induced Mechanical Deformations of Liquid Crystal Elastomers. *Crystals* 2020, *10*, 315.
11. Schindelin, J., Arganda-Carreras, I., Frise, E., Kaynig, V., Longair, M., Pietzsch, T., Preibisch, S., Rueden, C., Saalfeld, S., Schmid, B., Tinevez, J.Y., White, D.J., Hartenstein, V., Eliceiri, K., Tomancak, P. & Cardona, A. Fiji: an open-source platform for biological-image analysis. *Nature Methods* 2012, *9*, 676–682.
12. Hohne, G.W.H., Hemminger, W.F., Flammersheim, H.J. Differential Scanning Calorimetry. 2003, Springer Berlin Heidelberg, Berlin, Heidelberg.
13. Jean M. S., Jean G., Eric D., Allisson S., Laurent D., Glass Transition Temperature and Value of the Relaxation Time at Tg in Vitreous Polymers. *Macromol. Symp.* 2007, *258*, 152161
14. John M. Hutchinson, Determination of the glass transition temperature Methods correlation and structural heterogeneity. *J. Therm. Anal. Calorim.* 2009, *98*, 579589.
15. I. M. Hodge, Enthalpy relaxation and recovery in amorphous materials, *J Non-Cryst. Solids* 1994, *169*, 211-266.

Chapter 4 The electric field induced alignment of mesogens in the intrinsic auxetic liquid crystal elastomer precursor

In this chapter, we will move on to the electric field induced alignment of mesogens in the nematic homogeneous IALCE precursor through the application of an electric field. The main purpose of this thesis is to investigate and develop tuneable IALCE devices based on the auxetic response. The priority is to understand the mechanism of the auxetic response and find out the efficient and reliable ways to manipulate the auxetic responses, to lay the foundation for the subsequent development. The mechanism for auxetic responses of IALCEs has been experimentally proven to be the reduction in uniaxial order, accompanied by the emergence of the biaxial nematic order by Mistry *et al.* [1] and Raistrick *et al.* [2]. The starting point for the manipulation of the auxetic response has been introduced in Chapter 2. The macroscopic deformation characteristics of LCEs are inextricably linked to the microscopic alignment of mesogens, and hence the elastomeric backbone, inside the LCEs. The control of the macroscopic deformation can be achieved through the manipulation of the microscopic alignment of the mesogenic units. This relationship works, even for the unique category of IALCEs, remembering that the direction of applied strain on IALCEs must be orthogonal to the director to stimulate an auxetic response in the direction perpendicular to these two directions, as illustrated previously in Figure 2.7. Mistry *et al.* further showed that in-plane director control can manipulate the auxetic response; where the IALCEs are stressed at an angle between 54° and 90° to the director and different auxetic responses will be observed [3]. However, there is still a space to experimentally examine and manipulate the auxetic response with out-of-plane director control. The principle is to employ electric fields which have been proven to effectively manipulate LC directors in the depth of a device. In this chapter, we will start from the electro-optic experiment to introduce how the director deforms under an electric field and show manipulation of the mesogens out-of-plane in the IALCE precursor under an external electric field.

4.1 Director deformation under electric fields

4.1.1 The elastic property and elastic free energy of liquid crystals

As described in section 2.1, the LC exhibits anisotropic properties in several aspects, such as birefringence, dielectric constant, conductivity and so on. The anisotropic properties of an LC results in the director reorientation when an external field is applied. In this thesis, such director deformation (i.e. induced by an electric field) is a main focus. The director reorientation direction depends on the dielectric constant component $\varepsilon_{\parallel}$, which is parallel to the director, the dielectric constant component $\varepsilon_{\perp}$, which is perpendicular to the director, and their difference $\Delta\varepsilon = \varepsilon_{\parallel} - \varepsilon_{\perp}$, referred to as the dielectric anisotropy. The magnitude of $\Delta\varepsilon$ is determined by the intrinsic properties of the material. If $\Delta\varepsilon > 0$, the director tends to align parallel to the direction of an applied electric field once a threshold voltage has been exceeded, and such LCs are referred to as positive LCs. Conversely, if $\Delta\varepsilon < 0$, the director tends to align perpendicular to the electric field, and such LCs are classified as negative LCs. When the electric field is removed, the director tends to return to its original equilibrium state due to interactions such as those with a surface alignment layer. A brief procedure of applying an electric field on a planar aligned cell filled with a positive LC is shown in Figure 4.1.

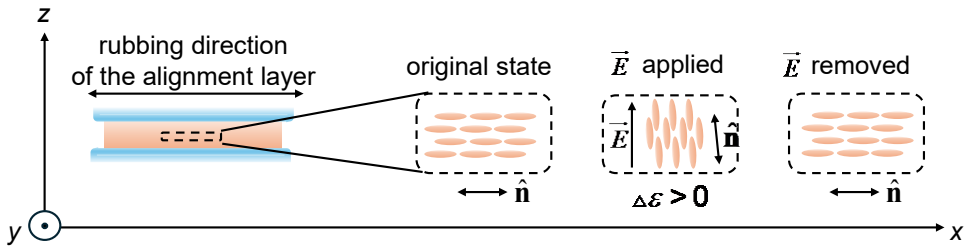

Figure 4.1. (a) The cell is planar aligned, with the arrow indicating the rubbing direction of the alignment layer. The zoom in part illustrates (b) the original alignment state in the centre part of a device without an electric field, the director aligns along the direction imposed by the alignment layer. (c) When an electric field is applied with voltage exceeding the threshold voltage of the LC, the director tends to align parallel to the electric field.(d) When the electric field is removed, the director returns to its original equilibrium state.

Upon applying an electric field, the director reorients according to the electric field direction and deviates from its initial equilibrium position, provided the threshold voltage

has been exceeded. This reorientation process causes an elastic deformation of the LC material, referred to as the director deformation. This deformation generates a restoring force within the system to resist the elastic distortions, and the strength of this resistance is characterized by the Frank elastic constants [4]. As shown in Figure 4.2, the nematic LC elastic deformations can generally be categorized into three types: splay, twist, and bend, which are described by the splay elastic constant K_{11}, the twist elastic constant K_{22}, and the bend elastic constant K_{33}, respectively. Although the actual deformation can be highly complex, it is always a combination of these three eigen-deformations. Generally, K_{11} and K_{33} are larger than K_{22}, indicating that, under the same conditions, twist deformations are usually easier to be induced in LC materials compared to splay or bend deformations.

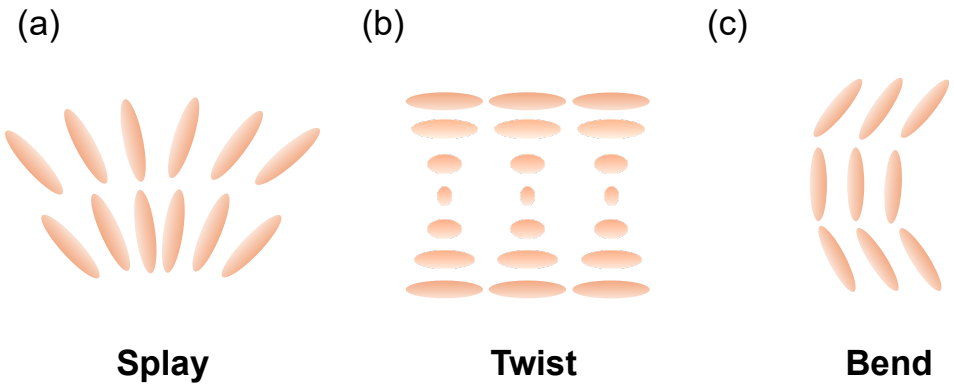

Figure 4.2 The three general elastic distortions, (a) Splay, (b) Twist and (c) Bend.

In nature, all systems tend to adopt the configuration that has the lowest free energy. In the absence of an external field or excitation, LCs are in a thermodynamic equilibrium state, in which the orientation of LC molecules is stable, the direction of the director is fixed, and the order parameter does not vary with the spatial position. Through the determination of the free energy of nematic LCs, the configuration that the system adopts will correspond to the condition when the free energy is minimized. The determination process was explored by Frank [4], Oseen [5] and Zocher [6], and the Frank free energy describes the free energy per unit volume when the LC system exhibit elastic deformations, denoted as:

$$F_{elastic} = \frac{1}{2}K_{11}(\nabla \cdot \hat{\mathbf{n}})^2 + \frac{1}{2}K_{22}\left[(\hat{\mathbf{n}} \cdot (\nabla \cdot \hat{\mathbf{n}})\right]^2 + \frac{1}{2}K_{33}\left[(\hat{\mathbf{n}} \times (\nabla \times \hat{\mathbf{n}})\right]^2 \quad (4.1)$$

where F_{elastic} is the Frank free energy, K is an elastic constant, ∇ is the divergence operator and $\hat{\mathbf{n}}$ is the director. The three terms on the right side are referred to the energy generated in the splay, twist and bend deformations, separately. A detailed mathematical discussion of the elastic properties of nematic liquid crystals is given in the “Physics of Liquid Crystals”

by P. G. de Gennes and J. Prost [7]. When an external electric field is applied, the director will reorient to minimise the free energy and an extra term is then added to Equation 4.1. The additional term describes the energy induced by the external electric field in the nematic LC and is denoted as:

$$F_{field} = -\frac{1}{2}\triangle\varepsilon(\hat{\mathbf{n}}\cdot\vec{E})^2 \tag{4.2}$$

The detailed mathematical discussions around the derivation of the free energy of nematic LCs can be found in “The Physics of Liquid Crystals” [7].

4.1.2 Fréedericksz transition alignment

In real alignment circumstances, the alignment of nematic LCs under an applied electric field is more complicated than that in free space. We need to consider limitations, for example the original alignment without an applied field, the anisotropic dielectric constants of LCs and the boundary conditions of any device that contains the LC. Consider a nematic cell with a uniform monodomain director profile as shown in Figure 4.3(a) (no voltage is applied when V = 0). When the alignment effects of the device boundary conditions conflicts with the alignment effect of an external electric field, the director will adopt the minimum energy profile to stay at a steady aligned state and such an alignment is called Fréedericksz transition alignment. More succinctly, the term ‘Fréedericksz transition alignment’ describes the equilibrium state of alignment of nematic LCs in a cell with certain boundary conditions when influenced by an external electric field. Due to the boundary conditions, a stabilizing generalized elastic force will be generated to counteract the destabilizing effects caused by the electric field during the fluctuation. The amount of the destabilizing effect depends on the strength of the electric field with respect to the threshold voltage V_{th}. The threshold voltage itself is a material-dependent quantity describing the voltage at which the destabilizing effect of the applied electric field just counterbalances the stabilizing effect of the boundary conditions (see equation 4.3 below).

Here in this thesis, we mainly focus on investigation of the alignment of IALCE precursor (with positive anisotropic dielectric constant) under an applied electric field in a planar aligned cell (of a thickness d). The nematic director deformation of LCs under an electric field has been explored by Dueling [8] and Welford [9], and here we follow the approach described in “Thermotropic Liquid Crystals Fundamentals” by Ger Vertogen and Wim H. de Jeu [10].

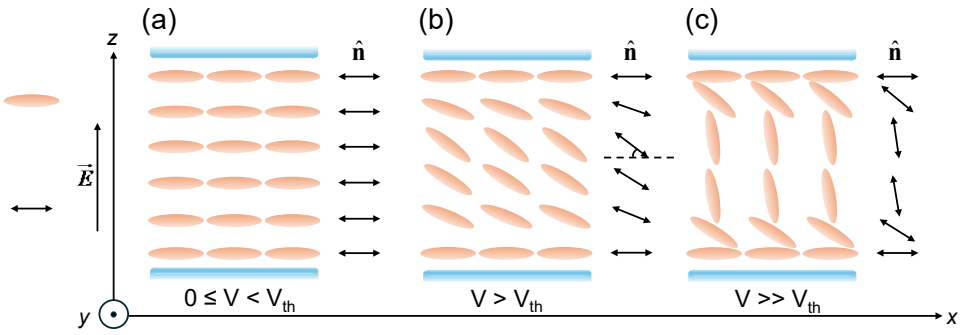

Figure 4.3 The Fréedericksz transition alignment of mesogens in a planar aligned cell under an external electric field. (a) For a low voltage, $V < V_{th}$, the director field remains homogeneous. (b) When the voltage increases just above V_{th}, the director reorients, and the maximum reorientation occurs in the centre of the cell. (c) For a sufficiently large voltage ($V >> V_{th}$), the director reorients to an approximately homeotropic state in the centre while any reorientation is prevented at the substrates due to the strong anchoring energy.

Figure 4.3 (a) shows the coordinate diagram of the cell without fields. The original alignment direction is along the *x*-axis and the electric field will be applied to the *z*-axis. The director will rotate to align towards the electric field $\vec{E}$ and the distorted director field is given by $\hat{n}_{field} = [\cos\theta_{field}, 0, \sin\theta_{field}]$ where the θ_{field} is the *z*-dependent director angle $\theta_{field} = \theta(z/d)$. No twist deformations are considered in this geometry. z/d represents the position in the cell with thickness d from one substrate z/d = 0 to the other substrate z/d = 1. Due to the strong boundary conditions, $\theta(z/d) = \theta(0) = \theta(1) = 0$. The Fréedericksz transition alignment is symmetric with the maximum angle θ_{max} occurring in the middle point of the device, at $z/d = 0.5$. The threshold voltage V_{th} of the Fréedericksz transition alignment is defined as [10]:

$$V_{th} = \pi\sqrt{\frac{K_{11}}{\varepsilon_o \Delta\varepsilon}} \tag{4.3}$$

where ε_0 = 8.854×10^{-12} Fm^{-1} is the permittivity of free space. The relationship between the voltage applied on the cell, V, and the angle of the director with respect to the fractional

distance through the cell, $\theta(z/d)$, can be described by [10]:

$$\frac{z}{d}\frac{V}{V_{th}} = \frac{1}{\pi}\int_0^{\theta(z/d)} \sqrt{\frac{\cos^2\phi + (\frac{K_{11}}{K_{33}})\sin^2\phi}{\sin^2\theta_{\max} - \sin^2\phi}}\, d\phi \qquad 0 \le z/d \le 0.5 \qquad (4.4)$$

where ϕ is a variable of integration and

$$\kappa = \frac{K_{33} - K_{11}}{K_{11}}. \qquad (4.5)$$

Equation 4.4 only defines $\theta(z/d)$ halfway through the cell; by symmetry, the other half is the mirror image at $z/d = 0.5$. Moreover, the relationship between the voltage applied to the cell, V and the maximum angle $\theta_{\max}$ is described by [10]:

$$\frac{V}{V_{th}} = \frac{2}{\pi}\int_0^{\frac{\pi}{2}} \sqrt{\frac{1+\kappa\sin^2\theta_{\max}\sin^2\psi}{1-\sin^2\theta_{\max}\sin^2\psi}}\, d\psi \qquad (4.6)$$

where ψ is a variable of integration. The detailed mathematical discussions of equations 4.4-4.6 are given in “Thermotropic Liquid Crystals Fundamentals” [10].

A schematic representation of Fréedericksz transition alignment of mesogens in a planar aligned cell with an external electric field for different applied fields is illustrated in Figure 4.3.

4.2 The electro-optic property of the intrinsic auxetic liquid crystal elastomer precursor

In Section 4.1, we have introduced the fundamental concepts of elastic constants, elastic free energy, and the Fréedericksz transition alignment of an LC. In Section 4.2, we will introduce the electro-optic experiment which is used to quantify key parameters of the mesogenic mixture (here the LCE precursor), for example, the V_{th}, thereby characterising the Fréedericksz transition alignment of the LCE precursor in a detailed way in Section 4.3.

4.2.1 The electro-optic experiment for threshold voltage

As introduced in Section 4.1.2, under a sufficiently high voltage, the director reorients towards an approximately homeotropic state at the centre of a planar-aligned cell, while strong anchoring at the substrate interfaces prevents reorientation. This nonuniform

director distribution gives rise to elastic restoring forces in the form of splay and bend deformations. By indirectly measuring the response of the director under an external electric field, the dielectric and elastic properties of the mesogenic mixture can be numerically analysed [11,12]. These measurements enable the characterization of key parameters of the mesogenic mixture by observing the changes of the light passing through the mesogenic mixture or, equivalently, changes in the capacitance of a cell. Electro-optics and capacitance experiments have proven to be efficient ways to obtain the elastic constants of mesogenic mixtures through numerical analysis of the retardance/capacitance vs voltage curves. In addition to the elastic constants, threshold voltage V_{th}, a fundamental and crucial parameter to induce and manipulate the Fréedericksz transition alignment, can be directly monitored from an electro-optics experiment. In this section, we focus on the basic electro-optic experiment for directly obtaining the V_{th} of a mesogenic mixture.

In Section 3.3.1, we have introduced that when polarized light is incident on an LC cell with a certain alignment, the electric field usually decomposes into two modes, experiencing either n_{e} or n_{o}, propagating at different speeds inside the cell. In the case where the incident polarisation is at 45˚ to both the ordinary and extraordinary axes, on leaving the cell, the recombination of the modes with a phase difference results in a phase retardance Γ applied to the polarised light, denoted as [7]:

$$\Gamma = \frac{2\pi \triangle \mathrm{n} d}{\lambda} \tag{4.7}$$

where the $\triangle \mathrm{n}$ is the birefringence, d is the thickness of the cell (light path) and λ is the wavelength of the light. Once the LC cells are constructed with certain alignment at a constant temperature, the retardance of the cell is a fixed value in the absence of a field. Then, the modulation of the transmitted polarized light by the LC cell is denoted as [7]:

$$I = I_o \sin^2(\Gamma / 2) \tag{4.8}$$

where I is the intensity of the polarized light transmitted through the LC cell and I_{o} is the initial intensity of the polarized light. For the auxetic LCE precursor undergoing Fréedericksz transition alignment, an electro-optic experiment is performed to investigate its phase retardance variation under an applied electric field. By monitoring the intensity of the transmitted light, the voltage at which the phase retardance begins to change is determined, corresponding to the threshold voltage V_{th} of the Fréedericksz transition. A schematic of the optical apparatus used in the electro-optic experiment is shown in Figure 4.4. Taking the crossed polarisers into consideration, the intensity of the light received by

the photodetector is [7]:

$$I = I_o \times \sin^2(2\beta) \times \sin^2(\Gamma / 2) \tag{4.9}$$

where β is the angle between the director and the polariser.

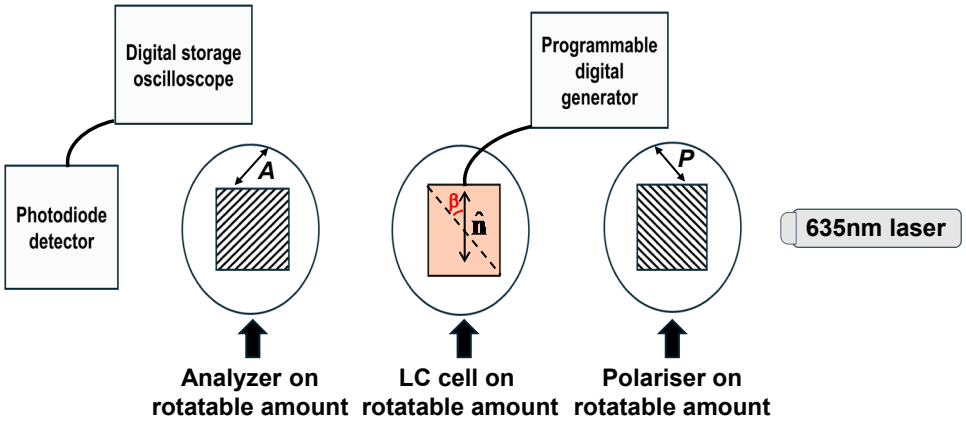

Figure 4.4 The set of the optical apparatus for the electro-optic experiment. *P* is the polarized direction of the polarizer while *A* is the polarized direction of the analyser. β is the angle between the director and the polariser. $\hat{\mathbf{n}}$ is the director.

The light source was a collimated laser diode module operating at 635nm (Thorlabs, UK) and the cell was a commercial cell with transparent Indium Tin Oxide electrodes and antiparallel alignment (Linkam Group Ltd., UK). The cell thickness was initially chosen to be 5 μm. The mesogenic mixture filled into the cell comprised 6OCB, A6OCB, RM82 and EHA in the same proportions as used in the LCE precursor, illustrated in Figure 3.1. MBF, the photoinitiator, was excluded to prevent the undesired polymerization from occurring during the measurement of the threshold voltage. Notably, the MBF content in the unpolymerized auxetic LCE precursor was maintained at 1.5 mol% and this was considered not sufficient to affect the threshold voltage of the precursor.

For measuring the V_{th} of the precursor, the following procedure was employed. First, the apparatus (excluding the LC cell) and with the polarisers uncrossed, was aligned along the optical path, ensuring that the laser beam passed through the centre of each component and the signal detected by the photodetector reached its maximum intensity. To do this, the 635 nm laser was first activated and allowed to stabilize so that the intensity didn't fluctuate during the experiment. After ensuring the optical alignment of the components, the polarizer and analyser were rotated to a crossed configuration, ensuring that the signal detected by the photodetector reached its minimum intensity. The LC sample was then put into the optical path, ensuring the beam passed through the centre of the

sample and with the cell perpendicular to the beam by viewing the back reflected light. The sample was then rotated until its optical axis was oriented at 45° relative to the crossed polarizers, at which point the signal displayed on the oscilloscope reached maximum intensity. Finally, a sinusoidal signal (10 KHz) was applied to the LC sample via the programmable signal generator, with the voltage increased in 0.1 V_{rms} steps from 0 V_{rms}. The voltage applied and corresponding light intensity were displayed on the oscilloscope and recorded once the retardance stabilized. The data were then plotted as light intensity versus applied voltage and analysed using OriginPro. The detailed data will be introduced in Section 4.2.2.

4.2.2 The electro-optic curve analysis

The electro-optic response of the mesogenic mixture (6OCB + A6OCB + RM82 + EHA) in a commercial cell of nominal thickness 5 μm is shown in Figure 4.5(a). The mixture shows has a V_{th} of ~0.86 V_{rms}, which we take 0.9 ± 0.1 V_{rms} and the cell acts a phase retarder from 0 to $\frac{5}{4}\lambda$. It will be recalled from Section 3.1.1 that in the mixture, EHA is a non-mesogenic component and is introduced to modulate the phase transition temperature of the auxetic LCE precursor and enhance backbone flexibility after polymerization. To evaluate the effect of EHA on V_{th}, a modified mixture (6OCB + A6OCB + RM82) was filled into a separate commercial 5 μm antiparallel cell and was measured with the same procedure. The result is shown in Figure 4.5(b). The phase retardation extends to a wider range from 0 to $\frac{3}{2}\lambda$ while the V_{th} is ~0.94 V_{rms}, remaining 0.9 ± 0.1 V_{rms}, suggesting no significant influence of EHA on V_{th}. However, the increased birefringence of the mixture, as evidenced by the extended phase retardation range, indicates that the presence of the EHA reduces the overall birefringence of the mixture. This reduction may be attributed to a decrease in the order parameter with increasing EHA concentration, as well as the intrinsically low refractive index of EHA [13].

According to Equation 4.5, V_{th} is an intrinsic material property and should remain unaffected by the cell thickness. To verify this, the original mesogenic mixture, (6OCB + A6OCB + RM82 + EHA) was filled into a commercial 20 μm antiparallel cell and measured under same conditions. The electro-optic curve shown in Figure 4.5(c) confirms the V_{th} of the mixture is ~0.86 V_{rms}, still at 0.9 ± 0.1 V_{rms}, consistent with the 5 μm device. We further

analysed the relationship of the relative phase retardance to the applied voltage based on Figure 4.5(c) and the result is shown in the Figure 4.5(d). The phase retardance directly reflects the optical path difference variation caused by the reorientation of the director. This implies that monitoring phase retardance enables a more precise detection of the onset of phase retardance transition, which corresponds to the threshold voltage. According to the data presented in Figure 4.5 (d), the applied voltage in the experiment was incremented in steps of 0.1 V_{rms}, leading to an uncertainty of ± 0.05 V_{rms}. Consequently, the V_{th} was confirmed to be 0.9 ± 0.05 V_{rms}. Considering the real experimental circumstances and that the data obtained from Figure 4.5 (d) was analysed on only Figure 4.5 (c), we finally take 0.9 ± 0.1 V_{rms} as the V_{th}.

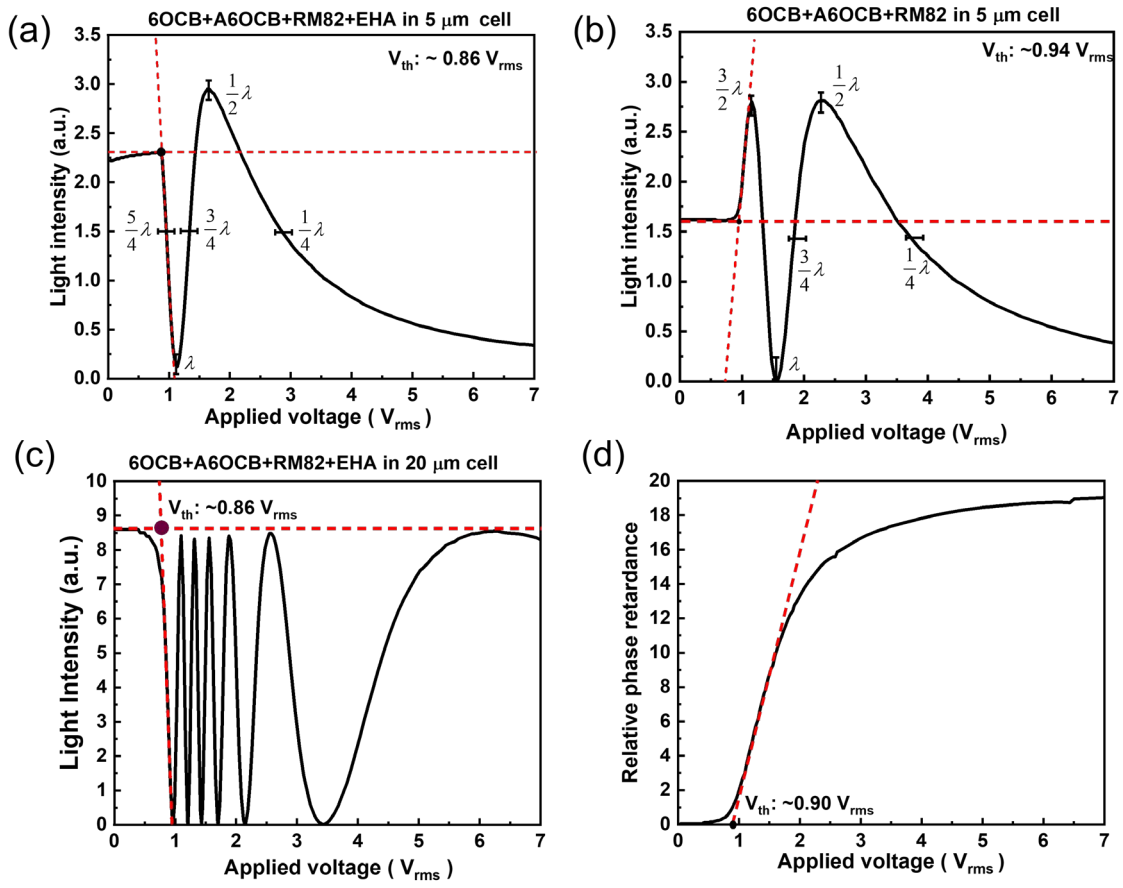

Figure 4.5 The electro-optics properties of (a) the mixture of 6OCB, A6OCB, RM82 and EHA and (b) the mixture of 6OCB, A6OCB and RM82 in a commercial 5 μm cell. (c) The electro-optics properties of the mixture of 6OCB, A6OCB, RM82 and EHA in a commercial 20 μm cell. (d) The relative phase retardance of the 20 μm cell as a function of applied voltage.

4.3 The electric field induced Fréedericksz transition alignment in the intrinsic auxetic liquid crystal elastomer precursor

In Section 4.2, we introduced the electro-optics experiment and characterization of the V_{th} of the unpolymerized auxetic LCE precursor in the absence of photoinitiator, MBF. The photoinitator concentration in the precursor is insufficient to influence the V_{th} which has been determined to be 0.9 ± 0.1 V_{rms}. In Section 4.3, we will investigate in detail how the Fréedericksz transition alignment of the auxetic LCE precursor can be varied using specific voltages.

To effectively induce and control the Fréedericksz transition alignment of the unpolymerized LCE precursor, at voltages above V_{th}, the elastic constants K_{11} and K_{33} of the precursor were determined, from the data in the electro-optic measurement. Equation 4.6 was then used to construct the relationship between V and θ_{max}. V_{th} was measured to be 0.9 ± 0.1 V_{rms}, as described in Section 4.2.2. The values of K_{11} and K_{33} were obtained by Dr. Thomas Raistrick, to be 4.6 pN and 4.3 pN, separately. The result of the calculation of θ_{max} is shown in Figure 4.6(a). Then $\theta(z/d)$ can be found for various values of applied voltage V (or equivalently, various values of θ_{max}) using Equation 4.4, as shown in Figure 4.6(b). The calculation using Equations 4.4 and 4.6 were performed via Matlab by Dr. Thomas Raistrick.

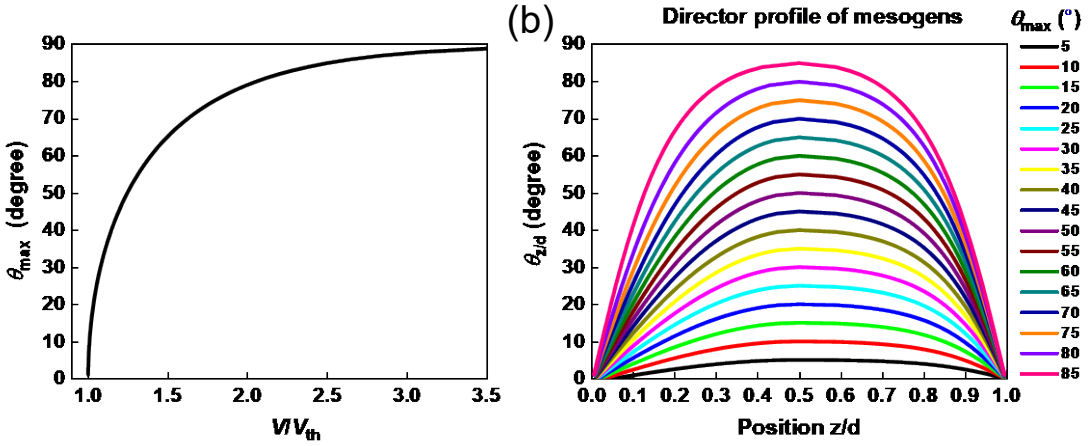

Figure 4.6 (a) The maximum angle θ_{max} in Fréedericksz transition alignment of the precursor mixture under different voltages. V is the applied voltage and V_{th} is the threshold voltage of the precursor. (b) The director profile through the cell from one substrate (z/d = 0) to the other substrate (z/d = 1) for each value of the maximum angle θ_{max} in Fréedericksz transition alignment. These calculations were carried out by Dr Thomas Raistrick.

Figure 4.6(a) describes the θ_{max} in the Fréedericksz transition alignment of mesogens within the precursor under varying applied voltages. No distortion of the director occurs when the V is smaller than the V_{th} and θ_{max} remains at 0°. However, once V exceeds V_{th}, the director of the precursor starts to reorient. θ_{max} increases rapidly at lower V / V_{th} values and gradually approaches 90° at a progressively slower rate as V / V_{th} increases. Notably, θ_{max} reaches approximately 80° when the ratio, V / V_{th} is about 2.1 and then ultimately saturates to near 90°. Figure 4.6(b) illustrates the director profile of the mesogens as a function of the normalized position z/d through the cell for different applied voltages. The curves represent the $\theta(z/d)$ at different θ_{max}, ranging from 5° to 85°. Each curve exhibits a symmetric profile, peaking at the centre of the cell (z/d=0.5) and decreasing towards the substrates at z/d=0 and z/d=1, consistent with the description of the Fréedericksz transition alignment in Section 4.1.

4.4 Summary

In this chapter, we introduced the deformation of the director under an external electric field by considering the elastic and dielectric properties of LCs, followed by an introduction to the Fréedericksz transition alignment. Based on key parameters of the Fréedericksz transition alignment, we described the electro-optical experiment, which was conducted to determine and characterize the V_{th} of the auxetic LCE precursor. This information is required for subsequent fabrication of auxetic LCE films or film regions with different director profiles. The measured V_{th} was 0.9 ± 0.1 V_{rms}. Furthermore, by incorporating the elastic constants of the precursor mixture, we obtained the relationship shown in Figure 4.6, which provides a comprehensive schematic of the relationships between V, θ_{max}, and $\theta(z/d)$ in the Fréedericksz transition alignment of the auxetic LCE precursor. In the following chapters, this relationship will serve as a foundation for sample fabrication, enabling an investigation into the manipulation and application of distinct auxetic responses through different Fréedericksz transition alignments. In the next chapter, we will first fabricate a well-

aligned homeotropic auxetic LCE sample with an electric field, a process that will allow experimental verification of the emergence of the nematic biaxial order during the auxetic response.

References

1. Mistry, D.; Connell, S. D.; Mickthwaite, S. L.; Morgan, P. B.; Clamp, J. H.; Gleeson, H. F. Coincident molecular auxeticity and negative order parameter in a liquid crystal elastomer. *Nat. Commun.* 2018, *9*, 5095.
2. T. Raistrick, Z. Zhang, D. Mistry, J. Mattsson, H. F. Gleeson. Understanding the physics of the auxetic response in a liquid crystal elastomer. *Phys. Rev. Research*, 2021, *3*, 023191.
3. Mistry, D., Gleeson, H. F. Mechanical Deformations of a Liquid Crystal Elastomer at Director Angles Between 0° and 90°: Deducing an Empirical Model Encompassing Anisotropic Nonlinearity. *J. Polym. Sci. Pol. Phys.*, 2019, *57*, 1367–1377.
4. Frank, F. C. liquid crystals. on the theory of liquid crystals, *Discuss. Faraday Soc.*, 1958, *25*, 19-28.
5. Oseen, C. W. The theory of liquid crystals. *Trans. Faraday Soc.*, 1933. *29*, 0883-0898.
6. Zocher, H. The effect of a magnetic field on the nematic state. *Trans. Faraday Soc.*, 1933. *29*, 0945-0957.
7. de Gennes, P. G., Prost, J. The Physics of Liquid Crystals. *Clarendon Press, Oxford, 2nd ed.*, 1993.
8. Deuling, H. J. Deformation of nematic liquid crystals in an electric field. *Mol. Cryst. Liq. Cryst.*, 1972,*19*, 123-131.
9. Welford, K. R., Sambles, J. R. Analysis of electric eld induced deformations in a nematic liquid crystal for any applied field. *Mol. Cryst. Liq. Cryst.*, 1987, *147*, 25-42.
10. Vertogen, G., De Jeu, W. H. Thermotropic Liquid Crystals Fundamentals. *Springer Science & Business Media*, 2012, 89–105.
11. Kaur, S., Tian, L., Liu, H., Greco, C., Ferrarini, A., Seltmann, J., Lehmann, M., Gleeson, H. F., The elastic and optical properties of a bent-core thiadiazole nematic liquid crystal: the role of the bend angle, *J. Mater. Chem. C*, 2013, *1*, 2416-2425.
12. Kaur, S., Liu, H., Addis, J., Greco, C., Ferrarini, A., Görtz, V., Goodby, J. W., Gleeson, H. F., The influence of structure on the elastic, optical and dielectric properties of nematic phases formed from bent-core molecules. *J. Mater. Chem. C*, 2013, *1*, 6667-6676.
13. Cooper, E. J.; Reynolds, M.; Raistrick, T.; Berrow, S. R.; Jull, E. I. L.; Reshetnyak, V.; Mistry, D.; Gleeson, H. F. Controlling the Optical Properties of Transparent Auxetic Liquid Crystal Elastomers. *Macromolecules* 2024, 57, 2030−2038.

Chapter 5 The intrinsic auxetic liquid crystal elastomers in high-quality planar alignment and homeotropic alignment

In the previous chapter, we introduced the elastic and dielectric properties of LCs, followed by an overview of the Fréedericksz transition alignment. We then illustrated the electro-optical experiment procedure and characterized the V_{th} of the unpolymerized intrinsic auxetic LCE precursor, which was determined to be 0.9 ± 0.1 V_{rms}. Additionally, we explored the manipulation of the θ_{max} and $\theta(z/d)$ in the Fréedericksz transition alignment of the intrinsic auxetic LCE precursor by the alteration of V, as shown in Figure 4.6.

In following chapters, we will focus on the fabrication of the intrinsic auxetic LCE under external electric fields and their application. Before moving on to the intrinsic auxetic LCEs with Fréedericksz transition alignment, we will start, in this chapter, with the fabrication of intrinsic auxetic LCEs in high-quality planar alignment and homeotropic alignment. These two modes are more simplified compared to the Fréedericksz transition alignments and offer the two extreme cases of director fields.

The research on intrinsic auxetic LCEs with homeotropic alignment has been published in “Direct Observation of Biaxial Nematic Order in Auxetic Liquid Crystal Elastomers. *Materials* 2022, *16*, 393.” and this chapter follows much of that paper. The samples are fabricated within homeotropically aligned cells, with the assistance of an electric field to achieve high-quality alignment. We will analyse these two (planar and homeotropic) auxetic samples through their mechanical deformations. The samples were also studied by Aidan Street and Dr. Thomas Raistrick who undertook Raman spectroscopy and conoscopy, to show that the emergence of biaxial nematic order is directly associated with the auxetic response in nematic intrinsic auxetic LCEs. The paper is reproduced in the remaining part of the chapter.

5.1 Introduction

The first experimental report of a negative Poisson’s ratio in a liquid crystal system was in the nematic elastomer synthesized by Mistry *et al.* [1]. For their side-chain LCEs, the auxetic response occurs above a threshold strain along an axis perpendicular to both the

initial director and the extension direction. Detailed features of the auxetic LCEs have been introduced in Section 2.2.3. The advantages of auxetic LCEs are clear; they respond on a molecular level and so are not limited to bulk applications, they are transparent, they are readily synthesized and as they are not porous, they do not have the inherent mechanical weakness that can plague re-entrant auxetic structures. However, to take full advantage of auxetic LCEs, it is critical to have a detailed understanding of the underlying physics that results in their negative Poisson's ratio.

According to Mistry *et al.* [1], the significant changes in birefringence of the auxetic LCE seen under strain indicated that there was a dramatic change in order associated with the auxetic response, hinting at an order-moderated mechanism. Raistrick et al. [2] explored the order of the LCE under strain using polarized Raman spectroscopy, a technique that allows both uniaxial and biaxial order parameters to be inferred. Fitting the Raman depolarization data with a biaxial model strongly suggested that the auxetic response was related to out-of-plane rotations of the mesogenic units and the emergence of biaxial order.

In this chapter, we will fabricate the IALCEs in high-quality planar and homeotropic alignment with three primary objectives. First, as we introduced in Section 3.1, the intrinsic auxetic LCEs throughout this thesis are fabricated with the same monomers as Mistry *et al.* [1] but using different proportions. Specifically, the amount of crosslinker is reduced to approximately half of that used by Mistry, allowing the auxetic threshold to be observed at lower strains. We will show analogous behaviour of the planar aligned intrinsic auxetic LCE synthesised with the recipe described in Section 3.1.1 to that described in previous reports [1], specifically the emergence of biaxial order as an inherent feature of the auxetic response. Secondly, we will present a successful fabrication of a high-quality homeotropically aligned auxetic LCE sample with the help of an external electric field and demonstrate the auxetic response directly occurring in the width, rather than thickness of the sample for this geometry. Last but not least, Raistrick *et al.*'s study stopped short of proving that the emergence of biaxiality was implicit in auxetic response of the LCE. We aim to experimentally prove the emergence of significant biaxiality for the auxetic LCE during deformation with intrinsic auxetic LCEs in high-quality homeotropic alignment.

5.2 Sample fabrication

The IALCE samples were made by photopolymerizing the nematic precursor mixture in a cell based on a conventional LC device. The cell fabrication and synthesis procedure for

planar alignment IALCEs are detailed in Section 3.2, while the process for homeotropic alignment IALCEs required slight modifications.

5.2.1 Fabrication of the homeotropic cell

The homeotropic cell was still assembled by one glass substrate, two 100μm spacers and one polymer substrate, however, the glass substrate was coated with Indium Tin Oxide (ITO) (Xinyan Technology Ltd., China) and the polymer substrate was ITO coated polyethylene terephthalate (PET) film (ITO-PET) (Sigma-Aldrich, Unite States), as shown in Figure 5.1(a).

For homeotropic alignment, a 0.5 wt.% cetyltrimethylammonium bromide (CTAB) (MP Biomedicals, France) solution was used instead of the conventional 0.5 wt.% polyvinyl alcohol (PVA) solution. The ITO-PET and ITO glasses were directly rubbed by a tissue rinsed in 0.5 wt.% CTAB solution, as shown in Figure 5.1(b), and after being rubbed by the tissue, the substrates were left at room temperature for 5min to allow drying and the self-assembly of the CTAB layer. When the alignment layer was ready, the homeotropic cell was finally assembled and prepared for the LCE synthesis.

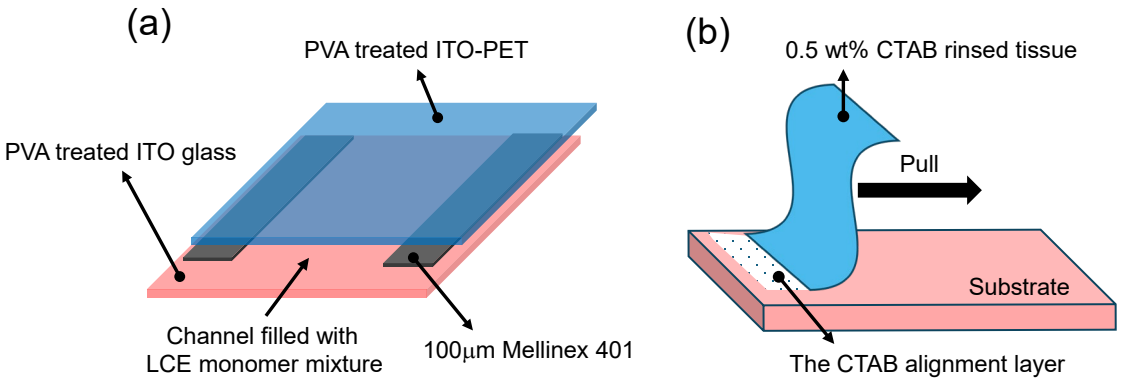

Figure 5.1 (a) A schematic showing the assembled LCE cell used to fabricate IALCEs with homeotropic alignment. (b) The process for depositing CTAB on the substrates as alignment layer.

5.2.2 Synthesis of homeotropic aligned intrinsic auxetic liquid crystal elastomers

The intrinsic auxetic LCE precursor was fabricated following the procedure outlined in Section 3.2, using monomers in the specific proportions detailed in Section 3.1. The LCE monomer mixture was filled into the moulds *via* capillary action in its isotropic phase (at 35 °C) and left for around 20 min to cool to room temperature. The mesogens align with

the alignment layers as the temperature decreases into the nematic phase. For the homeotropic sample, conductive tapes attached onto the edges of the cell allowed an alignment voltage of 40 V_{rms} at 1KHz to be applied, enhancing the surface alignment mechanism. Once aligned, the cells were placed under a low intensity UV florescence light source (365nm, 2.5 mW/cm^2) for 2 hours to cure, with the field maintained in the case of the homeotropic sample. After curing, the electric field was removed and the LCE was carefully peeled away, washed and dried.

5.3 Results and discussion

The geometries of the intrinsic auxetic LCE films and direction of the strain are shown in Figure 5.2(a). The quality of the alignment of the mesogens in the LCE films was monitored using POM. The POM images of LCE films with planar (P-LCE) and homeotropic alignment (H-LCE) are shown in Figure 5.2(b). The figure shows that for the P-LCE, when the director orientation is parallel to the crossed polarizers there is an excellent dark state while at 45° there is a uniform bright state. The high contrast in transmitted light between the two images of the P-LCE illustrates the high quality of the monodomain alignment and the anisotropy of the P-LCE sample. For the H-LCE, there is no light transmitted for either orientation, indicating excellent homeotropic alignment.

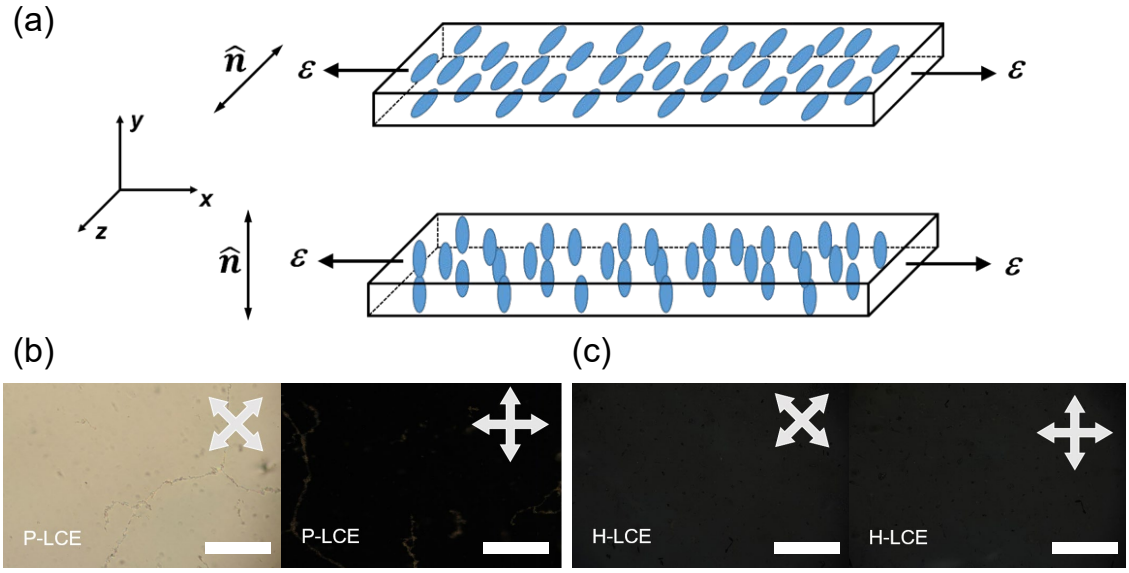

Figure 5.2 (a) Diagram describing the undeformed sample geometry with the liquid crystal director parallel to the *z*-axis for the planar LCE and to the *y*-axis for the homeotropic LCE. In this work, deformations (ε) are applied along the *x*-axis. The POM images for (b) P-

LCE and (c) H-LCE. The scale bar is 20μm and the white arrows indicate the crossed polarizers.

For the mechanical measurements, the procedure was detailed in Section 3.2.2. The strains ε_x and ε_z were determined by analysis of photographs of the samples, while ε_y was inferred using the conserved volume conditions known for these samples, referred to Equation 3.2 in Section 3.2.2. Figures 5.3 (a) and (c) show the behaviour of ε_y and ε_z for a strain in the *x*-direction (ε_x), measured for the P-LCE sample. The deformations of the P-LCE sample in the *x*-*y* and *x*-*z* planes are highly anisotropic. For the deformations in the *x*-*z* plane, ε_z decreases with increasing ε_x. The deformation of the P-LCE in the *x*-*y* plane is highly anomalous; ε_y approaches a minimum when ε_x is ~0.58 ± 0.05 and then increases to almost the original sample thickness. The auxetic behaviour of the P-LCE is clear; the sample gets thicker in the *y*-direction perpendicular to ε_x above strains of ~0.58 ± 0.05. To further analyse the auxetic response of each film, we calculated Poisson's ratio ν in *x*-*y* and *x*-*z* plane of each film during mechanical measurements. The Poisson's ratio, ν, can be calculated for each deformation direction as follows. All the strains shown in Figure 5.3 are engineering strains, ε_{eng}. By converting them into true strains, ε_{true} through:

$$\varepsilon_{true} = \ln\left(\varepsilon_{eng} + 1\right) \tag{5.1}$$

and then fitting a polynomial, the Poisson's ratio, $\nu = -(d\varepsilon_{trans} / d\varepsilon_{expan})$, i.e. the ratio of the relative deformation in the transverse direction of expansion to the relative expansion as described in Section 2.2.3, can be calculated. Here, the deformations in *y*- and *z*-directions are the transverse deformations and the strain in the *x*-direction is the relative expansion. The Poisson's ratio of the P-LCE is shown in Figure 5.3(e); it is always positive for deformations in the *x*-*z* plane, while in the *x*-*y* plane there is a threshold strain, ε_x ~0.58 ± 0.05 beyond which the Poisson's ratio becomes negative and the system is therefore auxetic.

Figures 5.3(b) and (d) show the corresponding behaviour of the ε_y and ε_z strains for the H-LCE sample. Now, the auxetic response occurs in the *x*-*z* plane, ε_z reaching a minimum when ε_x is ~0.56 ± 0.05 and then increasing. The threshold strain for the auxetic behaviour of the H-LCE is ~0.56 ± 0.05 (seen from Figure 5.3 (f) as the point where the Poisson's ratio becomes negative), in excellent agreement with that of the P-LCE. In each case, the direction of the auxetic response is perpendicular to the direction of both the strain and the

initial director alignment direction.

Both types of LCE sample show an auxetic response with threshold strains in excellent agreement; 0.56 ± 0.05 for the H-LCE and 0.58 ± 0.05 for the P-LCE. The two LCE samples have very different aspect ratios (in the reference frame of the nematic director), however, the onset and extent of the auxetic behaviour in the H-LCE and P-LCE is essentially the same. Therefore, we can conclude that (*i*) the auxetic response is not related to the sample aspect ratio and (*ii*) that the auxetic response is related to the geometry of the applied strain with respect to initial nematic director, which matches the introduction in Section 2.2.3. This further indicates that the auxetic response is likely due to out-of-plane rotations.

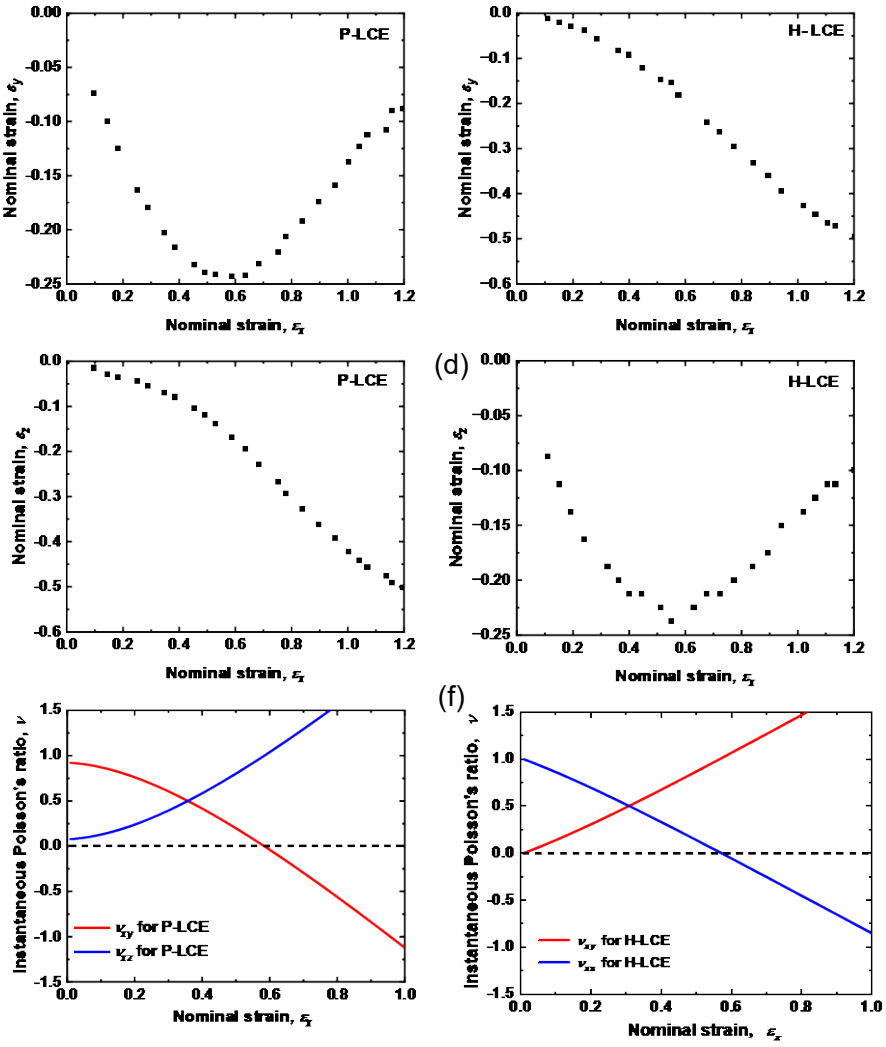

Figure 5.3 The ε_x-ε_y strains measured for (a) P-LCE and (b) H-LCE, the ε_x-ε_z strains measured for (c) P-LCE and (d) H-LCE and instantaneous Poisson's ratio, ν_{xy} and ν_{xz} measured for (e) P-LCE and (f) H-LCE. Reproduced from [3].

One key advantage of the homeotropic geometry is that it allows direct and straightforward observation of the auxetic response of the LCE. The mechanical deformation process of the H-LCE is shown in Figure 5.4 with photography displayed sequentially at an increasing step of ~0.1 strain. The photograph is arranged in a grid format, and each corresponds to a specific strain step in Figure 5.3 (d), with strain values (ε_x and ε_z) labelled in each panel. The red numbers in the corner represent the sequential steps of the mechanical deformation. The first image in the top-left corner represents the initial undeformed state with ε_x = 0.00 and ε_z. As ε_x increases, ε_z decreases, representing the reduction in the width of the H-LCE. When the strain reaches ~0.55, the H-LCE width reaches its minimum. As ε_z continues to increase, the ε_z begins to increase towards positive, accompanied with the increase in the width of the LCE. When the ε_x reaches ~1.4, the H-LCE width recovers to nearly its original width, with ε_z.= -0.06.

To enhance the contrast and highlight the auxetic response in the *z*-direction of H-LCE, we pick photomicrographs of the H-LCE sample at various strain steps (ε_x at 0.00, ~0.55 and ~1.40) and zooming them in Figure 5.5. The sequence shows the width change of the sample in *z*-direction as the sample extends in the *x*-direction. When the strain reaches ~0.55, the width of the sample is a minimum and beyond this it increases; a direct demonstration of the auxetic behaviour of the H-LCE sample. The POM figures confirm the initial homeotropic alignment (the black state) when no strains applied and as the strain increases, the bright state emerges due to the reorientation of the mesogens. The colour emerges due to the birefringence changes in the deformation process, which will be discussed more in Section 6.3.2.

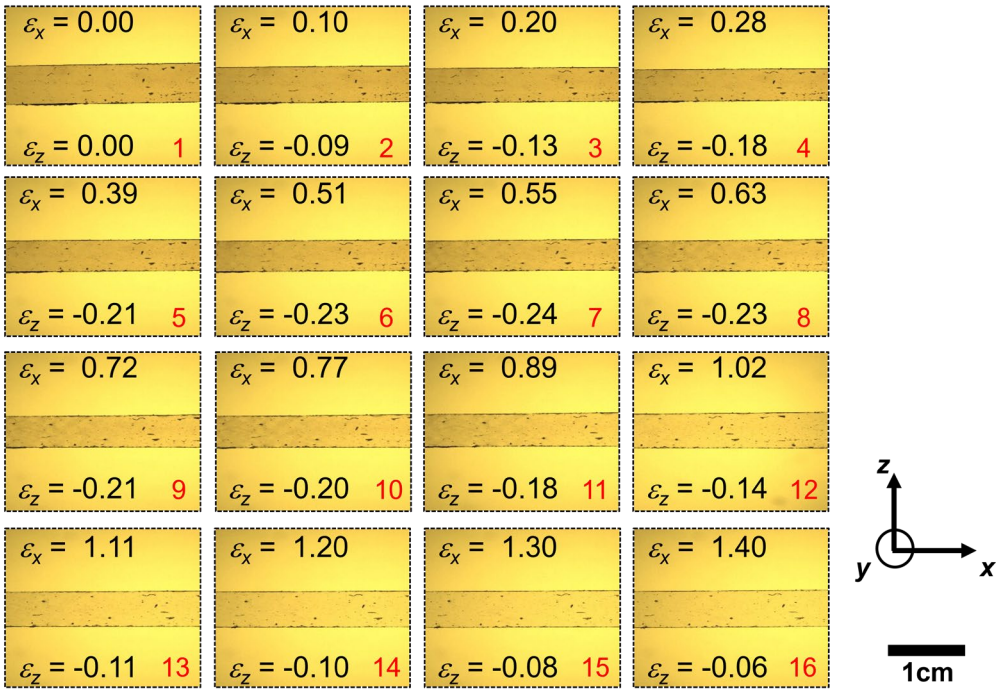

Figure 5.4 The whole mechanical deformation process of the H-LCE with photography displayed sequentially in increasing steps of ~0.1 strain. The scale bar is 1cm.

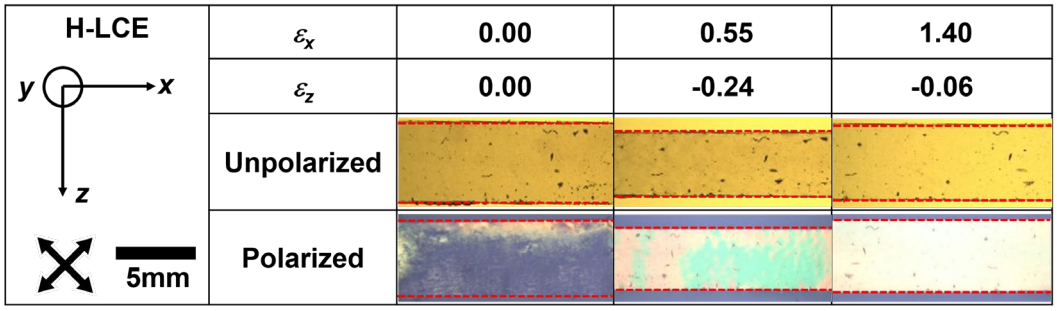

Figure 5.5 Photomicrographs of the H-LCE at various strains during mechanical deformation in the *x-z* plane. The red dashed lines clarify the positions of the sample edges. When ε_x is ~0.55, the width of the LCE is a minimum, beyond which it clearly increases with further strain, i.e. it shows an auxetic response. The H-LCE sample has almost regained its original width at a strain of ~1.4. Reproduced from [3].

Order parameter measurement. The order parameter measurement carried out on the P-LCE during mechanical deformation was performed and analysed by Aidan Street with a Renishaw *Via* Raman Microscope in backscattering geometry with a 532nm solid state laser. Polarized Raman spectroscopy (PRS) is a particularly useful technique in this regard as it allows the 2nd and 4th rank order parameters to be determined. The procedure to determine uniaxial and biaxial order parameters in LCEs has been described previously [2],

however, the key equations and experimental technique are both briefly described in Ref. [3].

Raman measurements of the uniaxial order parameters, $\langle P_{200} \rangle$ and $\langle P_{400} \rangle$, taken for the planar sample are shown in Figure 5.6. The initial (unstrained) values were $\langle P_{200} \rangle$=0.60 ± 0.05 and $\langle P_{400} \rangle$=0.31 ± 0.05, very similar to those determined for a related LCE [2]. ⟨P200⟩ reduced rapidly from its initial value to effectively zero at a strain of ε_x = 1.0 and ⟨P400⟩ reduced more slowly to a minimum of $\langle P_{400} \rangle$=0.07 ± 0.05 at a strain of ε_x = 1.14 ± 0.05. Note that in the region where ⟨P200⟩ is effectively zero, indicated by the vertical dashed lines in Figure 5.6, the value of ⟨P400⟩ deduced using the uniaxial model is greater than that of ⟨P200⟩.

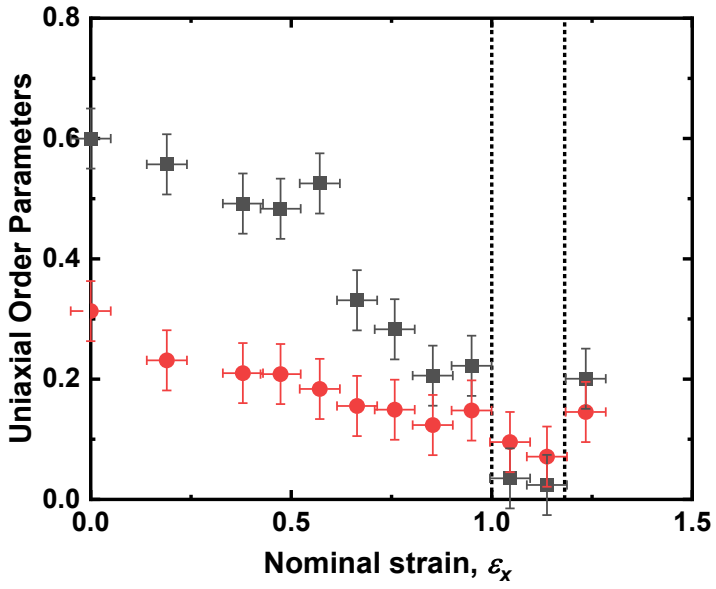

Figure 5.6 The uniaxial order parameters $\langle P_{200} \rangle$ (black squares) and $\langle P_{400} \rangle$ (red circles) as a function of the strain of the sample. The strain domain denoted by the vertical dashed lines shows the region in which $\langle P_{200} \rangle$ appears to be lower than $\langle P_{400} \rangle$. Reproduced from [3].

The PRS method also allows for measurement of the director angle in the plane of the sample, initially set to be at 89 ± 1° to the long axis of deformation by the rubbing direction of the planar alignment. The director remained constant with strain until ε_x ~1.0, Figure 5.7, the regime where $\langle P_{200} \rangle$~0. At this strain the director rapidly reorients to align with the axis of deformation, a phenomenon known as a mechanical Fréedericksz transition (MFT) [2,4], as mentioned in Section 2.2.2. For this LCE, the MFT occurs at a threshold strain of ε_x~1.0,

much later in the strain regime than the auxetic threshold, in contrast to the related LCE reported previously [2,5] where the MFT was approximately coincident with it. This point is returned to later.

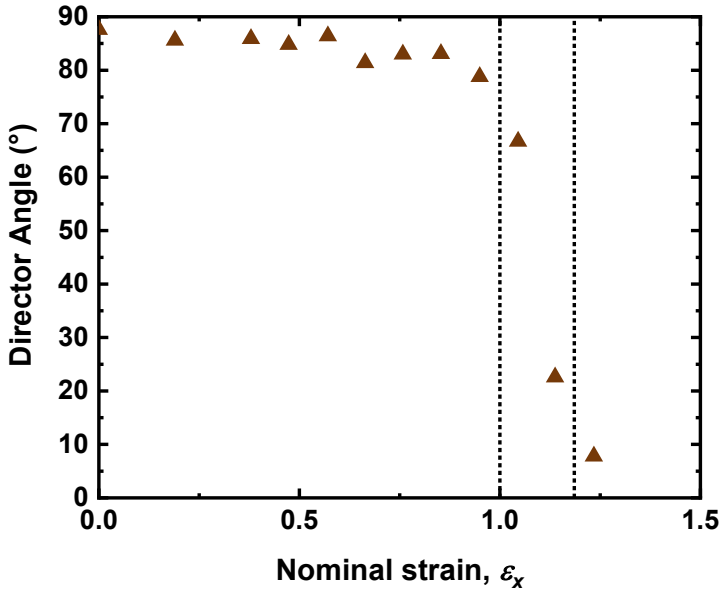

Figure 5.7 The director angle with respect to the axis of deformation (long axis of the sample) as a function of the strain of the P-LCE sample. The dotted region is the same as Figure 5.6, in this region the director rapidly reorients to align with the axis of deformation. Reproduced from [3].

The apparent reduction of $\langle P_{200} \rangle$ to values below $\langle P_{400} \rangle$ is an interesting result as it appears to violate Maier-Saupe theory, a mean-field treatment of the long-range intermolecular potential which has had enormous success in describing liquid crystal systems [6]. The deviation from Maier-Saupe theory can be seen in Figure 5.8. Such a deviation can be assumed to be attributed to the emergence of biaxial order and values for the biaxial order parameters can be generated as follows [2]. The value of $\langle P_{200} \rangle$ is used to generate idealised values of $\langle P_{400} \rangle$ in accordance with Maier-Saupe theory, then the biaxial order parameters are allowed in the fit to the PRS data. Figure 5.9 shows the deduced behavior of $\langle P_{220} \rangle$, $\langle P_{420} \rangle$ and $\langle P_{440} \rangle$, over the whole extension regime. The 4th order terms, $\langle P_{420} \rangle$ and $\langle P_{440} \rangle$ change little; the former showing no particular trend and the latter remaining close to zero up to a strain of ε_x = 0.85 ± 0.05 where a positive value is observed with a maximum value at $\varepsilon_x = 0.95$ ± 0.05. $\langle P_{220} \rangle$ shows the biggest variation, with significant changes for strains of beginning at $\varepsilon = 0.6$ where the value of $\langle P_{220} \rangle$ rapidly becomes

maximally negative, $\langle P_{220} \rangle$ = 0.02 ± 0.005 at a strain of ε_x = 1.05 ± 0.05. The increasingly negative value seen in $\langle P_{220} \rangle$ is indicative of an increasing population of molecules aligned with the strain axis [2]. In contrast, the 4th order biaxial order parameters are expected to drive a distribution of molecules aligned out of plane in the direction that the auxetic response is observed [2].

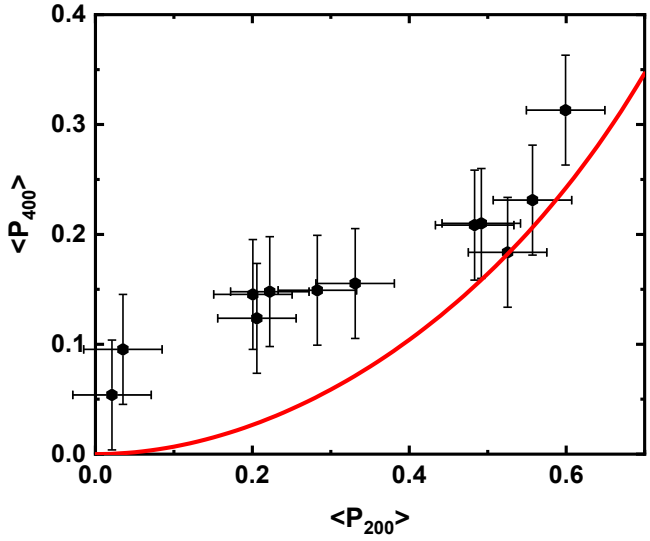

Figure 5.8 The values of $\langle P_{400} \rangle$ plotted as a function of $\langle P_{200} \rangle$ compared to the theoretical prediction of Maier-Saupe theory (red line). A clear deviation can be seen at higher strain (lower $\langle P_{200} \rangle$ and $\langle P_{400} \rangle$ values). Reproduced from [3].

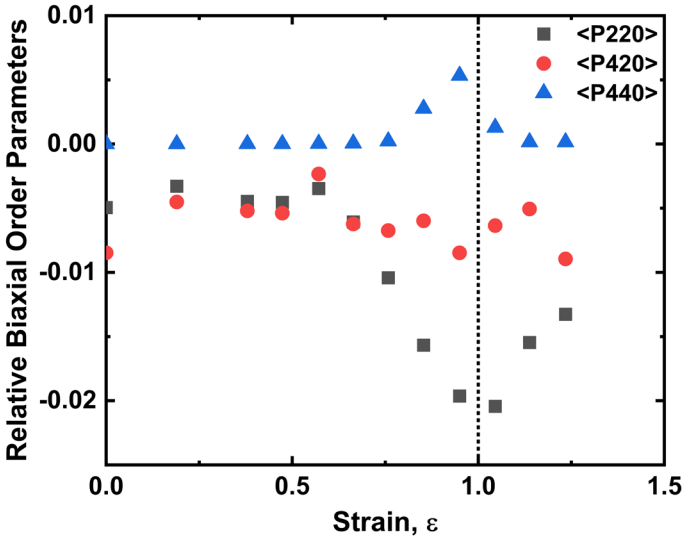

Figure 5.9 The biaxial order parameters $\langle P_{220} \rangle$ (black squares), $\langle P_{420} \rangle$ (red circles) and $\langle P_{440} \rangle$ (blue triangles) as a function of strain. The dotted line denotes where the maximum value of $\langle P_{440} \rangle$ is seen, a point that coincides with the MFT of the material. Reproduced from [3].

The results obtained showed that biaxiality is induced in the system through the application of a strain perpendicular to the initial nematic director and the emergence of biaxial order is inferred by the Polarized Raman spectroscopy (PRS) analysis both for this system and for that previously studied [2].

Conoscopy measurement. The conoscopy measurement of the H-LCE during mechanical deformation was performed and analysed by Dr. Thomas Raistrick with a Leica DM 2700P polarizing microscope in transmission mode under cross-polarized conditions. The conoscopy figures obtained by Dr. Thomas Raistrick indicated an increase in biaxiality within this system upon increasing applied strain and provided a direct observation of biaxiality.

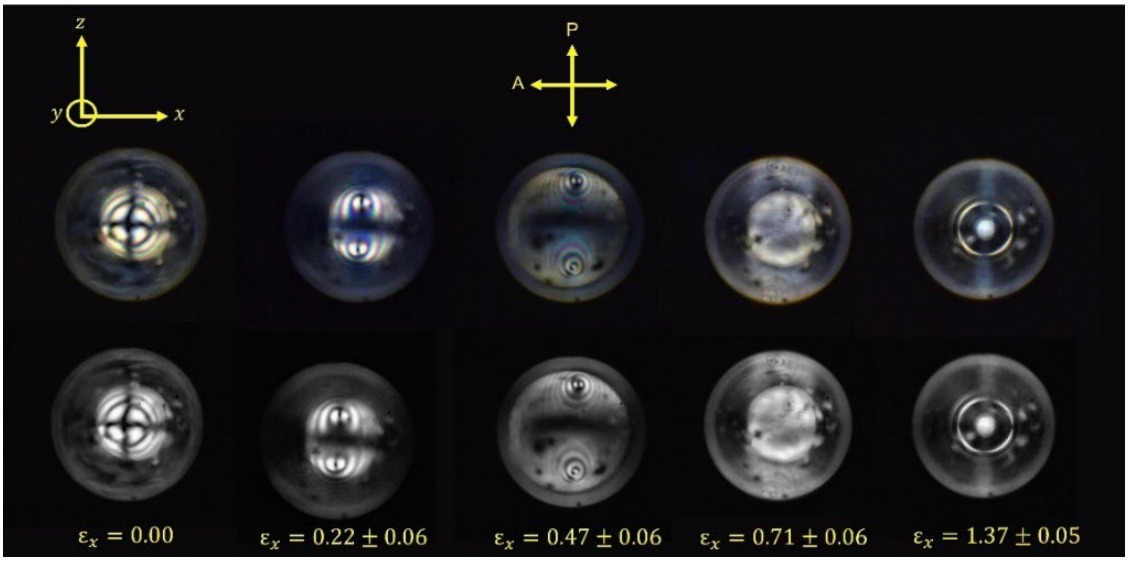

Figure 5.10. Conoscopic patterns for the homeotropically aligned LCE. The initial nematic director is aligned along the y-axis and strains are applied along the x-axis with a polarizer and analyzer aligned along the x- and z- axes respectively. The development of two melatopes with applied strain (increasing strain from the left to the right of the figure) is indicative of biaxiality within the system. The bottom row shows grey-scaled images of the top row. Reproduced from [3].

Figure 5.10 shows clearly that the unstrained, homeotropically aligned LCE has uniaxial symmetry with zero pre-tilt as evidence by a dark symmetric “Maltese cross”

pattern in the centre of the conoscopic image [7]. On the application of a strain of ε_x = 0.22 ± 0.06 along the *x*-axis, the LCE sample clearly becomes biaxial as evidenced by the two melatopes in the image [8] which suggests that the sample is being investigated perpendicular to the acute bisectrix [9]. On increasing strain, the melatopes separate further apart, and higher order isochromes become visible, both of which are indicative of an increasing difference in the retardation of polarized light travelling through the sample. From Figure 5.10, it can be seen that, in the geometry required for conoscopic investigation of the homeotropic LCE, the distance the light travels through the sample always decreases with applied strain (i.e. light is travelling along *y* which shows non-auxetic behavior). Therefore, the greater separation of the melatopes and the increase in the order of isochromes visible in the conoscopic figures are both indicative of an increase in biaxiality within this system upon increasing applied strain.

5.4 Summary

In this chapter, we introduced the fabrication of the intrinsic auxetic LCEs in high-quality planar and homeotropic alignments and characterized their mechanical deformations. This work represents the first successful attempt to obtain homeotropic alignment in 100μm thick films of auxetic LCEs using electric-field alignment. The POM figures of the sample, with their high contrast, show excellent, monodomain planar and homeotropic alignment in the unstrained LCE samples. For the mechanical deformation characterizations, both types of LCE sample show an auxetic response with threshold strains in excellent agreement; 0.56 ± 0.05 for the H-LCE and 0.58 ± 0.05 for the P-LCE. The H-LCE displayed auxetic response visually and clearly as a change in the width of the sample. Through the Raman scattering results obtained by Aidan Street, biaxiality was again inferred in this auxetic system. Importantly, the excellent quality, macroscopic homeotropic sample allowed Dr. Thomas Raistrick to undertake conoscopy, unequivocally demonstrating that the system became biaxial even at very low strains. In fact, the emergence of biaxiality was proven to be an intrinsic feature of the auxetic response in nematic LCEs. In the next chapter, we will induce the Fréedericksz transition alignment in intrinsic auxetic LCEs and show that voltages allow tuneability of the auxetic responses. The various auxetic responses will be described and analysed to lay foundation for the design of the tuneable liquid crystal elastomer devices.

References

1. Mistry, D.; Connell, S. D.; Mickthwaite, S. L.; Morgan, P. B.; Clamp, J. H.; Gleeson, H. F. Coincident molecular auxeticity and negative order parameter in a liquid crystal elastomer. *Nat. Commun.* 2018, *9*, 5095.
2. Raistrick, T.; Zhang, Z.; Mistry, D.; Mattson, J.; Gleeson, H. F. Understanding the physics of the auxetic response in a liquid crystal elastomer, *Phys. Rev. Research* 2021, *3*, 023191.
3. Wang, Z.; Raistrick, T.; Street, A.; Reynolds, M.; Liu, Y. J.; Gleeson, H. F. Direct observation of biaxial nematic order in auxetic liquid crystal elastomers. *Crystals* 2022, *12*, 393.
4. Mistry, D.; Morgan, P. B.; Clamp, J. H.; Gleeson, H. F. New insights into the nature of semi-soft elasticity and “mechanical-Fréedericksz transitions” in liquid crystal elastomers, *Soft Matter.* 2018, *14*, 1301.
5. Yeganeh-Haeri, A.; Weidner, D. J.; Parise, J. B. Elasticity of α-cristobalite: A silicon dioxide with a negative Poisson’s ratio. *Science* 1992, *257*, 650–652.
6. Luckhurst, G. R.; Zannoni, C. Why is the Maier-Saupe theory of nematic liquid crystal so successful? *Nature* 1977, *267*, 412-414.
7. Hartshorne, N. H. Microscopy of liquid crystals, 1st ed.; *Microscope Publications: London*, United Kingdom, 1974; pp. 20-26.
8. Van Horn, B. L.; Winter. H. H. Conoscopic Measurement of Birefringence and Orientation in Biaxially Stretched Polymer Films and Sheets. *Macromolecules* 2003, *36*, 8513-8521.
9. Palangana, A. J. Refractive Index Studies. In Biaxial Nematic Liquid Crystals: Theory, Simulation, and Experiment, 1st ed.; Luckhurst G. R., Sluckin, T. J.; *John Wiley & Sons: Oxford*, United Kingdom, 2015; pp. 242-250.

Chapter 6 The auxetic liquid crystal elastomer with the Fréedericksz transition alignments

In the previous chapter, we introduced the fabrication of IALCEs in high-quality planar alignment and homeotropic alignment and characterized their auxetic responses through mechanical deformation measurements. We showed that both types of LCE sample exhibited an auxetic response with threshold strains in excellent agreement; 0.56 ± 0.05 for the H-LCE and 0.58 ± 0.05 for the P-LCE, which indicates that the auxetic response of the IALCEs is related to the geometry of the applied strain with respect to initial nematic director, instead of the sample aspect ratio. Besides, through the mechanical deformation of H-LCE, we revealed the auxetic response directly through visual observations of the change in the sample width. Most importantly, we presented data that confirmed the IALCEs showed anomalous behaviour similar to the ones fabricated by Mistry *et al.* and the emergence of biaxiality was proven to be an intrinsic feature of the auxetic response in nematic LCEs, through the order parameter measurements obtained by Aidan Street and conoscopy measurements obtained by Dr. Thomas Raistrick.

Following the introduction to IALCEs in planar and homeotropic alignments, we will now move on to the fabrication and characterizations of IALCEs with the Fréedericksz transition alignments. In this chapter, we will induce the Fréedericksz transition alignment that can be produced within a film of the IALCEs through applying an external electric field during polymerization. We will describe the fabrication of IALCEs with various Fréedericksz transition alignments, distinguished by the maximum angles of the director induced by specific applied voltages in Fréedericksz transition alignment. The first part of the chapter will show the thermal-mechanical deformation measurements of the samples and then confirm the introduction of Fréedericksz transition alignments through birefringence measurements of the IALCE films. Subsequently, we will characterize the manipulation of the auxetic response through mechanical deformation, demonstrating the influence of the Fréedericksz transition alignments on the auxetic properties of the films. DSC measurement is utilized to confirm that the voltage-tuned auxetic response originates from changes in the director profile rather than significant variations in the backbone structures. Additionally, a simple mathematical model was considered by Dr. Thomas Raistrick to better understand the tuneability of the auxetic responses. Finally, the hyper-elasticity of

the samples was also determined by strain-stress curves.

6.1 Introduction and motivation

The purpose of this thesis is to design and implement tuneable liquid crystal elastomer devices with electric-field induced alignment. Achieving this goal requires a comprehensive understanding of the stimulus-response characteristics of the LCEs employed and the influence of electric field alignment on these responses. The auxetic response features of the IALCEs employed in this thesis have been introduced in Section 2.2.3 and Section 5.3. The uniqueness of this category of LCEs lies in the auxetic response exhibited during mechanical deformation, a characteristic that can be leveraged for the fabrication of devices with strain-induced morphological changes. In addition to utilizing the morphological variations (such as changes in thickness or width), we can also utilise the optical features that emerge in the auxetic response. Specifically, during the mechanical deformation, the uniaxial order parameter will decrease as the strain increases and the biaxial order increases. When the biaxial optical indicatrix changes sign, the material exhibits a dark state under crossed polarizers [1,2]. This dark state has also been described as a negative order parameter state and occurs close to the threshold strain for the auxetic response [3]. This optical feature, which is less obvious than morphological changes in auxetic responses, expands the potential applications of tuneable devices in the optical field.

After roughly determining the application direction of the tuneable devices, we now need to consider how tunability can be achieved. Regardless of whether the application is morphological or optical, all functionalities are fundamentally based on the auxetic response of the synthesised IALCEs. As demonstrated in Section 5.3, the mechanical deformation of IALCEs with both parallel and perpendicular alignments indicates that once the IALCE is fabricated, its auxetic response remains fixed. Only by achieving tunability of the auxetic response can we truly realize tuneable devices based on IALCEs. In Section 2.2, we revealed the intrinsic correlation between the macroscopic deformation of LCEs and the director profile. By manipulating the director profile, the macroscopic deformation of LCEs can be controlled, a principle that also applies to auxetic LCEs. As discussed in Section 5.3, the auxetic response is independent of the sample aspect ratio, and it is determined by the geometry of the applied strain relative to the initial nematic director. Clearly, by altering the director field, we can achieve some tunability of the auxetic response.

Previously, Mistry demonstrated that in-plane orientational control also influences the auxetic response [4]. Here, we will induce the Fréedericksz transition alignments in IALCEs via applying external electric fields during polymerization, thereby implementing out-of-plane control of the director orientation and investigating the tunability of the auxetic response. Based on Figure 4.6, we can control the maximum angle θ_{max} induced in the central region through adjusting the applied voltage V , thereby inducing distinct Fréedericksz transition alignments in the IALCEs. Table 6.1 shows the θ_{max} with the corresponding V , for the precursor mixture, at 10° intervals and for V_{th} of 0.9 ± 0.1 V_{rms}.

Table 6.1 The maximum angle to the corresponding applied voltage based on Figure 4.6

θ_{max} (°)	10	20	30	40	50	60	70	80
V (V_{rms})	0.91	0.93	0.97	1.05	1.14	1.25	1.50	2.00

Here, we selected four voltages: 1.05 V_{rms}; 1.25 V_{rms}; 1.50 V_{rms}; and 2.00 V_{rms} to fabricate IALCEs with maximum angles θ_{max} of approximately 40°, 60°, 70°, and 80°, respectively. The selection of these voltages during polymerization was based on the following considerations. As discussed in Section 4.3, once V exceeds V_{th}, θ_{max} increases rapidly initially and gradually approaches 90° at a progressively slower rate as the voltage increases. When V is smaller than 0.97 V_{rms}, a small voltage variation can result in significant changes in the θ_{max} , so we selected 1.05 V_{rms} as the first voltage. Additionally, minor deviations in actual experiments, such as cable resistance and slight variations in precursor composition during sample preparation—could lead to inconsistencies, causing the actual θ_{max} to deviate from the expected θ_{max} , not to mention that the measurement accuracy of the V_{th} is limited to ±0.1 V_{rms}. Therefore, we selected 1.25 V_{rms}, 1.50 V_{rms}, and 2.00 V_{rms} to achieve a balance between θ_{max} control and practical experimental circumstances. Moreover, in addition to polymerizing with voltages slightly above V_{th}, we also fabricated samples with θ_{max} approaching 90 degrees to facilitate comparison with

IALCEs in homeotropic alignments. To fabricate IALCEs with θ_{max} at approximately 90 degrees, the θ_{max} *vs* voltage data presented in Figure 4.6 were extended through nonlinear fitting using an exponential model in OriginPro 2022. The fitting results are summarized in Table 6.2, while the extended curve is illustrated in Figure 6.1. The fitting achieved a high degree of accuracy at low voltages, with a coefficient of determination (R^2) of 0.99. Here, we will apply a 40 V_{rms} to fabricate the IALCEs with a θ_{max} at 88°, according to Figure 6.1.

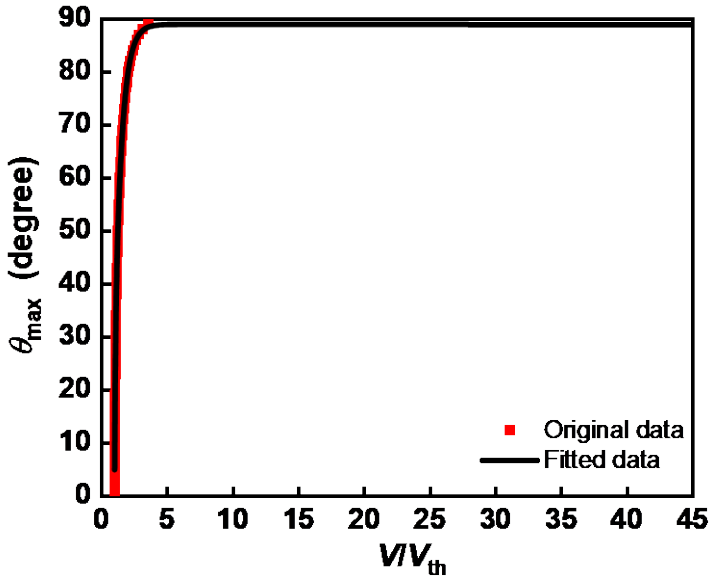

Figure 6.1 The extended curve based on Figure 4.6, with V/V_{th} in range from 0 to 45 V_{rms}.

Table 6.2. The fitting result of the data in Figure 4.6

Fitting mode	Exponential	
Output equation	$\theta_{max} = A_1 \times \exp(-(V/V_{th})/t_1) + A_2 \times \exp(-(V/V_{th})/t_2) + A_0$	
A_1	t_1	A_2
-1.5 ± 1.69	0.05 ± 0.003	-395.4 ± 26.52
t_2	A_0	R^2
0.53 ± 0.017	88.9 ± 0.51	0.99

6.2 Experimental details

6.2.1 Fabrication of IALCEs with Fréedericksz transition alignments

The IALCEs samples were fabricated by polymerizing the nematic precursor mixture in a conductive planar-aligned cell under an electric field. The detailed fabrication procedure is illustrated in Figure 6.2. The fabrication process is fundamentally similar to procedure introduced in Section 3.2, while certain modifications were required. The cell used to fabricate IALCEs with Fréedericksz transition alignments was assembled with an ITO-glass substrate and an ITO-PET substrate and the alignment layer was made by spin-coating 0.5 wt.%PVA.

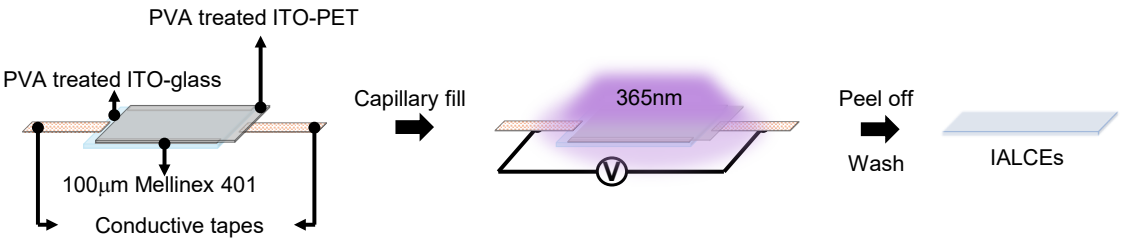

Figure 6.2 The schematic for fabricating the IALCEs with Fréedericksz transition alignments.

During polymerization, a 10 KHz electric field was applied at 1.05 V_{rms}, 1.25 V_{rms}, 1.50 V_{rms}, 2.00 V_{rms} and 40.00 V_{rms}, respectively. Here, we call the IALCE polymerized with θ_{max} at 40° as 40°–IALCE and the same format will be used to name IALCEs that are polymerized with different θ_{max} in the following.

6.2.2 The thermal-mechanical deformation measurement

The thermal mechanical deformation measurements were conducted to determine the thickness variation of LCE samples during heating, as illustrated in Figure 6.3. The measurements were performed with a Linkam THMS600 hot stage (±1°C accuracy) and a Leica DM2700 P polarizing microscope. The prepared IALCE sample was placed on a coverslip spread with silicone oil, minimizing the friction and ensuring the unrestricted deformation of the film. Prior to measurement, the sample was left on the coverslip for 30min to monitor any dimensional changes, ensuring that the oil did not swell the sample.

After no swelling was observed, the coverslip was moved to the hot stage at 30°C and maintained for 10min to allow thermal equilibrium of the IALCE sample.

Thickness measurements were performed using the 20X objective lens of the microscope. Frist, reference points were marked on both the edge of the IALCE sample and an adjacent region of the coverslip. The 20X objective lens was then focused on the reference point on the sample and the dial on the fine adjustment knob of the microscope was recorded. Next, the lens was adjusted with the fine adjustment knob to focus on the reference mark on the coverslip and the dial reading was recorded again. The difference between these readings represented the vertical displacement of the lens, corresponding to the thickness of the IALCE sample at the given temperature. The microscope's fine adjustment dial was pre-calibrated by an object of known thickness, with each unit of the dial corresponding to 1 μm. Notably, all measurements were conducted in air to avoid the alteration in the optical path of the observed light due to the birefringence of the IALCE film, which is caused by temperature-induced variations in the order parameter. Subsequently, the temperature was then increased from 30°C to 180°C at a rate of 5°C/min, with increments of 15°C per step. At each temperature step, the sample was held for 10min to ensure thermal equilibrium before repeating the thickness measurement procedure. The final thickness change of the sample during the deformation was obtained by averaging the results of five measurement cycles on the same sample.

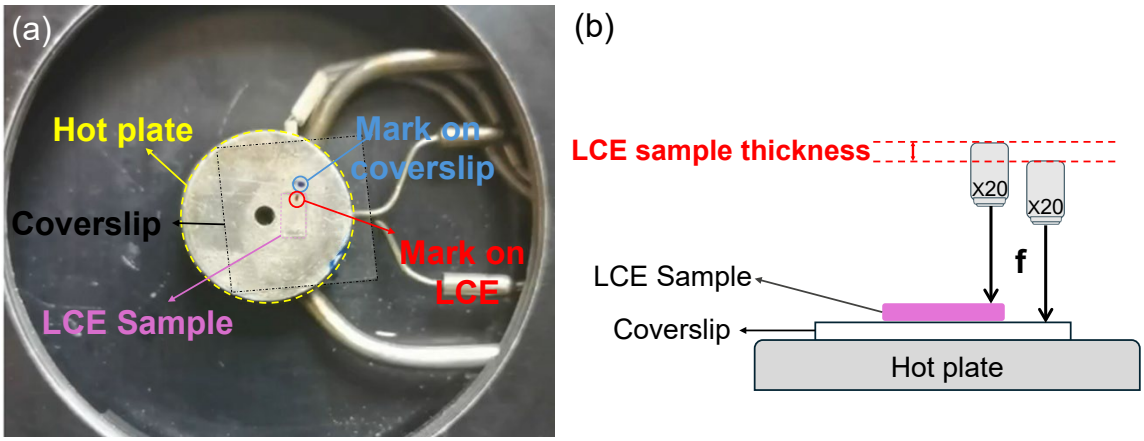

Figure 6.3 Experimental set up for thermal mechanical deformation measurement (a) A photographe of the experimental set up. The IALCE sample was put on a coverslip spread withsilicon oil and the coverslip was on a hot plate. The reference marks on the sample and the coverslip are highlighted in blue and red, respectively. (b) A schematic diagram of the experimental set up. The f is the focal length of the 20X lens. The 20X lens moves

along the vertical axis to focus on each surface, and the sample thickness is determined by how far the lens moves.

6.2.3 The birefringence measurement

The birefringence of synthesised IALCE samples was measured using a Leica DM2700 P polarising microscope equipped with a Berek compensator [5]. As we introduced in Section 4.2.1, the retardation is related to the birefringence and the thickness of the sample. When the IALCE sample is set in a POM with the optical axis oriented at 45° to the two crossed polarisers, the light is retarded. The insertion of the Berek compensator will induce an extra retardance in the optical path. This extra retardance could match the retardance of the IALCE sample and a black fringe would be observed through the microscope eyepiece, enabling the measurement of the birefringence of the IALCE sample. The Berek compensator is an optical device made up with a tiltable birefringent material, here Titanium Dioxide (TiO_2). A brief schematic of the Berek compensator is illustrated in Figure 6.4. To measure the retardance of the film, the following methodology is used. Firstly, set the sample with the director parallel to the analyser or polariser. Secondly, insert the compensator into the POM with the polarization direction (the fast axis shown in Figure 6.4) oriented at 45° to the crossed polarisers and then rotate the sample to align the director perpendicular to the fast axis. Then adjust the dial around the fast axis of the compensator, depicted in Figure 6.4, to match the retardance of LC. Record the angle of the dial and then calculate the birefringence. The tilt angle of the birefringent material is related to retardance Γ, through [5]:

$$\Gamma = n_{oB} d_B \left(\sqrt{(1 - sin^2 \alpha_{avg}) / {n_{oB}}^2} - \sqrt{(1 - sin^2 \alpha_{avg}) / {n_{eB}}^2}\right) \tag{6.1}$$

where d_B is the thickness of the compensator, α_{avg} is the average pretilt angle of the optical axis of TiO_2, n_{oB} and n_{eB} are the ordinary and extraordinary refractive indices of the compensator. d_B , n_{oB} and n_{eB} are taken from the compensator data sheet and the birefringence of the sample is calculated by dividing the retardance of the compensator by the IALCE sample thickness. The accuracy of the birefringence measurement with a Berek compensator is 0.001.

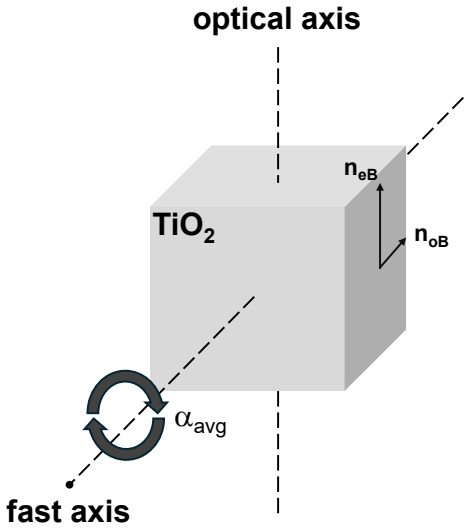

Figure 6.4 Brief schematic representation of the Berek compensator utilizing a TiO_2 crystal.

6.3 Results and discussion

6.3.1 The thermal mechanical deformation measurement

After the sample fabrication, the first thing to do is to confirm the introduction of the Fréedericksz transition alignment. One efficient method is to observe the macroscopic deformation of the samples; it is expected that the varying director orientation through the thickness of the sample influences the anisotropic expansion of the film. As mentioned in Section 2.2.2, upon heating from anisotropic phase to isotropic phase, the loosely crosslinked mesogens in LCEs exhibit a decrease in order and LCEs possess obvious shrinkage strain along the director. Additionally, LCEs exhibit anisotropic expansion behaviours, meaning they expand or contract differently along different directions when subjected to external stimuli, and this anisotropy arises from the director. Upon heating, the mesogens lose their orientational order (i.e., undergo a nematic-to-isotropic transition), leading to a contraction along the director and an expansion perpendicular to the director. The anisotropic expansion coefficients are expressed as:

$$\alpha_{\parallel} = \frac{1}{L_{\parallel}} \frac{dL_{\parallel}}{dT}, \alpha_{\perp} = \frac{1}{L_{\perp}} \frac{dL_{\perp}}{dT} \tag{6.2}$$

where $\alpha_{\parallel}$ is the contraction coefficient along the director and is typically negative, indicating

thermal contraction, while $\alpha_{\perp}$, the expansion coefficient perpendicular to the director, is typically positive, indicating thermal expansion. The expansion and contraction coefficient are different with respect to the director during heating. Considering the introduction of Fréedericksz transition alignments, due to the change of the director profile, the film thickness change of the samples with Fréedericksz transition alignments will be in-between that of the planar sample and the homeotropic sample. The thermal mechanical deformation measurement of samples (P-LCE, H-LCE, 80°–IALCEs and 88°–IALCEs) are conducted and the results are shown in Figure 6.5.

According to Section 2.2.2, during the heating process, the sample order parameter will reduce, ultimately transitioning from anisotropy to isotropy; the LCE film deforms due to the change in order as the backbone is coupled to the mesogenic units. The actuation strain ε is calculated as $(L_0 - L_{iso}) / L_0$, where L_0 and L_{iso} are the original and final lengths of the LCEs, respectively. The deformation process is illustrated in Figure 6.5. In fact, the extent of the deformation is influenced by the elastic properties of the LCE backbone and the order parameter. For the IALCE samples here, the elastic properties of the backbones remain identical with the same material (discussed further in Section 6.3.3), and the only difference is the patterned director. Consequently, the introduction of Fréedericksz transition alignments leads to a reduction in fractional thickness change during heating.

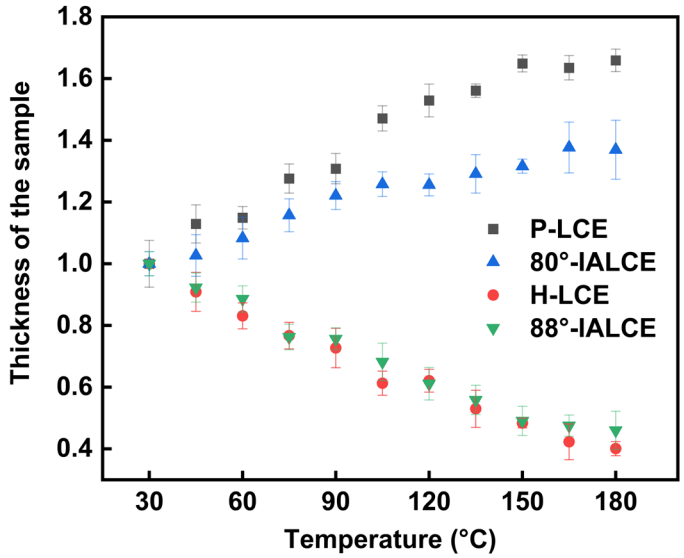

Figure 6.5 The fractional thickness change of P-LCE, H-LCE, 80°–IALCEs and 88°–IALCEs during thermal mechanical deformations. The initial sample thickness is calibrated as 1.0.

By inducing a θ_{max} at 80°, in comparison of P-LCE and 80°–IALCEs, the fractional thickness changes of these two samples with increasing temperature exhibit different deformation amplitudes, with the P-LCE showing a greater increase in thickness. When the temperature reaches 180°C, the fractional thickness of the P-LCE has increased to 1.65 ± 0.03, while the thickness of the 80°–IALCE has only increased to 1.36 ± 0.10. The introduction of Fréedericksz transition alignment with θ_{max} of 80° results in a strain difference of ~0.3 in thickness direction. In contrast, the thermal response of 88°–IALCEs is almost the same to that of H-LCE. When the temperature reaches 180°C, both the H-LCE and 88°–IALCEs exhibit ~-0.5 ± 0.05 strain in the thickness direction, indicating that the Fréedericksz transition alignment introduced under 40V_{rms} has achieved a nearly homeotropic alignment.

6.3.2 The birefringence measurement

To further investigate and confirm the introduction of the Fréedericksz transition alignment, we undertook birefringence measurements of the samples that were polymerized with low voltages (1.05 – 2.00 V_{rms}).

When the director reorients, the birefringence will change correspondingly. For the director profile throughout the cell for the specific values of distinct θ_{max} shown in Figure 4.6 (b), we can calculate the magnitude of the effective extraordinary refractive index, n_e through the cell [6], using:

$$n_e(z/d) = \frac{n_e n_o}{\sqrt{n_e^2 sin^2\theta(z/d) + n_o^2 cos^2\theta(z/d)}}. \quad (6.3)$$

The result is shown in Figure 6.6 (a). Then, by integrating birefringence through the cell, we can obtain values for the final effective birefringence of the sample, using equation 6.4:

$$\langle \triangle n \rangle = \int_0^1 (n_e(z/d) - n_o) d(z/d). \quad (6.4)$$

Combining this with the relationship of θ_{max} to the applied voltage shown in Figure 4.6 (a), we can plot the effective birefringence as a function of applied voltage, see Figure 6.6 (b). Here, we are using n_o = 1.529 and n_e = 1.659, the effective refractive indices measured by Emily Cooper [7] on a uniform planar aligned LCE which was synthesised with the same recipe as that used for IALCEs. We can see that, as the θ_{max} increases, the effective n_e in the central region decreases towards n_o. The corresponding effective birefringence change,

shown in Figure 6.6 (b), provides a good reference for measuring the birefringence of the polymerized IALCEs and determining the introduction of the Fréedericksz transition alignment.

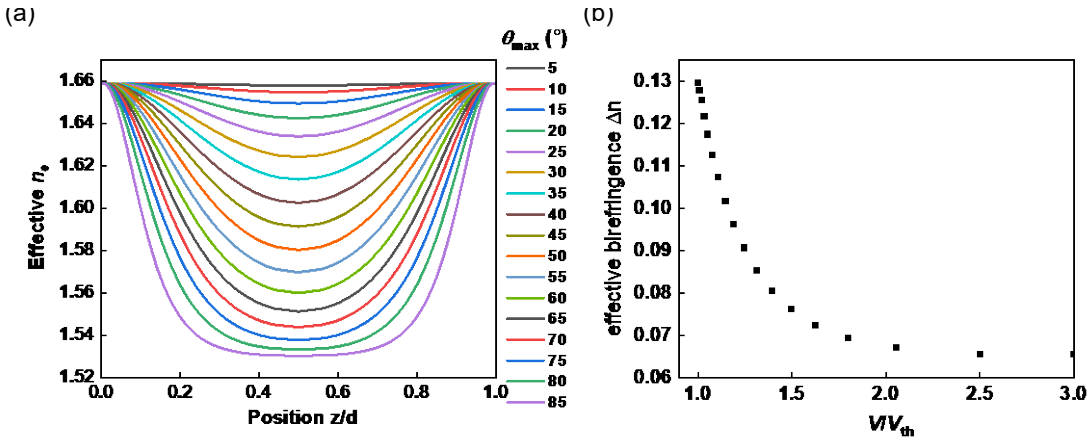

Figure 6.6 (a) The distribution of effective n_e through the cell under circumstances with various θ_{max}. (b) The relationship between the voltage applied and the effective birefringence of the sample.

The result of the birefringence measurement is shown in Figure 6.7, and the measured birefringence was added to the calculated relationship shown in Figure 6.6 (b) to show the comparison between the estimated effective birefringence and the experimental results, see Figure 6.7.

Birefringence measurement	
P-LCE	0.125±0.015
40°–IALCEs	0.107±0.018
60°–IALCEs	0.111±0.009
70°–IALCEs	0.099±0.105
80°–IALCEs	0.082±0.010

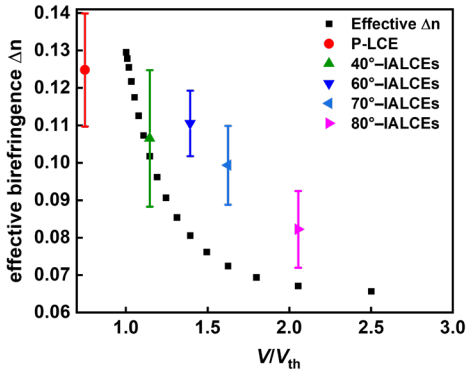

Figure 6.7 The birefringence measurement results and the data plotted in comparison with the calculated effective birefringence.

In comparing the measured to the calculated birefringence, several conclusions can be drawn. Firstly, the birefringence of the fully-planar P-LCE sample has a birefringence of 0.125, in good agreement with the predicted value of 0.13. For the remaining data, although

variation remains, the measured birefringence follows a similar trend to the estimated effective birefringence. These variations arise from several factors. First, the sample was thick and not flat enough, which caused the light passing through the sample scatter and affected the measurement. Additionally, the anisotropic deswelling of the sample during wash affected the director orientation. After the polymerization process under electric fields, the director aligns according to the Fréedericksz transition alignments. However, during the process for washing out the unreacted 6OCB, the sample experiences anisotropic deswelling according to the director's profile, as illustrated in Figure 6.8 (a) (obtained by Dr. Matthew Reynolds). For IALCEs, in the case of planar alignment, anisotropic deswelling induces approximately 3%-dimensional contraction along the director and 30%-dimensional contraction perpendicular to the director, while isotropic samples exhibit dimensional contraction of approximately 25% in both directions (Figure 6.8 (b)). When it comes to Fréederisksz transition alignment, the anisotropic deswelling induces anisotropic alterations in the sample dimensions based on the Fréedericksz transition alignment profile. The complicated deswelling process may result in deviations of the director from the intended alignment.

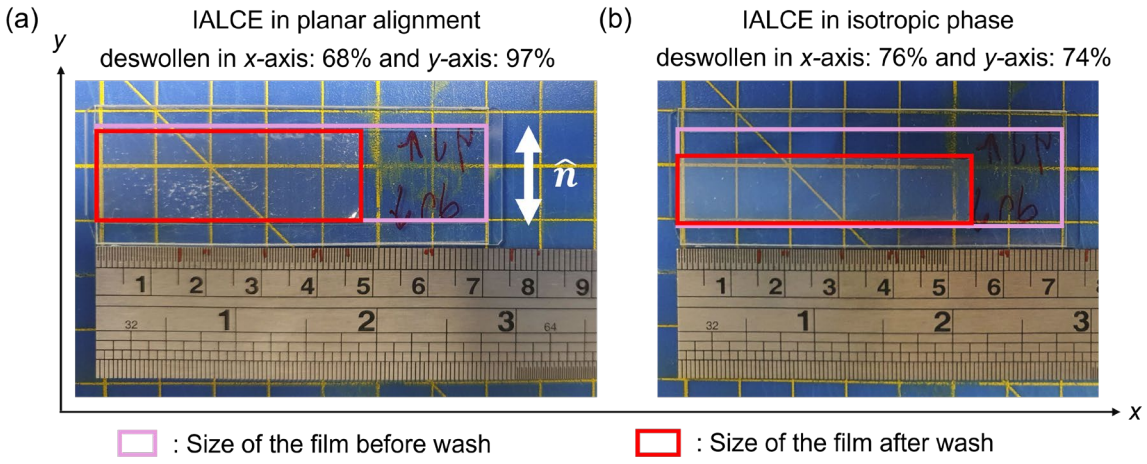

Figure 6.8 (a) The anisotropic deswelling in a parallel-aligned IALCE, demonstrating dimensional contraction of ~3% along the director ($\hat{n}$) and ~30% perpendicular to the director. The white arrow represents the initial alignment direction. (b) Isotropic deswelling behaviour, characterized by dimensional contraction of ~25% in all directions due to the absence of molecular orientation. Photographs are credited to Dr. Matthew Reynolds.

For the 88°–IALCEs, a value for the birefringence could not be obtained due to the nearly homeotropic alignment, which appeared dark under POM. Additionally, as shown in Figure 6.1, θ_{max} eventually saturates near 90°. Once saturation occurs, predicting the

director profile based solely on the θ_{max} becomes impractical. In practice, as voltage increases, the director near the central region progressively aligns toward the vertical orientation, illustrated in Figure 6.9. Consequently, birefringence calculations with Equation 6.1 and 6.2 for θ_{max} at 88° can only provide an estimated birefringence of the director profile when θ_{max} reaches 88° for the first time.

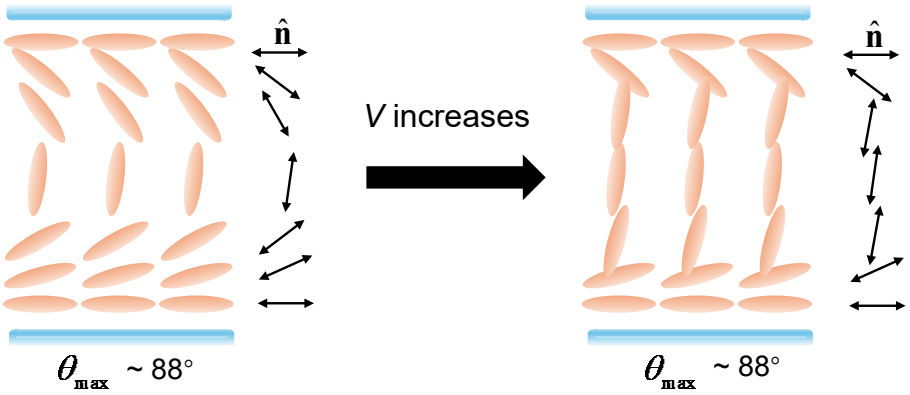

Figure 6.9 The schematic for showing the change of the director profile when the θ_{max} saturates to near 90° and the voltage applied increases.

Overall, the measured birefringence confirms the introduction of the Fréedericksz transition alignment, though the actual director profile may slightly deviate from the ideal intended alignment.

6.3.3 The mechanical deformation measurement

6.3.3.a IALCE samples fabricated with low voltages (1.05 V_{rms} to 2.00 V_{rms})

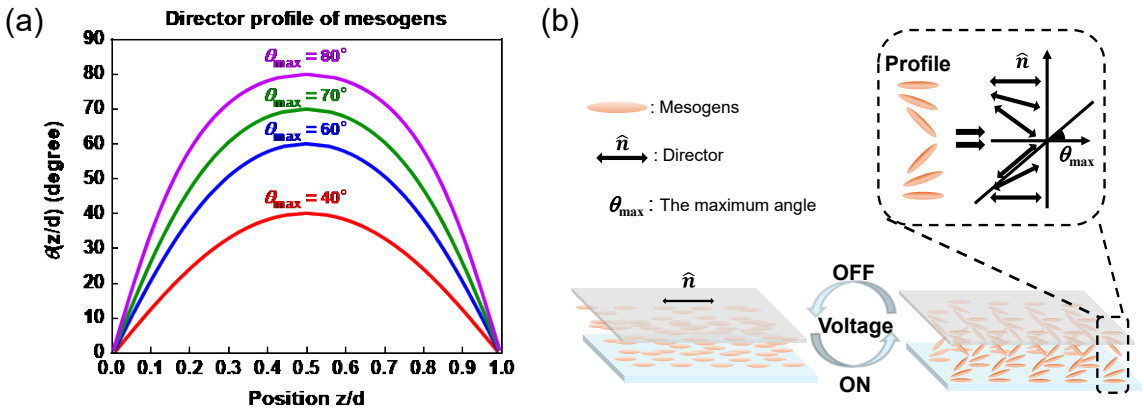

Figure 6.10 (a) The director profile through the cell from one substrate (z/d = 0) to the other (z/d = 1) for θ_{max} at 40°, 60°, 70° and 80°. *V* is the voltage applied. (b) A schematic

of Fréedericksz transition alignment of the director. The director is initially uniformly planar aligned in the cell with no electric field applied. When the electric field in turned on, the director reorients and adopts the minimum energy alignment profile in the final steady state. The orientation profile and the corresponding director directions are shown in the zoomed figure.

After confirming the introduction of the Fréedericksz transition alignments, we now move on to the mechanical deformation measurements to characterize the influence of the Fréedericksz transition alignments on the auxetic response. Here, the 88°-IALCE was fabricated to achieve an approximately homeotropic alignment using the Fréedericksz transition alignments, so it is discussed later in comparison with the H-LCE. We will first focus on the IALCE samples fabricated with low voltages (1.05 V_{rms} to 2.00 V_{rms}). The detailed angle distribution through the cell for each profile was shown in Figure 6.10 (a), with the schematic of the alignment profile shown in Figure 6.10 (b). In the schematic, we used the symmetrical alignment profile at the central position to clearly illustrate the alignment profile corresponding to Figure 6.10 (a). The quality of the director alignment was verified by POM and the POM figures are shown in Figure 6.11. When the initial director (determined by the cell alignment direction) is parallel to the analyser in crossed-polarizers, an excellent dark state is shown while at 45° to the crossed-polarizers, there is a bright state instead. The high contrast between the dark and bright states shows the high quality of the anisotropic alignment of IALCEs even after polymerization with electric fields.

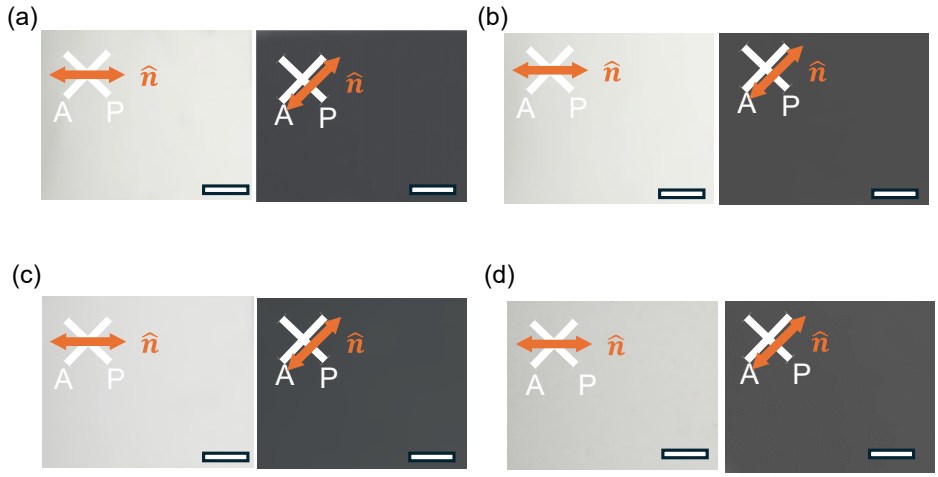

Figure 6.11 The POM images for (a) 40°– (b) 60°– (c) 70°– and (d) 80°– IALCE. The white crossed lines indicate the crossed polarizers and the orange arrows indicate the initial director direction determined by the cell alignment direction. The scale bar is 10 mm.

For all the IALCE samples, mechanical measurements were performed to determine the impact of the Fréedericksz transition alignment on auxetic responses. For comparison, we also added the observation of the auxetic response of the IALCE sample in planar alignment, which was introduced in Section 5.3. The diagram illustrating the mechanical measurements was shown in Figure 3.6 and the detailed measurement process was described in Section 3.3.2. As mentioned above in Section 6.1, during the auxetic response, due to the decrease of the uniaxial order parameter, the sample shows a dark state under crossed polarizers near the threshold strain ε_{th} of the auxetic response. To investigate this phenomenon, the mechanical measurement of each film, including the planar aligned IALCE sample is shown in Figure 6.12, displayed in frames with increasing strains in a 5% increment.

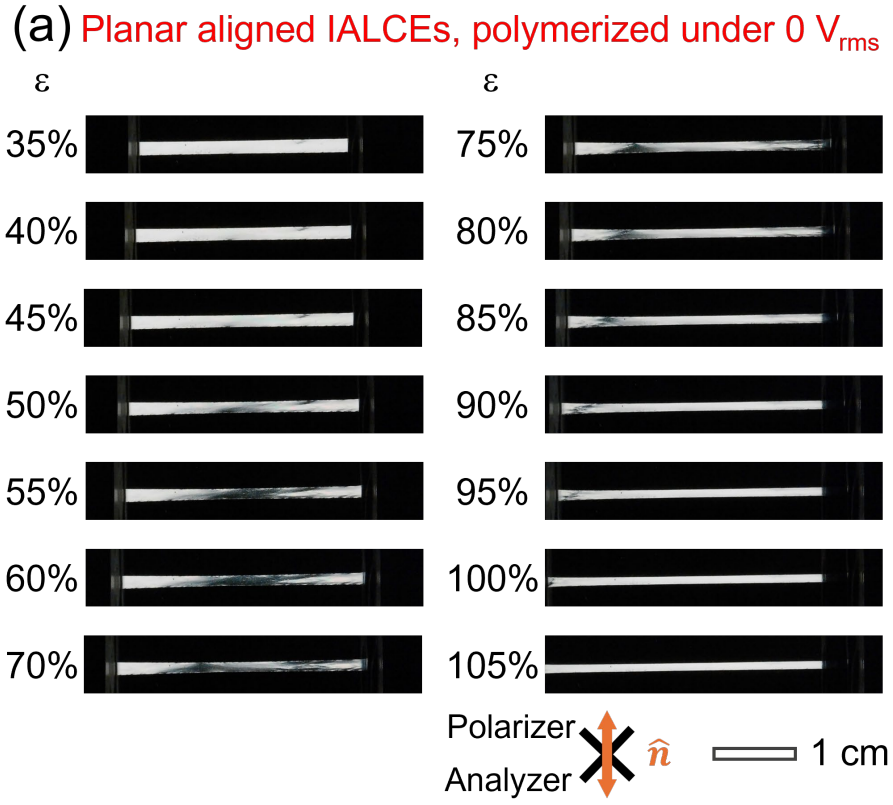

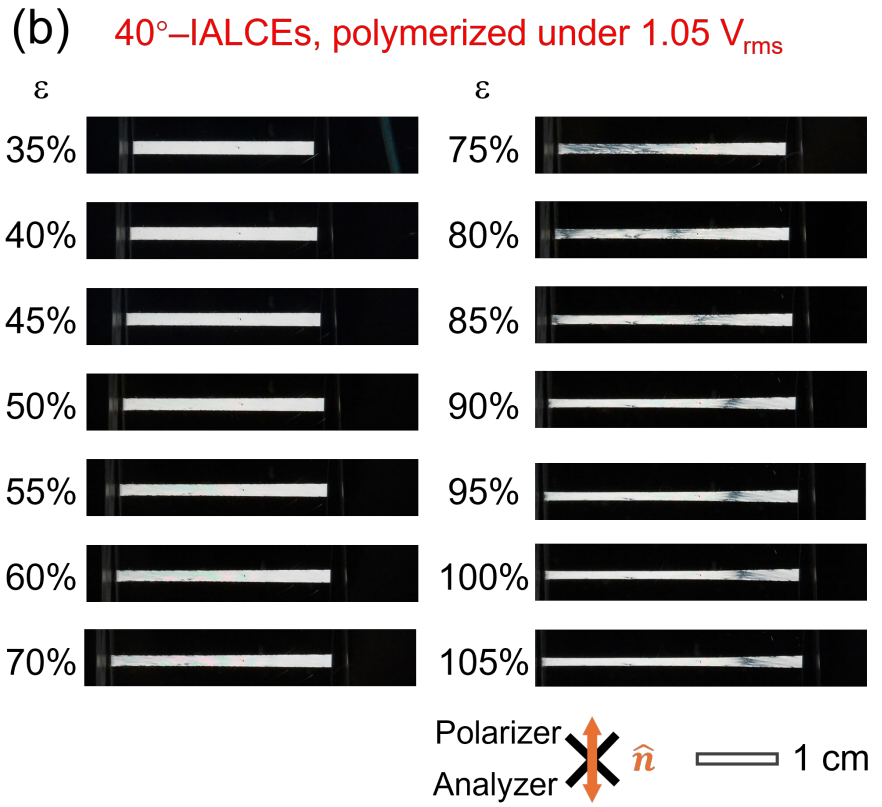
(b)
40°–IALCEs, polymerized under 1.05 V$_{rms}$
ε
ε
35%
40%
45%
50%
55%
60%
70%
75%
80%
85%
90%
95%
100%
105%
Polarizer
Analyzer
$\hat{n}$
1 cm

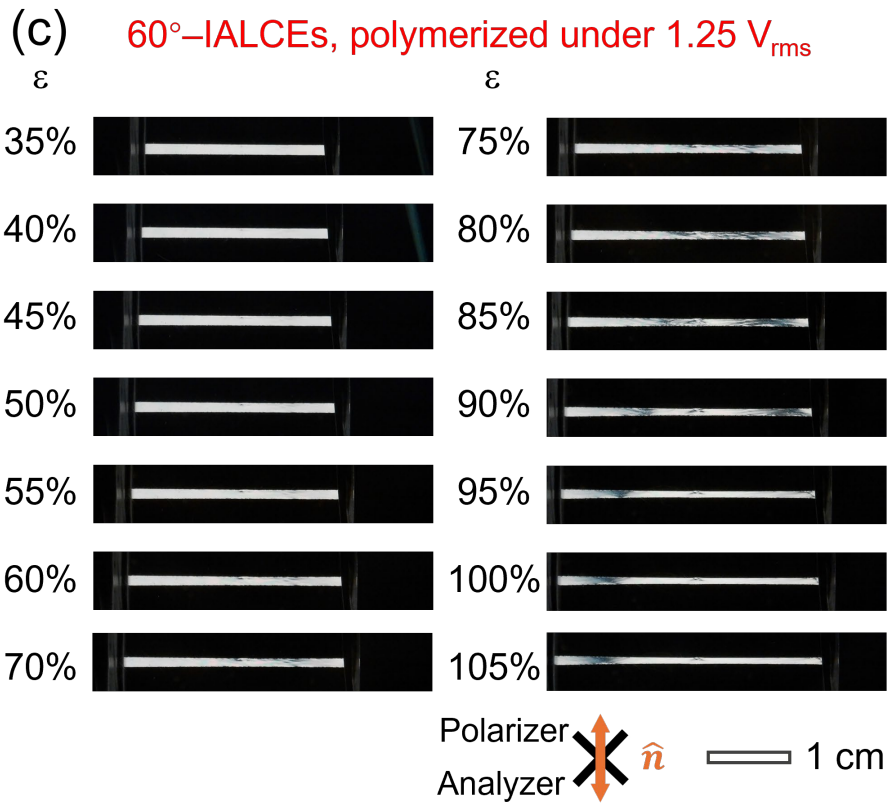
(c)
60°–IALCEs, polymerized under 1.25 V$_{rms}$
ε
ε
35%
40%
45%
50%
55%
60%
70%
75%
80%
85%
90%
95%
100%
105%
Polarizer
Analyzer
$\hat{n}$
1 cm

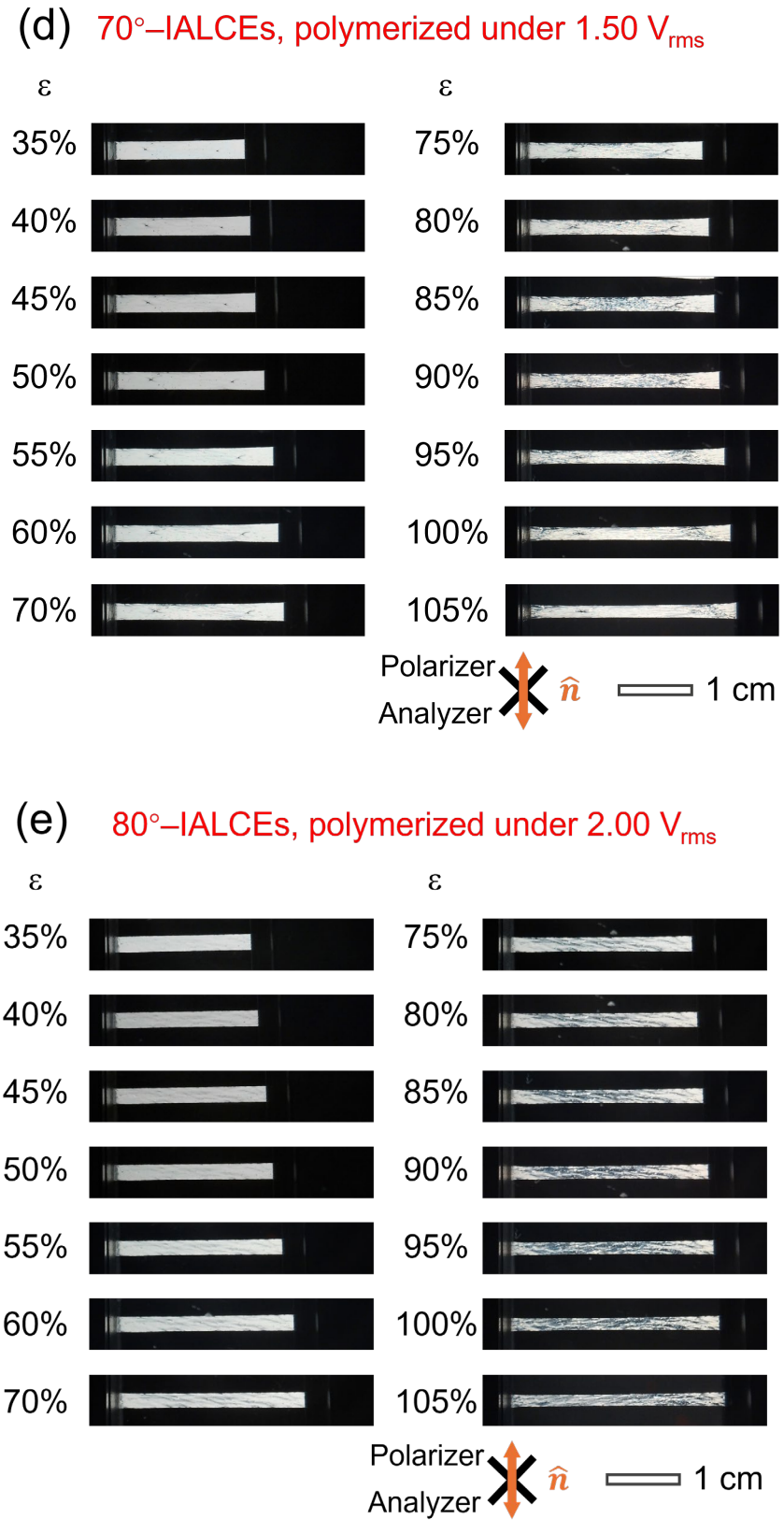

Figure 6.12 The mechanical deformation measurement of (a) planar aligned AILCE, (b) 40°– (c) 60°– (d) 70°– and (e) 80°– IALCE under crossed polarisers with the director at

45° to the crossed polarizers. The director is initially determined by the alignment director of the cell during polymerizations. The scale bar is 1 cm.

The planar aligned IALCE (0°–IALCE) was the sample that was characterized in Chapter 5. According to Figure 5.3, the threshold strain ε_{th} of the planar aligned IALCE was 0.56 ± 0.05, therefore, we excluded the initial mechanical deformation process at lower strains (0~30%), during which the film consistently stayed bright under crossed polarizers. Instead, we show the process starting with the frame taken at a strain of 35% and display at increments of 5%. For comparison, the mechanical deformation observation of other samples was using the same visualization format. For the P-LCE, at a strain of 50%, a dark state begins to emerge in the central region of the film and becomes more uniformly distributed between 55% and 60%. Subsequently, as the strain exceeds 70%, the dark state starts to propagate towards the edges, while the central region gradually transitions back to a bright state. The deformation process observed under POM exhibits an analogous behaviour to that reported by Mistry [1], further confirming the change of the order parameter. While for the distribution of the dark state, a possible explanation for this phenomenon is that during stretching, the material near the edges is constrained due to clamping effects, whereas the central region, being farther from the clamps, experiences less restriction and can deform more freely. The cumulative effect of this displacement results in the maximum displacement occurring in the central region. In this thesis, we do not extensively discuss the strain distribution but rather focus on the emergence of dark state during the auxetic response. All the rest samples behave similarly under POM. For the 40°–IALCE, the dark state emergences when the strain reaches near 75% in the left part of the film while for the 60°–IALCE, the dark state emergences around 80% and then propagate to both sides as the strain increases. For 70°–IALCE, the dark state appears near 80% and covers more area at 85%. It can be observed that as the applied voltage during polymerization increases, the dark area still emerges; however, its uniformity gradually decreases. This phenomenon is particularly evident in the 70°–IALCE and 80°–IALCE. For the 80°–IALCE, when the dark state appears at an early stage, near 75%, and lasts until 105%. For the explanation of the non-uniformity of the dark area, besides the nonuniform distribution of the strain, another possible reason is the anisotropic deswelling of the sample during wash, mentioned in Section 6.3.2. The complicated deswelling process results in deviations of the director from the intended alignment. Consequently, the final director profile exhibits a non-uniform distribution, leading to a nonuniform distribution

of order parameter. Since phase retardance is directly related to birefringence and thickness of the sample, assuming the sample maintains a uniform thickness, the non-uniformity can contribute to distinct decreasing process of order parameters. An example helps to demonstrate this phenomenon is shown in Figure 6.13, which is a POM figure of 70°–IALCE at a strain of 85%. The non-black regions in the central area exhibit interference colors with different phase retardance.

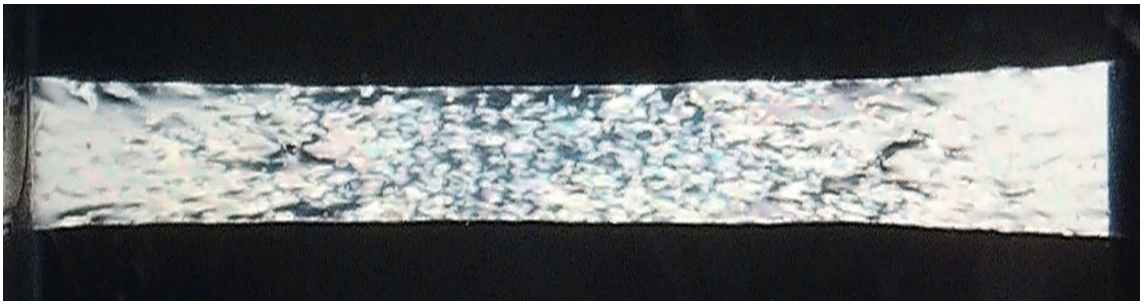

Figure 6.13 The non-uniform distribution of interference colours in non-dark regions indicates variations in the director alignment, resulting from deviations in the anticipated alignment profile during the deswelling process.

To analyse the mechanical deformation of each film in a detailed way, we measured the strain change of each film and the procedure was detailed in Section 3.3.2. Figure 6.14 (a) and (b) show the relationship of ε_y and ε_z to ε_x. The mechanical deformation of the P-LCE has been introduced in Section 5.3, and all the Fréederisksz transition aligned IALCEs exhibit analogous processes. For the deformation of all the samples in x-y plane, ε_y decreases as ε_x increases while for the deformation in x-z plane, ε_z experiences an auxetic response. During the deformation, ε_z decreases as ε_x in the beginning and then reaches the minimum near ε_{th}. Afterwards, ε_z increases with further ε_x and the thickness of the film increases towards the initial thickness. Once ε_z reaches its maximum, the thickness will saturate upon further stretching. Overall, for all these auxetic responses, the auxetic response is delayed as the voltage applied during polymerization increases, with a thinner minimum thickness near the ε_{th}. For example, the thinnest thickness of P-LCE corresponds to the thickness with a ε_z near -0.24, whereas for 60°–IALCE, it occurs with a ε_z near -0.30. Even though the thickness gradually recovers towards the initial state, for the IALCE film polymerized under higher voltages, the maximum thickness that can be approached during the auxetic response decreases as the applied voltage increases. For instance, the final thickness of P-LCE saturates at $\varepsilon_z \approx -0.10$, while the thickness of 80°–IALCE saturates at

$\varepsilon_z \approx -0.15$.

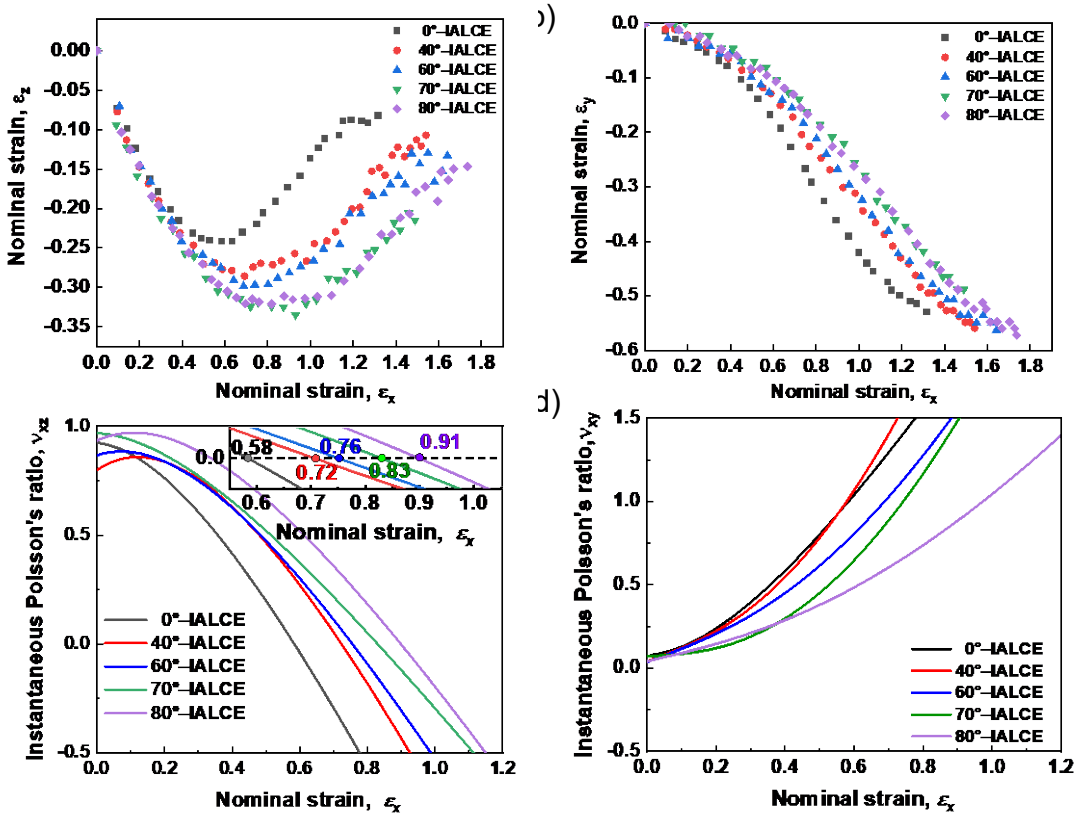

Figure 6.14 The nominal strain (a) ε_z-ε_x and (b) ε_y-ε_x measured for all the samples. The instantaneous Poisson's ratio (c) υ_{xz} and (d) υ_{xy} measured for all the samples. The inset figure in (c) zooms the cross section of each instantaneous Poisson's ratio line to the 0, indicating the strain of the V_{th}.

To further analyse the ε_{th} of each film, we calculated the Poisson's ratio ν in the x-y and x-z plane of each film during mechanical measurements and the results are shown in Figure 6.14 (c) and (d). The calculation process was described in Section 5.3. The Poisson's ratio in x-y plane, ν_{xy} is always positive during deformation, which means there is no auxetic response in the y-direction. However, in the x-z plane, there is a threshold strain beyond which the Poisson's ratio in x-y plane ν_{xz} would get negative and the whole system therefore behaves auxetic. The inset figure in Figure 6.14 (c) shows the zoomed part around the threshold strain for each film. The threshold strain of IALCEs polymerized under different voltages are shown in Table 6.3.

Table 6.3 Variation of the auxetic threshold strain with the maximum director angle, θ_{max}, determined by polymerizing the precursor mixture under different applied voltages.

Polymerization voltage, V [V_{rms}]	0.00	1.05	1.25	1.50	2.00
Maximum director angle, θ_{max} [°]	0	40	60	70	80
Auxetic threshold strain, ε_{th}	0.58±0.05	0.72±0.05	0.76±0.05	0.83±0.05	0.91±0.05

The POM figures of each IALCE film with the applied strain indicated, which is near the ε_{th}, are shown in Figure 6.15. Notably, the emergence of the black state occurs near the threshold strain as the uniaxial order parameter decreases during the progress of the mechanical deformation. It is important to clarify that while the black state, to some extent, signifies the start or progression of the auxetic response, the strain at which dark state emerges does not strictly correspond to the ε_{th} of the auxetic response. During mechanical deformation, the progression of the auxetic response is accompanied by the emergence of biaxial order, which occurs concurrently with a reduction in uniaxial order. These two processes—biaxial order emergence and uniaxial order decrease—operate in parallel. However, the decrease in uniaxial order is further modulated by external factors, such as strain distribution and the mesogenic alignment. Consequently, while the onset of an auxetic response of IALCEs is typically associated with the appearance of a black state, the strain at which the black state manifests does not strictly correlate with the ε_{th} of the auxetic response.

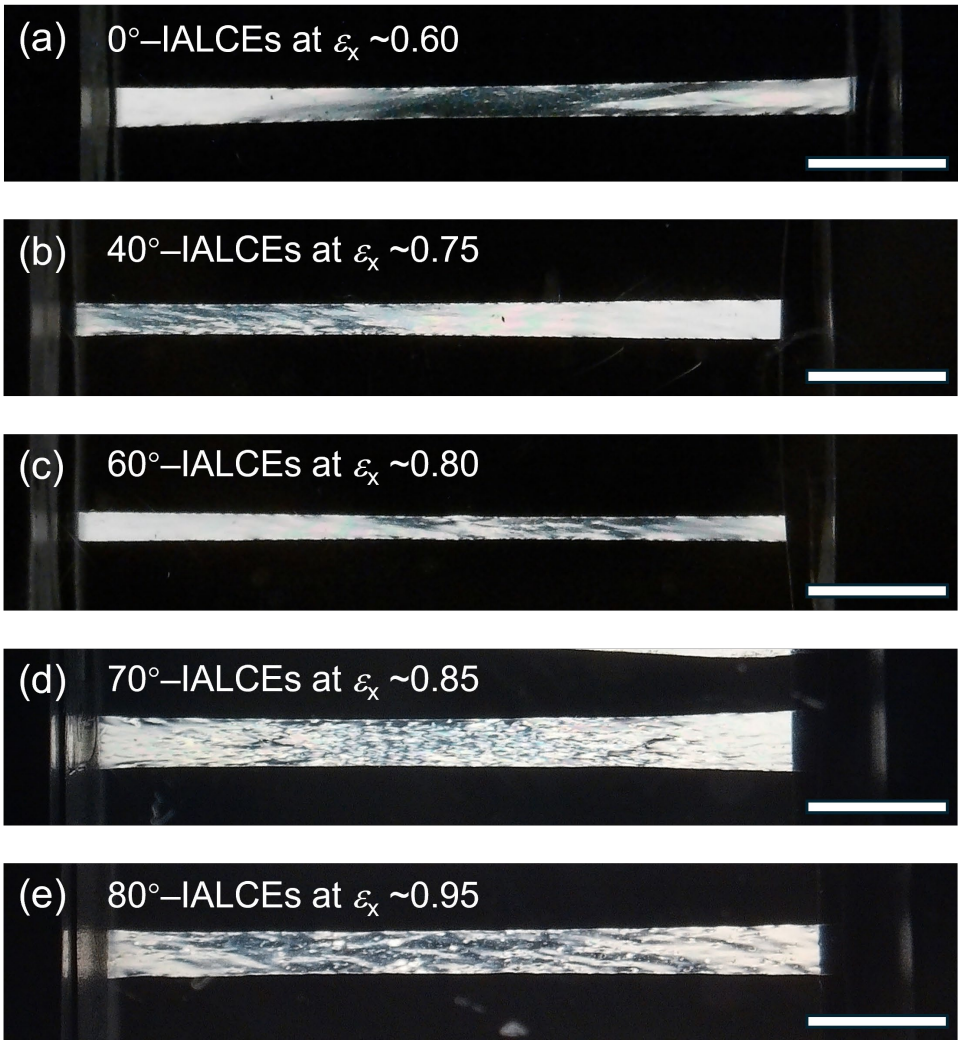

Figure 6.15 The POM figures of (1) 0°– (2) 40°–, (3) 60°– (4) 70°– and (5) 80°–IALCE with applied strains near the threshold strain. The scale bar is 1 cm.

6.3.3.b IALCE samples fabricated with 40 V_{rms}

As illustrated in **Section 6.1** and **Section 6.3.2**, the central maximum angle will first reach 88° when the V/V_{th} reaches near 3. As the applied voltage further increases, the maximum angle stays 88° while the rest mesogens will adopt the electric field alignment effect and further rorate, as the director profile shown in Figure 6.9. In addition to investigating the influence of the Fréederisksz transition alignment on the auxetic response of planar aligned IALCEs under low-voltage conditions, we extended our study to compare the IALCE with approximately homeotropic alignment induced through Fréederisksz transition alignment with H-LCE. The width-direction deformation (ε_y-ε_x) and Poisson's ratio for both H-LCEs (data from Section 5.3) and 88°–IALCEs (polymerized under 40 V_{rms}, much larger than the voltage which induces the maximum

angle just at 88°) are presented in Figure 6.16. To confirm that the alignment of the 88°–IALCE approximates to homeotropic alignment, mechanical deformation was conducted with strains applied not only parallel but also perpendicular to the director direction determined by the cell. The results show that 88°–IALCEs exhibits a nearly identical auxetic response to H-LCE. The Poisson's ratio revealed ε_{th} of 0.56 ± 0.05 (parallel strain) and 0.57 ± 0.05 (perpendicular strain) for 88°–IALCEs, almost the same as ε_{th} of H-LCE. The consistence illustrates that the 88°–IALCEs achieves approximately homeotropic alignment through the Fréederisksz transition alignment.

Overall, induced with Fréederisksz transition alignments, the ε_{th} of IALCEs was proven to be delayed to higher strain as the θ_{max} increases. By altering the applied voltages, the ε_{th} of the auxetic responses could be tuned from 0.58 ± 0.05 to 0.91 ± 0.05 within 2 V_{rms}. Further, a 40 V_{rms} could realize approximately homeotropic alignment in IALCEs, irrespective of the fact that the initial alignment of the cell used in polymerization was planar.

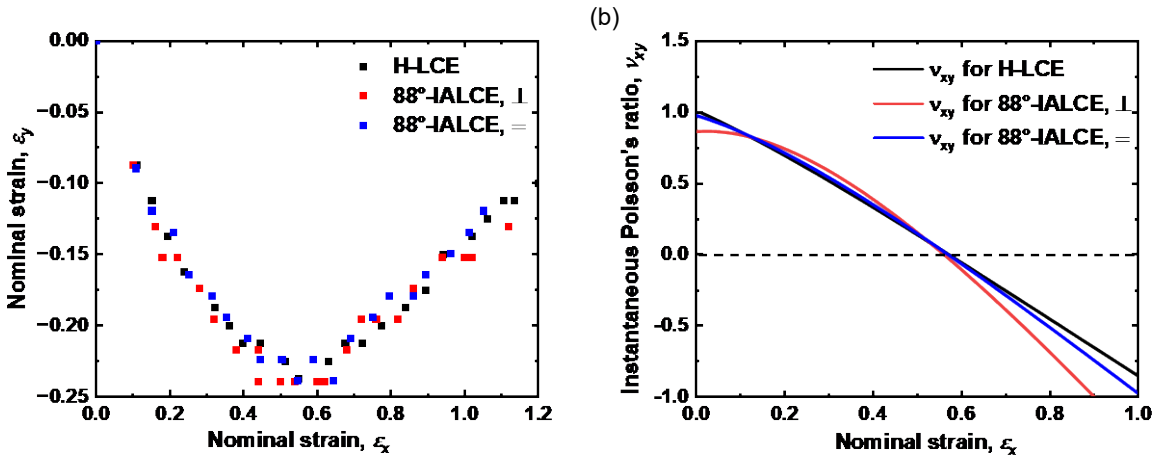

Figure 6.16 (a) The nominal strain ε_y-ε_x for H-LCE and 88°–IALCE all the samples. (b) The instantaneous Poisson's ratio υ_{xy} measured for H-LCE and 88°–IALCE. ⊥ stands for the perpendicular strain to the initial alignment direction of the cell while = represents that the strain is parallel to the initial alignment direction of the cell.

6.3.4 The glass transition temperature measurements

The introduction of the Fréedericksz transition alignment was confirmed and the tuneability of the ε_{th} in auxetic responses was illustrated. To investigate whether the change in ε_{th} of the auxetic response after introducing the Fréedericksz transition alignment is determined

solely by the alteration in the director profile, we conducted DSC measurements to determine the T_g of all samples. As discussed in Section 3.1.2, the backbone structure of IALCEs, is reflected in the T_g of the IALCE sample, and that also has been shown to significantly influence the ε_{th} of their auxetic response. By measuring T_g, we can assess whether the backbone structure of IALCEs was changed during polymerization under electric fields. The DSC measurement procedure and the analysis of DSC curve were detailed in Section 3.3.3, and measurements are presented in Figure 6.17. The measured T_g values for all samples are summarized in Table 6.4. The DSC curve of the planar aligned IALCE is as provided in Section 3.3.3. It can be observed that T_g values of all the analysed samples exhibit remarkable consistency in comparison with that of the P-LCE IALCE. The observed deviations are confined to a narrow range of ±1°C, well within the experimentally defined tolerance threshold, thereby validating the reproducibility of the thermal response across the sample set. Therefore, we conclude that the factor influencing the ε_{th} of auxetic responses is the change of the director profile, due to the introduction of the Fréedericksz transition alignment, rather than the change in the backbones.

Table 6.4 The glass transition temperature T_g of IALCE samples

Sample	T_g
P-LCE	15.8°C
40°–IALCEs	14.3°C
60°–IALCEs	16.1°C
70°–IALCEs	14.4°C
80°–IALCEs	16.5°C
H-LCE	15.0°C
40°–IALCEs	16.2°C

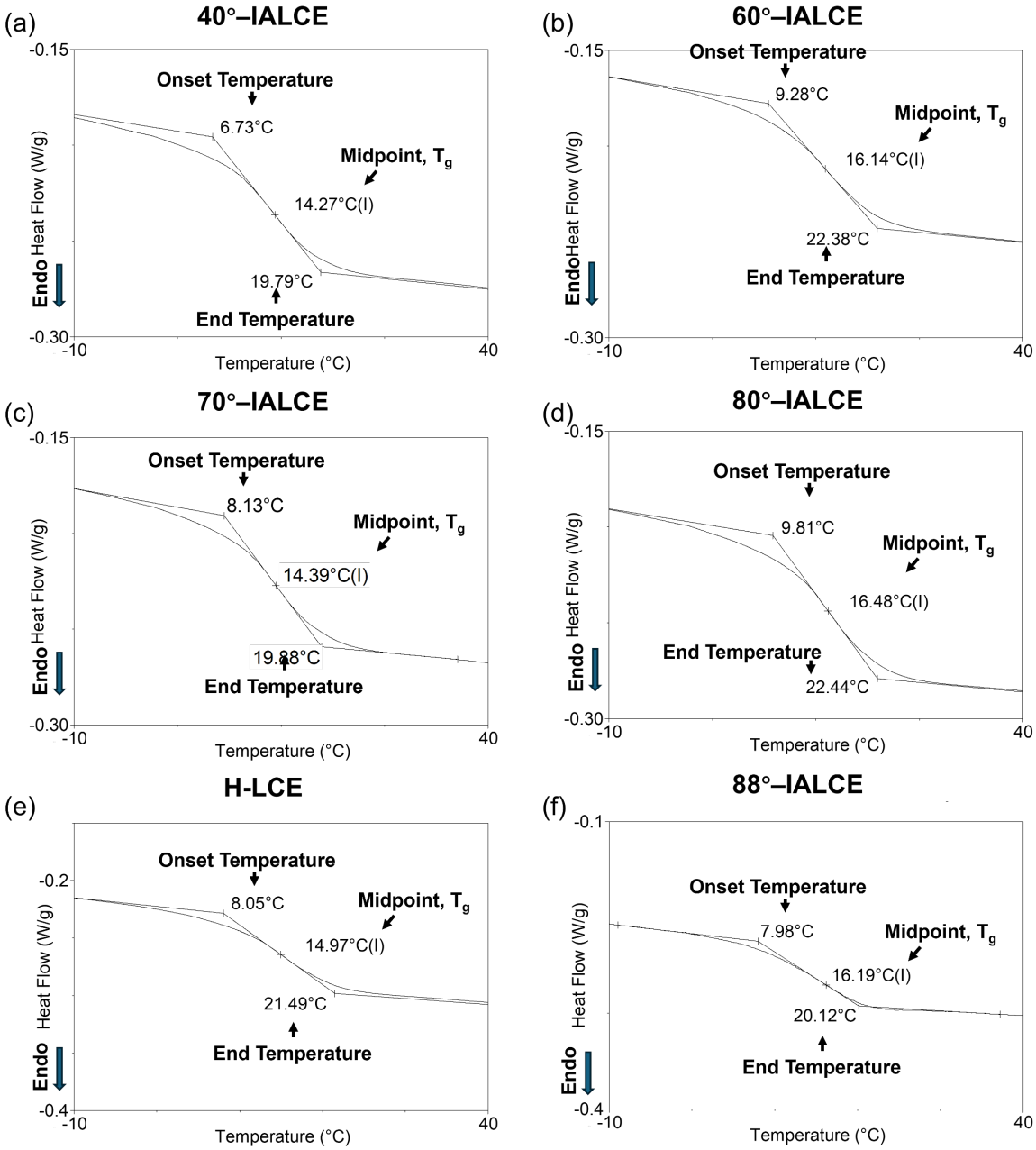

Figure 6.17 The T_g analysis through DSC measurements of (a) 40°–IALCEs, (b) 60°–IALCEs, (c) 70°–IALCEs, (d) 80°–IALCEs, (e) H-LCE and (f) 88°–IALCEs. The T_g of each sample is the midpoint temperature illustrated in each figure.

6.3.5 The stress-strain curve measurements

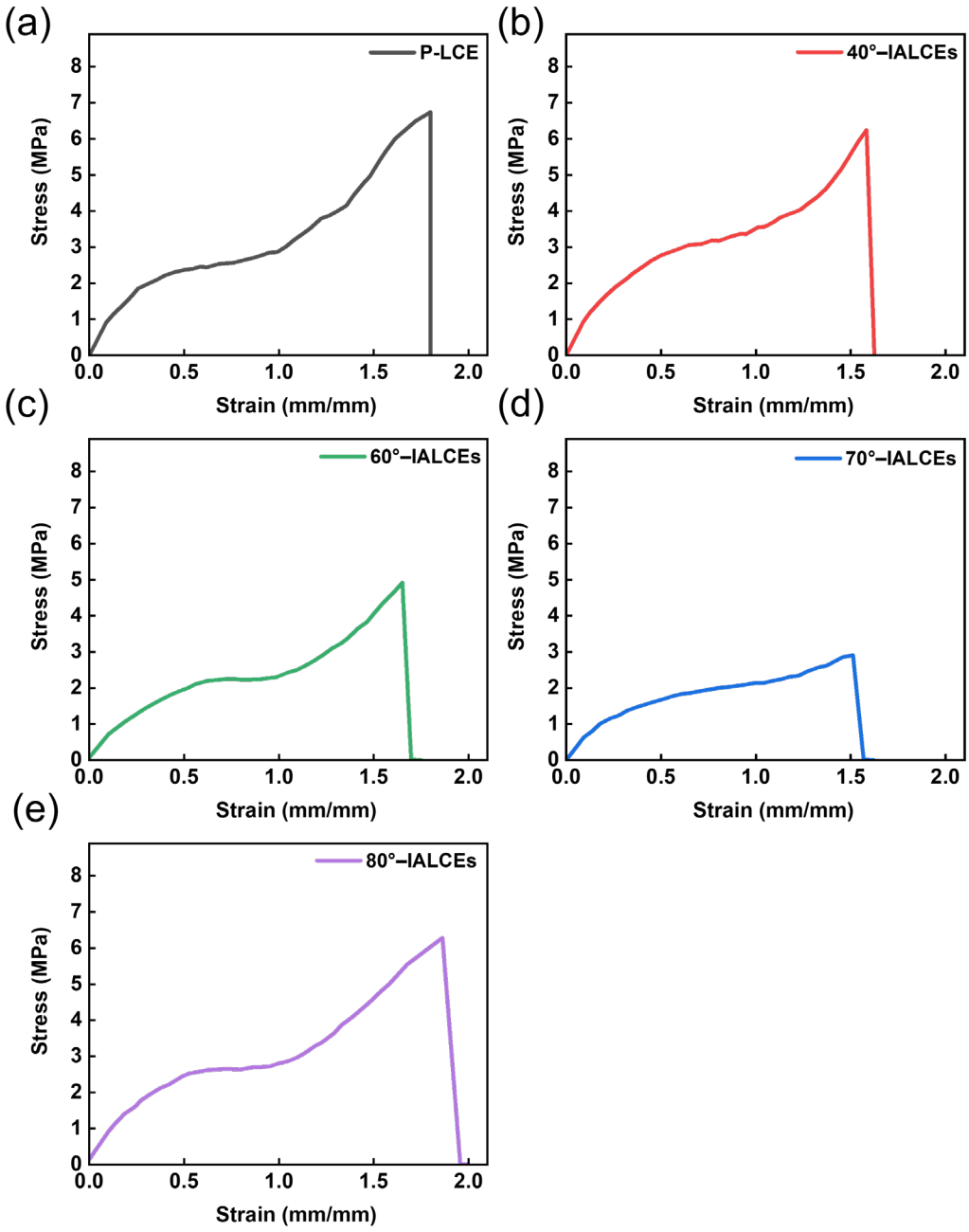

Figure 6.18 The stress-strain curves of (a) P-LCE, (b) 40°–IALCEs, (c) 60°–IALCEs, (d) 70°–IALCEs and (e) 80°–IALCEs.

The stress-strain curve measurement was conducted to verify the hyper elasticity of all the IALCE samples, as a supplementary supply to the DSC measurement, to indicate that the IALCE samples not only exhibit consistent T_g but also share the similar backbone structures. Considering the obvious tuneability of the ε_{th} in auxetic responses, we ran the test on the P-LCE and the samples polymerized under low voltages (≤ $2V_{rms}$) for comparison. The

measurement process was described in Section 3.3.2 and Figure 6.18 shows the stress-strain curve of each sample. Considering the practical variations arising from factors such as sample fabrication and sample loading, we do not conduct a direct comparison of the specific mechanical properties of the sample set. Instead, we focus on the overall performance trends of the samples. During mechanical deformation, the samples soften with increasing strain. The stress–strain curves are clearly analogous to a semi-soft elastic response. However, instead of mesogen reorientation along the strain direction, biaxial order emerges during deformation. As a result, all the samples exhibit hyper elastic behavior.

6.3.6 A simple mathematical model for explaining the tuneability of the auxetic responses

To better understand that the tuneability of the auxetic response is due to the various director profiles, a simple mathematical model is considered by Dr. Thomas Raistrick. The precursor mixture is polymerized under an applied field with the nematic director angle following the form presented in Figure 4.6. The Poisson ratio of the IALCE as a function of strain is known for the planar and homeotropic orientation and is volume conserving. The model assumes that the Poisson's ratio of LCE film with a varying director angle through the thickness can be approximated by finite slices of LCE with angles $\theta_{z/d.}$ A slice of IALCE film with a director at an angle $\theta_{z/d}$ has Poisson's ratios, ν_s , in the *z* and *y* axis in the form:

$$\nu_{s,z} = \nu_z \cos\theta_{z/d} + \nu_y \sin\theta_{z/d} \tag{6.5}$$

$$\nu_{s,y} = \nu_z \sin\theta_{z/d} + \nu_y \cos\theta_{z/d} \tag{6.6}$$

It is assumed that the bulk response of the IALCE is the sum of the finite slices in the form:

$$\nu_{b,z} = \sum_i^N \nu_{si.z} = \sum_i^N (\nu_z \cos\theta_{zi/d} + \nu_y \sin\theta_{zi/d}) \tag{6.7}$$

$$\nu_{b,y} = \sum_i^N \nu_{si.y} = \sum_i^N (\nu_z \sin\theta_{zi/d} + \nu_y \cos\theta_{zi/d}) \tag{6.8}$$

the bulk Poisson's ratio, ν_b, of the film is assumed to be the sum of the slices shown in Figure 6.19, for various θ_{max} (obtained by Dr. Thomas Raistrick). For the smaller values of θ_{max} (< 60°), there is an increase in the auxetic threshold strain, which is qualitatively similar to the experimental observations in Figure 6.14(c). However, the increase in the auxetic threshold due to the application of voltage is much greater than what is observed experimentally. Additionally for the largest θ_{max} value (80°) an auxetic response is not

predicted by the model, however, an auxetic response is observed experimentally. These two differences may be explained by a distortion of the director profile during the deswelling step, as described in Section 6.3.2.

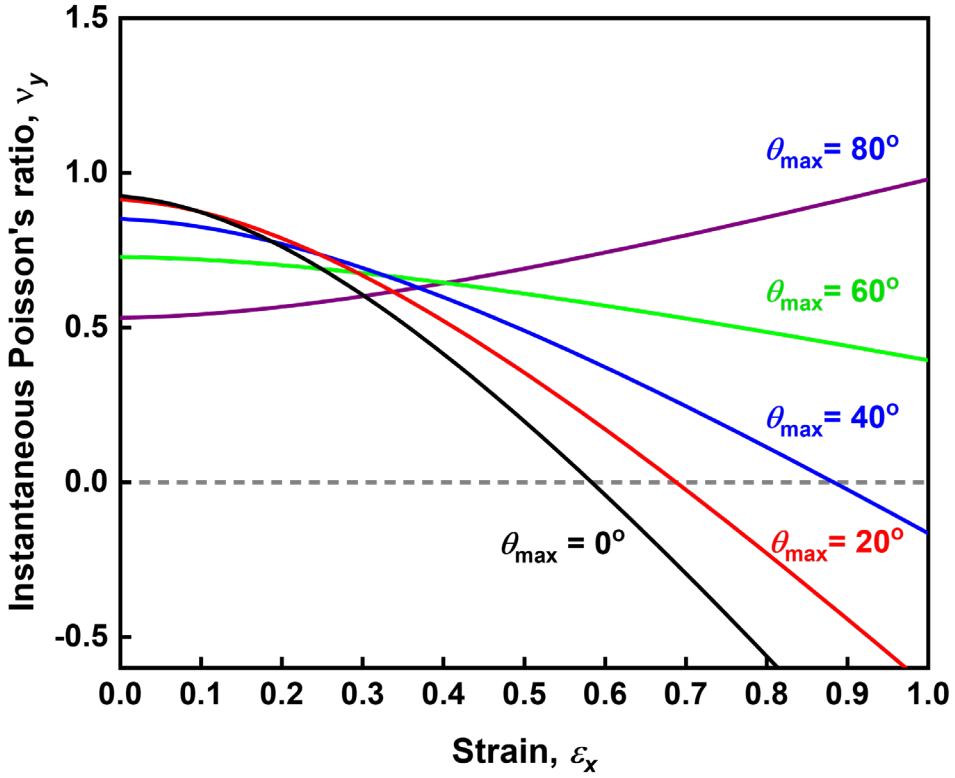

Figure 6.19 ν_y as a function of strain, ε_x. Data are produced by considering a simple model considering the director profile of a Fréedericksz cell. The IALCE is split into slices and the Poisson ratio of each slice is determined, the response of the bulk LCE is assumed to be the sum of the response of these slices. This figure is obtained by Dr. Thomas Raistrick.

6.4 Summary

In this chapter, we explored the tunability of auxetic responses in IALCEs by introducing Fréedericksz transition alignments through electric field modulated polymerization. By adjusting V, we fabricated IALCEs with distinct director profiles, exhibiting θ_{max} from 40° to 88°. Thermal deformation and birefringence measurements confirmed the successful introduction of the Fréedericksz transition alignment, showing that IALCEs with the Fréedericksz transition alignment exhibited minimized actuations due to modified order parameters. The mechanical characterization illustrated that increasing the ε_{th} was delayed as the increase of θ_{max}. A wide tuneable range of ε_{th}, from 0.58 to 0.91, can be realized by

a small voltage (≤ $2V_{rms}$). Additionally, DSC and stress-strain curve measurements confirmed consistent T_g and hyper elasticity across all samples, indicating that the tunability of the auxetic responses relied solely on the modified director profile. A simplified mathematical model further assisted in support of it.

In the next chapter, we will move on to the application of the tuneable auxetic responses. We will use the optical feature during the auxetic responses, the appearance of the dark state, to realize a multilevel information storage and encryption for 2D optical information.

References

1. Mistry, D.; Connell, S. D.; Mickthwaite, S. L.; Morgan, P. B.; Clamp, J. H.; Gleeson, H. F. Coincident molecular auxeticity and negative order parameter in a liquid crystal elastomer. *Nat. Commun.* 2018, *9*, 5095.
2. Wang, Z.; Raistrick, T.; Street, A.; Reynolds, M.; Liu, Y. J.; Gleeson, H. F. Direct observation of biaxial nematic order in auxetic liquid crystal elastomers. *Crystals* 2022, *12*, 393.
3. Raistrick, T., Zhang, Z., Mistry, D., Mattsson, J., Gleeson, H. F. Understanding the physics of the auxetic response in a liquid crystal elastomer. *Phys. Rev. Research*, 2021, *3*, 023191.
4. Mistry, D., Gleeson, H. F. Mechanical Deformations of a Liquid Crystal Elastomer at Director Angles Between 0° and 90°: Deducing an Empirical Model Encompassing Anisotropic Nonlinearity. *J. Polym. Sci. Pol. Phys.*, 2019, *57*, 1367–1377.
5. DeVore J. R. Refractive Indices of Rutile and Sphalerite. *J. Opt. Soc. Am.* 1951, *41*, 416-419.
6. Blinov, L. M., Chigrinov, V. G. Electrooptic effects in liquid crystal materials. Springer Verlag, 1994, 149.
7. Cooper, E. J.; Reynolds, M.; Raistrick, T.; Berrow, S. R.; Jull, E. I. L.; Reshetnyak, V.; Mistry, D.; Gleeson, H. F. Controlling the Optical Properties of Transparent Auxetic Liquid Crystal Elastomers. *Macromolecules* 2024, *57*, 2030−2038.

Chapter 7 Multidimensional, Multilevel Information Storage and Encryption Based on Intrinsic Auxetic Liquid Crystal Elastomers

In the previous chapter, we systematically investigated the manipulation of auxetic responses of the IALCEs through the introduction of the Fréedericksz transition alignments. We demonstrated that, through altering the V from 1.05 V_{rms} to 2.00 V_{rms}, distinct Fréedericksz transition alignments with various θ_{max} ranging from 40° to 80° were achieved and a wide tuneable range of ε_{th}, from 0.58 ± 0.05 to 0.91 ± 0.05, was obtained. Furthermore, when V reached 40 V_{rms}, an approximately homeotropic IALCE could be realized. We conducted thermal deformation and birefringence measurements to confirm the introduction of the Fréedericksz transition alignment. Moreover, the DSC and stress-strain measurements were demonstrated to show the tuneability of the auxetic responses was solely due to the modification of the director profile, with a supplementary mathematical model provided by Dr. Thomas Raistrick to help understand it.

In this chapter, building on the investigation of the tunable auxetic responses, we will shift our focus towards potential applications. Based on the distinct features of the auxetic behavior, we aim to explore and propose application scenarios where such features can be effectively leveraged. Utilizing the unique feature during auxetic responses–the appearance of the dark state and the morphology changes, we will try to realize the information encryption applications of 2D optical information and 3D tactile information based on the tuneable auxetic responses of the IALCEs. We will encrypt the optical/tactile information into IALCEs through patterned polymerization and decrypt the information by stretching the film. Through polymerization under low voltages (0.9~2.0 V_{rms}) with exposure masks, 3-level 2D optical information (in format of binary signals) and 3D tactile information (in format of Braille haptic letters) respectively are selectively stored and encrypted into IALCEs at the polymerization stage. Subsequently, the multilevel information is decrypted stage-by-stage by mechanically stretching the IALCEs to certain strains. The decryption processes of 2D and 3D information do not interfere with each other and only through applying a specific strain in a defined stretching direction is the correct information shown.

7.1 Introduction and motivation

With the booming development of information technologies, for example Artificial Intelligence (AI) technology and 5G networks, our general life has come into a prosperous information age. The rapid transmission of information has led to an increasing demand for information storage, and in the meantime, more and more people are suffering from false information and sometimes even worse, the leakage of personal information. Information storage and security are receiving tremendous attention, promoting the requirement for advanced technologies and materials for storage and encryption. In recent years, experts in different areas have made enormous efforts to explore new strategies for information storage and encryption, including metasurfaces [1–3], photonic materials [4–6], holograms [7–9] and fluorescent/phosphorescent imaging [10–13]. Through precise fabrication processes, the information is stored in systems that are designed to avoid replication. However, the information coding processes are complicated, and costly equipment is generally necessary for the complex encryption process. Therefore, it is still a challenge to achieve multidimensional, multilevel information storage and encryption (M^2ISE) with techniques that are simply manufactured and conveniently operated.

Playing a vital role as a class of polymerized soft materials which have been explored and utilized to handle the challenges aimed at M^2ISE [15–19], LCEs have also demonstrated their capabilities in the areas of information storage and encryption [20–28]. Such applications take advantage of LCE's controllable optical properties and programmable shape deformations. For instance, in 2024 Ko's group realized high-resolution, multilevel patterning and transmittance modulation for rewritable information through laser-induced dynamic crosslinking [20]. Li and his team achieved dual-mode, multilevel information encryption and real-time, rewritable information display by modifying the chemical composition of LCEs [21]. Generally, the information encryption strategy of LCEs relies on the utilization of unique anti-counterfeiting techniques[20,21,24-28] or a combination of multiple stimuli that trigger the decryption[22,23,27,28]. The strategy for accomplishing the decryption and display of information is based on the transmittance or color change of LCEs caused by 1) intrinsic phase transitions [20,21] ; 2) mesogen reorientation [24,25,28]; 3) phosphorescence/fluorescence[22,23,28] or 4) structural color change [24–27]. Storage capacity and safety have been assured through the integration of different encryption techniques and the combination of various decryption triggers.

However, the encryption processes are usually complicated and various triggers easily interfere with each other. There is still space and opportunity for implementing easily fabricated and conveniently operated LCEs to realize M^2ISE.

In addition to their optical properties, it is worth noting that the programmable stimulus-responsive deformations of LCEs could expand the modes of information storage from 2D to 3D, the latter of which could be stored as tactile information [29-32]. Nowadays, the widely used tactile displays are pin type displays which convey textual information to visually impaired people by expressing 2.5D information [29–35]. These refreshable and height adjustable displays are generally rigid and require bulky hardware comprised of a mechanical driver and actual moving parts. Polymerized soft materials, with reversible stimulus-responsive deformations have proposed new strategies for making the flexible actuator-based tactile displays [36–37]. For example, Hwang *et al.* have made tactile displays assembled using a bilayer poly(*tert*-butyl acrylate) (P*t*BA)-PDMS polymer and a near-infra-red light-emitting diode array. The pneumatic pressure on each pixel is generated by a photothermal actuation, to realize a reversible and height-adjustable topological expression [36]. The programmable properties of LCEs show promise in helping tactile displays get rid of their clumsy mechanical drivers and several notable attempts have been made. Torras *et al.* fabricated a tactile display array by assembling micro-LCE-pillars in 2013 [31]. Their thermally-actuated LCE array demonstrated the feasibility of LCE-based tactile displays. In 2023, Terentjev's group synthesized a LCE with millimetre-scale protruding features and realized a complete Braille dynamic display [32]. Presently, LCEs still have great potential to be tapped and developed in the aspect of multilevel tactile information storage and encryption.

7.2 Experimental details

7.2.1 The Fabrication of 2D optical M^2ISE IALCE

The fabrication process is quite similar to the fabrication of general IALCEs, and the only difference is the mask involved in the polymerization process. After capillary filling the precursor into the cell and leaving the sample to room temperature to achieve good, homogeneous alignment, an exposure mask with a 3×3 array of transparent 'holes' was used to coding the binary signal into the IALCE. The pixel of the exposure array was in a 3 mm × 1.5 mm ellipse shape. According to Berrow *et al.* [39], the polymerization process

would be completed using a 365 nm UV light at 2.5 mW/cm^2 in 15min. For the first round of information coding, the corresponding exposure areas were polymerized under 0 V_{rms} with a 365 nm UV light at 10 mW/cm^2 for 10min, ensuring the full polymerization of the coded area. After the first-round coding, the cell was heated to 50 °C, held for 5min and then left at room temperature again so that the nematic phase aligns. The second and third round of coding information repeat the same process as the first round but now the exposure areas were switched at a voltage of 1.05 V_{rms} for the second round and 1.50 V_{rms} for the third round. After the final round, the cell was heated to 50 °C and fully polymerized with a 365 nm UV light at 10 mW/cm^2 for 20 min. Finally, the film is peeled off and washed with a DCM solution (30% in methanol).

7.2.2 The Fabrication of 3D tactile M^{2}ISE IALCE.

For the coding of the tactile information, each film stands for a separated haptic pixel. All the coding process utilized the same exposure mask, and the exposure region was in an 8 mm × 5 mm ellipse shape. The tactile information was coded by polymerizing the exposure area under 0 V_{rms}, 1.25 V_{rms} and 1.50 V_{rms}, separately, with a 365 nm UV light at 10 mW/cm^2 for 10min, and after coding, the cell was heated to 50 °C and the remaining area was fully polymerized in the isotropic phase, using 365 nm UV light at 10 mW/cm^2 for 20min. Finally, after the film was removed from the cell and the 6OCB washed away by DCM solution (30% in methanol), the tactile film was ready to be used.

7.2.3 Surface Morphology Measurement

The surface morphology of demonstration film for tactile information was measured by a laser scanning microscope (VK-X1000, Keyence Pte. Ltd., Singapore). The instantaneous laser scanning figures were obtained with a 10X objective lens. When all the samples were stretched and strain released, the 10X objective lens would be used to scan across the surface of each film pixel-by-pixel with a resolution of 2 × 2 mm^2. The resolution of topological profile measurement is about 0.1 mm. The topological profile was analyzed with software “Anytest”.

7.3 Results and discussion

7.3.1 IALCEs for 2D Optical M^2ISE

7.3.1.a The Encryption and Decryption Design

The foundation of using IALCEs as a M^2ISE material for 2D optical information is based on the phenomenon that the IALCE film exhibits a dark state under crossed polarizers close to the auxetic threshold strain, shown schematically in Figure 7.1 (a) and seen directly in Figure 6.15. Furthermore, by controlling the voltage during polymerization, we can regulate the auxetic threshold strain, leading to a clear relationship between the voltage applied during polymerization and the strain when the dark state appears, as shown in Figure 7.1 (b). Each optional voltage represents a level of storage and encryption of information, and the order of the encryption levels is arranged according to the voltage. Through polymerization under applied voltages in the presence of specific exposure masks, we fabricated a M^2ISE IALCE demonstration of three-level information storage and encryption in the form of patterns that can be switched between black and white under crossed polarizers. Only a single set of electrodes was used to control the voltage applied on the whole precursor during polymerizations, and the pixelated patterned polymerization or fully curing was realized by using exposure masks. In the final decryption process, by stretching the sample, the corresponding optical information will be displayed in black under crossed polarizers at the corresponding strain. The encryption and decryption design for 2D optical M2ISE IALCEs is detailed in Figure 7.1 (c) and (d), separately.

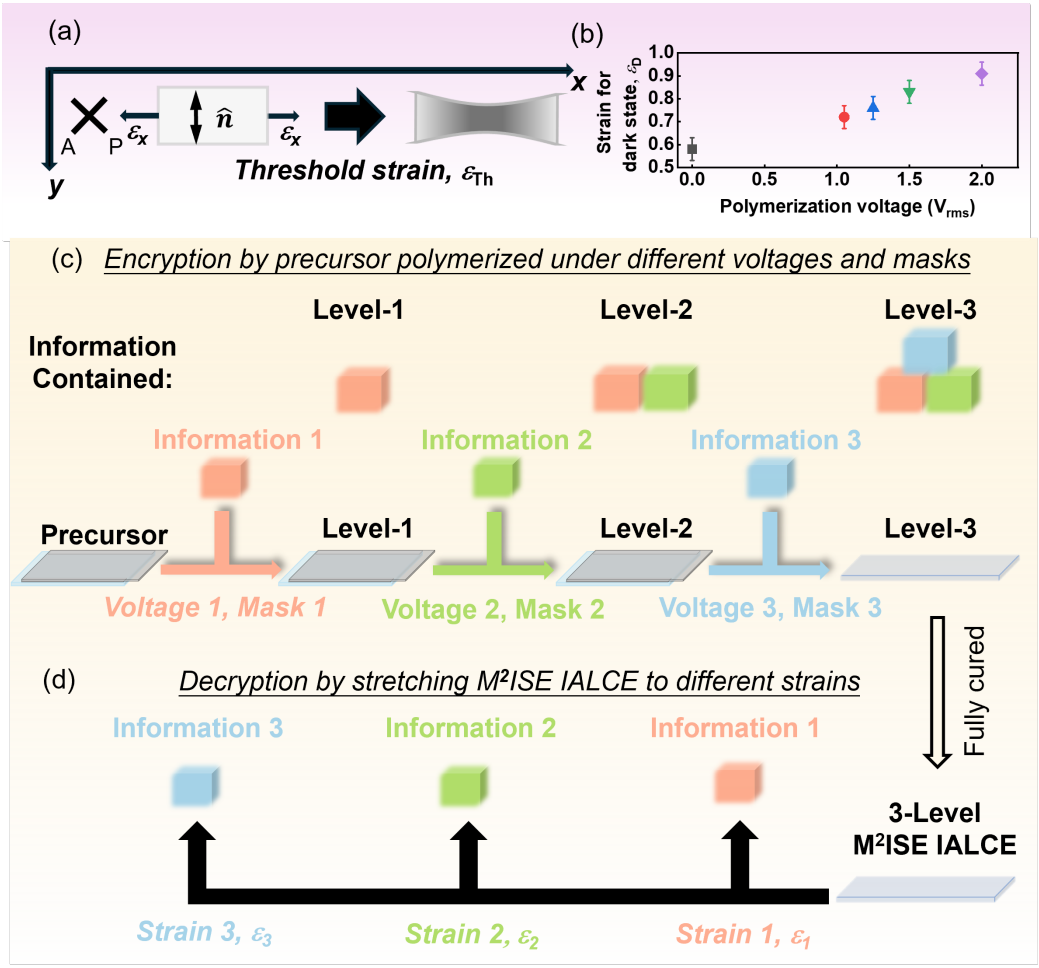

Figure 7.1 The encryption design for 2D optical M²ISE IALCEs. (a) The concept diagram showing the optical state change of IALCEs close to the auxetic threshold strain under crossed polarizers. The director is at 45° to the crossed polarizers and the tensile strain is applied along the x-direction. (b) The strains that are necessary to promote the dark state, ε_D, for the various polymerization voltages in the IALCE precursor. (c) The encryption design for 2D optical M²ISE IALCEs. The polymerization is carried out for specific areas of the film exposed by the mask, with different voltages applied sequentially, allowing information 1 to 3 to be coded into the precursor in optical format. The upper part shows the information contained for each level. (d) The decryption design for 2D optical M²ISE IALCEs. During the decryption process of the 2D optical M²ISE IALCEs, sequential information was decrypted by stretching the 3-level M²ISE IALCEs to different strains.

7.3.1.b Fabrication and Characterization of 2D Optical M²ISE IALCEs

As a proof-of-concept experiment, we fabricated a 3-level optical information storage and

encryption IALCE sample. The three pieces of optical information to be encrypted are shown in Figure 7.2(a). In this demonstrator, to improve the information density of the encrypted information and make full use of the black-and-white switching characteristics under crossed polarizers, we encrypted the complex information in the form of a matrix binary signal. The information content is shown in Figure 7.2(a), information 1 represents binary information (000 100 110), information 2 represents binary information (011 001 000) and information 3 represents binary information (100 010 001). Based on the previously described properties of the information displayed in black under crossed polarizers, we reversely designed the masks as shown in the lower part of Figure 7.2(a). Masks 1, 2 and 3 correspond to the exposure mask used when binary information 1, 2 and 3 are coded. The preparation process is shown in Figure 7.2(b), and the detailed process is in the experimental section. As for the voltage choice, we use voltage 0 V_{rms}, 1.05 V_{rms} and 1.50 V_{rms} for the 3-level information encryption. The deswelling of the isotropic region is a dimensional contraction of ~25% in all directions. As a result, to ensure a uniform shape of the patterned area after washing and to prevent defects at the interface between the patterned and isotropic regions, the patterned region is designed with a width-to-length ratio of ~3:2.

By design, binary information 1 was encoded under 0 V_{rms}, so during the decryption display process, the binary information (000 100 110) would be shown at a strain of ~0.58 ± 0.05. Binary information 2 was encoded under 1.05 V_{rms} which means the binary information (011 001 000) will be displayed at a strain of ~0.72 ± 0.05. Binary information 3 was encoded under 1.50 V_{rms}, so binary information (100 010 001) will be displayed at a strain of ~0.83 ± 0.05. The main body of the 2D optical M^2ISE IALCE sample is synthesized with the precursor in the isotropic phase.[38]

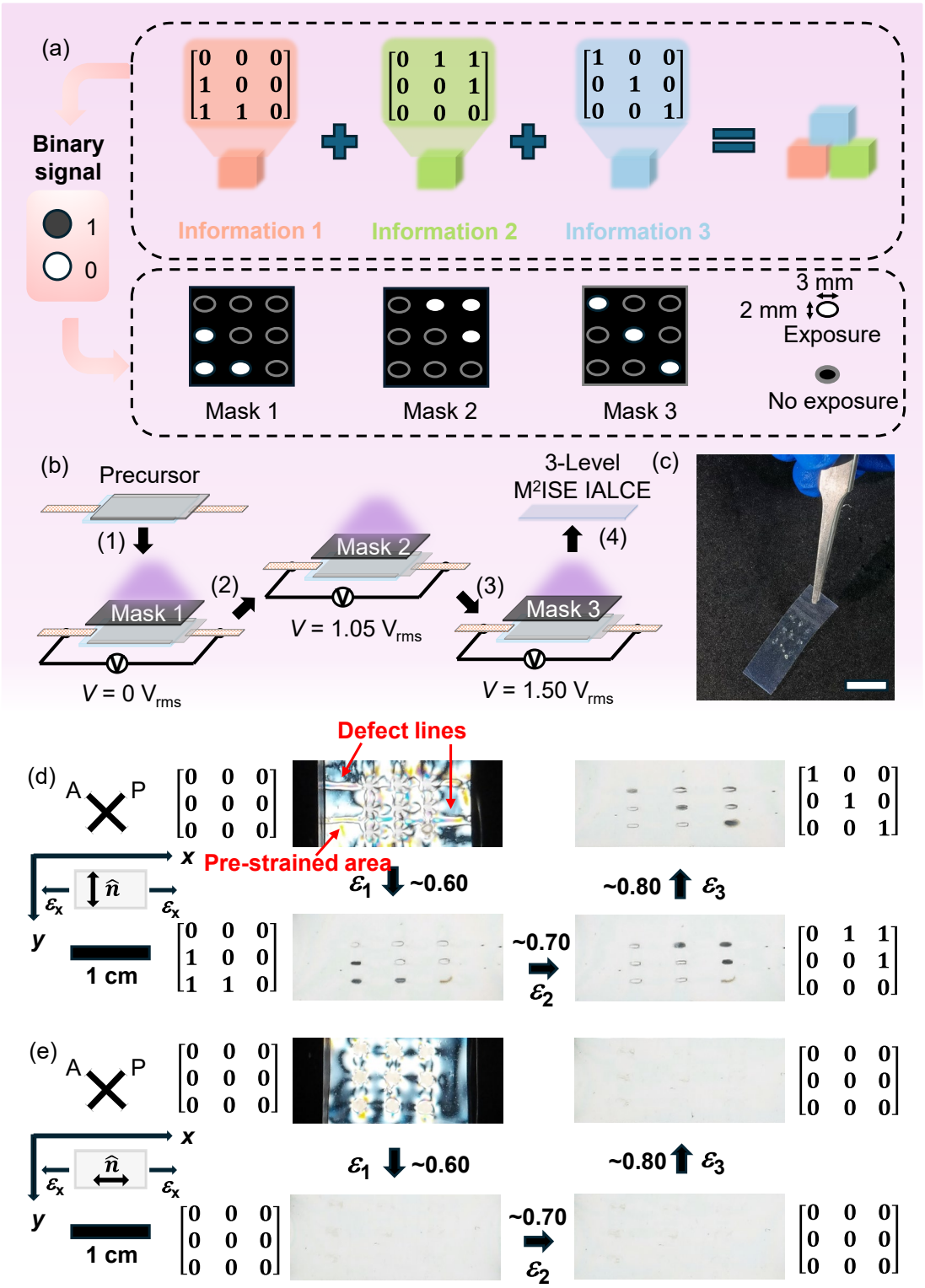

Figure 7.2 (a) Based on optical information in the format of a binary signal, the three-level information is inversely designed into three masks. For the binary signal, black represents "1" while white represents "0". In the exposure mask, each pixel is a 3 mm × 2 mm ellipse shape and for each level, the areas are exposed to be coded as a binary signal "1". (b) The sample fabrication process for 2D optical M²ISE IALCEs. (1) The precursor is

exposed with mask 1 under 0 V_{rms} for the first level coding, then the sample is heated to 50 °C and cooled to room temperature again to ensure high-quality liquid crystal alignment. (2) The sample is subsequently polymerized with mask 2 with 1.05 V_{rms} applied, for the second level coding. The process is then repeated until (3) when the last level information is encoded with mask 3 and 1.50 V_{rms}. (4) After all the information is coded, the sample is heated to 50 °C and then fully cured with the unpolymerized part in an isotropic state, without masks and voltages. Followed by being washed in DCM solutions, the 2D optical M^2ISE IALCE is prepared. (c) The real image of the 2D optical M^2ISE IALCEs sample under white light. The scale bar is 1 cm. (d) The decryption process of the 2D optical M^2ISE IALCEs with initial director direction at 45° to the crossed polarizers and perpendicular to the strain, ε_x. When stretched to ε_1 ~0.60, the first level binary information (000 100 110) is shown in dark state. Then, with further stretch, the second level binary information (011 001 000) is shown at ε_2 ~0.70. The last level binary information (100 010 001) appears at strain ε_3 ~0.80. (e) The security guarantee of the information. By stretching the sample with the initial director at 45° to the crossed polarizers and parallel to the strain, ε_x, no information will be shown during the stretching process.

During the stretching process, the isotropic mesogenic groups become oriented along the stretching direction [14] and since the stretching direction was 45° to the crossed polarizers, the main body of the film always appeared bright under crossed polarizers, improving the contrast and offering a better display of the decrypted information. The mechanical behavior of the isotropic sample, which is chemically identical to the IALCE used for encryption, is shown in Figure 7.3 and the mechanical deformation process is shown in Figure 7.4.

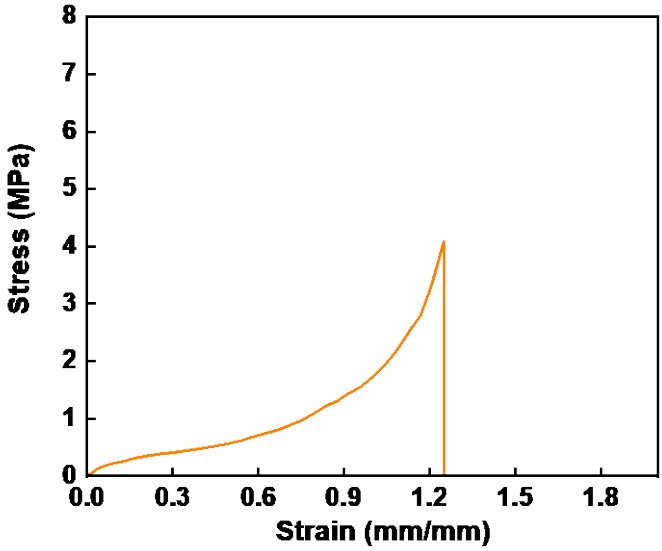

Figure 7.3 The stress-strain curve of the isotropic IALCE sample.

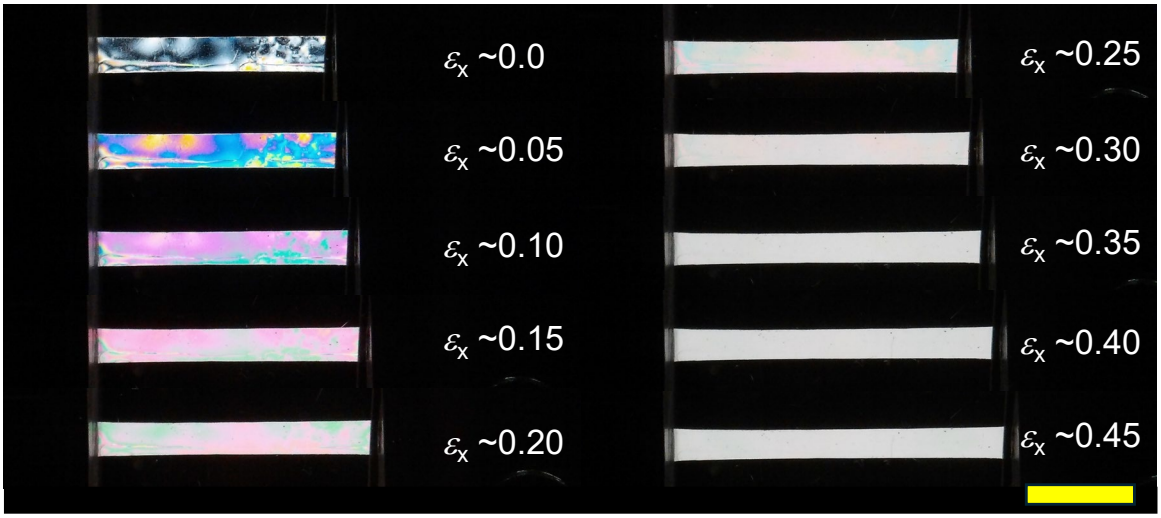

Figure 7.4 The mechanical deformation process of isotropic IALCE sample. When strain is beyond 0.45, the sample keeps bright state with no colours. The scale bar is 1cm.

The actual image of the 2D optical M²ISE IALCE sample is shown in Figure 7.2(c). Figure 7.2(d) shows the decryption process of the 2D optical M²ISE IALCE film under crossed polarizers after all the information is fully coded and encrypted. The whole decryption process is shown in Figure 7.5. The initial director direction and the stretching direction are demonstrated in the schematic figure shown on the left part, with the initial director at 45° to the crossed polarizers and perpendicular to the strain, ε_x. For the unstretched sample, there is no information shown. The coded parts are bright while the

main body stays in a dark state. The defect lines and partial bright state in the main body, indicated in Figure 7.2(d), are due to pre-strain and anisotropic deswelling during the fabrication process, which will not affect the decryption process. When the sample is strained to ~ 0.60, the first level of information is decrypted and binary information 1 (000 100 110) is displayed in black format in the coded area. Upon straining to ~0.70, binary information 1 is hidden again as the strain is beyond the threshold strain of 0 V_{rms}-IALCEs while the binary information 2 (011 001 000) appears. At the strain ~0.80, the last level of encrypted binary information (100 010 001) is shown while all other information is hidden. The whole decryption process is consistent with our design.

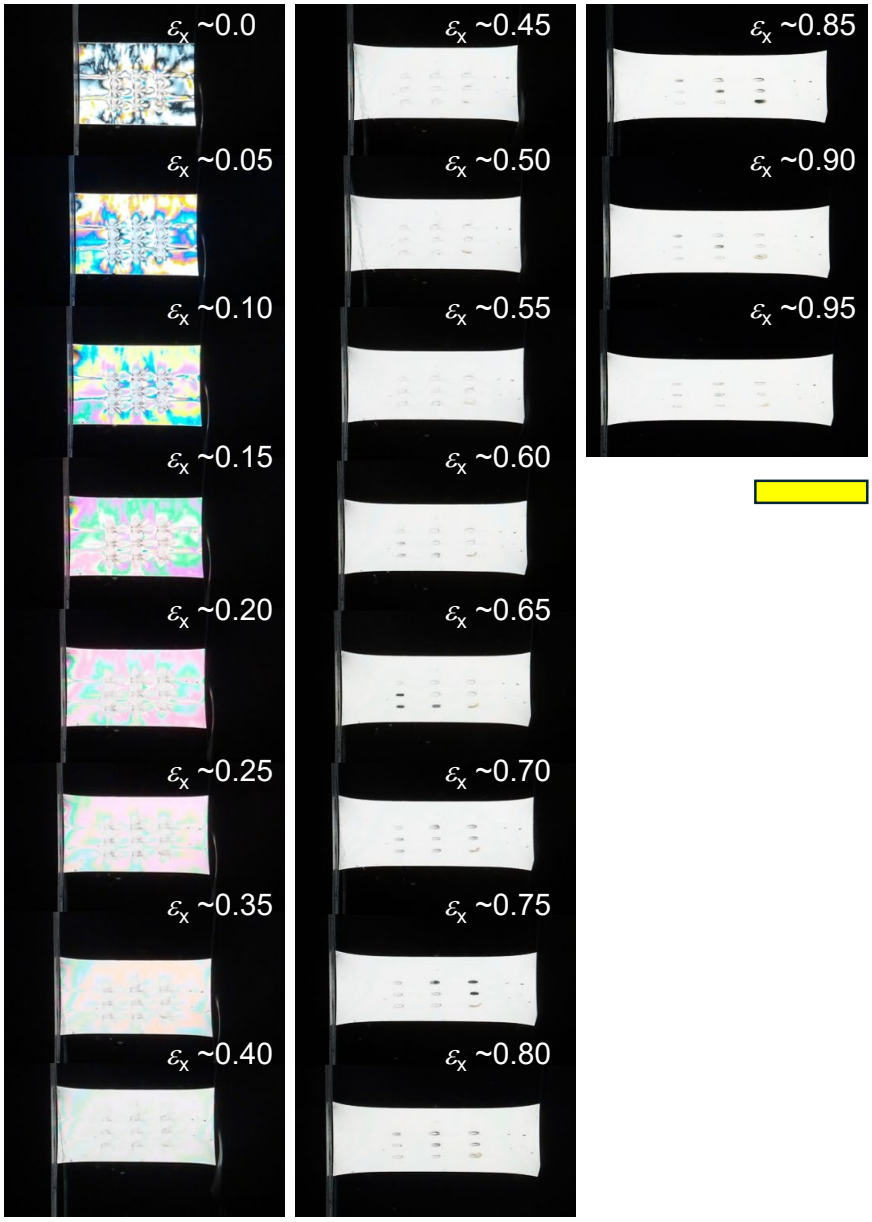

Figure 7.5 The whole decryption process of the 2D optical information under crossed polarisers. The strain is applied perpendicularly to the initial director. The scale bar is 2cm.

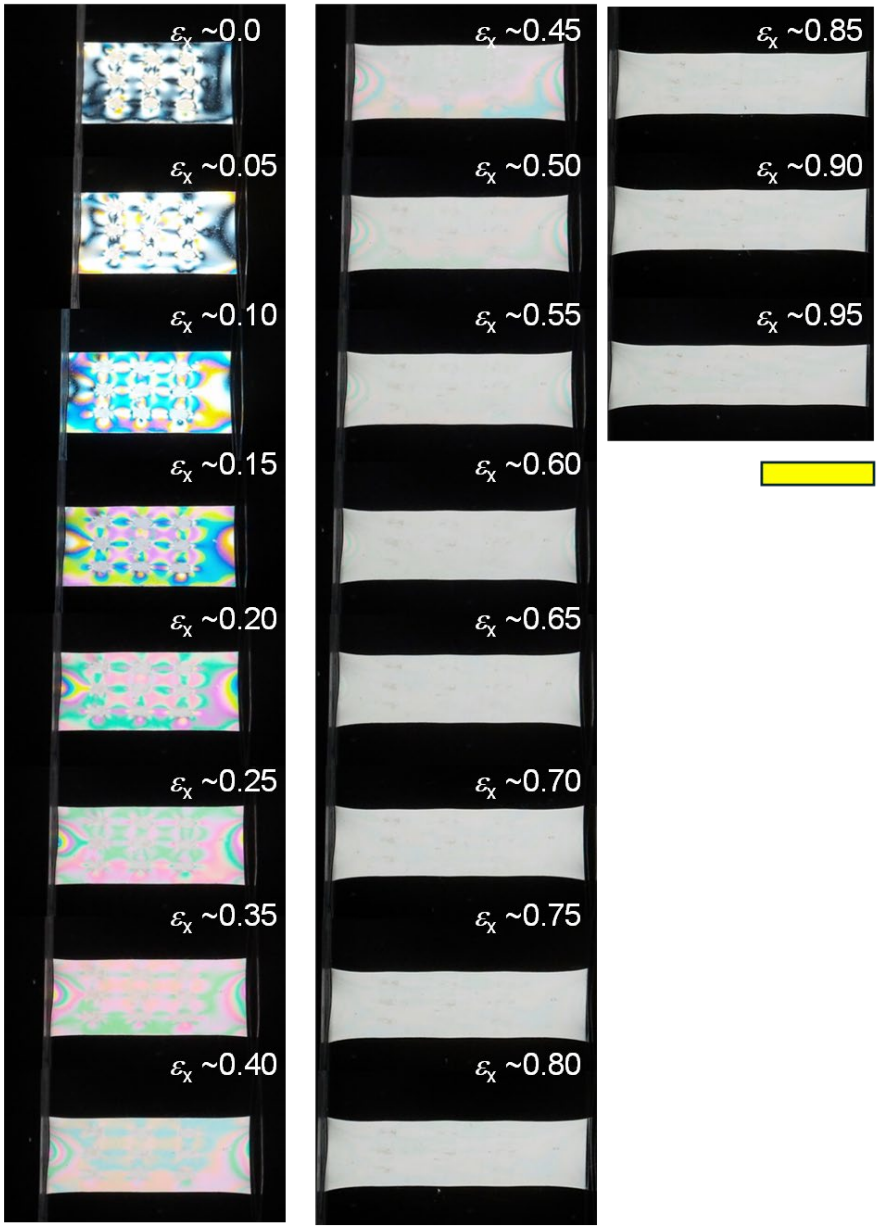

Figure 7.6 The mechanical process under crossed polarisers for demonstrating the information security. The strain is applied parallelly to the initial director The scale bar is 2cm.

In this system, the security of encrypted information is guaranteed, because in the process of information decryption, not only the strain but also the stretching direction are vital decryption elements. In the deformation process of IALCEs, the stretching direction must be perpendicular to the initial director's direction to achieve the specific auxetic response. Therefore, in this system, only by stretching the M²ISE IALCE sample to a fixed strain in a specific stretching direction can achieve complete information decryption. This feature offers significant security of the stored information. As a proof-of-concept

experiment, as shown in Figure 7.2(e), we prepared new samples with the same procedures and stretched the sample in the direction parallel to the initial director's direction; no optical information appeared during the entire stretching process. The whole process is shown Figure 7.6.

7.3.2 IALCEs for 3D Tactile M^{2}ISE

7.3.2.a The Encryption and Decryption Design

The auxetic response of a uniform monodomain IALCE film is shown in Figure 7.7(a)(1). For such a film, the auxetic response is a macroscopically uniform change in thickness. By patterning different areas in the sample with a chosen applied voltage, we can achieve height controllable surface morphology fluctuations, as shown in Figure 7.7(a) (2). Through polymerization in the presence of a voltage, with selected exposure masks, tactile information is coded into two adjacent areas to have different auxetic responses. Height-controllable surface protrusions will emerge throughout the stretching process because of the anisotropic thickness change between the distinct alignment areas and the shear tension generated between different parts of the sample. On the basis of the emergence of protrusions, we could realize the tactile information in format of Braille haptic letters. A Braille haptic letter is generally a set of cylinders with a diameter of ~1.4 mm and a height of ~0.5 mm.[32] The IALCE sample was synthesized in a thickness of 100 μm, which was significantly thinner than the height of a unit in a Braille haptic letter. However, our previous study has demonstrated that the PET-RAFT polymerization can increase the sample thickness without altering its auxetic properties.[39] Here, we primarily demonstrate the height-tunable protrusions to present in the form of Braille haptic letters to illustrate the feasibility of using IALCEs for applications in height-tunable haptic displays. It is worth noting that since the intrinsic auxetic response of this material system is based on molecular reorientation on the microscopical level, the macroscopic change will reflect in the overall thickness change, in other words, the same tactile information will appear simultaneously on both sides of the sample along the auxetic response direction. This feature can enhance the storage capacity of IALCEs in haptic information applications through vertical flipping and shape symmetry, which will be further discussed later in the text. To increase the display contrast of tactile information and better control the height of surface protrusions, we use an isotropic LCE without an auxetic response as the main body

of the tactile display sample, and nematic IALCE with controllable auxetic response as the information carrier part to realize the surface protrusions.

By choosing appropriate polymerization voltages for the tactile information carrier region, we can achieve height controllable multi-level tactile information storage and encryption. As shown in Figure 7.7(b), here we take a three-level information storage and encryption IALCE sample as an example. As the polymerization voltage increases, the auxetic response of the tactile information carrier region becomes more and more delayed (in terms of strain) as the threshold strain of the auxetic response becomes larger and larger. We define the polymerization voltages as V_1, V_2 and V_3 ($V_1 < V_2 < V_3$), and the corresponding auxetic response thresholds are ε_{V1}, ε_{V2} and ε_{V3}. During the decryption process, when $\varepsilon_{V1} < \varepsilon < \varepsilon_{V2}$, the information carrier region polymerized under V_1 first undergoes an auxetic response and forms a surface protrusion (height is h_1). The protrusions formed at this strain are the decryption display of the tactile information for the first level. When $\varepsilon_{V2} < \varepsilon < \varepsilon_{V3}$, the information carrier region polymerized under V_2 undergoes auxetic response and forms new protrusions (height is h_2). In the meantime, with the further increase of the strain since first level decryption, the tactile information carrier polymerized under V_1 continues to behave auxetically and gets thicker. These thicker protrusions together with the newly generated protrusions constitute the decryption display of the tactile information for the second level. When $\varepsilon_{V3} < \varepsilon$, similarly, the latest protrusions and the part of the tactile information carrier regions polymerized under V_1 and V_2 together constitute the decryption display of the tactile information for the third level. Each IALCE film was coded with only one tactile information, so after coding the tactile information into the IALCE films, the final step in the entire encryption process is to arrange the films containing different tactile information in a matrix according to the required order to achieve the desired decrypted display of the multi-level Braille haptic information.

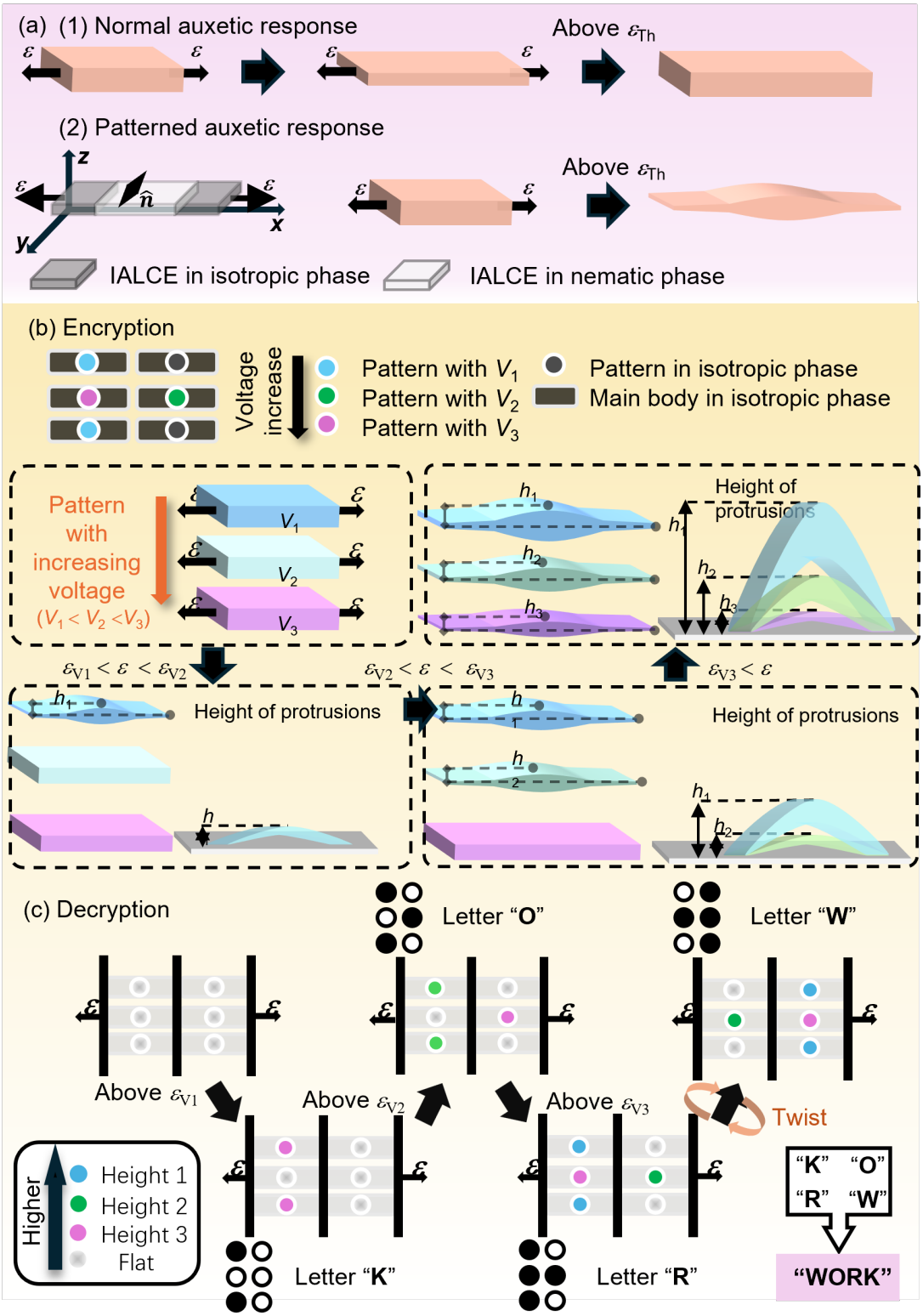

Figure 7.7 (a) The morphology changes of (1) uniform IALCEs and patterned IALCEs with schematics of their auxetic response. The isotropic phase is used to help emphasise the protrusion on the surface. The (b) encryption and (c) decryption designs for 3D tactile M^{2}ISE IALCEs. By arranging the patterned 3D tactile M^{2}ISE IALCEs patterned with 3

voltages, we can realize the Braille haptic letters “K”, “O”, “W” and “R” sequentially in through a single stretching cycle.

The design whereby information is conveyed by assembling single strips of 3D tactile M^{2}ISE IACLE film enriches the tactile information that IALCEs can convey and demonstrates that IALCEs have the capability to handle complex haptic information requirements in practical applications. All it takes to implement this function is simply taking out the corresponding tactile information film from the 3D tactile M^{2}ISE IALCEs basement and assembling it in a certain order. For convincing, the decryption process of the tactile information encrypted in Figure 7.7(b) is shown in Figure 7.7(c), as an example. During stretching, the encrypted Braille haptic letters “K”, “O”, “R” and “W” are revealed through the protrusions shown in order. Interestingly, the letters “R” and “W” are displayed simultaneously on the front and back sides of the film at the same information level. This feature originates from the intrinsic nature of the material's auxetic response and the symmetry of these particular Braille haptic letters, and further demonstrates the diversity of information that can be conveyed by this application.

7.3.2.b Fabrication and Characterization of 3D Tactile M^{2}ISE IALCEs

As a proof-of-concept experiment, we fabricated a group of 3D tactile M^{2}ISE IALCEs. To achieve better control over the height of surface protrusions, we first prepared an isotropic IALCE sample, which phase was subsequently used as the main body of the strips to generate shear tension. The mechanical deformation characterization of the isotropic sample, along with a comparative analysis with anisotropic IALCE samples, is presented in Figure 7.8. Due to the hyper elasticity of anisotropic IALCEs, during the initial stages of mechanical deformation, the reduction in thickness of isotropic samples occurs more gradually compared to anisotropic samples, while the reduction in width is faster in isotropic samples than that in anisotropic samples. Once the anisotropic samples begin to exhibit an auxetic response, the isotropic sample becomes thinner than the anisotropic samples, ensuring the formation of surface protrusions. To ensure a sufficient strain range at each step for the accumulation of the auxetic response, allowing for effective tactile information display, and to guarantee that there is enough tactile information visible prior to 100% strains, we use voltages of 0 V_{rms}, 1.25 V_{rms} and 1.50 V_{rms} as V_1, V_2 and V_3 mentioned in the encryption design for the 3-level 3D tactile information encryption. The corresponding strains ε_{V1}, ε_{V2} and ε_{V3} are ~0.58 ± 0.05，~0.76 ± 0.05 and ~0.83 ± 0.05, separately.

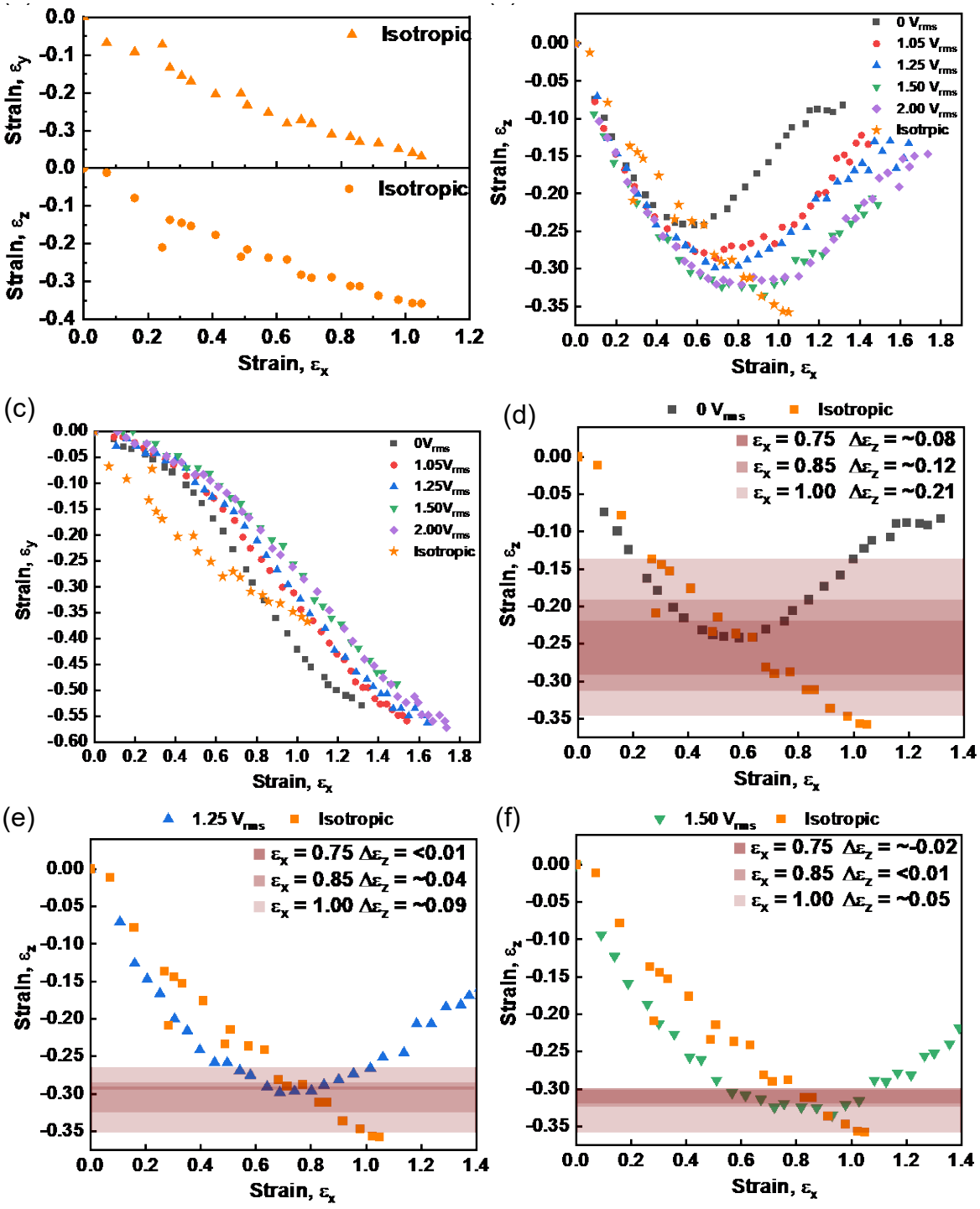

Figure 7.8 (a) The mechanical deformation measurement of the isotropic IALCE sample. The comparison of mechanical deformation between isotropic IALCE samples and anisotropic samples in (b) z-axis and (c) y-axis. The strain difference in z-axis ($\Delta\varepsilon_z$) at strain of 0.75, 0.85 and 1.00 between isotropic IALCEs and samples polymerized under (d) 0 V_{rms}, (e) 1.25 V_{rms} and (f) 1.50 V_{rms}.

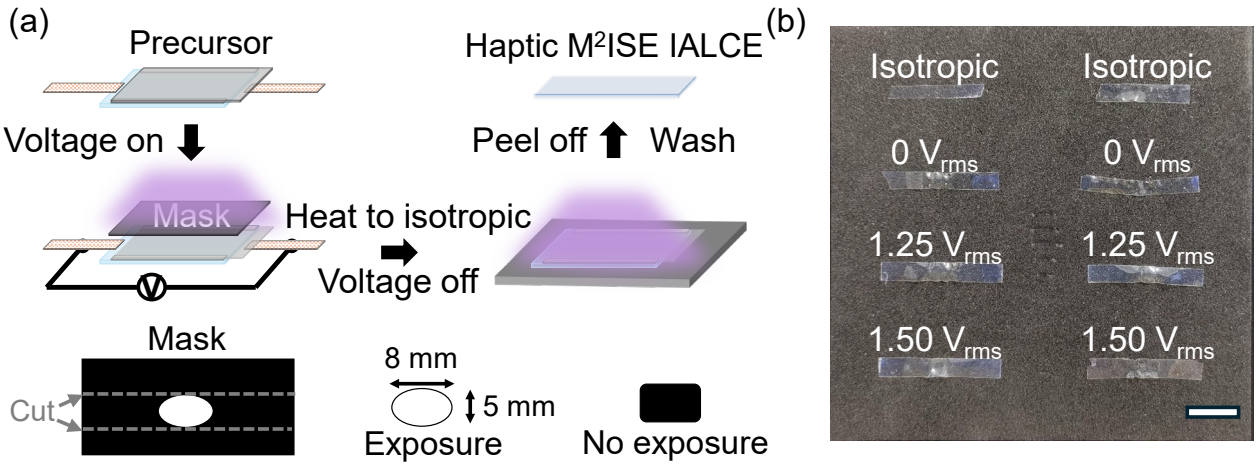

Figure 7.9 (a) The fabrication process of a single 3D tactile M2ISE IALCE film. The precursor is polymerized with an exposure mask defining the required pattern under chosen voltages and finally the remaining areas are polymerized in the isotropic phase. After peeling the film off the substrates and washing in DCM to remove unreacted elements of the precursor mixture, the single 3D tactile M2ISE IALCE film is prepared. The exposure area in the mask is an 8 mm × 5 mm ellipse shape . The isotropic regions next to the patterned area along the director were cut to reduce unflattens caused by anisotropic deswelling during the wash process. (b) The real image of the 3D tactile M2ISE IALCE films library, including 4 pairs of IALCE films. One pair of strips was prepared in the isotropic phase (and so shows no auxetic behaviour) and other 3 pairs are patterned with 0 Vrms, 1.25 Vrms and 1.50 Vrms. The scale bar is 1 cm.

Figure 7.9 (a) shows a schematic of the fabrication process of 3D tactile M^{2}ISE IALCE films and the details are shown in the experimental sections. A real image under white light of the 3D tactile M^{2}ISE IALCEs is shown in Figure 7.9 (b). In accordance with the design schematic in Figure 7.7(c), we used four 3D tactile M^{2}ISE IALCE films for the base, including two films with tactile information coded at 0 V_{rms}, and two films with tactile information coded at 1.25 V_{rms} and 1.50 V_{rms}, respectively. These films were arranged in order according to Figure 7.7(c) and the tactile information was then decrypted by stretching them simultaneously. By design, through the ordered arrangement of the tactile-information-coded IALCE strips, the Braille haptic letter “K” coded under 0 V_{rms} is the only letter that is apparent in the strain in range from ~0.58 ± 0.05 to ~0.76 ± 0.05. When the strain increases to the range from ~0.76 ± 0.05 to ~0.83 ± 0.05, the middle-right region responds auxetically and the haptic letter “O” appears. The last level for the 3D tactile information, the Braille haptic letter “R”, emerges when the sample is stretched above the

strain of ~0.83 ± 0.05. By rotating the 3D tactile M^{2}ISE IALCE device, another Braille haptic letter “W” would replace the Braille haptic letter “R”.

In practical scenarios, by comparing the mechanical deformations of different samples, we can determine the height variation of protrusions of each strip at certain strain levels during the deformation. We primarily compared the deformation processes of isotropic samples with samples polymerized under 0 Vrms, 1.25 Vrms, and 1.50 Vrms, with the results presented in Figure 7.8. By comparison in Figure 7.8, for the tactile information-coded strips, protrusions only form when the central region (polymerized under voltage) undergoes an auxetic response, causing its thickness to exceed that of the isotropic region. Considering that the display of 3D tactile information results from the accumulation of the auxetic response, our measurements and characterization are conducted after the staged accumulation of the auxetic response. For example, the first-stage information, the Braille letter “K” which emerges at strain of ~0.58 ± 0.05, is measured at the onset strain of the second stage, around ~0.76 ± 0.05. All measurements are performed within the 1.00 strain range. Accordingly, in the final decryption process, we conduct information acquisition at strain of 0.75, 0.85, and 1.00. Based on Figure 7.8, at these three strain levels, the $\Delta\varepsilon_z$ between anisotropic and isotropic regions, as well as the expected protrusion height on each surface (ΔH_i) for a thickness of 100 μm, are presented in Table 7.1. Due to the delayed auxetic response, the protrusion height accumulated within strips under 1.25 V_{rms} and 1.50 V_{rms} is lower than that without voltages (0 V_{rms}). At a strain of 0.75, the 1.25 V_{rms} region is near the ε_{th} and no auxetic response accumulates. The $\Delta\varepsilon_z$ is less than 0.01, which is negligible. A similar phenomenon is observed for the 1.50 V_{rms} region at a strain of 0.85. Notably, at a strain of 0.75, the $\Delta\varepsilon_z$ between the 1.50 V_{rms} region and the isotropic region is smaller than 0, preventing protrusion formation. The reason is, as mentioned earlier, attributed to the difference in elasticity properties of anisotropic and isotropic IALCEs.

Table 7.1 The $\Delta\varepsilon_z$ between adjacent regions and the expected protrusion height (ΔH_i) on each surface during decryption process.

ε_x	0 V_{rms} / Isotropic		1.25 V_{rms} / Isotropic		1.50 V_{rms} / Isotropic	
	$\Delta\varepsilon_z$	ΔH_i(μm)	$\Delta\varepsilon_z$	ΔH_i(μm)	$\Delta\varepsilon_z$	ΔH_i(μm)
0.75	~0.08	~4.0	<0.01	~0	~-0.02	~-1
0.85	~0.12	~6.0	~0.03	~1.5	<0.01	~0
1.00	~0.21	~10.5	~0.07	~3.5	~0.05	~2.5

The POM image of a set of 3D tactile M^{2}ISE IALCEs in a thickness of 100 μm at different nodes in the mechanical decryption process are shown in Figure 7.10.

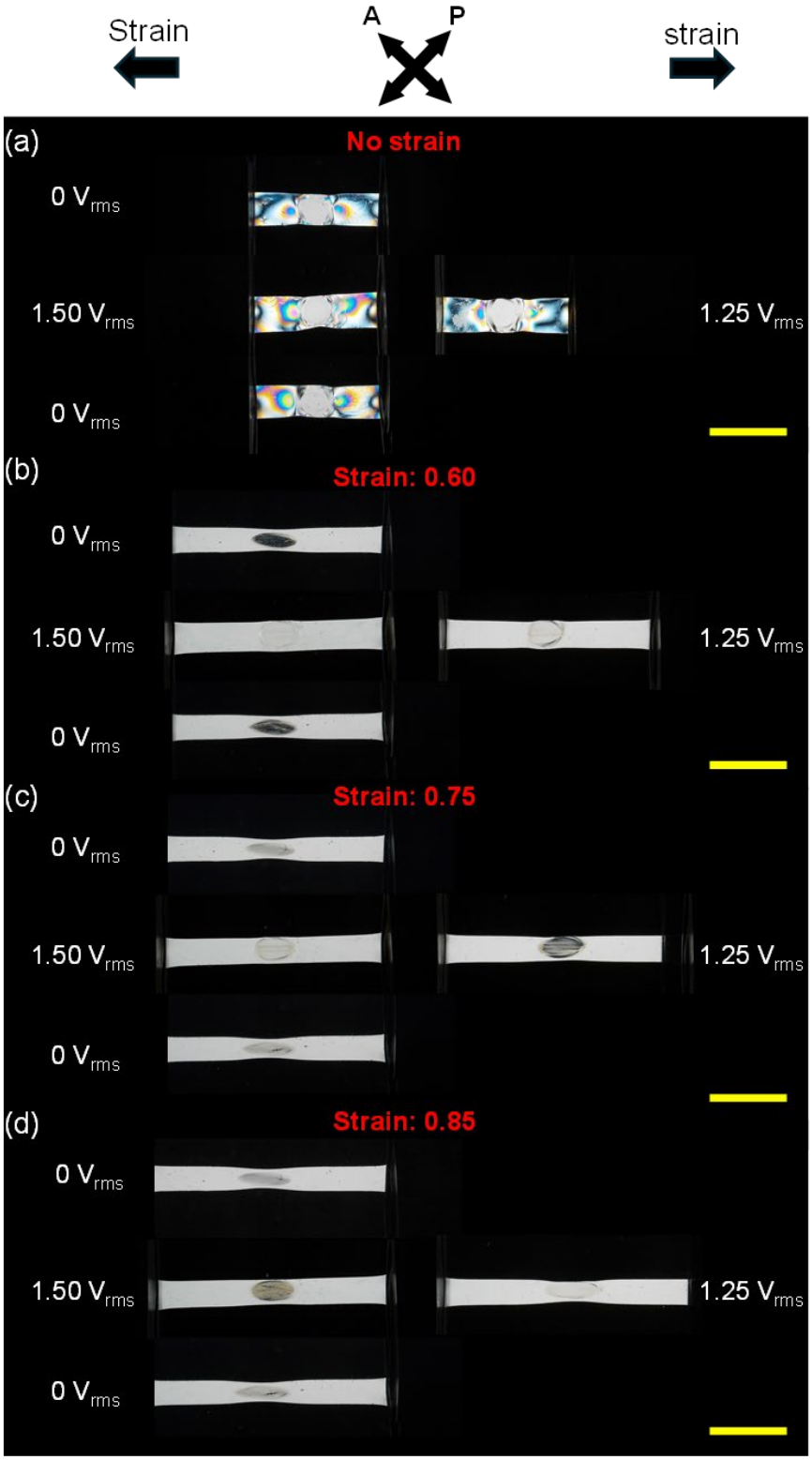

Figure 7.10 The POM image under crossed polarisers of a set of 3D tactile M^{2}ISE IALCEs under the conditions of a) no strain, b) ε = 0.60, c) ε = 0.75 and d) ε = 0.85. a) When no

strain is applied, the central (patterned) part of all the M^{2}ISE IALCEs is in a monodomain state while the main body is in an isotropic phase. b) When the ε = 0.60, the central part of the M^{2}ISE IALCE polymerized with no applied voltage turns dark, indicating proximity to the auxetic response of the patterned regions, while for the rest M^{2}ISE IALCEs, there is no auxetic responses. The first stage of 3D tactile information for haptic letter “K” starts appearing. c) As the strain increases to 0.75, the first stage of 3D tactile information has completely appeared, and the 1.25 V_{rms} patterned area starts experiencing an auxetic response. The second stage of 3D tactile information for haptic letter “O” starts appearing. The 1.50 V_{rms} area still experiences no auxetic response. d) When the total strain further increases to 0.85, 3D tactile information for haptic letter “O” has completely appeared and the auxetic response of the 1.50 V_{rms} region begins, while the third and fourth stages of 3D tactile information for haptic letter “W” and “R” start appearing. The scale bar is 1cm.

As described above, the dark states in the auxetic response are related to the beginning of the auxetic response. To characterize the staged 3D tactile information generated by the cumulative auxetic deformations, Figure 7.11(a) illustrates the practical decryption process of the 3D tactile M^{2}ISE IALCE device and Figure 7.11(b) shows the instant 3D images of the tactile information carrier regions measured by laser scanning microscopy, with the measured protrusion height, ΔH indicated. ΔH was obtained by averaging the topological profile with software, ‘‘Anytest’’ and the ΔH of strips at each stage is summarized in Table 7.2.

Table 7.2 The measured protrusion height (ΔH) of strips at each stage during decryption process (unit: μm).

ε_x	0 V_{rms} (Upper)	1.25 V_{rms}	1.50 V_{rms}	0 V_{rms} (Lower)
0.75	5.1	~0	-0.2	3.8
0.85	7.5	6.2	~0	7.6
1.00	15.0	8.9	4.2	10.8
1.00 (inversion)	13.0	9.2	3.0	12.6

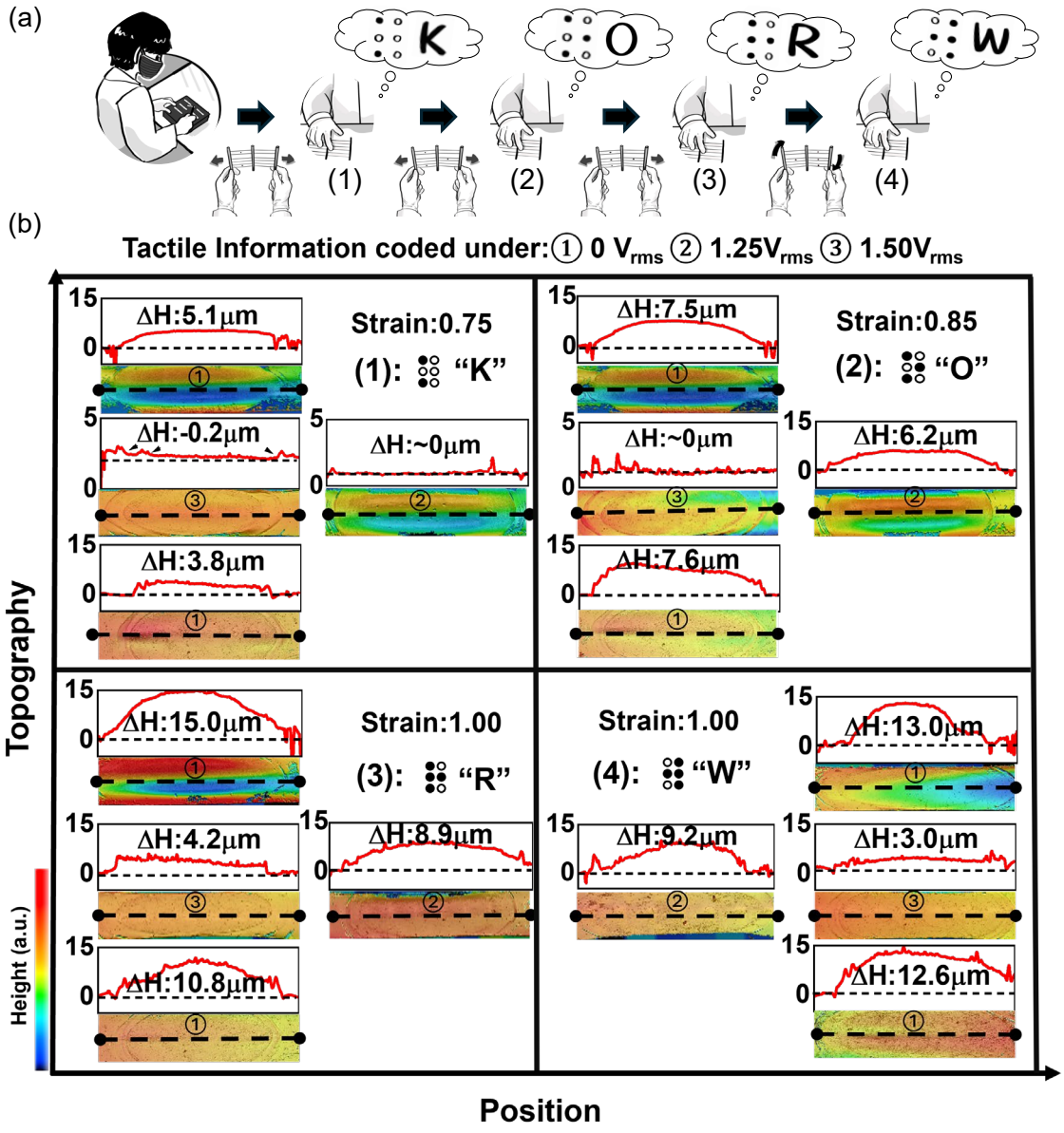

Figure 7.11 (a) The concept schematic of using the set of 3D tactile M2ISE IALCEs to show the multi-level Braille haptic letters. By stretching (1) e~75%, (2) e~85%, (3) e~100% (4) e~100%, the Braille haptic letters "K" "O" "R" and "W" appear sequentially. (b) The laser scanning microscopy images of the tactile information included in the films from stages (1)-(4), separately.. Number 1 to 3 represents the tactile information coded-IALCE strips cured under 0 Vrms, 1.25 Vrms and 1.50 Vrms, separately. The upper graph in each image shows the height profile measured across the encoded area indicated in the photograph below. The ΔH is the measured protrusion height and the dotted line in the upper graph stands for the base line of the ΔH measurement.

Figures 7.11(b) (1) to (4) correspond to the stages (1)-(4) shown in Figure 7.11(a). In stage 1, the two tactile information carrier regions coded at 0 V_{rms} undergo auxetic

responses and protrusions appear, while for the tactile information carrier regions coded under 1.25 V_{rms} and 1.50 V_{rms}, no auxetic response happens. The surface of the region coded under 1.25 V_{rms} stays flat, while for the 1.50 V_{rms} one, the central is about 0.2 μm lower than the isotropic region. The concave connection parts are pointed out by the black arrows in Figure 7.11(b)(1). The characterization of the surface morphology of this level matches the haptic letter “K”. With further stretching, the tactile information carrier region coded under 1.25 V_{rms} becomes auxetic and the tactile information shows as the haptic letter “O”. At stage 3, all the tactile information carrier regions respond auxetically and the haptic letter “R” appears. The final image (4), shows the laser scanning images of the opposite sides of the films, confirming that the intrinsic auxetic response ensures equivalent tactile information on both sides of the film, so that the haptic letter “W” displays.

Throughout the mechanical deformation process of the entire set, the height variation of protrusions on each strip closely follows our predictions, though with numerical deviations, generally trending higher than expected. Among them, the protrusion height variation in the strip patterned with 1.5 V_{rms} aligns most closely with the predictions in Table 7.1. At a strain of 0.75, the anisotropic region is lower than the isotropic areas, and at a strain of 1.00, the protrusion height reaches 4.2 μm (3.0 μm after inversion). While the strip patterned with 1.25 V_{rms} exhibit the largest deviation from Table 7.1. At a strain of 1.00, the height of a single-side protrusion reaches 9 μm, which is significantly higher—approximately twice our predicted range of 3–4 μm. For the 0 V_{rms} strip, the highest protrusion height at a strain of 1.00 reaches 15 μm, exceeding our expected value of 10.5 μm by approximately 50%. The deviation in the decryption process may be attributed to the increasing proportion of the anisotropic region in the strip, which causes the strain distribution across the strip to be less uniform compared to single-phase samples. Besides, the anisotropic deswelling of the sample will cause defects in the connection between adjacent regions in different phases and affect the shape of the coding area, which further affects the distribution of the strain during the decryption. Further investigation is required to fully understand this phenomenon. Overall, the whole process observed under the laser scanning microscope illustrates that a single stretch would successfully accomplish the encrypted display of individual haptic letters and the encrypted display of the word "WORK" by sequentially assembling four functioning films.

The tactile information and optical information share the same information security level, that is, the decryption of tactile information also requires the two decryption factors of strain

and stretching direction to work together. However, importantly, unlike 2D optical M^2ISE, in the storage and encryption of three-dimensional tactile information, the information is displayed in stages, remaining as successive auxetic thresholds are exceeded, rather than as instantaneous changes that occur and then disappear which is the case optically. Thus, the information displayed during the haptic decryption process is cumulative rather than transient. These different M^2ISE characteristics make this system a unique decryption method, coding 2D optical and 3D tactile information in the same sample. The decryption process for the 2D optical and 3D tactile information do not interfere with each other, which further enhances the security and reliability of the M^2ISE function. Moreover, the intrinsic auxetic response of the film expands the dimensions of the mechanical deformation from only one side to both surfaces of the film. This unique feature would also further enhance the information richness and design flexibility.

7.4 Summary

This chapter, as the final experimental chapter of this thesis, encapsulates the core theme and demonstrates the tunable information devices based on the tunable auxetic responses of IALCEs. We demonstrated the implementation of IALCEs in applications of multilevel, multidimensional information storage and encryption, utilizing the unique optical and morphological properties of IALCEs during auxetic responses. Based on the optical features of IALCEs in various auxetic responses, we ingeniously designed a 3-level information storage and encryption application on 2D optical information. The binary information (000 100 110), (011 001 000) and (100 010 001) were encrypted into one IALCE film by masked polymerization under an electric field and were decrypted sequentially by stretching the film to strains of ~0.60, ~0.70 and ~0.80, separately. Further, considering the morphological features, we designed and realized a 3-level information storage and encryption application using 3D tactile information. The haptic letters “K”, “O” and “R” were coded into a set using 4 IALCE films. By sequentially stretching the set to over strains ~0.75, ~0.85 and ~1.00, the haptic letters “K”, “O” and “R” were shown in order. The intrinsic property of the auxetic response expands the haptic information to the fourth level — a haptic letter “W”. A complete haptic word “WORK” is displayed in the decryption process of this 3-level information storage and encryption application. The encryption and decryption process of either 2D optical information or 3D tactile information does not interfere with each other. What is more, all the information is highly secured as the decryption parameters

include not only strain but also the stress direction.

In the next chapter, we will give a conclusion of the whole thesis and give outlooks on future works, which is mainly about introducing the dynamic bonds inside the IALCEs to make the auxetic reponses programmable.

References

1. K. Li, J. Wang, W. Cai, H. He, M. Cen, J. Liu, D. Luo, Q. Mu, D. Gerard, Y. J. Liu, *Nano Lett.* 2021, *21*, 7183–7190.
2. H. -L. Wang, H. -F. Ma, T. -J. Cui, *Adv. Sci*. 2022, *9*, 2204333.
3. J. Wang, K. Li, H. He, W. Cai, J. Liu, Z. Yin, Q. Mu, V. KS Hisao, D. Gérard, D. Luo, G. Li, Y. J. Liu, *Laser Photon. Rev.* 2022, *16*, 2100396.
4. H. Huang, H. Li, J. Yin, K. Gu, J. Guo, C. Wang, *Adv. Mater.* 2023, *35*, 22111117.
5. B. Liu, C.-L. Yuan, H.-L. Hu, H. Wang, Y.-W. Zhu, P.-Z. Sun, Z.-Y. Li, Z.-G. Zheng, Q. Li, *Nat. Commun*. 2022, *13*, 2712.
6. H. Li, M. Zhu, F. Tian, W. Hua, J. Guo, C. Wang, *Chem. Eng. J.* 2021, *426*, 130683.
7. H, Zeng, Z. He, Y. Wu, S. Gao, F. Mao, H. Fan, X. Fan, W. Kan, Y. Zhu, H. Zhang, B. Assouar, *Adv. Func. Mater.* 2024, *34*, 2405132.
8. G, Qu, W. Yang, Q. Song, Y. Liu, C. -W. Qiu, J. Han, D. -P. Tsai, S. Xiao, *Nat. Commun*. 2020, *11*, 5484.
9. X. Guo, J. Zhong, B. Li, S. Qi, Y. Li, P. Li, D. Wen, S. Liu, B. Wei, J. Zhao, *Adv. Mater.* 2021, *34*, 2103192.
10. Z. Yu, K. Zhao, Y. Zhao, M. Wu, B. Cheng, R, Qian, S. Chen, C. Ye, *J. Mater. Chem. C* 2023, *47*, 16527–16535.
11. Q. Wang, Z. Qi, Q. -M. Wang, M. Chen, B. Lin, D.- H. Qu, *Adv. Func. Mater.* 2022, *32*, 2208865.
12. Z. Quan, Q. Zhang, H. Li, S. Sun, Y. Xu, *Coordin. Chem. Rev.* 2023, *493*, 215287.
13. Y. Xie, X. Zhao, H. Wang, Y. Tian, C. Liu, J. Wu, J. Cui, Z. Zhou, J. Chen, X. Chen, *Angew. Chem. Int. Ed.* 2024, e202414846.
14. D. Mistry, M. Nikkhou, T. Raistrick, M. Hussain, E. I. L. Jull, D. L. Baker, H. F. Gleeson, *Macromolecules* 2020, *53*, 3709–3718.
15. J. Bai, L. Zhang, Z. Shi, X. Jiang, *Adv. Funct. Mater.* 2023, *33*, 2212556.
16. J. -B. Hou, X. -S. Chen, Y. Zhao, *Adv. Funct. Mater.* 2024, *34*, 2314510.
17. X. Wang, K. Yang, B. Zhao, J. Deng, *Small* 2024, *20*, 2404576.
18. X. Sang, A. Khan, R. Xu, K. Zhang, Y. Tian, Y. Li, M. Feng, L. Liu, F. Song, W. Huang, *Adv. Opt. Mater.* 2024, *12*, 2400064.
19. L. Yu, B. Chen, Z. Li, Q. Huang, K. He, Y. Su, Z. Han, Y. Zhou, X. Zhu, D. Yan, R. Dong, *Chem. Soc. Rev.* 2023, *52*, 1529–1548.
20. S. H. Choi, J. H. Kim, J. Ahn, T. Kim, Y. Jung, D. Won, J. Bang, K. R. Pyun, S. Jeong, H. Kim, Y. G. Kim, S. H. Ko, *Nat. Mater.* 2024, *23*, 834–843.
21. H. -Q. Wang, Y. Tang, Z. -Y. Huang, F. -Z. Wang, P. -F. Qiu, X. Zhang, C. -H. Li, Q. Li,

Angew. Chem. Int. Ed. 2023, *62*, e202313728.
22. J. Gao, Y. He, X. Cong, H. Yi, J. Guo, *ACS Appl. Mater. Interfaces* 2022, *14*, 53348−53358.
23. J. Gao, M. Tian, Y. He, H. Yi, J. Guo, *Adv. Funct. Mater.* 2022, *32*, 2107145.
24. M. Schwartz, G. Lenzini, Y. Geng, P. B. Ronne, P. Y. A. Ryan, J. P. F. Lagerwall, *Adv. Mater.* 2018, *30*, 1707382.
25. Y. Geng, R. Kizhakidathazhath, J. P. F. Lagerwall, *Adv. Funct. Mater.* 2021, *31*, 2100399.
26. Z. -Y. Xu, L. Li, X. Yin, L. -Y. Shi, K. -K. Yang, Y. -Z. Wang, *Adv. Mater. Technol.* 2024, *9*, 2302009.
27. S. Zhang, C. Sun, J. Zhang, S. Qin, J. Liu, Y. Ren, L. Zhang, W. Hu, H. Yang, D. Yang, *Adv. Funct. Mater.* 2023, *33*, 2305364.
28. J. -X, Yang, X. -L. Zhang, L. Yin, J. Jiang, T. Liu, J. -Y. Liu, Z. -T. Xu, H. -Y. Bai, H. -W. Ma, Y. Zhao, Y. Li, L. Han, *Chem. Eng. J.* 2025, *507*, 160312.
29. Y. Zhai, Z. Wang, K. -S. Kwon, S. Cai, D. J. Lipomi, T. N. Ng, *Adv. Mater.* 2021, *33*, 2002541.
30. T. Ohzono, M. O. Saed, Y. Yue, Y. Norikane, E. M. Terentjev, *Adv. Mater. Interfaces* 2020, *7*, 1901996.
31. N. Torras, K. E. Zinoviev, J. Esteve, A. Sánchez-Ferrer, *J. Mater. Chem. C* 2013, *1*, 5183.
32. A. Gablier, E. M. Terentjev, *Nano Select* 2023, *4*, 324−332.
33. M. Shinohara, Y. Shimizu, A. Mochizuki, *IEEE Trans. Rehab. Eng.* 1998, *6*, 249–256.
34. D. Leithinger, S. Follmer, A. Olwal, H. Ishii, *IEEE Comput. Grap. Appl.* 2015, *35*, 5–11.
35. W. Yang, J. Huang, R. Wang, W. Zhang, H. Liu, J. Xiao, *IEEE Trans. Haptics* 2021, *14*, 712–721.
36. I. Hwang, S. Mun, J. -H. Youn, H. J. Kim, S. K. Park, M. Choi, T. J. Kang, Q. Pei, S. Yun, *Nat. Commun*. 2024, *15*, 2554.
37. A. Richter, G. Paschew, *Adv. Mater.* 2009, *21*, 979–983.
38. E. I. L. Jull. R. J. Mandle, T. Raistrick, Z. Zhang, P. J. Hine, H. F. Gleeson, *Macromolecules* 2022, *55*, 4320−4330.
39. S. R. Berrow, R. J. Mandle, T. Raistrick, M. Reynolds, H. F. Gleeson, *Macromolecules* 2024, *57*, 5218−5229.
40. S. Kaur, H. Liu, J. Addis, C. Greco, A. Ferrarini, V. Görtz, J. W. Goodby, H. F. Gleeson, *J. Mater. Chem. C* 2013, *1*, 6667−6676.
41. S. Kaur, L. Tian, H. Liu, C. Greco, A. Ferrarini, J. Seltmann, M. Lehmann, H. F. Gleeson, *J. Mater. Chem. C* 2013, *1*, 2416-2425.
42. K. R. Welford, J. R. Sambles. *Mol. Cryst. Liq. Crys.* 1987, *147*, 25–42.

Chapter 8 Conclusion and preliminary explorations for future work

8.1 Conclusion

This thesis explored the interactions between the director profile and the tuneable auxetic responses of IALCEs. The microscopic orientation of LCEs plays a significant role in determining their macroscopic deformation characteristics, which applies to IALCEs as well. The overall aim of this thesis was to pattern an out-of-plane director profile in IALCEs to manipulate their auxetic responses, through applying an electric field during polymerization, and furthermore leverage these distinct auxetic responses to develop information encryption devices.

Chapters 2 and 3 introduced the theoretical and experimental fundamentals of the whole thesis. Chapter 2 introduced the relevant background of this thesis, such as the fundamentals of LCs and LCEs, the deformation and actuation of LCEs and the unique category-the IALCEs. The detailed alignment method of LCEs was summarized in Section 2.3 to better comprehend methods that facilitate the manipulation of the anisotropic response of LCEs. This discussion establishes the context for employing an electric field to pattern the director profile in later chapters while emphasizing the feasibility of this approach. Chapter 3 summarized the fundamental methods used throughout the experimental work. It introduces the chemical compounds used in synthesizing IALCEs, details the fabrication process of planar-aligned IALCEs, and outlines key experimental techniques, including POM, mechanical deformation characterization, and DSC.

Following the introduction to the fundamental background, Chapter 4 shifted focus to the orientation characteristics of the IALCE precursor under an applied electric field. Chapter 4 explored the deformation of the director under an external electric field by considering the elastic and dielectric properties of LCs, followed by an introduction to the Fréedericksz transition alignment. Utilizing key parameters of this alignment, we detailed the electro-optical experimental procedure designed to determine and characterize the V_{th} of IALCE precursor, which is essential for the subsequent fabrication of auxetic LCE films or film regions with varying director profiles. The measured threshold voltage was 0.9 ± 0.1 V_{rms}. Subsequently, by integrating the elastic constants of the precursor mixture, the

relationships between V , θ_{max} , and $\theta(z/d)$ in the Fréedericksz transition alignment of the auxetic LCE precursor were illustrated in Figure 4.5. This schematic comprehensively depicted the interdependence of key parameters in the Fréedericksz transition alignment of the auxetic LCE precursor, which served as a foundational framework for sample fabrication in the following chapters, facilitating the exploration of how different Fréedericksz transition alignments can be leveraged to manipulate distinct auxetic responses.

Chapters 5 and 6 moved on to the experimental scenario of IALCE fabrication and characterization. Chapter 5 first introduced the IALCEs with the director profile in two extreme cases, the high-quality planar and homeotropic alignment. Their excellent monodomain alignment was characterized by POM. The mechanical deformation characterization showed that both types exhibited auxetic responses with threshold strains in excellent agreement: 0.56 ± 0.05 for H-LCE and 0.58 ± 0.05 for P-LCE. This was an important result as it confirmed that the auxetic response was not dependent on the aspect ratio of the film and in fact was identical whether the auxetic dimension was of the order of microns or centimetres. The Raman scattering analysis conducted by Aidan Street suggested the presence of biaxiality within this auxetic system, confirming earlier conclusions reached by Raman scattering on a similar, but more highly crosslinked system. Importantly, the well-aligned homeotropic sample enabled Dr. Thomas Raistrick to perform conoscopic measurements, providing definitive evidence that the system became biaxial even at low strain levels, unequivocally confirming that the emergence of biaxiality is an intrinsic characteristic of the auxetic response in nematic LCEs.

Chapter 6 explored the tunability of auxetic responses in IALCEs by introducing Fréedericksz transition alignments through electric field modulated polymerization. By adjusting V , we fabricated IALCEs with distinct director profiles, exhibiting θ_{max} from 40° to 88°. Thermal deformation and birefringence measurements confirmed the successful introduction of the Fréedericksz transition alignment, showing that IALCEs with the Fréedericksz transition alignment exhibited minimized actuations due to modified director orientation. The mechanical characterization illustrated that the ε_{th} was delayed (increased) with the increase of θ_{max} . A wide tuneable range of ε_{th} , from 0.58 to 0.91, can be realized by application of a small voltage to the precursor mixture (≤ $2V_{rms}$). Additionally, DSC and

stress-strain curve measurements confirmed consistent T_g and hyper elasticity across all samples, indicating that the tunability of the auxetic responses relied solely on the modified director profile. A simplified mathematical model further assisted in understanding the mechanism behind it.

After the characterization of tuneable auxetic responses of Fréedericksz transition aligned IALCEs, Chapter 7 demonstrated the implementation of IALCEs in applications of multilevel, multidimensional information storage and encryption, utilizing the unique optical and morphological properties of IALCEs during auxetic responses. Based on the optical properties of IALCEs during the mechanical deformations whereby, under crossed polarizers, the IALCEs exhibit optically isotropy near the threshold strain of the auxetic response, we ingeniously designed a 3-level information storage and encryption application on 2D optical information. The binary information (000 100 110), (011 001 000) and (100 010 001) were encrypted into one IALCE film by masked polymerization under an electric field and were decrypted sequentially by stretching the film to strains of ~0.60, ~0.70 and ~0.80, separately. Further, considering the film morphology, through the consecutive pattern distribution of IALCE films with distinct auxetic responses, we designed and realized a 3-level information storage and encryption application using 3D tactile information. The haptic letters “K”, “O” and “R” were coded into a set using 4 IALCE films. By sequentially stretching the set to over strains ~0.75, ~0.85 and ~1.00, the haptic letters “K”, “O” and “R” were shown in order. What is more, due to the intrinsic property of the auxetic response, the haptic letter could be felt on both surfaces, which in principle expands the haptic information to the fourth level — a haptic letter “W”. A complete haptic word “WORK” is displayed in the decryption process of this 3-level information storage and encryption application. The encryption and decryption process of either 2D optical information or 3D tactile information does not interfere with each other. What is more, all the information is highly secured as the decryption parameters include not only strain but also the stress direction.

8.2 Preliminary explorations for future work

8.2.1 Introduction and motivation

In this thesis, we demonstrate the tunability of the auxetic response following electric field-induced alignment and present a proof-of-concept demonstration of applications in

information storage and encryption. Our findings highlight the applicability of IALCEs in both 2D and 3D information, achieving multi-level binary and tactile information storage and encryption. During the fabrication and characterization of our samples, we identified areas for improvement in our auxetic materials.

Specifically, due to the presence of 6OCB, post-polymerization washing is required to remove unreacted 6OCB. This process induces anisotropic deswelling, which strongly depends on the director profile of the sample. As the profile complexity increases, so does the complexity of the anisotropic deswelling. Post-deswelling morphological changes may lead to distortions in the director profile and residual strain in the sample, which, in turn, results in an inhomogeneous strain distribution during mechanical deformations. Furthermore, when the director profile is not mirror-symmetric through the cell, for example, hybrid alignment and twist alignment, the difference in surface stress after anisotropic deswelling leads to fragile, curled, and non-flatten samples, significantly affecting their usability in experiments. Addressing the challenges posed by anisotropic deswelling would enable the development of intricate alignment systems and facilitate a wide range of applications. Fortunately, this issue has recently been resolved by Dr. Stuart R. Berrow [1]. By replacing 6OCB with the synthesized compound M1, Dr. Berrow's approach eliminates the need for post-polymerization washing while preserving the auxetic properties of the sample (threshold strain ~0.76). This advancement paves the way for further investigations into complex alignment configurations.

Additionally, in the application of IALCEs for 2D information storage and encryption, the contrast between the bright and dark states is not perfect. As shown previously, the 2D information shown in different samples has various contrast and defects exist. To address this limitation, we propose the exploration of alternative strategies, such as utilizing cholesteric LCEs (CLCEs) to investigate novel encoding methods. Moreover, the potential physical phenomenon that arises when the CLCEs with cholesteric director profiles undergo auxetic remain an exciting direction for exploration.

Furthermore, in our current IALCE system, the alignment direction, strain direction, and auxetic response direction are all fixed. When the alignment direction is predetermined, optimal auxetic responses necessitate that the strain direction be perpendicular to the alignment direction, with the auxetic response occurring in the direction perpendicular to both. Consequently, once the alignment direction is finalized during polymerization, all three directions are inherently determined, thereby constraining the operational flexibility of

IALCEs. As a unique class of LCEs, if the auxetic response of IALCEs could be programmably controlled, both the magnitude and direction of the auxetic response could be arbitrarily customized even with one polymerized, significantly expanding their functional scenarios. To achieve this objective, we made some initial attempts into programmable auxetic responses.

We tried to induce dynamic bonds inside the polymer backbones of IALCEs to make the auxetic responses programmable, using the shape memory effect. Shape memory effect refers to a material's ability to be deformed and fixed into a temporary shape by mechanical force and, only when triggered by an external stimulus, would return to its original form [2,3]. Shape-memory polymers are highly flexible materials that can be programmed to recover their memorized shape in response to external stimulus as a one-time effect, known as one-way shape memory. However, the shape memory function can also operate as a reversible effect by controlling the macromolecular orientation of actuation units and the skeleton structure of geometry-determining units within the polymer, known as two-way shape memory. In recent years, researchers have investigated the combination of shape memory effect into the LCE to realize the two-way shape memory function, where two different shapes could be memorized and recovered depending on external stimulus [4,5]. When they are reprogrammed into different shapes, both their recovery and actuation properties are adjustable. The inducement of dynamic bonds is proven to be an efficient way to realize the two-way shape memory functions of LCEs [4,6], through controlling the skeleton structure of geometry-determining units. Dynamic bonds are defined as bonds which can go through dissociation and reassociation [7]. The inducement of dynamic bonds enables the polymer skeleton to lock in a temporary shape, in addition to the initial shape locked by permanent cross-links with covalent bonds. For example, Guo *et al.* used dynamic hydrogen bonds to combine the shape memory effect into LCEs and realize reversible actuation of the LCEs when they are programmed into different shapes [4]. Hydrogen bonds are dynamic bonds that break and reform due to the temperature change or the pH change [6]. In Guo et al.'s study, the first memorized shape is the initial shape determined by the cell. As shown in Figure 8.1, the shape programming is achieved by heating the sample above 100°C, reaching the skeleton reset temperature (T_R), at which hydrogen bonds break. The sample is then mechanically deformed to second memorized shape and cooled to room temperature, allowing the hydrogen bonds to reform and stabilize the new shape. The reversible actuation of the second memorized shape LCE

occurs within the temperature range between T_{ni} and T_R. The recovery of the first memorized shape or program of the second memorized shape can be achieved by reheating the sample above T_R and repeating the cycle.

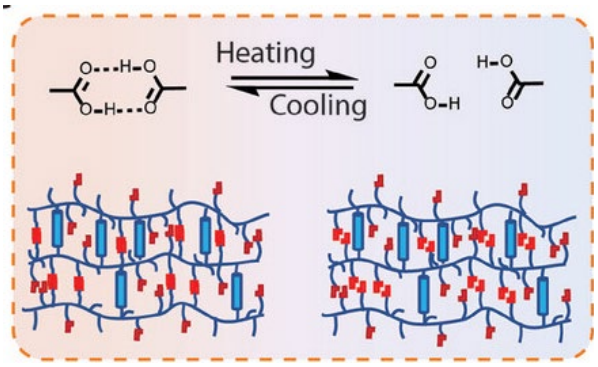

Figure 8.1 The shape-memory programming relies on hydrogen bond breaking and reforming upon heating and cooling, respectively. Reproduced from [4].

We used a similar approach to endow the polymer skeleton of IALCEs with shape memory effects, by inducing the dynamic hydrogen bonds. We call the IALCEs with hydrogen bonds introduced as HB-IALCEs. Our strategy was to partially replace covalent crosslinkers in the skeleton, RM82, with the dynamic hydrogen bonds, enabling programmable alignment through the shape memory effect and further realizing the programmable auxetic responses. The first memorized shape, predetermined by the cell, was in the isotropic phase. By heating the sample to near 100°C, the hydrogen bonds were broken, allowing the alignment of the director through mechanical stretching. Once properly stretched and aligned, the sample was cooled to room temperature to memorize the second shape, during which hydrogen bonds reform and temporary alignment is locked. According to this design, in this second memorized shape, the IALCE exhibits an auxetic response due to the locked director profile. Moreover, the feature of this auxetic response can be tuned based on the stretching alignment process, achieving the desired programmability.

(a)

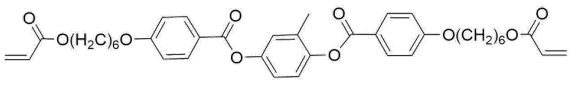

RM82

(b)

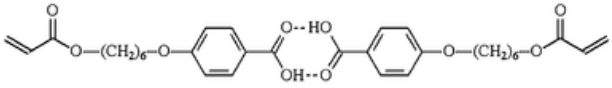

6OBA

Figure 8.2 The structure of (a) RM82 and (b) 6OBA. Reproduced from [8].

To achieve better mixing, we employed 6OBA, a compound with a chemical structure highly similar to RM82 [8], as shown in Figure 8.2. While 6OBA itself is a smectic LC [9], previous studies have demonstrated that mixing structurally similar liquid crystals can broaden the nematic phase range [10], which is also the role of 6OCB in our original IALCE recipe. Therefore, by adjusting the ratio of RM82 to 6OBA, a nematic precursor can be obtained. When introducing new chemical components, we maintained a constant total crosslinker concentration at 8% of the total polymerized composition, regardless of whether the crosslinking originates from covalent or dynamic bonds. Only the proportion of RM82 was altered, with 6OBA substituting partial RM82. The total content of RM82 and 6OBA remained at 8% of the final polymerized sample. Preliminary rapid tests showed that the auxetic property could still be preserved when the RM82 content was reduced to as low as 2% of the original formulation. We used a RM82:6OBA ratio of 1:1 and detailed chemical formulations are listed in Table 8.1. Specific experimental procedures and preliminary results will be presented in the following sections.

Table 8.1. Chemical composition of the hydrogen-bond-induced IALCE before and after wash

Component	% by mol. of each component in the sample	
	Precursor mixture	Final IALCE
6OCB	54.6	0
A6OCB	24.4	55.6
RM82	1.75	4.0
6OBA	1.75	4.0
EHA	16.0	36.4
MBF	1.5	0

8.2.2 Experimental methods

The fabrication and characterization of the HB-IALCEs are quite similar to the initial IALCEs, with the primary difference being the preparation of the precursor before polymerization. According to Ref. 9, the hydrogen bond in 6OBA is particularly strong and its melting point is approximately 195°C. There, DCM was used as a solvent to dissolve the compounds. The mesogenic precursor compounds were dissolved in DCM while stirred at 200 rpm and 100°C on a magnetic hot plate until the DCM was totally evaporated. The temperature was then lowered to 70 °C, at which point MBF and EHA were added. After a further 2 minutes of stirring, the precursor was filled into the cell at 70°C in its isotropic phase by capillary

action.

After filling, for the 100μm planar HB-IALCE sample, the cell was then left for 20 mins to cool to room temperature, into its nematic phase and then polymerized under a UV light (365nm, 2.5 mW/cm^2) for 30min. While for the 300μm isotropic HB-IALCEs, the cell was prepared using 300 μm thick PET film spacers, and after filling, the sample was polymerized at 70°C under a UV light (365nm, 30 mW/cm^2) for 30min. To determine the phase transition temperature, we run the DSC measurement on the precursor exclude MBF, and the result is shown in Figure 8.3, indicating a phase transition occurring at approximately 46.4 °C.

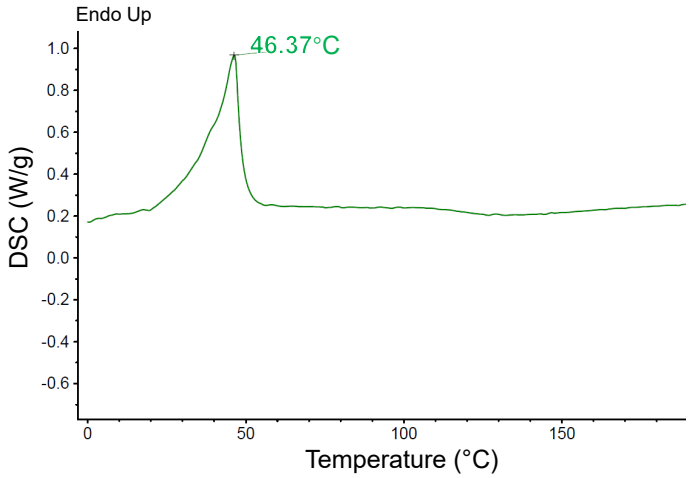

Figure 8.3 The DSC measurement of the precursor.

8.2.3 Results and discussion

8.2.3.a Characterizations of HB-IALCEs

After introducing hydrogen bonding into the system, we first fabricated 100 μm planar HB-IALCE samples and conducted mechanical deformation measurements to verify whether the auxetic response is preserved. The experimental results are presented in Figure 8.4. Figures 8.4(a) and (b) display the evolution of strain ε_z and ε_y as a function of ε_x. The deformation behavior of the HB-IALCE sample in both the *x*–*y* and x–z plane exhibits highly anomalous characteristics compared to P-LCEs. In the *x*–*z* plane, ε_z reaches a minimum when $\varepsilon_x \approx 1.20 \pm 0.05$, after which it begins to increase. The Poisson's ratio of the HB-IALCE in the *x*–*z* and *x*–*y* plane is shown in Figures 8.4(c) and (d). The Poisson's ratio remains positive in the *x*–*y* plane throughout the deformation, while a clear threshold strain appears

in the *x*–*z* plane at $\varepsilon_x = 1.17 \pm 0.05$, beyond which the Poisson's ratio becomes negative. This indicates that the system retains its auxetic behavior after the introduction of hydrogen bonds.

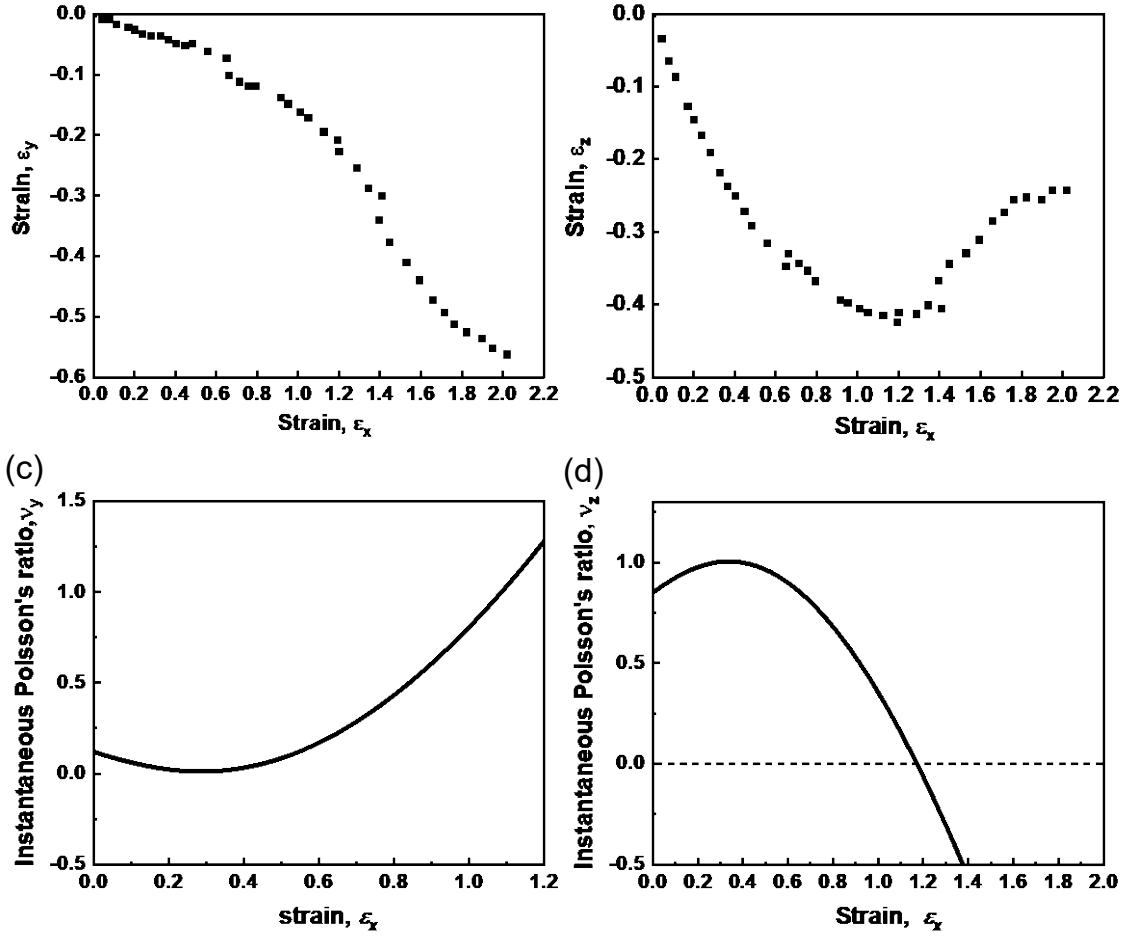

Figure 8.4 Strains (a) ε_x-ε_y and (b) ε_x-ε_z, and instantaneous Poisson's ratio (c) ν_y and (d) ν_z measured for a 100μm planar HB-IALCE.

Subsequently, we measured the T_g of the polymerized HB-IALCE sample, as shown in Figure 8.5. The T_g of the HB-IALCE was found to be 20.4 °C. This result is consistent with our discussion in Section 2.2.3, where we noted that an increase in T_g tends to increase the threshold strain of the auxetic response.

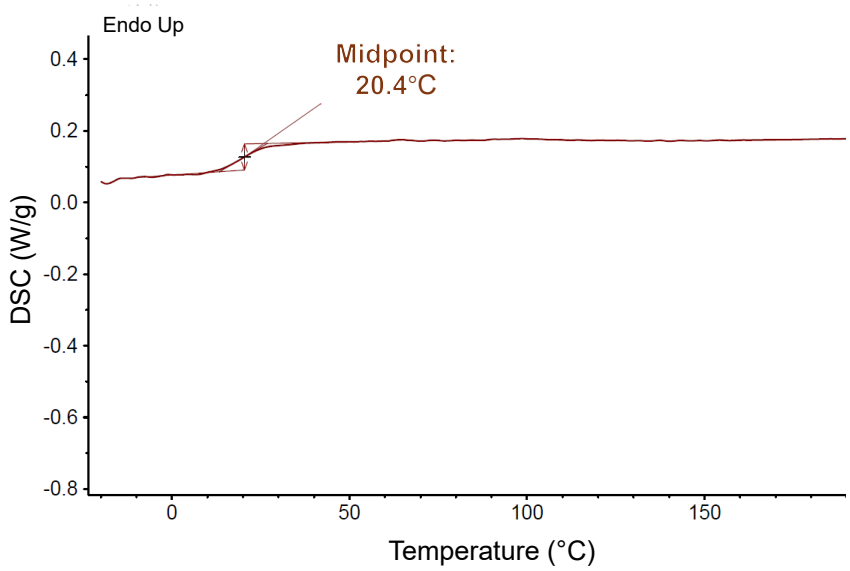

Figure 8.5 The glass transition temperature measurement of a polymerized 100μm planar HB-IALCEs.

8.2.3.b Strategy for the programmable auxetic response based on the shape memory effect

To realize a programmable auxetic response by introducing hydrogen bonds into the IALCE system, we propose the design illustrated in Figure 8.6. In this design, temperature modulation is used to control the breaking and reformation of hydrogen bonds, thereby enabling the lock of both the polymer skeleton and mesogen alignment.

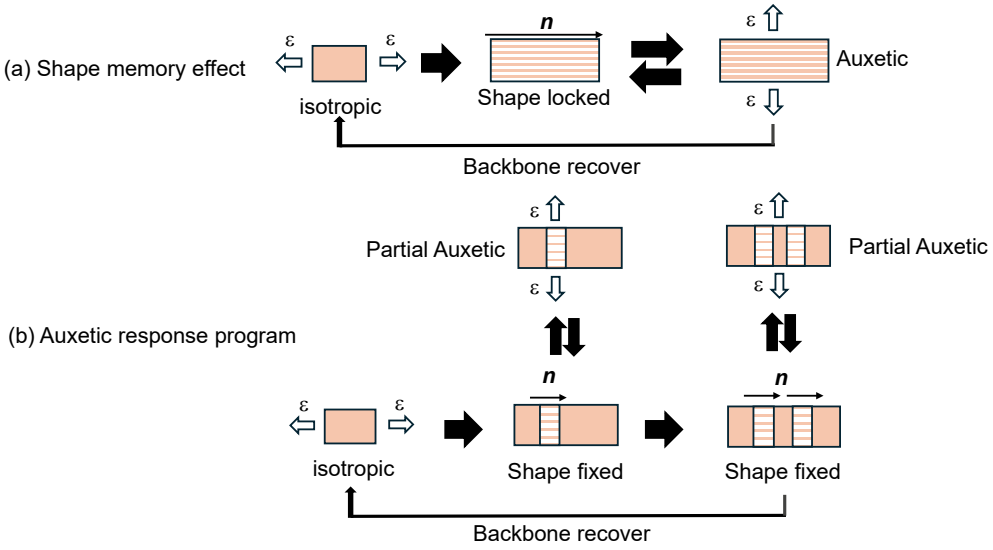

Figure 8.6 Schematic illustration of (a) the shape memory cycle enabled by hydrogen bonding in HB-IALCEs and (b) the strategy of programmable auxetic responses.

As shown in Figure 8.6(a), we will first fabricate an isotropic HB-IALCE sample with a thickness of 300 μm to investigate the shape memory effect of HB-IALCEs. As discussed in Section 2.2.1, the second step in the two-step crosslinking method for LCEs typically involves mechanical stretching to align the mesogen. According to Ref. [4], achieving effective mesogen alignment via mechanical stretching requires strains in the range of 150%–200%. The thickness of the 300 μm sample provides efficient thickness to explore the optimal stretching range for mesogen alignment. Even after alignment, the sample also retains sufficient mechanical robustness from the rest thickness to undergo further mechanical deformation measurements. Once the sample is prepared, it will be stretched at 100 °C to induce monodomain alignment of mesogens. While holding the stretched shape, the sample is cooled to room temperature to lock the skeleton configuration. The oriented sample will then be subjected to mechanical deformation measurements to investigate whether it is auxetic. Following the shape memory effect demonstration in Figure 8.6(a), we will further investigate the effects of different alignment degrees by stretching isotropic HB-IALCEs to varying strain levels (initially 150%, with adjustments based on results). This will allow us to examine how the degree of mesogen alignment influences the subsequent auxetic response.

It is worth mentioning that the stretching is performed at elevated temperatures, rather than heating the sample after stretching. This is because once the mesogen is aligned, the sample exhibits anisotropic actuation behavior. Even if the skeleton is not yet fixed, heating the stretched sample may induce thermal actuation due to the anisotropy of the mesogen alignment. As shown in Figure 8.7, thermal actuation measurements on a 100 μm planar HB-IALCE sample revealed approximately 13% strain in both length (parallel to $\hat{n}$) and width (perpendicular to $\hat{n}$) direction at around 100 °C. Therefore, stretching at high temperature followed by cooling is more desirable for skeleton locking compared to heating the sample after stretching.

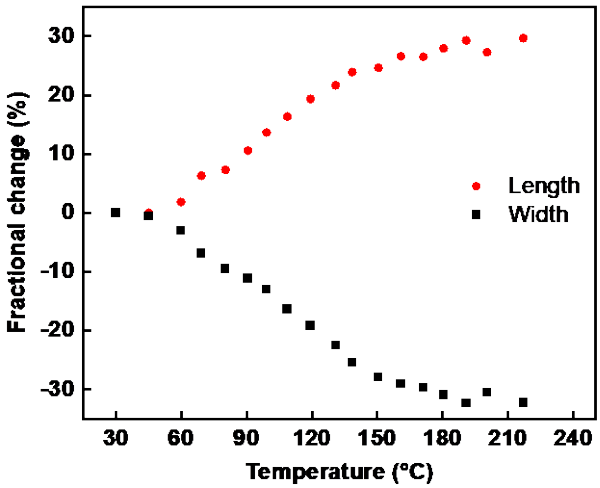

Figure 8.7 The thermal actuation measurement of a 100μm planar HB-IALCE sample in length and width direction.

Building upon realizing the shape memory effect in Figure 8.6(a), a more advanced programming strategy for auxetic response is illustrated in Figure 8.6(b). By locally locking different regions of the isotropic HB-IALCE with varying alignment degrees, programmable pattern control of the auxetic responses can be achieved. Furthermore, the same sample can undergo multiple cycles of erasure and reprogramming of its auxetic responses.

8.2.3.c A proof-of-concept experiment of the shape memory effect

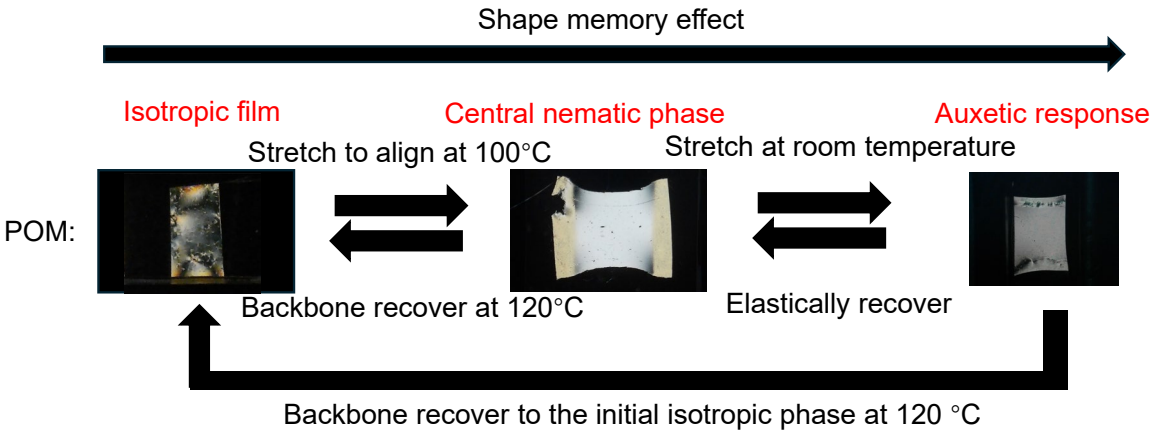

Figure 8.8 The investigation of the shape memory effect of a 300μm isotropic HB-IALCE.

As a proof-of-concept experiment, we fabricated an isotropic HB-IALCE sample with a thickness of 300 μm. Considering that the introduction of hydrogen bonds increases the

sample's adhesion to rough surfaces, we employed a hot air gun with adjustable temperature instead of a hot plate to heat the samples. The experimental schematic for investigation of the shape memory effect is illustrated in Figure 8.8. Initially, the 300μm HB-IALCE sample is in an isotropic phase, as shown in the left image, with no mesogen alignment present. Upon heating to 100 °C, the sample is mechanically stretched, inducing a uniaxial alignment of the mesogens and forming a nematic phase in the central region, as depicted in the middle image. This aligned configuration is then fixed by cooling the sample back to room temperature, where hydrogen bonds reform and lock the molecular orientation, effectively preserving the induced anisotropy. The aligned sample is subsequently subjected to mechanical deformation at room temperature to show an auxetic response, demonstrating the successful programming of shape and auxetic response through the shape memory effect enabled by dynamic hydrogen bonds. At any stage, the sample could recover to the initial isotropic phase through heating at 120°C.

In the experimental circumstances considered, we observed that the samples exhibited limited stretchability. Specifically, when the strain exceeded 110% at 100 °C, the samples tended to fracture. Only shape memory effects within 100% strain were successfully realized. We speculate that this phenomenon may be caused by uneven surface stress distribution resulting from non-uniform heating. The nozzle of the air gun has a relatively small area, and the generated hot airflow does not diffuse uniformly across the sample surface. During stretching, as the sample is stretched, this uneven heat distribution becomes more pronounced. Moreover, the clamped ends of the sample cannot be effectively heated, leading to a mismatch in mechanical strength between the heated central region and the unheated ends. This difference increases the likelihood of fracture at the interface between the sample and the clamps. Further experiments are needed to verify this hypothesis and optimize the experimental conditions accordingly.

The mechanical deformation behavior of a mechanically aligned sample, fixed at 100% strain, is shown in Figure 8.9. Figures 8.9 (a) and (b) show the behaviour of ε_z and ε_y for ε_x. The deformations of the mechanical aligned HB-IALCE sample in the *x-y* and *x-z* plane are highly comparable to that of the planar HB-IALCE. For the deformation in *x-z* plane, ε_z approaches a minimum when ε_x is ~1.50 ± 0.05 and then increases. The Poisson's ratio of the HB-IALCE in *x-z* and *x-y* plane is shown in Figure 8.8(c) and (d); it is always positive for deformations in the *x-y* plane, while in the *x-z* plane there is a threshold strain, ε_x ~1.47 ± 0.05 beyond which the Poisson's ratio becomes negative and the system is therefore still

auxetic. Compared to the planar HB-IALCEs, the threshold strain for the auxetic response in the stretched-aligned HB-IALCEs is noticeably delayed. This may be attributed to the limited strain (only 100%) applied during the thermal stretching process, which was insufficient to achieve a high-quality monodomain alignment of the mesogen. As a result, complex mesogen orientations remain, contributing to the delayed auxetic response. To better understand and control the alignment degree, further experimental design and validation will be required.

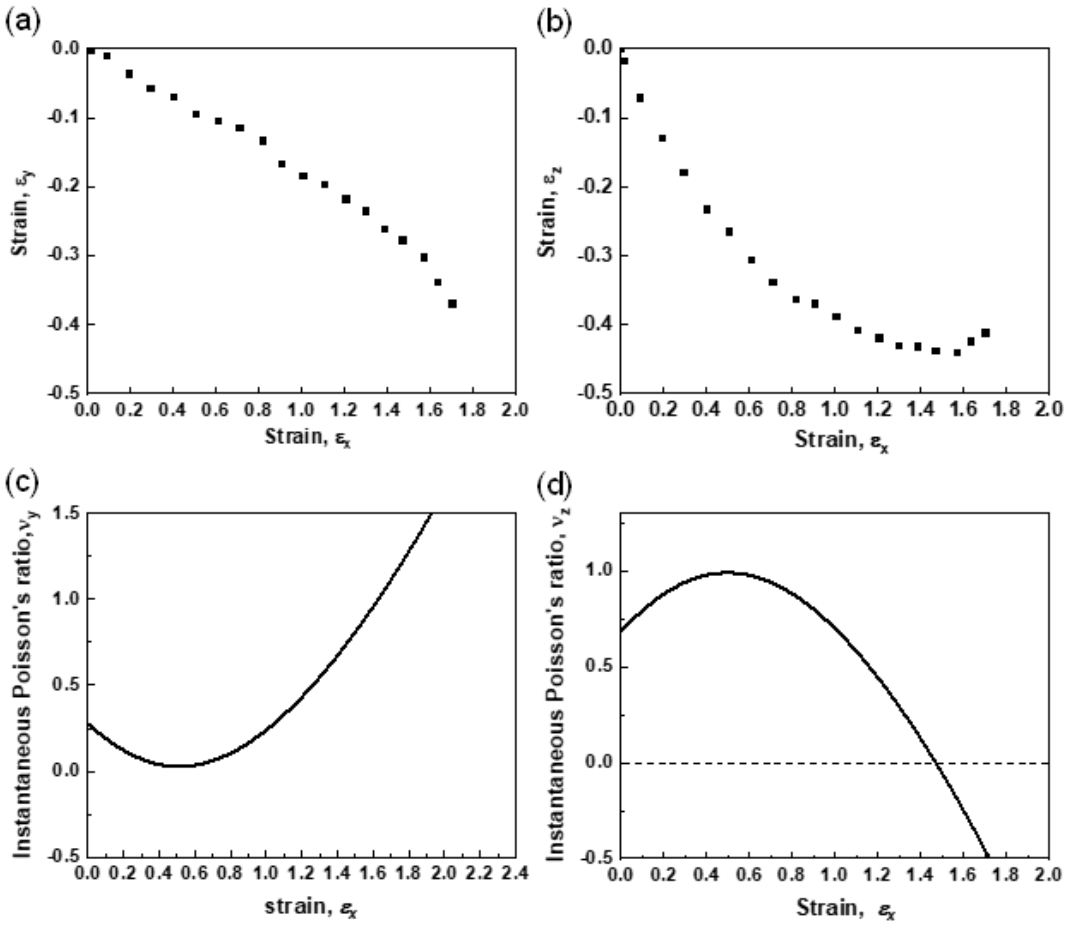

Figure 8.9 Strains (a) ε_x-ε_y and (b) ε_x-ε_z, and instantaneous Poisson's ratio (c) ν_y and (d) ν_z measured for a mechanical aligned isotropic HB-IALCE, fixed at a 100% strain.

Furthermore, the hypothesis for the complex alignment is indirectly supported by the POM taken during the mechanical deformation measurements. During stretching, we observed the phenomenon of the biaxial emergence. As shown in Figure 8.10, at around 90% strain, two optical axes begin to appear and converge at the center at approximately 120% strain. With further stretching, the axes move outward. This observation is consistent with our earlier discussion in Section 5.3, which links the auxetic response to the

emergence of biaxial order. To explain this, the reason might be that in regions where mesogens were not well-aligned or remained in a polydomain state, further rotation of mesogens occurred under mechanical strain in the mechanical deformation measurement. These orientation changes introduced new birefringence across the optical path—similar to the effect of a Berek compensator—allowing us to observe biaxial emergence during the auxetic response. In addition to the insufficient 100% strain during stretching, which may not be enough to achieve a well-aligned monodomain structure, another possible reason for the observed phenomenon is the non-uniform heating of the sample during the stretching process. Uneven temperature distribution may cause hydrogen bonds to break and reform in some regions while remaining intact in others, leading to heterogeneous alignment across the sample. Further experiments are required to verify and better understand the underlying mechanisms of this phenomenon.

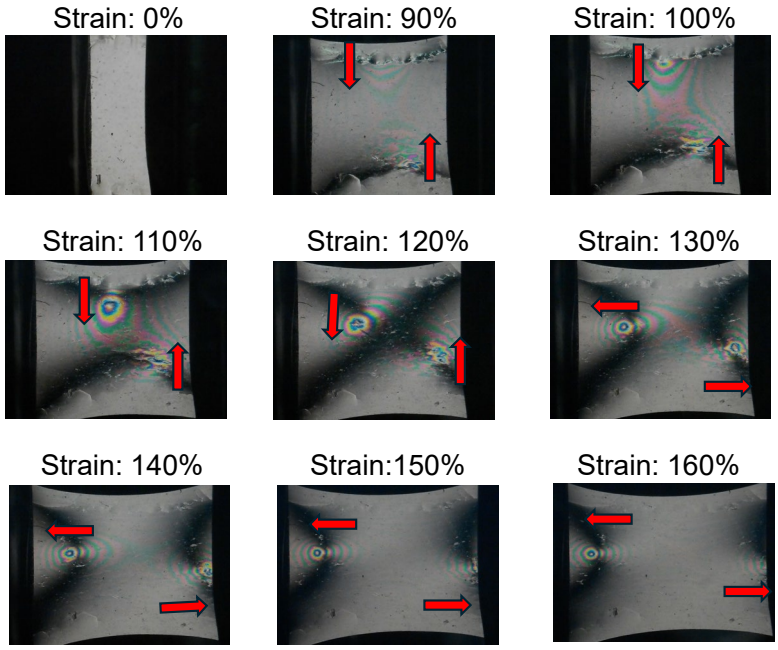

Figure 8.10 The observation of mechanical deformation measurement of a mechanical aligned isotropic HB-IALCE sample under POM. The red arrows indicate the emergence and movement of optical axis.

8.2.4 Discussion and Outlook

In the preliminary exploration of the shape memory effect in HB-IALCEs, we identified several limitations and areas for optimization. As discussed earlier, the ideal mesogen alignment requires a stretching strain beyond 150%; however, in our current setup, the alignment process could not exceed 120% strain due to frequent sample break, especially

when the film thickness is below 150 μm. This issue may originate from: (1) the limited heating area of the hot air gun, which causes inhomogeneous temperature distribution across the film surface, leading to stress concentration and eventual tearing during stretching; (2) intrinsic thermal actuation (~13% strain) in the anisotropic HB-IALCEs, or insufficient film thickness; and (3) the influence of crosslinking density on elasticity and actuation behavior, which in turn affects the thermal-stretching process. To overcome these limitations, we propose several strategies. We first considered introducing photothermal dyes to incorporate photothermal effect with laser to locally induce hydrogen bond breaking and reforming; however, achieving localized temperatures above 100 °C would require extremely efficient photothermal dyes or high-powered lasers, which is technically demanding and not the primary focus of this work. Instead, we plan to explore alternative approaches:

(1) Chemical control of hydrogen bonding through environmental pH modulation [6,7]. For instance, as shown in Figure 8.11, isotropic HB-IALCEs can be immersed in 1 M KOH solution to break dynamic hydrogen bonds, followed by mechanical stretching, and subsequently treated with 1 M HCl solution to restore hydrogen bonding and lock the aligned skeleton. This method offers a promising and controllable path to realize the shape memory effect without relying on thermal stimuli.

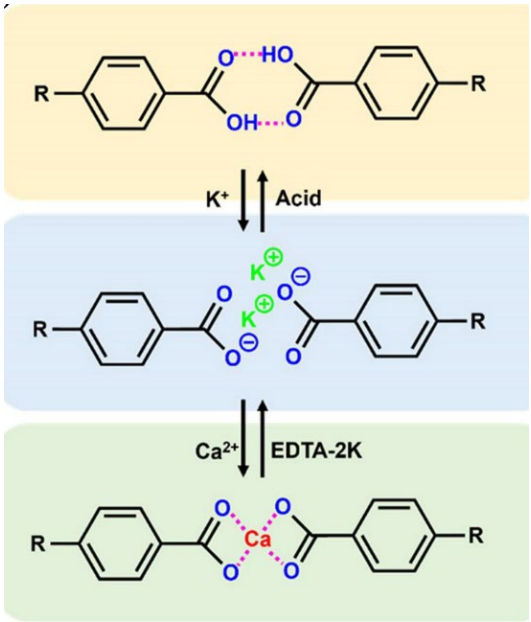

Figure 8.11 Chemical structures of the monomers containing benzoic acid (hydrogen bonds) used in dynamic ionic bonding in LCP or LCE. Reproduced from [6].

(2) Softening and strengthening the film by increasing the proportion of EHA in the formulation and modifying the crosslinking density; tuning the polymerization conditions to yield softer isotropic films with improved elasticity.

(3) Dynamic hydrogen bonds might not be the most suitable choice of dynamic bonds, given the high temperature involvement during mechanical stretching in the current shape memory effect cycle. The anisotropic actuation of mesogens during heating complicates the alignment-locking process. As a backup strategy, we even consider replacing hydrogen bonds with some other dynamic bond mechanism, such as Se–Se bond exchange [11], as shown in Figure 8.12, which can be photo-controlled.

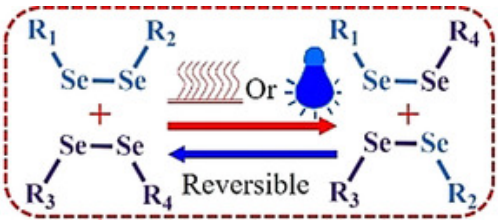

Figure 8.12 Schematic illustration of the metathesis of diselenide bonds. Reproduced form [11].

In our current experimental study, there are still some critical characterizations yet to be carried out. One of the most essential is Fourier Transform Infrared Spectroscopy (FTIR). FTIR is a widely used spectroscopic technique for probing molecular structures, functional groups, and vibrational modes of chemical bonds within materials [12]. By analysing the specific absorption peaks corresponding to hydrogen bonding interactions, FTIR can provide crucial insights into the dynamic behaviour of hydrogen bonds in the HB-IALCEs system under different thermal conditions. This information would be particularly valuable for understanding how temperature affects the breaking and reformation of hydrogen bonds within the polymer skeleton, thereby helping us to optimize the thermal parameters for programming the auxetic response. Through such characterization, we aim to determine the most suitable temperature for achieving effective alignment locking and maximizing the shape memory effect. The FTIR characterization of the dynamic hydrogen bond change is shown in Figure 8.13.

Figure 8.13 The FTIR characteristic spectra change of dynamic hydrogen bond change. Reproduced from [12]

Another essential characterization is Wide-Angle X-ray Scattering (WAXS). WAXS is a powerful technique that utilizes X-ray diffraction to probe short-range order and molecular packing within materials, typically detecting structural features on the scale of 0.1–1 nm [13]. It is particularly effective for examining the ordering of liquid crystal molecules. As mentioned in Section 8.2.1, 6OBA exhibits a smectic liquid crystal phase in its pure state. However, after polymerization, it is essential to verify whether the final HB-IALCE system remains in the nematic phase. Moreover, during thermal stretching, WAXS can provide valuable information about the mesogen alignment within the sample. By analysing the anisotropy in WAXS patterns under different strain levels, we can quantitatively assess the degree of orientation and its correlation with the applied mechanical strain. This information is critical for identifying the optimal alignment conditions that facilitate the most effective shape memory effect and auxetic response.

During our experimental process, we also observed some intriguing phenomena. Specifically, when preparing 100 μm planar HB-IALCE samples with a precursor mixing ratio of 6OBA:RM82 = 3:1 (total crosslinking density stays 8%), the resulting samples did not exhibit auxetic behaviour. However, a highly unusual thermal actuation profile was recorded, as shown in Figure 8.14.

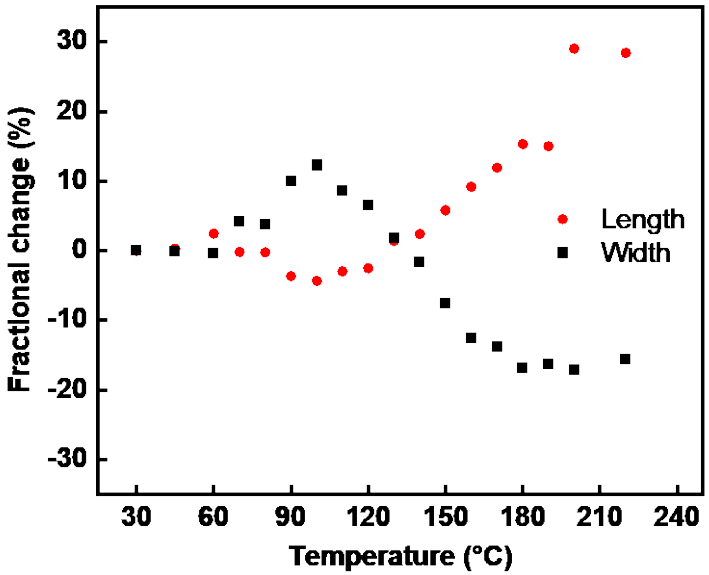

Figure 8.14 The thermal actuation of the 100μm planar HB-IALCE with a RM82:6OBA at 1:3.

Upon heating to 100°C, instead of the typical contraction along the alignment direction seen in conventional anisotropic LCEs, the sample initially expanded by approximately 15% along the alignment direction before subsequently contracting. This counterintuitive two-step actuation behaviour may be closely related to the presence of smectic LC phase within the precursor mixture. The existence of smectic layering might introduce a more complex molecular reorientation during thermal actuation, potentially leading to an initial expansion due to layer spacing changes, followed by contraction as the material transitions into a more disordered or nematic-like state. According to Yao *et al.* [14], introducing the chevron smectic C–smectic A–isotropic phase transition would cause an unexpected reversal in the strain distribution within LCEs, which results in ambidirectional deformation, such as successive expansion or contraction, as well as twisting and tilting in opposite directions. Further investigations will be required to clarify the underlying mechanism of this actuation behaviour.

References

1. S. R. Berrow, T. Raistrick, R. J. Mandle, H. F. Gleeson, Auxetic Liquid Crystal Elastomers: Overcoming Barriers to Scale-Up. *ACS Appl. Polym. Mater.* 2025. https://doi.org/10.1021/acsapm.5c00212.
2. A. Lendlein, S. Kelch, Shape-Memory Polymers. *Angew. Chem. Int. Ed.* 2002, *41*, 2034-2057.
3. A. Lendlein, O. E. C. Gould, Reprogrammable recovery and actuation behaviour of shape-memory polymers. *Nat. Rev. Mater.* 2019, *4*, 116–133.
4. H. Guo, T.-P. Ruoko, H. Zeng, A. Priimagi, Hydrogen-Bonded Liquid Crystal Elastomers Combining Shape Memory Programming and Reversible Actuation. *Adv. Funct. Mater.* 2024, *34*, 2312068.
5. G. Chen, J. Dong, X. Xu, W. Zou, B. Jin, W. Peng, Q. Zhao, T. Xie, N. Zheng, Converse two-way shape memory effect through a dynamic covalent network design. *J. Mater. Chem. A* 2022, *10*, 10350.
6. R. Lan, X.-G. Hu, J. Chen, X. Zeng, X. Chen, T. Du, X. Song, H. Yang, Adaptive liquid crystal polymers based on dynamic bonds: From fundamentals to functionalities. *Responsive Mater.* 2024, *2*, e20230030.
7. S. Samanta, S. Kim, T. Saito, A. P. Sokolov, Polymers with Dynamic Bonds: Adaptive Functional Materials for a Sustainable Future. *J. Phys. Chem. B* 2021, *125*, 9389-9401.
8. Y. Zhan, D. J. Broer, D. Liu, Perspiring Soft Robotics Skin Constituted by Dynamic Polarity-Switching Porous Liquid Crystal Membrane. *Adv. Mater.* 2023, *35*, 2211143.
9. K. D. Harris, C. W. M. Bastiaansen, J. Lub, D. J. Broer, Self-Assembled Polymer Films for Controlled Agent-Driven Motion. *Nano Letters* 2005, *5*, 1857-1860.
10. M. Dai, O. T. Picot, J. M. N. Verjans, L. T. de Haan, A. P. H. J. Schenning, T. Peijs, C. W. M. Bastiaansen, *ACS Appl. Mater. Interfaces* 2013, *5*, 4945–4950.
11. L. Chen, H. K. Bisoyi, Y. Huang, S. Huang, M. Wang, H. Yang, Q. Li, Healable and Rearrangeable Networks of Liquid Crystal Elastomers Enabled by Diselenide Bonds. *Angew. Chem. Int. Ed.* 2021, *60*, 16394.
12. C. Berthomieu, R. Hienerwadel, Fourier transform infrared (FTIR) spectroscopy. *Photosynth Res* 2009, *101*, 157–170.
13. S. Rabiej, A. Wlochowicz, SAXS and WAXS investigations of the crystallinity in polymers. *Angew. Makromol. Chem.* 1990, *175*, 81-97.
14. Y. Yao, A. M. Wilborn, B. Lemaire, F. Trigka, F. Stricker, A. H. Weible, S. Li, R. K. A. Bennett, T. C. Cheung, A. Grinthal, M. Zhernenkov, G. Freychet, P. Wąsik, B. Kozinsky, M. M. Lerch, X. Wang, J. Aizenberg, Programming liquid crystal elastomers for multistep ambidirectional deformability. *Science* 2024, *386*, 1161-1168.